INTERNATIONAL DOCTORAL
SCHOOL OF THE USC

Manuela
Cedrún Morales

PhD Thesis

Engineering smart nano metal-organic frameworks for biomedical applications

Santiago de Compostela, 2024

Doctoral Programme in Materials Science

ESCOLA DE DOUTORAMENTO
INTERNACIONAL DA USC

DOCTORAL THESIS

ENGINEERING SMART NANO METAL-ORGANIC FRAMEWORKS FOR BIOMEDICAL APPLICATIONS

Author

Manuela Cedrún Morales

Supervisors: Pablo Alfonso del Pino González de la Higuera, Pablo Taboada Antelo

PHD PROGRAMME IN MATERIALS SCIENCE

SANTIAGO DE COMPOSTELA

Acknowledgments

Quiero dar las gracias a mis directores de tesis, los doctores Pablo del Pino y Pablo Taboada, por toda su ayuda, guía, y tiempo proporcionados que han hecho posible este trabajo. También querría agradecer a las doctoras Beatriz Pelaz y Ester Polo su labor como supervisoras de tesis y su constante apoyo para sacar adelante todos los proyectos.

Igualmente, estoy muy agradecida al Dr. David Fairen, del CEB por haberme dado la oportunidad de realizar en su grupo mi estancia doctoral, por acogerme desde el primer momento y permitirme aprender de su grupo de investigación.

Doy las gracias, también, a todos los técnicos de la Unidad de Microscopía electrónica y Rayos X de RIAIDT por realizar las diversas mediciones, fundamentales para el desarrollo de esta tesis. Asimismo, agradezco a la Universidad de Santiago de Compostela, al CiQUS y a todos sus técnicos que hayan puesto a mi disposición los medios necesarios para desarrollar este trabajo.

Por último, quiero expresar mi sincero agradecimiento a la AEI por la beca FPU (FPU19/03155) por su apoyo financiero, imprescindible para la realización de esta tesis doctoral.

USC
UNIVERSIDADE DE SANTIAGO DE COMPOSTELA

USC
UNIVERSIDADE
DE SANTIAGO
DE COMPOSTELA

Contents

Acknowledgments i

Contents iii

List of abreviations vii

Summary ix

Resumo xvii

1. Introduction 1

1.1. NANOTECHNOLOGY AND METAL ORGANIC FRAMEWORKS 5
1.1.1. Nanotechnology 5
1.1.2. Metal-organic frameworks 7
1.1.3. Classification of MOFs: Reticular chemistry, SBUs 8
1.1.4. Synthesis of nanometric-size MOFs (NMOFs) 9
1.1.5. Synthesis of inorganic nanoparticles and nMOFs nanocomposites 10
1.1.6. Cargo Loading inside MOF´s pores. 11
1.1.6.1. Post-synthesis encapsulation 11
1.1.6.2. In situ encapsulation 13
1.1.7. Surface modification 14
1.1.7.1. Coordinative PSM 15
1.1.7.2. Covalent PSM 15
1.1.7.3. “Core-shell” strategies 16
1.1.7.4. Cell membrane coating 16
1.1.8. Stability 17
1.1.8.1. Colloidal stability 17
1.1.8.2. Chemical stability 18
1.1.9. NMOFs in biological media 19
1.1.9.1. Size and agglomeration 20
1.1.9.2. Surface chemistry 20
1.1.9.3. Biological chemical stability 21

1.2. METALLIC NANOPARTICLES FOR NMOFs COMPOSITES 21
1.2.1. Plasmonic nanoparticles 21
1.2.2. Catalytic nanoparticles 24
1.2.3. Magnetic nanoparticles 25

1.3. NMOFS FOR BIOAPPLICATIONS 26
1.3.1. Drug delivery: Stimuli-responsive NMOF-based DDS. 26
1.3.1.1. pH responsive NMOFs 27
1.3.1.2. Magnetic responsive NMOFs 28
1.3.1.3. Light-mediated therapy, or phototherapy 28
1.3.2. NMOFs platforms as nanoreactors in living cells 30

USC UNIVERSIDADE DE SANTIAGO DE COMPOSTELA

1.3.3. Metal organic frameworks for biomedical imaging 33
1.3.4. Metal−Organic Frameworks as Efficient Oral Detoxifying Agents 34
1.4. OBJECTIVES 37
1.4.1. Chapter 1 37
1.4.2. Chapter 2 38
1.4.3. Chapter 3 38
2. Materials and methods 41
2.1. REAGENTS 43
2.2. SYNTHESIS OF GOLD NANOBIPYRAMIDS (AuBy) 43
2.2.1. Synthesis of penta-twinned seeds 43
2.2.2. Gold bipyramids (AuBy) synthesis 44
2.2.3. PEGylation and phase transfer of gold bipyramids (AuBy) 44
2.3. NMOFS SYNTHESIS 44
2.3.1. ZIF-8 44
2.3.2. UiO-67 44
2.3.3. NU-1000 45
2.3.4. PCN-222 45
2.3.4.1. Zr cluster 45
2.3.4.2. PCN-222 synthesis 45
2.4. SYNTHESIS OF AuBy@NMOFS COMPOSITES 45
2.4.1. AuBy@ZIF-8 45
2.4.2. AuBy@NU-1000 46
2.4.3. AuBy@PCN-224 46
2.5. CARGO ENCAPSULATION 46
2.5.1. Cresyl violet (CV) 46
2.5.2. Calcein 47
2.5.3. Drug loading 47
2.6. SURFACE FUNCTIONALIZATION 48
2.6.1. PMA functionalization procedure 48
2.6.1.1. PMA synthesis 48
2.6.1.2. PMA modification 49
2.6.1.3. PMA functionalization 49
2.6.1.4. Click chemistry. 50
2.6.2. PEGylation 51
2.6.2.1. MeO-PEG-PO_3 synthesis 51
2.6.2.2. MeO-PEG-PO_3 functionalization procedure 52
2.6.3. DNA based functionalization 52
2.6.3.1. DNA-PO_3 functionalization of Zr MOFs 52
2.6.3.2. DNA-N_3 Hybridization 52
2.6.4. Protein functionalization 52
2.6.4.1. BSA functionalization with Cy5-NHS 52
2.6.4.2. BSA-Cy5 functionalization with DBCO-NHS 53

USC UNIVERSIDADE DE SANTIAGO DE COMPOSTELA

2.6.4.3. UiO-67(Calc)@DNA functionalization with BSA 53
2.6.5. NIR laser irradiation experiments 53
2.7. CHARACTERIZATION TECHNIQUES 54
2.7.1. Thermogravimetric analysis (TGA) 54
2.7.2. Optical characterization (UV-Vis) 55
2.7.3. Fourier transform infrared spectroscopy (FTIR) 55
2.7.4. Dynamic light scattering (DLS) and ζ -potential 55
2.7.5. Nanoparticle tracking analysis (NTA) 55
2.7.6. Quantification by Fluorescence Measurements 55
2.7.7. Scanning electron microscopy (SEM) 56
2.7.8. Inductively coupled plasma-optical emission spectrometry *(ICP-OES)* 56
2.7.9. Powder X-Ray diffraction (PXRD) 56
2.7.10. N_2 adsorption–desorption analysis 56
2.7.11. Colloidal stability tests 56
2.7.12. High performance liquid chromatography (HPLC): 58
2.7.13. Cargo loading stability. 58
2.8. IN VITRO STUDIES 58
2.8.1. Cell culture 58
2.8.2. MTT toxicity assay 58
2.8.3. Flow cytometry 59
2.8.3.1. Concentration calculations of NMOFs 59
2.8.3.2. VitroCheck NanoParticle Reference Kit: concentration calculation 59
2.8.4. Microscopy imaging 59
2.8.5. Spheroids 60
2.8.6. LIVE/DEAD assay 60
2.8.7. Statistical analysis 60
3. Results and discussion 61
3.1. CLICKABLE POLYMER-BASED FOR CUSTOMIZING THE INTERACTION OF NMOFS WITH LIVING CELLS 63
3.1.1. Synthesis and characterization of NMOFs 65
3.1.2. PMA surface functionalization 67
3.1.3. Cresyl violet cargo encapsulation 75
3.1.4. Click chemistry-based surface functionalization. 85
3.1.5. Cell studies 88
3.2. POST-SYNTHESIS SURFACE MODIFICATION OF Zr NMOFs 93
3.2.1. Concentration analysis: NTA vs flow cytometry 95
3.2.2. Phosphate modified DNA and PEG coordinative PSM of Zr NNMOFs 103
3.2.3. Click chemistry protein functionalization of UiO-67 107
3.2.3.1. Protein surface functionalization 108
3.2.3.2. Structural characterization 110
3.2.3.3. 2D cell culture experiments 113
3.3. LIGHT RESPONSIVE NANOANTENAS INTEGRATED INTO NMOFS FOR PHOTOTHERMAL DRUG DELIVERY 119

USC UNIVERSIDADE DE SANTIAGO DE COMPOSTELA

3.3.1. NCs synthesis and characterization 120
3.3.2. Colloidal stability 125
3.3.3. Thermal characterization 128
3.3.4. Thermoplasmonic behavior inside living cells in 2D 131
3.3.5. Drug loading - Efficiency as drug delivery systems 136
3.3.6. DDSs efficiency inside living cells in 3D cell culture 141
4. Conclusions 149
References 153
Appendices – Rights & Permissions 167
Appendix I: Conflict of interest 167
Appendix II: PhD publications and permissions 168
Appendix III: Permissions to publish images, tables, and figures. 170
Appendix IV: All the other images, tables, and figures 172

USC UNIVERSIDADE DE SANTIAGO DE COMPOSTELA

List of abreviations

AA	Acetic acid
AMF	Alternating magnetic field
API	Active pharmaceutical ingredient
ASA	Acetylsalicylic acid
AuNPs	Gold nanoparticles
AuNSs	Gold nanostar
BET	Brunauer, Emmett & Teller
BSA	Bovine serum albumin
BTP	Bis-tris-propane buffer
CbPt	Carboplatin
CPPs	Cell penetrating peptides
CPT	20-(S)-camptothecin
CT	Computed tomography
CTA^+	Hexadecyltrimethylammonium salts
CuAAC	Cu(I)-catalyzed azide–alkyne cycloaddition
CuNPs	Copper nanoparticles
CUS	coordinatively unsaturated metal sites
CV	Cresyl Violet
DBCO	Dibenzo cyclooctyne group
DCA	Sodium dichloroacetate
DDA	Dodecylamine
DDSs	Drug delivery systems
DEF	Dimethylformamide
DLS	Dynamic light scattering
DMEM	Dulbecco's Modified Eagle Medium
DMF	Dimethylformamide
DMSO	Dimethylsulfoxide
DOX	Doxorubicin
FAM	Fluoresceinamine
FBS	Foetal bovine serum
FTIR	Fourier transform infrared spectroscopy
GI	Gastrointestinal
GSH	Glutathione
HCl	Hydrochloric acid
HNO_3	Nitric acid
HOE	Hoechst H 33258
HSAB	Hard soft acid-base
HT	Human transferrin
ICA	Imidazolate-2-carboxaldehyde
ICP-MS	Inductively coupled plasma mass spectrometry
iNPs	Inorganic NPs
LDH	Lactate dehydrogenase
LSP	Localized surface plasmon
LSPR	Localized surface plasmon resonance
MeOH	Methanol
MMPs	Matrix metalloproteinases
MNPs	Metal nanoparticles
MNPs	Magnetic nanoparticles
MOFs	Metal-organic frameworks
MeO-PEG-N_3	Methoxy PEG-azide
MPS	Mononuclear phagocyte system
MR	Magnetic resonance

USC UNIVERSIDADE DE SANTIAGO DE COMPOSTELA

MRI	Magnetic resonance imaging
MTT	3-[4,5-dimethylthiazol-2-yl]-2,5-diphenyltetrazolium bromide
NBPs	Nanobipyramids
NCs	Nanocomposites
NCus	Nanocubes
NDDSs	NP drug delivery systems
NIR	Near infrared
NMOFs	Nano-Metal Organic Frameworks
NNI	National Nanotechnology Innitiative
NPs	Nanoparticles
NR	Nanoreactors
NRs	Nanorods
NSMs	Nanostructured materials
NSs	Nanostars
NTA	Nanoparticle tracking analysis
NTs	Nanotriangles
OI	Optoacoustic imaging
OXA	Oxaliplatin
PAI	Photoacoustic imaging
PBS	Phosphate buffer saline
PCN	Porous coordination networks
PdNC	Palladium nanocube
PdNP	Palladium nanoparticle
PDT	Photodynamic therapy
PEG	Polyethylene glycol
PET	Positron emission tomography
PMA	Poly- [isobutylene-alt-maleic anhydride]-graft-dodecyl
PSF	Phagolysosomal simulated fluid
PSM	Post-synthetic modification
PSs	Photosensitizers
PTAs	Phototherapeutic agents
PTT	photothermal therapy
PVP	Poly(vinylpyrrolidone)
PXRD	Powder X-Ray diffraction
R6G	Rhodamine 6G
ROI	Region of interest
ROS	Reactive oxygen species
RT	Room temperature
SBU	Secondary Building Units
SEM	Scanning electron microscopy
SN	Supernatant
SPAAC	Strain-promoted alkyne azide cycloaddition
SP	Surface plasmon
TAMRA	5-carboxytetramethylrhodamine
TEM	Transmission electron microscopy
TFA	Trifluoroacetic acid
TGA	Thermogravimetric analysis
THF	Tetrahydrofuran
TMCs	Transition metal catalysts
TPL	Two-photon luminescence
UiO	Universitetet i Oslo
ZIF	Zeolitic imidazolate framework
ZnP	Zinc-phthalocyanine

USC UNIVERSIDADE DE SANTIAGO DE COMPOSTELA

Summary

Nanotechnologies have become indispensable in the biomedical field, driving significant advancements in disease diagnosis, therapy, and monitoring. Their ability to operate at the nanoscale allows for precise interactions with cells and tissues, thereby enhancing treatment selectivity and effectiveness. Among their many applications, nanoparticles (NPs) stand out as versatile drug delivery vehicles, facilitating controlled and targeted release to minimize adverse effects. Additionally, NPs can be tailored for early detection of biomarkers, thereby improving diagnostic accuracy. The integration of nanotechnologies opens up promising avenues for personalized medicine, where treatments can be customized based on individual characteristics.

Among the diverse array of nanomaterials investigated for therapeutic applications, nano Metal-Organic Frameworks (NMOFs) have garnered considerable interest due to their unique structural characteristics and customizable properties. NMOFs are crystalline materials composed of metal ions or clusters coordinated with organic ligands, resulting in porous structures with high surface areas and tunable pore sizes. These features render NMOFs highly attractive for the development of advanced drug delivery platforms tailored to meet the specific demands of modern medicine. A crucial factor relies on governing the synthesis and design of NMOFs. By cautiously selecting metal ions, organic linkers, and synthetic conditions, the structural and chemical properties of NMOFs can be finely tuned to accommodate various therapeutic agents. Furthermore, the integration of functional groups within the NMOF framework enables precise targeting and controlled release of drugs, thereby enhancing therapeutic efficacy while minimizing systemic toxicity.

Functionalization plays a pivotal role in augmenting the performance and versatility of NMOFs for drug delivery applications. Post-synthesis modification (PSM) techniques are extensively explored as means to enhance stability, biocompatibility, and cargo-loading capacities of NMOFs. Additionally, PSM approaches enable the introduction of targeting ligands onto the surface imparting functionalities crucial for precise drug delivery. Several strategies have been developed for surface functionalization, including covalent modification, coordination chemistry, core-shell approaches, and cell membrane coatings.

Moreover, the combination of light responsive agents, as gold nanoparticles, with NMOFs to respond to external stimuli such as NIR light represents an especially attractive feature for controlled and targeted drug delivery. In particular, NIR light has the capability to penetrate deep into biological tissues with minimal absorption and scattering, enabling precise activation of drug loaded NMOFs in specific areas of the body.

Considering all of this, the main objective of this doctoral thesis is the design, development, and optimization of NMOFs based systems for biomedical applications, and more specifically for drug delivery.

The first chapter of this thesis aims to develop a novel surface coating method using an amphiphilic polymer that can be modified with dibenzo cyclooctyne (DBCO) groups, making it universally applicable for post-synthetic modification. This method is applied to various

USC
DE SANTIAGO
DE COMPOSTELA

NMOFs, including UiO-67, NU-1000, PCN-222, and ZIF-8, selected for their potential biomedical utility. The primary objective is to enhance their stability within biological environments. The chapter begins with synthesizing and meticulously characterizing the NMOFs to ensure high monodispersity and uniformity, with sizes of approximately 150 nm. Subsequently, these NMOFs are coated with the chosen amphiphilic polymer (PMA) using a core-shell approach. This coating not only improves their colloidal stability but also preserves their structural integrity in diverse biologically relevant media. Notably, it proves effective in stabilizing NMOFs from the Zr family, which typically degrade in aqueous and phosphate-based solutions. Colloidal and structural stability assessments, utilizing DLS, electron microscopy, and PXRD measurements, consistently demonstrate notable improvements in water, DMEM, and PSF media for PMA-coated NMOFs. Prior to PMA application, only Zr MOFs retain their morphology in both water and cell media, while ZIF-8 experiences evident degradation within 5 hours. However, the crystallinity of Zr MOFs is noticeably compromised upon exposure to aqueous media. Upon PMA coating, all colloidal, morphological, and crystalline structures remain intact, affirming the efficacy of PMA in preserving sample stability.

Following this, the NMOFs are loaded with a fluorescent molecule, Cresyl Violet (CV), to assess their encapsulation capacity. Subsequent coating with PMA ensures cargo retention and NMOF stability. Release studies in water, DMEM and PSF media, comparing particles with and without polymer coating via fluorescence measurements, demonstrate markedly improved cargo retention with PMA coating. Specially ZIF-8 and UiO-67 NMOFs present a clear decrease in the CV released when the PMA is on the surface of the particles. This underscores the NMOFs' high loading capacity and stability in biological media, critical for drug delivery applications. Additionally, the retention of the cargo is confirmed by toxicity assays, especially in ZIF-8 and UiO-67, where the non-coated nanoparticles show a reduction in cell viability at concentrations over 10 pM due to the release of the CV. On the other hand, when NMOFs are functionalized with PMA, the samples do not present any toxicity even at high concentrations.

The last part of the chapter involves the further functionalization of the loaded NMOFs, focusing particularly on ZIF-8 and UiO-67. Leveraging the previous polymer coating as an anchor point, various biologically relevant molecules—such as polyethylene glycol, mannose, and cell-penetrating peptides—are attached to the NMOF surfaces using click chemistry-based biorthogonal reactions. Click chemistry offers high yields, broad applicability, low cytotoxicity, stereospecificity, and simple conditions. It's compatible with various functional groups, making it versatile for NMOF surface modification. Copper-free click chemistry, specifically strain-promoted alkyne azide cycloaddition (SPAAC), has rapid, non-cytotoxic reactions, ideal for cell use. In this work, PMA is previously modified with DBCO groups to allow click chemistry reactions with the azide modified molecules.

ZIF-8 and UiO-67 are selected for these studies, both loaded with CV. Additionally, non-loaded ZIF-8 functionalization is also studied with comparative purposes. To track them intracellularly, Cy5-N_3 is attached to the surface following the same click chemistry procedure. Structural characterization precedes the study of internalization processes of these derivatized NMOFs into cancer cells, with DLS and ζ-potential measurements proving the correct functionalization. By comparing the uptake efficiency of NMOFs with different surface

modifications, the research aims to elucidate their impact on cellular uptake mechanisms. Flow cytometry experiments are carried out to see the internalization of the NMOFs using the fluorescence of the encapsulated CV. Particles are incubated at three different concentrations for three hours with A549 cells. ZIF-8 results indicate increased internalization with CPP on the MOF surface and reduced uptake with PEG, while mannose-functionalized particles exhibit no significant difference compared to PMA-coated MOFs. UiO-67 shows similar tendency in all cases. As anticipated, CPP enhances system recognition abilities and boosts cell internalization, while PEG imparts particle stealthiness, resulting in reduced cell recognition. These studies are corroborated with confocal microscopy, where fluorescence quantification of the images shows high coherence with flow cytometry. Again, CPP in the surface of both ZIF-8 and UiO-67 increases the cell internalization and PEG reduces it, whereas mannose coated systems do not present significant differences with the PMA coated MOFs. Moreover, ZIF-8 samples with Cy5 are also analyzed with microscopy images, showing differences with the previous cases. Specially, there is a high increase for mannose functionalized particles, that may stem from a synergistic effect arising from the conjunction of Cy5 and mannose on the particle surface, potentially augmenting cell recognition. These findings affirm the efficacy of click chemistry-based functionalization in altering cell recognition and uptake.

Overall, the chapter showcases the effectiveness and versatility of the proposed coating approach in enhancing the stability and functionality of NMOFs for biomedical applications, particularly in targeted drug delivery and imaging.

Chapter 2 aims to develop new surface functionalization methods via DNA-based coordinative post-synthetic modification (PSM) across various Zr family MOFs, facilitated by the availability of free Zr sites on the MOF surfaces for coordinating phosphate or carboxylate-modified molecules. The investigation involves UiO-67, NU-1000, and PCN-222 Zr NMOFs previously synthesized. For comparison, PEG is employed in analogous functionalization studies. The subsequent functionalization of the DNA-coated surfaces involves the hybridization of complementary azide-modified DNA oligos, serving as anchoring points for click chemistry conjugation with bioactive molecules featuring DBCO groups. Notably, this study is focused on calcein-loaded UiO-67 nanoparticles, with DBCO-modified BSA chosen for subsequent bioactive functionalization.

Before functionalization studies, thorough concentration analyses are conducted using nanoparticle tracking analysis (NTA) and flow cytometry. Accurate quantification of nanoparticle concentration is crucial for understanding their interactions with cells. Thus, robust methodologies are essential to precisely measure the total concentration and size distribution of the NMOFs being studied. NTA is a valuable tool for nanoparticle characterization, offering high-resolution size measurements and count-based concentration determination without the need for fluorescent markers. However, its sensitivity to different nanomaterial types can affect measurement accuracy. Moreover, it requires specialized equipment and software, posing logistical challenges and cost constraints for some researchers. Despite limitations, NTA provides crucial insights into nanoparticle properties, aiding in various scientific investigations.

Flow cytometry presents a viable alternative for nanoparticle concentration characterization, due to its availability in most biology laboratories. Despite its primary use in

USC DE COMPOSTELA

cell analysis, this instrument can offer both qualitative and quantitative analysis of NPs size and concentration through measurements of scattering and fluorescence. However, conventional flow cytometers typically have a lower size detection limit for light scattering, ranging from 200 to 500 nm, while fluorescence measurements tend to be more sensitive. To capitalize on the diverse nature of selected Zr NMOFs (UiO-67, NU-1000, and PCN-222), a comparative analysis between NTA and flow cytometry experiments is conducted to determine NP concentration for subsequent in vitro experiments.

NMOFs concentrations are first analyzed with NTA and then with flow cytometry. In the last case, particles per mL are calculated using the scattering of the selected particles as well as their own florescence properties in the case of the NU-1000 and PCN-222. To further confirm the results, 100 nm FITC-like beads were added to the solution of particles. Results show similar ranges of concentration in all cases. However, values obtained for UiO-67 using flow cytometry are higher with respect to NTA due to possible background present in the solution used in flow cytometry that leads to an overestimation of the concentration. On the other hand, with NU-1000 and PCN-222, due to the fluorescence properties of these materials it is easier to distinguish the particle populations and the results are slightly lower than NTA values. Overall, these findings underscore the significant potential of flow cytometry in nanoparticle concentration and size analysis. Additionally, it demonstrates a main advantage over NTA measurements, based on the ability of performing rapid and automatic measurements.

After the concentration characterization, coordinative PSM is studied for the three Zr MOFs. DNA and PEG molecules modified with phosphate groups are used to functionalize the surface of the particles. Due to surface Zr defects, facilitating functionalization with phosphate groups, Zr−O−P coordination bonds are formed. After the functionalization, particles are characterized showing no differences in the size, morphology, or absorption spectra. Moreover, the introduction of DNA results in a notable decrease in total charge, rendering all samples negatively charged, indicating successful NMOF coating. Addition of PEG imparts neutrality to particles due to free methoxy groups at the molecule's extremity. The colloidal stability of the systems is assessed in water, DMEM and PSF, proving that both functionalizations prevents particle aggregation specially in cell media.

Subsequently, a novel functionalization approach utilizing DNA as an anchor point is investigated. In this study, UiO-67 is selected as the model NMOF, and to facilitate further in vitro experiments, particles are loaded with calcein molecules. Initially, following DNA-PO_3 functionalization, the complementary chain modified with an azide group is introduced to the structure, allowing N_3 groups to remain free on the particle surface. Following this, DBCO-modified BSA is added to the structure via click chemistry reactions between the azide and the DBCO, thereby establishing a covalent bond between the protein and the NMOF. BSA is also marked with fluorescence (Cy5) to allow characterization experiments. Concurrently, particles are functionalized with PEG to enable comparative experiments.

Particles characterization indicates no changes in the morphology nor the size of the structures, besides a slight increment when DNA and BSA are added. ζ-potentials show changes that manifest the correct functionalization. Moreover, fluorescence measurements and UV-Vis allow the quantification of BSA in the surface of the particles. Then, toxicity studies are performed to determine the cell viability of the particles, proving high viability in all cases. Cell

uptake studies are conducted on NMOFs using fluorescence microscopy and flow cytometry. The presence of green fluorescence within cells in these experiments indicated successful dye encapsulation within the NMOFs, given calcein's inability to permeate interact cell membranes.

Initially, flow cytometry quantitatively assesses NMOF uptake with the A549 cell line. UiO-67 NMOFs undergo incubation periods of 0.5, 1, and 3 hours. Uptake data are adjusted using a correction factor derived from fluorescence measurements of samples at the same concentration employed in the uptake experiments. Given previous differences in calcein signal among samples, standardizing uptake values relative to total NMOF fluorescence is crucial. These results were confirmed using fluorescence microscopy experiments. Confocal imaging vividly illustrates the robust internalization of calcein-loaded nanoparticles, consistent with trends observed in flow cytometry analyses. The impermeability of calcein alone across cell membranes underscores the efficient internalization facilitated by NMOFs. Additionally, the incorporation of an early endosome marker (HT) validates the endocytic pathway involved. Colocalization between calcein and HT confirms sample presence within endosomes, with BSA (Cy5 channel) colocalization indicating intact coating even after translocating into lysosomes. This method proves effective for surface modification, offering diverse possibilities for biomolecule attachment.

This novel protein functionalization approach for NMOFs holds promise for various applications, including vaccine development. Immobilizing proteins onto NMOF surfaces can create a stable and biocompatible platform for vaccine delivery, enhancing antigen stability, controlling release kinetics, and modulating immune responses. Utilizing viral proteins for functionalization could mimic natural infection processes, eliciting potent immune responses. Precise control over protein density and configuration on NMOF surfaces could yield highly efficient and specific vaccine formulations.

Overall, the approach proposed in this chapter offers opportunities for targeted drug delivery and therapy, where precise control over biomolecule attachment and release kinetics can enhance treatment efficacy while minimizing side effects. By leveraging the distinctive properties of NMOFs and incorporating protein functionalization, personalized therapeutic interventions for a range of diseases can be developed, marking a significant advancement in the field of medical treatment.

On the other hand, besides some NMOFs show remarkable properties as high drug loading capacity, biocompatibility, and controlled release kinetics, their inherent lack of responsiveness to external stimuli presents a limitation in designing dynamic drug delivery systems. Last chapter of this thesis explores a novel approach by integrating light-responsive nanoantennas into NMOFs to enhance their functionality as smart drug delivery platforms.

Gold nanoparticles, owing to their plasmonic properties, exhibit unique characteristics in light interaction, particularly advantageous in the NIR biological window. Within this spectral range, NIR light can penetrate biological tissues with minimal absorption and scattering, allowing for deeper tissue penetration compared to visible light. These properties stem from the collective excitation of electrons on the nanoparticle's surface when irradiated with light. This phenomenon enables gold nanoparticles to efficiently absorb and scatter light, making them valuable tools in a wide range of applications, from biomedical sensing to nanotechnology. This

property allows them to generate heat under appropriate laser irradiation, showing great potential in hyperthermia therapies for diseases like cancer, where localized temperature elevation can be employed to selectively destroy malignant cells. This response can be utilized for other purposes, as to trigger the release of encapsulated cargoes in selected DDSs. Specifically, in core-shell nanosystems comprising a gold nanoparticle core and a shell composed of NMOF, the gold nanoparticles can function as nanoantennas, provoking the diffusion of encapsulated payloads within the pores of the NMOF structure due to the temperature increase.

The integration of gold bipyramid (AuBy) nanoantennas into two distinct NMOFs, namely ZIF-8 and NU-1000, leads to the formation of core@shell nanosystems with inherent photothermal capabilities. This integration is motivated by the potential to leverage NIR light for controlled drug release, offering spatiotemporal precision in drug delivery.

First, AuBys are synthetized following previous protocols. The obtained nanoparticles present sizes of 80 nm and a clear absorption band in the NIR (808 nm) corresponding to the longitudinal LSPR. Using the AuBys, two NMOFs are selected as the shell of the structure: ZIF-8 and NU-1000. Both systems are synthetized obtaining particles of ~150 nm presenting one AuBy per MOF. Then, using CV as a model drug, the loading and release dynamics of the core@shell nanosystems are meticulously analyzed. Further polymer functionalization is performed using previously studied coatings of PMA and PEG-PO_3 for ZIF-8 and NU-1000 NCs, respectively. After the loading and surface coating, NCs are deeply characterized using DLS, electron microscopy, PXRD and N_2 adsorption measurements. Additionally, stability studies are performed in biological media to check the ability of the samples to maintain colloidal and structural integrity. In both cases, similarly to previous chapters, the NCs present high stability in water and cell media, while samples without the polymers are clearly degraded or lose the crystallinity.

The subsequent investigation is focused on studying the thermoplasmonic properties of the systems. A NIR laser is utilized to irradiate various concentrations of NCs dispersed in water, employing different irradiances between 7.5 and 12 $W \cdot cm^{-2}$. Heating curves obtained from these experiments reveal a temperature increase of up to 70 ºC in the most concentrated samples, attributed to the thermoplasmonic response of the AuBys in the core of the structures. Furthermore, controlled release triggered by NIR light is examined. Post-irradiation, samples are centrifuged, and the supernatant is characterized via fluorescent measurements, indicating a significant increase in the percentage of CV released from the NCs. These findings underscore the stimuli-responsiveness of the systems, highlighting their potential for drug delivery applications.

To validate this capability in 2D cell culture, particles are incubated with A549 cells for 6 hours. Subsequently, microscopy experiments are conducted using a Leica laser scanner. Selected regions of interest are irradiated with the laser, and images taken immediately afterward reveal an increase in CV fluorescence, attributed to thermodiffusion through the pores of the internalized NMOFs. Additionally, the release kinetics are investigated over time. In both systems, a notable increase in CV fluorescence intensity is observed post-irradiation, followed by diffusion through the cell over the subsequent 5 minutes, resulting in partial loss of the dye. In the case of the NU-1000 NCs, the colocalization of the particles with lysosomes is

investigated using a lysotracker. The images reveal a distinct and pronounced colocalization between CV and the employed lysotracker probe. This observation serves as strong evidence confirming that post-internalization, the particles indeed accumulate within lysosomes.

Overall, the results demonstrate a controlled drug release profile under NIR light stimulation, validating the efficacy of the integrated nanoantennas in facilitating light-triggered drug release. Furthermore, *in vitro* studies conducted in living cells elucidate the potential of these nanocomposites as DDSs. Photothermal studies reveal the nanosystems ability to release encapsulated cargo upon NIR irradiation, showcasing their suitability for spatiotemporal control over drug delivery.

To assess the translational potential of this approach, the NU-1000 nanocomposite is loaded with clinically relevant chemotherapeutic agents ─ Doxorubicin, Carboplatin, and Oxaliplatin ─. Subsequently, the loaded NCs are further functionalized with PEG-PO_3, as in previous cases. After thorough characterization, the system undergoes evaluation in both 2D and 3D cell cultures. MTT toxicity assays demonstrates the high viability of the drug-loaded particles compared to free drugs. Additionally, post-irradiation, toxicity results indicate a significant decrease in cell viability, whereas non-loaded NCs do not exhibit any toxicity even after irradiation. This highlights that the heat generated by the systems is sufficient to trigger cargo release without inducing cell death via hyperthermia.

In 3D cell culture experiments, particles are incubated with A549 spheroids for 24 hours. Microscopy and flow cytometry analysis conducted at 24- and 72-hours post-irradiation reveals noteworthy findings. Spheroid images shows a reduction in total size when loaded NCs were irradiated, whereas controls maintain their initial size (~600 µm). A live/dead assay using flow cytometry indicates minimal percentages of calcein-positive cells 24 hours after irradiation of the loaded NMOFs. Conversely, non-loaded NCs, free drugs, and control spheroids exhibit high percentages of calcein-positive cells, indicative of robust cell survival. After 72 hours, there is a reduction in calcein-positive cells across all cases, with a significant difference observed in loaded and irradiated NCs.

The results underscore the effectiveness of the nanosystem in facilitating cellular internalization and achieving therapeutic NIR activation, highlighting its promise for targeted cancer therapy. Therefore, this chapter proves that the incorporation of stimuli-responsive elements, such as light-responsive nanoantennas, into NMOFs represents a significant advancement in drug delivery technology. This study lays the foundation for the development of next-generation smart drug delivery platforms capable of precise and on-demand drug release, offering new avenues for personalized and effective therapeutic interventions in various diseases, particularly cancer.

In conclusion, this thesis endeavors to provide a comprehensive overview of the design, functionalization, and cargo-loading strategies of NMOFs for drug delivery applications in biomedicine. By showing the principles governing NMOF-based drug delivery systems and exploring innovative approaches for triggered release with NIR light, this work aims to contribute to the advancement of precision medicine and the development of next-generation therapeutics with enhanced efficacy and safety profiles.

USC UNIVERSIDADE DE SANTIAGO DE COMPOSTELA

USC
UNIVERSIDADE
DE SANTIAGO
DE COMPOSTELA

Resumo

As nanotecnoloxías convertéronse en indispensables no campo biomédico, impulsando avances significativos no diagnóstico, terapia e monitorización de enfermidades. A súa capacidade para operar a escala nanométrica permite interaccións precisas con células e tecidos, mellorando así a selectividade e eficacia do tratamento. Entre as súas moitas aplicacións, as nanopartículas (NPs) destacan como vehículos versátiles de administración de fármacos, facilitando a liberación controlada e dirixida para minimizar os efectos adversos. Ademais, as NPs poden ser adaptadas para a detección precoz de biomarcadores, mellorando así a precisión diagnóstica. A integración das nanotecnoloxías abre vías prometedoras para a medicina personalizada, onde os tratamentos poden ser personalizados en función de características individuais.

Entre a ampla gama de nanomateriais investigados para aplicacións terapéuticas, os NMOFs (Nano Estructuras Metal-Orgánicas) destacan polo seu interese considerable debido ás súas características estruturais únicas e propiedades personalizables. Os NMOFs son materiais cristalinos compostos por ions metálicos ou conglomerados coordinados con ligandos orgánicos, dando lugar a estruturas porosas con áreas de superficie elevadas e tamaños de poro axustables. Estas características fan que os NMOFs sexan moi atractivos para o desenvolvemento de plataformas avanzadas de administración de fármacos adaptadas para satisfacer as demandas específicas da medicina moderna. Un factor crucial recae na gobernanza da síntese e deseño dos NMOFs. Ao seleccionar coidadosamente ions metálicos, ligandos orgánicos e condicións sintéticas, as propiedades estruturais e químicas dos NMOFs poden axustarse con precisión para acomodar varios axentes terapéuticos. Ademais, a integración de grupos funcionais dentro do marco de NMOF permite a orientación precisa e a liberación controlada de fármacos, aumentando así a eficacia terapéutica mentres se minimiza a toxicidade sistémica.

A funcionalización xoga un papel crucial en aumentar o rendemento e a versatilidade dos NMOFs para aplicacións de administración de fármacos. As técnicas de modificación post-síntese (PSM) son amplamente exploradas como medios para mellorar a estabilidade, biocompatibilidade e capacidades de carga de carga dos NMOFs. Ademais, os enfoques de PSM permiten a introdución de ligandos de direccionamento na superficie, impartindo funcionalidades cruciais para a administración precisa de fármacos. Foron desenvolvidas varias estratexias para a funcionalización superficial, incluíndo modificación covalente, química de coordinación, enfoques núcleo-casca e revestimentos de membrana celular.

Ademais, a combinación de axentes sensibles á luz, como as nanopartículas de ouro, con NMOFs para responder a estímulos externos, como a luz NIR, representa unha característica especialmente atractiva para a administración controlada e dirixida de fármacos. En particular, a luz NIR ten a capacidade de penetrar profundamente nos tecidos biolóxicos con absorción e dispersión mínimas, permitindo a activación precisa dos NMOFs cargados con fármacos en áreas específicas do corpo.

USC
UNIVERSIDADE DE SANTIAGO DE COMPOSTELA

Tendo en conta todo isto, o obxectivo principal desta tese de doutoramento é o deseño, desenvolvemento e optimización de sistemas baseados en NMOFs para aplicacións biomédicas, e máis concretamente para a administración de fármacos.

O primeiro capítulo desta tese ten como obxectivo desenvolver un novo método de revestimento superficial utilizando un polímero anfifílico que pode ser modificado con grupos de dibenzo ciclooctino (DBCO), facéndoo universalmente aplicable para modificación post-sintética. Este método aplícase a varios NMOFs, incluíndo UiO-67, NU-1000, PCN-222 e ZIF-8, seleccionados polo seu potencial utilidade biomédica. O obxectivo principal é mellorar a súa estabilidade dentro de entornos biolóxicos. O capítulo comeza coa síntese e caracterización meticulosa dos NMOFs para garantir unha alta monodispersidade e uniformidade, con tamaños de aproximadamente 150 nm. Posteriormente, estes NMOFs son revestidos co polímero anfifílico elixido (PMA) utilizando un enfoque núcleo-casca. Este revestimento non só mellora a súa estabilidade coloidal, senón que tamén preserva a súa integridade estrutural en diversos medios biolóxicos relevantes. Destacadamente, proba ser eficaz na estabilización de NMOFs da familia Zr, que normalmente se degradan en solucións acuosas e baseadas en fosfato. As avaliacións de estabilidade coloidal e estrutural, utilizando medidas de DLS, microscopía electrónica e PXRD, demostran consistentemente melloras notables en auga, DMEM e medios de PSF para NMOFs revestidos con PMA. Antes da aplicación de PMA, só os MOFs de Zr conservan a súa morfoloxía en auga e medios celulares, mentres que o ZIF-8 experimenta unha degradación evidente en 5 horas. Con todo, a cristalinidade dos MOFs de Zr comprométese notabelmente ao exposición a medios acuosos. Tras o revestimento con PMA, todas as estruturas coloidais, morfolóxicas e cristalinas permanecen intactas, afirmando a eficacia de PMA en preservar a estabilidade das mostras.

A continuación, os NMOFs son cargados con unha molécula fluorescente, Violeta de Cresilo (CV), para avaliar a súa capacidade de encapsulamento. Os estudos de liberación en auga, DMEM e medios de PSF, comparando partículas con e sen revestimento de polímero a través de medidas de fluorescencia, demostran unha retención de carga considerablemente mellorada co revestimento de PMA. Especialmente os NMOFs ZIF-8 e UiO-67 presentan unha diminución clara na liberación de CV cando o PMA está na superficie das partículas. Isto subliña a alta capacidade de carga e estabilidade dos NMOFs en medios biolóxicos, crítico para aplicacións de administración de fármacos. Ademais, a retención da carga confírmase por ensaios de toxicidade, especialmente en ZIF-8 e UiO-67, onde as nanopartículas non revestidas mostran unha redución na viabilidade celular a concentracións superiores a 10 pM debido á liberación do CV. Pola contra, cando os NMOFs están funcionalizados con PMA, as mostras non presentan ningún tipo de toxicidade, mesmo a altas concentracións.

A última parte do capítulo implica a funcionalización adicional dos NMOFs cargados, centrando particularmente en ZIF-8 e UiO-67. Facendo uso do revestimento de polímero anterior como punto de ancoraxe, varias moléculas biolóxicamente relevantes, como o polietileno glicol, a manosa e péptidos de penetración celular, son unidas ás superficies dos NMOFs utilizando reaccións de química click baseadas en biortogonalidade. A química de click ofrece altos rendementos, ampla aplicabilidade, baixa citotoxicidade, estereoespecificidade e condicións simples. É compatible con varios grupos funcionais, o que a fai versátil para a modificación superficial de NMOFs. A química click sen cobre, en particular a cicloaddición

azida-alquino promovida por tensión (SPAAC), ten reaccións rápidas e non citotóxicas, ideais para o uso celular. Neste traballo, o PMA é previamente modificado con grupos DBCO para permitir reaccións de química click cos grupos azida modificados.

ZIF-8 e UiO-67 son seleccionados para estes estudos, ambos cargados con CV. Ademais, tamén se estuda a funcionalización de ZIF-8 non cargado con fins comparativos. Para rastrealos intracelularmente, o Cy5-N_3 é unido á superficie seguindo o mesmo procedemento de química click. A caracterización estrutural precede ao estudo dos procesos de internalización destes NMOFs derivatizados nas células cancerosas, coas medidas de DLS e potencial zeta probando a funcionalización correcta. Ao comparar a eficiencia de internalización de NMOFs con diferentes modificacións superficiais, a investigación pretende elucidar o seu impacto nos mecanismos de internalización celular. Realizáronse experimentos de citometría de fluxo para observar a internalización dos NMOFs usando a fluorescencia do CV encapsulado. As partículas son incubadas a tres concentracións diferentes durante tres horas con células A549. Os resultados de ZIF-8 indican un aumento na internalización co CPP na superficie do MOF e unha redución na absorción co PEG, mentres que as partículas funcionalizadas con manosa non presentan diferenzas significativas en comparación cos MOFs revestidos con PMA. UiO-67 mostra unha tendencia similar en todos os casos. Como se anticipaba, o CPP aumenta as capacidades de recoñecemento do sistema e aumenta a internalización celular, mentres que o PEG confire furtividade ás partículas, o que resulta nun recoñecemento celular reducido. Estes estudos son corroborados con microscopía confocal, onde a cuantificación da fluorescencia das imaxes mostra unha alta coerencia coa citometría de fluxo. Novamente, o CPP na superficie tanto de ZIF-8 como de UiO-67 aumenta a internalización celular e o PEG redúcea, mentres que os sistemas revestidos con manosa non presentan diferenzas significativas cos MOFs revestidos con PMA. Ademais, as mostras de ZIF-8 con Cy5 tamén son analizadas con imaxes de microscopía, mostrando diferenzas cos casos anteriores. Especialmente, hai un alto aumento para as partículas funcionalizadas con manosa, que pode derivar dun efecto sinérxico resultante da conxunción de Cy5 e manosa na superficie da partícula, potencialmente aumentando o recoñecemento celular. Estes achados afirman a eficacia da funcionalización baseada en química click na alteración do recoñecemento e a internalización celular.

En conxunto, o capítulo mostra a eficacia e versatilidade do enfoque de revestimento proposto para mellorar a estabilidade e funcionalidade dos NMOFs para aplicacións biomédicas, especialmente na administración de fármacos dirixida e na imaxe.

O Capítulo 2 ten como obxectivo desenvolver novos métodos de funcionalización superficial a través de modificación pos-sintética (PSM) coordinativa baseada en ADN en varios MOFs da familia Zr, facilitada pola dispoñibilidade de sitios de Zr libres nas superficies dos MOF para coordinar moléculas modificadas con fosfato ou carboxilato. A investigación implica os Zr NMOFs UiO-67, NU-1000 e PCN-222 previamente sintetizados. Para comparación, emprégase PEG en estudos de funcionalización análogos. A funcionalización subsequente das superficies revestidas de ADN implica a hibridación de oligonucleótidos de ADN complementarios modificados con azida, que serven como puntos de ancoraxe para a conjugación química click con moléculas bioactivas que conteñen grupos DBCO. É especialmente destacable que este estudo se centre en nanopartículas de UiO-67 cargadas con calceína, co BSA modificado con DBCO elixido para a funcionalización bioactiva subsequente.

Antes dos estudos de funcionalización, realízanse análises exhaustivas de concentración utilizando análise de rastrexo de nanopartículas (NTA) e citometría de fluxo. A cuantificación precisa da concentración de nanopartículas é crucial para comprender as súas interaccións coas células. Polo tanto, metodoloxías robustas son esenciais para medir precisamente a concentración total e a distribución de tamaño dos NMOFs estudados. A NTA é unha ferramenta valiosa para a caracterización de nanopartículas, que ofrece medidas de tamaño de alta resolución e determinación de concentración baseada en contaxe sen necesidade de marcadores fluorescentes. Con todo, a súa sensibilidade a diferentes tipos de nanomateriais pode afectar a precisión das medidas. Ademais, require equipo e software especializado, o que supón desafíos loxísticos e restricións de custos para algúns investigadores. A pesar das limitacións, a NTA ofrece información crucial sobre as propiedades das nanopartículas, axudando en varias investigacións científicas.

A citometría de fluxo presenta unha alternativa viable para a caracterización da concentración de nanopartículas, debido a súa dispoñibilidade na maioría dos laboratorios de bioloxía. A pesar do seu uso principal no análise celular, este instrumento pode ofrecer tanto análise cualitativa como cuantitativa do tamaño e concentración de NPs a través de medidas de dispersión e fluorescencia. Con todo, os citómetros de fluxo convencionais típicamente teñen un límite de detección de tamaño inferior para a dispersión de luz, que varía de 200 a 500 nm, mentres que as medidas de fluorescencia adoitan ser máis sensibles. Para capitalizar a natureza diversa dos NMOFs seleccionados (UiO-67, NU-1000 e PCN-222), realízase un análise comparativa entre experimentos de NTA e citometría de fluxo para determinar a concentración de NP para experimentos in vitro subsecuentes.

As concentracións de NMOFs son primeiro analizadas con NTA e despois con citometría de fluxo. Neste último caso, os cálculos de partículas por mL son realizados utilizando a dispersión das partículas seleccionadas, así como as súas propiedades de fluorescencia no caso dos NU-1000 e PCN-222. Para confirmar os resultados, engadíronse á solución de partículas microesferas FITC de 100 nm. Os resultados mostran rangos similares de concentración en todos os casos. Con todo, os valores obtidos para UiO-67 usando citometría de fluxo son máis altos en relación coa NTA debido á posible presenza de fondo na solución utilizada en citometría de fluxo, que leva a unha sobrestimación da concentración. Por outra banda, con NU-1000 e PCN-222, debido ás propiedades de fluorescencia destes materiais, é máis fácil distinguir as poboacións de partículas e os resultados son lixeramente inferiores aos valores de NTA. No conxunto, estes achados subliñan o significativo potencial da citometría de fluxo na análise da concentración e tamaño de nanopartículas. Ademais, demostra varias vantaxes sobre as medidas de NTA, incluída a capacidade de manexar valores de baixa concentración e volumes de mostra pequenos, así como ofrecer medidas de alta precisión e rápidas.

Tras a caracterización da concentración, estúdase a PSM coordinativa para os tres MOFs de Zr. Moléculas de ADN e PEG modificadas con grupos fosfato utilízanse para funcionalizar a superficie das partículas. Debido a defectos de superficie de Zr, que facilitan a funcionalización con grupos fosfato, fórmanse enlaces de coordinación Zr-O-P. Tras a funcionalización, as partículas son caracterizadas sen amosar diferenzas no tamaño, morfoloxía ou espectros de absorción. Ademais, a introdución de ADN resulta nunha diminución notable da carga total, facendo que todas as mostras sexan cargadas negativamente, o que indica o

revestimento exitoso dos NMOFs. A adición de PEG confire neutralidade ás partículas debido ós grupos metoxi libres na extremidade da molécula. A estabilidade coloidal dos sistemas é avaliada en auga, DMEM e PSF, demostrando que ambas funcionalizacións previenen a agregación de partículas especialmente en medios celulares.

Posteriormente, investígase un novo enfoque de funcionalización utilizando ADN como punto de ancoraxe. Neste estudo, UiO-67 é seleccionado como o NMOF modelo, e para facilitar experimentos in vitro posteriores, as partículas son cargadas con moléculas de calceína. Inicialmente, seguindo a funcionalización con DNA-PO_3, introdúcese a cadea complementaria modificada con azida na estrutura, permitindo que os grupos N_3 permanezan libres na superficie da partícula. Despois disto, BSA modificada con DBCO engádese á estrutura a través de reaccións de química click entre a azida e o DBCO, establecendo así unha unión covalente entre a proteína e o NMOF. O BSA tamén está marcado con fluorescencia (Cy5) para permitir experimentos de caracterización. Simultaneamente, as partículas son funcionalizadas con PEG para permitir experimentos comparativos.

A caracterización das partículas indica que non hai cambios na morfoloxía nin no tamaño das estruturas, salvo un pequeno incremento cando se engade ADN e BSA. Os potenciais zeta mostran cambios que manifestan a correcta funcionalización. Ademais, as medidas de fluorescencia e UV-Vis permiten a cuantificación de BSA na superficie das partículas. A continuación, realízanse estudos de toxicidade para determinar a viabilidade celular das partículas, demostrando alta viabilidade en todos os casos. Realízanse estudos de internalización celular en NMOFs usando microscopía de fluorescencia e citometría de fluxo. A presenza de fluorescencia verde dentro das células nestes experimentos indica unha encapsulación exitosa da calceína dentro dos NMOFs, dada a incapacidade da calceína para atravesar membranas celulares sen axuda.

Inicialmente, a citometría de fluxo avalía cuantitativamente a captación dos NMOFs coa liña celular A549. Os NMOFs UiO-67 son sometidos a períodos de incubación de 0,5, 1 e 3 horas. Os datos de captación son axustados cun factor de correción derivado de medidas de fluorescencia de mostras na mesma concentración empregada nos experimentos de captación. Dadas as diferenzas previas no sinal de calceína entre as mostras, estandarizar os valores de captación en relación á fluorescencia total de NMOF é crucial. Estes resultados confírmanse utilizando experimentos de microscopía de fluorescencia. A imaxe confocal ilustra vívidamente a robusta internalización das nanopartículas cargadas de calceína, consistente cos patróns observados nos análises de citometría de fluxo. A impermeabilidade da calceína soa a través das membranas celulares subliña a eficiente internalización facilitada polos NMOFs. Ademais, a incorporación dun marcador de endosoma precoz (HT) valida a vía endocítica implicada. A colocalización entre calceína e HT confirma a presenza da mostra dentro dos endosomas, coa colocalización de BSA (canle Cy5) indicando o revestimento intacto mesmo despois de translocar ás lisosomas. Este método demostra ser eficaz para a modificación da superficie, ofrecendo diversas posibilidades para a adhesión de biomoléculas.

Este novo enfoque de funcionalización de proteínas para NMOFs ten promesas para varias aplicacións, incluída o desenvolvemento de vacinas. Inmobilizar proteínas nas superficies de NMOF pode crear unha plataforma estable e biocompatible para a entrega de vacinas, mellorando a estabilidade do antíxeno, controlando as cinéticas de liberación e modulando as

respostas inmunolóxicas. Utilizar proteínas virais para a funcionalización podería imitar procesos de infección natural, provocando potentes respostas inmunolóxicas. O control preciso sobre a densidade e configuración de proteínas nas superficies de NMOF podería producir formulacións de vacinas altamente eficientes e específicas.

No conxunto, o enfoque proposto neste capítulo ofrece oportunidades para a entrega e terapia de medicamentos dirixidos, onde o control preciso da adhesión de biomoléculas e cinéticas de liberación pode mellorar a eficacia do tratamento mentres se minimizan os efectos secundarios. Ó aproveitar as propiedades distintivas dos NMOFs e incorporar a funcionalización de proteínas, poden desenvolverse intervencións terapéuticas personalizadas para unha variedade de enfermidades, marcando un avance significativo no campo do tratamento médico.

Por outra banda, aínda que algúns NMOFs mostran propiedades notables como alta capacidade de carga de fármacos, biocompatibilidade e cinéticas de liberación controlada, a súa falta intrínseca de resposta a estímulos externos presenta unha limitación no deseño de sistemas dinámicos de liberación de fármacos. O último capítulo desta tese explora un novo enfoque mediante a integración de nanoantenas fotosensibles en NMOFs para mellorar a súa funcionalidade como plataformas intelixentes de entrega de fármacos.

As nanopartículas de ouro, grazas ás súas propiedades plasmónicas, exhiben características únicas na interacción coa luz, especialmente vantaxosas na xanela biolóxica do infravermello cercano (NIR). Nese rango espectral, a luz NIR pode penetrar nos tecidos biolóxicos con absorción e dispersión mínimas, permitindo unha penetración tecidual máis profunda en comparación coa luz visible. Estas propiedades derivan da excitación colectiva de electróns na superficie da nanopartícula cando é irradiada con luz. Este fenómeno permite que as nanopartículas de ouro absorban e disperxan eficientemente a luz, facéndoas ferramentas valiosas nun amplo rango de aplicacións, desde a detección biomédica ata a nanotecnoloxía. Esta propiedade permite xerar calor baixo irradiación láser apropiada, mostrando un gran potencial en terapias de hipertermia para enfermidades como o cancro, onde a elevación localizada da temperatura pode empregarse para destruír selectivamente células malignas. Esta resposta pode ser utilizada para outros fins, como desencadear a liberación de cargas encapsuladas en sistemas DDS seleccionados. Concretamente, en nanosistemas núcleo-casca que comprenden un núcleo de nanopartículas de ouro e unha casca composta por NMOF, as nanopartículas de ouro poden funcionar como nanoantenas, provocando a difusión de cargas encapsuladas dentro dos poros da estrutura de NMOF debido ao aumento de temperatura.

A integración de nanoantenas de bipirámides de ouro (AuBy) en dous NMOFs distintos, nomeadamente ZIF-8 e NU-1000, conduce á formación de nanosistemas núcleo@casca con capacidades fototérmicas inherentes. Esta integración motívase polo potencial de aproveitar a luz NIR para a liberación controlada de fármacos, ofrecendo precisión espaciotemporal na entrega de fármacos. Primeiro, as AuBys son sintetizadas seguindo protocolos previos. As nanopartículas obtidas presentan tamaños de 80 nm e unha banda de absorción clara no NIR (808 nm) correspondente á LSPR longitudinal. Utilizando as AuBys, elixíronse dous NMOFs como a cáscara da estrutura: ZIF-8 e NU-1000. Ambos sistemas son sintetizados obtendo partículas de ~150 nm presentando unha AuBy por MOF. A continuación, utilizando CV como fármaco modelo, analízanse meticulosamente a dinámica de carga e liberación dos

nanosistemas núcleo@casca. Realízase unha funcionalización adicional de polímeros utilizando revestimentos previamente estudados de PMA e PEG-PO_3 para NCs de ZIF-8 e NU-1000, respectivamente. Tras a carga e o revestimento da superficie, os NCs son caracterizados en profundidade utilizando DLS, microscopía electrónica, PXRD e medidas de adsorción de N_2. Ademais, realízanse estudos de estabilidade en medios biolóxicos para comprobar a capacidade das mostras de manter a integridade coloidal e estrutural. En ambos os casos, de maneira semellante aos capítulos anteriores, os NCs presentan alta estabilidade en auga e medios celulares, mentres que as mostras sen os polímeros están claramente degradadas ou perden a cristalinidade.

A investigación subsequente está enfocada en estudar as propiedades termoplasmónicas dos sistemas. Utilízase un láser NIR para irradiar varias concentracións de NCs dispersos en auga, empregando diferentes irradianzas entre 7.5 e 12 $W \cdot cm^{-2}$. As curvas de calefacción obtidas destes experimentos revelan un aumento de temperatura de ata 70ºC nas mostras máis concentradas, atribuído á resposta termoplasmónica das AuBys no núcleo das estruturas. Ademais, examínase a liberación controlada desencadeada pola luz NIR. Despois da irradiación, as mostras son centrifugadas, e o sobrenadante é caracterizado mediante medidas fluorescentes, indicando un aumento significativo no porcentaxe de CV liberado dos NCs. Estes achados subliñan a capacidade de resposta ós estímulos dos sistemas, destacando o seu potencial para aplicacións de entrega de fármacos.

Para validar esta capacidade en cultivos celulares 2D, as partículas son incubadas con células A549 durante 6 horas. Posteriormente, realízanse experimentos de microscopía utilizando un escáner láser Leica. As rexións de interese seleccionadas son irradiadas co láser, e as imaxes tomadas inmediatamente despois revelan un aumento na fluorescencia de CV, atribuído á termodifusión a través dos poros dos NMOFs internalizados. Ademais, investíganse as cinéticas de liberación ó longo do tempo. En ambos sistemas, obsérvase un aumento notable na intensidade da fluorescencia de CV despois da irradiación, seguido da difusión a través da célula nos 5 minutos seguintes, o que resulta nunha perda parcial do tinte. No caso dos NCs NU-1000, investigase a colocalización das partículas cos lisosomas utilizando un lisotracker. As imaxes revelan unha colocalización distinta e pronunciada entre CV e a sonda de lisotracker empregada. Esta observación serve como forte evidencia de que, despois da internalización, as partículas acumúlanse dentro dos lisosomas.

En xeral, os resultados demostran un perfil de liberación controlada de fármacos baixo estimulación de luz NIR, validando a eficacia das nanoantenas integradas na facilitación da liberación de fármacos desencadeada pola luz. Ademais, os estudos in vitro realizados en células vivas elucidan o potencial destes nanocompositos como DDSs. Os estudos fototérmicos revelan a capacidade dos nanosistemas de liberar carga encapsulada tras a irradiación NIR, mostrando a súa idoneidade para o control espaciotemporal sobre a entrega de fármacos.

Para avaliar o potencial translacional deste enfoque, o nanocomposito NU-1000 é cargado con axentes quimioterapéuticos clinicamente relevantes ─ Doxorrubicina, Carboplatino e Oxaliplatino ─. Posteriormente, os NCs cargados son funcionalizados adicionalmente con PEG-PO_3, como en casos anteriores. Tras unha caracterización exhaustiva, o sistema é sometido a avaliación en cultivos celulares 2D e 3D. Os ensaios de toxicidade MTT demostran a alta viabilidade das partículas cargadas con fármacos en comparación cos fármacos libres. Ademais,

USC DE SANTIAGO

despois da irradiación, os resultados de toxicidade indican unha diminución significativa na viabilidade celular, mentres que os NCs non cargados non exhiben toxicidade algunha incluso despois da irradiación.

Nos experimentos de cultivo celular 3D, as partículas son incubadas con esferoides A549 durante 24 horas. Os análises de microscopía e citometría de fluxo realizados ás 24 e 72 horas despois da irradiación revelan achados notables. As imaxes de esferoides mostran unha redución no tamaño total cando os NCs cargados son irradiados, mentres que os controis manteñen o seu tamaño inicial (~600 μm). Un ensaio de viabilidade en vivo/morto utilizando citometría de fluxo indica porcentaxes mínimos de células positivas para calceína 24 horas despois da irradiación dos NMOFs cargados. Polo contrario, os NCs non cargados, os fármacos libres e os esferoides de control exhiben altos porcentaxes de células positivas para calceína, indicativo dunha robusta supervivencia celular. Despois de 72 horas, observase unha redución nas células positivas para calceína en todos os casos, con unha diferenza significativa observada nos NCs cargados e irradiados.

Os resultados subliñan a efectividade do nanosistema na facilitación da internalización celular e na consecución da activación terapéutica do NIR, destacando o seu potencial para a terapia dirixida contra o cancro. Por iso, este capítulo proba que a incorporación de elementos sensibles a estímulos, como nanoantenas sensibles á luz, en NMOFs representa un avance significativo na tecnoloxía de entrega de fármacos. Este estudo establece a base para o desenvolvemento de plataformas de entrega de fármacos intelixentes da próxima xeración capaces de liberación precisa e baixo demanda, ofrecendo novos camiños para intervencións terapéuticas persoalizadas e eficaces en diversas enfermidades, especialmente o cancro.

En conclusión, esta tese procura proporcionar unha visión global da deseño, funcionalización e estratexias de carga de cargas de NMOFs para aplicacións de entrega de fármacos na biomedicina. Ao mostrar os principios que gobernan os sistemas de entrega de fármacos baseados en NMOF e explorar enfoques innovadores para a liberación desencadeada con luz NIR, este traballo pretende contribuír ao avance da medicina de precisión e ao desenvolvemento de terapias da próxima xeración con eficacia e perfís de seguridade mellorados.

USC
UNIVERSIDADE DE SANTIAGO DE COMPOSTELA

1. Introduction

USC
UNIVERSIDADE
DE SANTIAGO
DE COMPOSTELA

USC
UNIVERSIDADE
DE SANTIAGO
DE COMPOSTELA

Part of the information presented in the following chapter is published in:

"Nanosized metal–organic frameworks as unique platforms for bioapplications" Chemical Communications. **2023.**

Manuela Cedrún-Morales[1], Manuel Ceballos[1], Ester Polo[1], Pablo del Pino[1] and Beatriz Pelaz[1]

[1]*Center for Research in Biological Chemistry and Molecular Materials (CiQUS), University of Santiago de Compostela, 15705 Santiago de Compostela, Spain.*

Contributions: Writing – original draft.

Impact Factor: 4.9. Q1 in Nanoscience & Nanotechnology.

USC UNIVERSIDADE DE SANTIAGO DE COMPOSTELA

USC
UNIVERSIDADE
DE SANTIAGO
DE COMPOSTELA

1.1. NANOTECHNOLOGY AND METAL ORGANIC FRAMEWORKS

1.1.1. Nanotechnology

Nanotechnology involves the engineering or manipulation of functional systems at the molecular scale. The prefix "nano" originates from Greek, meaning "dwarf," and represents a unit of length in the metric system equivalent to one billionth of a meter (10^{-9} m). Technology, on the other hand, refers to the application of scientific knowledge to solve problems or perform specific tasks.

According to the National Nanotechnology Initiative (NNI) in the United States, nanotechnology is defined as "The science, engineering, and technology conducted at the nanoscale (1 to 100 nm), where unique phenomena enable new applications in a wide range of fields, including physics, chemistry, biology, medicine, engineering, and electronics." In 1959, Richard Feynman introduced the concepts and discussed the notion of nanotechnology during a talk titled "There's Plenty of Room at the Bottom" at the American Physical Society. Fifteen years later, in 1974, Professor Norio Taniguchi of Tokyo Science University was the first to use and define the term "nanotechnology" as "the processing of separation, consolidation, and deformation of materials by one atom or one molecule."

To be classified as nanostructured, a material should have at least one dimension within the 1-100 nanometre range (Figure 1.1.1.), and the concept includes different shapes and morphologies as spherical nanoparticles (NPs), nanorods, nanowires, nanotubes, nanocomposites, …[1]

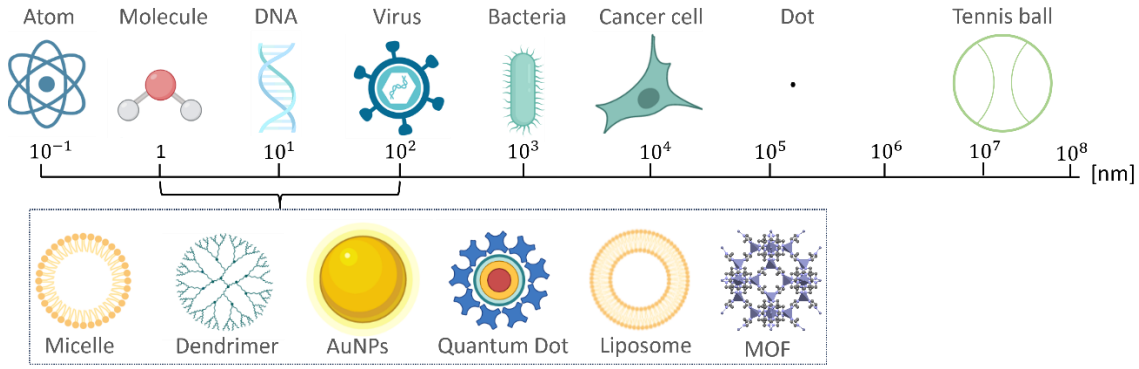

Figure 1.1.1. Schematic representation of the nanometer scale.

Nanoparticles (NPs) and nanostructured materials (NSMs) are at the forefront of research, demonstrating significant growth and widespread application across various fields. Their importance in technological advancements is underscored by the realization that nanotechnology is more than just a simple continuation of miniaturization from the micrometer scale to the nanometer scale.[2] Materials at the micrometer scale typically demonstrate physical properties similar to bulk materials. However, at the nanometer scale, materials may exhibit markedly different physical features. In this size range, materials possess tunable physicochemical characteristics such as melting point, wettability, electrical and thermal conductivity, catalytic activity, light absorption, and scattering. These unique properties often result in enhanced performance compared to their bulk counterparts.[2,3] Another fundamental aspect of nanoparticles (NPs) is the significant increase in surface area that occurs as particle dimensions decrease.[4] This property is crucial for many nanoparticle applications, as the

primary interactions often take place at the surface. Consequently, as the surface area increases, there is a corresponding enhancement in total reactivity, which ultimately influences their overall behavior.

The huge potential of nanomaterials in biomedicine for diagnosing and treating many human diseases is well-documented.[5] During recent decades, the applications of nanotechnology in numerous biology-related areas such as diagnosis, drug delivery, and molecular imaging have gained interest and have been increasingly investigated showing remarkable results.[6] In this context, nanoparticle drug delivery systems (DDSs) are extensively used in pharmaceutical research and in clinical settings to improve the efficacy of diagnostic agents and drugs, such as anticancer, antimicrobial, and antiviral drugs.[7] The term DDS is employed to describe a carrier that can deliver an active pharmaceutical ingredient (API) to a specific site in the body.[8] These systems can solve some of the main challenges associated to molecular drugs, such as poor stability and solubility, short circulation time in the blood, or low specificity, which can lead to multidrug resistance after long-term exposure.[8] Furthermore, the advancement of innovative DDSs has facilitated the precise delivery of bioactive molecules to particular tissues in the body, thereby reducing side effects linked with traditional therapies and improving their effectiveness. Throughout their production, chosen materials can be meticulously adjusted to meet particular biological requirements, such as optimizing entry pathways and loading mechanisms.[1]

To address limitations of DDSs such as inadequate retention or inefficient drug release, DDSs can be designed to respond to specific stimuli that trigger the release of loaded cargo (Figure 1.1.2.).[9] These stimuli fall into two categories: endogenous and external. Endogenous stimuli encompass internal environmental conditions for NPs, such as the acidic/hypoxic environment of tumors or elevated levels of matrix metalloproteinases (MMPs),[10] among others. Conversely, external stimuli are controlled stimuli applied outside the body, including ultrasound, light, magnetic fields, or temperature.[9] However, it is crucial for cargo delivery to occur precisely at the target site to minimize side effects and enhance treatment efficacy. NPs can be provided with recognition capabilities by modifying them with peptides, nucleic acids, etc., to optimize delivery and overcome physiological barriers. Despite these possibilities, drawbacks still exist that hinder their approval for clinical use and must be addressed, such as limited targeting abilities or reduced cellular uptake.

Given these challenges, metal-organic frameworks (MOFs) have emerged as alternative materials in the biomedical field due to their distinctive physicochemical properties. These crystalline and highly porous materials feature ordered pores whose size and chemical environment are precisely determined through design.[11] Due to these features, MOFs´ applicability has been exploited for different purposes such as catalysis, gas storage, or sensing.[11] Features such as their large pore volumes, high surface areas (up to 8000 $m^2 \cdot g^{-1}$), well-defined tunable structures, and permanent porosities, make them excellent candidates for biomedical applications.[12] Furthermore, their highly adaptable surface functionalities, coupled with the capacity to encapsulate a diverse array of active pharmaceutical ingredients (APIs) such as drugs, enzymes, and nucleic acids, and subsequently release them in a controlled manner, along with a generally favorable biocompatibility profile, enable these materials to address some of the primary drawbacks previously mentioned.[13]

USC UNIVERSIDADE DE SANTIAGO DE COMPOSTELA

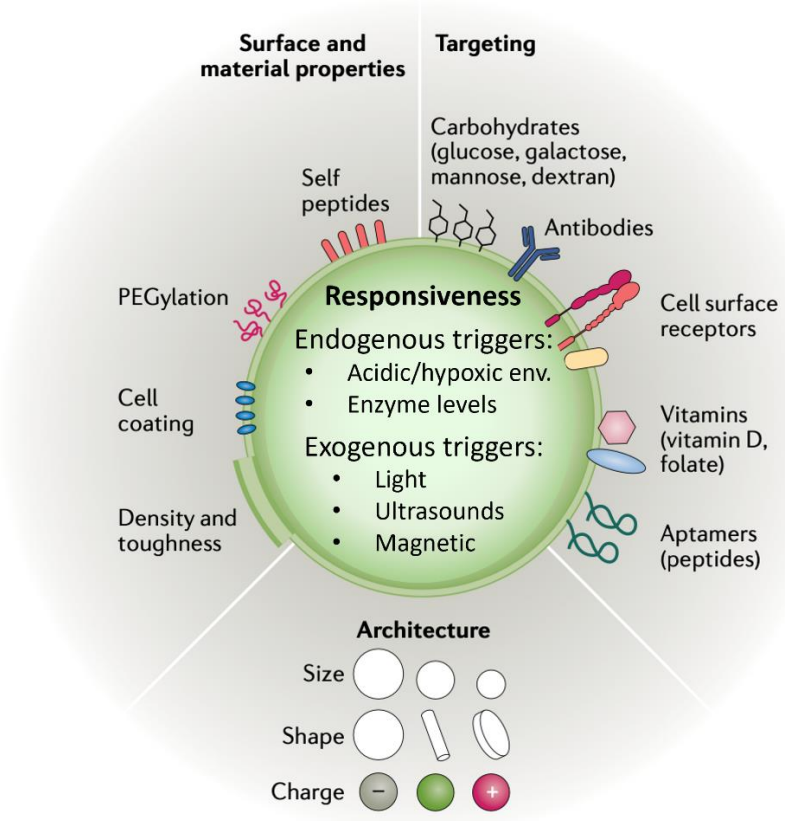

Figure 1.1.2. Stimuli-responsive nanosystems. Adapted with permission from Ref[10]. Copyright 2021, Nature Reviews Drug Discovery.

1.1.2. Metal-organic frameworks

MOFs are extended structures formed by the coordination of metal ions or inorganic polynuclear clusters, also known as SBUs (Secondary Building Units), to organic linkers. These SBUs serve as the structural nodes of MOFs and comprise metal ions (such as Cu(I), Zn(II), or Zr(IV)) and non-metals (such as oxygen or nitrogen). Meanwhile, the organic linkers, typically in bi-, tri-, or tetratopic forms, commonly contain Lewis bases such as carboxylate, phosphonate, pyridyl, imidazolate, or other azolate-functional groups (Figure 1.1.3.).[14]

The term SBU simplifies and categorizes MOF structures based on their net topology, contributing to the vast structural diversity observed in MOFs. Notably, experimentally described SBUs include a broad spectrum of transition metals, main-group metals, alkali metals, alkaline earth metals, lanthanides, and actinides. The number of metal atoms in these units can range from one to eight or even more. The connectivity and geometry of the ligand within a given SBU significantly influence the final structure of the MOF, imparting features such as permanent porosity, thermal stability, and chemical stability, which are highly relevant for their application in biomedicine.[14] Furthermore, the bonds between the SBUs and the linkers represent the most reactive sites within the MOF structure. Consequently, post-synthesis modifications of the NPs typically occur at these locations.

USC UNIVERSIDADE DE SANTIAGO DE COMPOSTELA

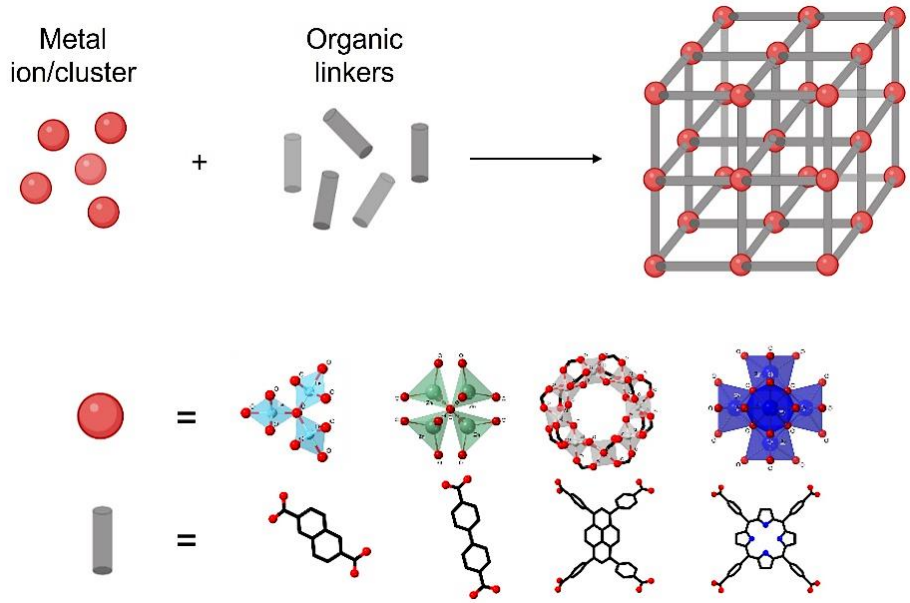

Figure 1.1.3. Schematic representation of MOFs, showing some SBUs and linkers.

1.1.3. Classification of MOFs: Reticular chemistry, SBUs

SBUs frequently serve as the starting point for discovering new porous materials. Unlike single-metal atoms acting as nodes, the diverse chemical compositions, architectures, and spatial arrangements of atoms in polynuclear SBUs provide MOFs with enhanced structural stiffness and directionality. This allows for the development of highly crystalline materials with precise properties, including ultra-high porosity and intricate structural complexity.[14]

Coordination networks were first reported in 1959, where Cu^{+} ions were employed as nodes with adiponitrile [$NC(CH_2)_4CN$] molecules as linkers.[15] However, this kind of materials with single-metal nodes have structures that are limited by the coordination number and geometries allowed. A very common example of MOFs with single-metal nodes is the zeolitic imidazolate framework (ZIF), which gives place to the synthesis of a huge number of ZIFs materials.[16] This sub-group of MOFs is constituted by transition divalent metal ions (M^{2+}) tetracoordinated with imidazolate units or their derivates. ZIF-8 is one of the most popular materials in the MOFs community and is highly employed in different applications due to its versatility, facile and green synthesis,[17] in addition to forming composites with a large number of materials.[18-20] On other hand, MOFs in which the nodes are constituted by clusters of atoms as SBUs have been very attractive since the discovery of MOF-5[21] and HKUST-1.[22] These MOFs have greatly contributed to understand the role of the spatial disposition of the organic ligands and inorganic moieties for determining the MOF´s structure.[23]

SBUs can be organized in different geometries such as tetrahedra, trigonal bipyramids, and octahedra, among others, sharing some atoms (generally oxygen) in the vertices of the polyhedrons. A typical example of SBU is the Zr_6 cluster in the UiO (Universitetet i Oslo) MOF family, where each Zr is connected to four Zr atoms through Zr-O-Zr bond, and each Zr atom can be bonded to two bidentate ligands, creating a $Zr_6O_4(OH)_4$ cluster surrounded by, in theory, twelve linkers.[24] The maximum number of ligands in an SBU in a MOF is determined by the disposition of these atoms and their coordination number. However, each SBU does not necessarily have each atom with a full coordination sphere. That is the case of the Zr_6 cluster present in UiO and PCN (Porous coordination network), where the most common geometry is

12-connected (12-c), being the SBU viewed as a cubic octahedron.[25,26] The lowest connectivity of Zr_6 SBU reached is 4-c in NU-1400 reported by Farha's group,[27] which is built using an elongated terphenyl-3,3'',5,5''-tetracarboxylic acid. Other connectivities for the Zr_6 SUB such as 6-c, 8-c, 9-c, 10-c,11-c or 12-c have been reported (Figure 1.1.4.).[28-33] All these parameters provide us an idea about the endless possibilities of creating structures that MOFs provide.

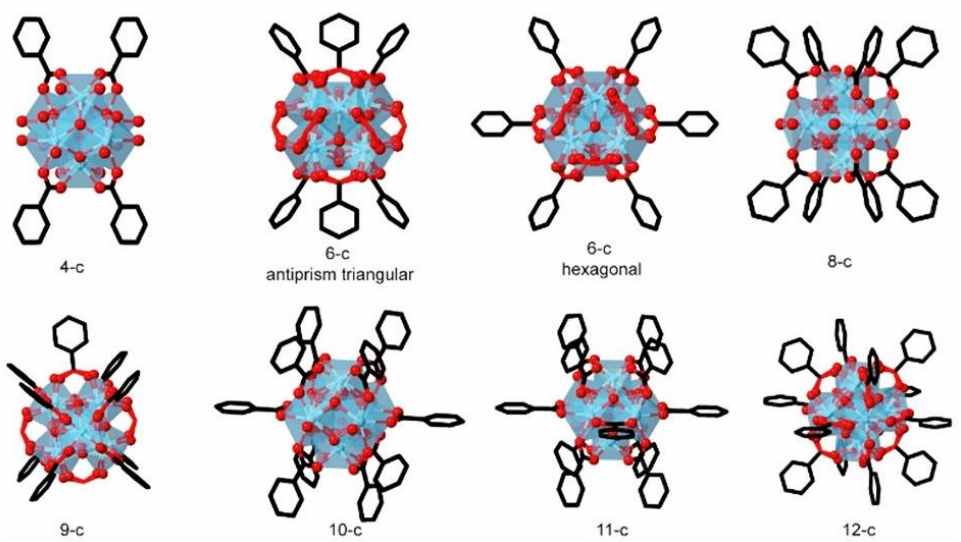

Figure 1.1.4. Connectivities of Zr_6 SBUs with different geometries.

1.1.4. Synthesis of nanometric-size MOFs (NMOFs)

Achieving nanometric size of MOFs particles is crucial for biomedical applications. The synthesis of nanosized MOFs (NMOFs) is currently being widely studied. Several methodologies have been developed to control the size, shape, and surface area among other physical and chemical properties.

As previously mentioned, one of the most extensively studied MOFs is ZIF-8, which offers the advantage of having water-soluble precursors. This characteristic enables synthesis under mild conditions, including room temperature, low reagent concentrations, and short reaction times.[34] However, to modify the physical and chemical properties of the material, many other methods such as solvothermal (in dimethylformamide (DMF) or methanol (MeOH)), microwave-assisted, sonochemical, or mechanochemical, among others have been employed.[35] The synthesis of ZIF-8 is also influenced by the presence of surfactants like hexadecyltrimethylammonium salts (CTA^+) and their co-ions (Cl^- or Br^-).[36] However, it can be also highly influenced by factors that might have been overlooked such as the gravitational forces.[37]

When it comes to MOFs with SBUs like Zr_6, a wide array of methods can be employed, offering versatility in synthesis. Generally, these methods facilitate the formation of metal-ligand bonds while also allowing for the breaking and reorganization of these bonds to enable structure propagation. Among these methods, solvothermal synthesis stands out as one of the most straightforward approaches. In solvothermal synthesis, the metal salt(s) and ligand(s) are dissolved in a high-boiling-point solvent such as DMF, DEF (dimethylformamide), or DMSO (dimethylsulfoxide) within a vial or closed vessel. The mixture is then heated for extended periods, typically 12 hours or longer, facilitating the synthesis process.[38] Usually, organic acids (i.e., acetic acid, formic acid, trifluoroacetic acid, benzoic acid, etc.) are used as

modulators to control the particle size.[39-41] This is possible as these acids enter into a competition with the organic linkers for the Zr sites available, avoiding the growth of the particles. Also, inorganic acids such as HCl are employed as modulators with the task of protonating the organic linkers decreasing their reactivity.[42]

1.1.5. Synthesis of inorganic nanoparticles and nMOFs nanocomposites

The synthetic methodologies for inorganic NPs (iNPs) allow their preparation with fine-tuning in order to control the size, shape and other properties such as purity, crystallinity, stability and, monodispersity.[43] As discussed above, the control of the NMOFs size is being studied to reduce the particle size.[44] With the aim of generating nanomaterials with improved and novel physicochemical properties, the synthesis of composites based on the combination of iNPs and NMOFs (iNPs@NMOFs) constitute one of the main interests for many research groups in this area. There are many different approaches for the synthesis of iNPs@NMOFs. The most common ones are: i) the post-impregnation of the NMOF with metallic salts solutions, followed by the reduction of the metallic ions and, ii) the core-shell approach wherein the mixture of the reaction contains the metal node or cluster, organic linker, and functionalized NPs (Figure 1.1.5.).

The impregnation of NMOFs with metallic salts to reduce them to form small clusters of atoms has been achieved for Cu, Ag,[38] Ni,[39] Au,[45] Pt,[46] alloys,[47] among others. In most cases, the impregnation step involves the physisorption of metallic species within the MOF matrix, but in some cases, the processes involved the formation of coordinated bonds between an electron donor group from the organic linker and the metal ion. That is the case of UiO-67-bipyridine, where the linker 2,2'-bipyridine-5,5'-dicarboxylic acid has in its structure two nitrogen atoms and which are capable of coordinating metals for being reduced in a second process, like Au for the generation of reactive oxygen species (ROS) or Pd[48] as a catalyst for Suzuki reactions.[49]

The core-shell approach has some limitations, as the needed affinity of the previously synthesized iNPs with the metallic node or cluster and the organic linker, or the compatibility with the reaction conditions. This last one is rather critical as the reaction condition in most cases involve high temperatures or organic solvents that may lead to the degradation of the iNPs. There are several methods to avoid this reshaping, as the surface coating using amphipathic polymers as polyethylene glycol (PEG) that provides the particles with stability in organic media.[50]

The use of surfactants such as CTAB has been identified as a helper to produce an adequate surface on colloids *i.e.*, gold or palladium NPs to grow a NMOF shell. This approach has been explored by us to create ZIF-8 shells onto individual NPs to create core@shell composites with controlled size. This approach is suitable to work on different NPs´ sizes and morphologies including anisotropic materials.[18-20]

USC UNIVERSIDADE DE SANTIAGO DE COMPOSTELA

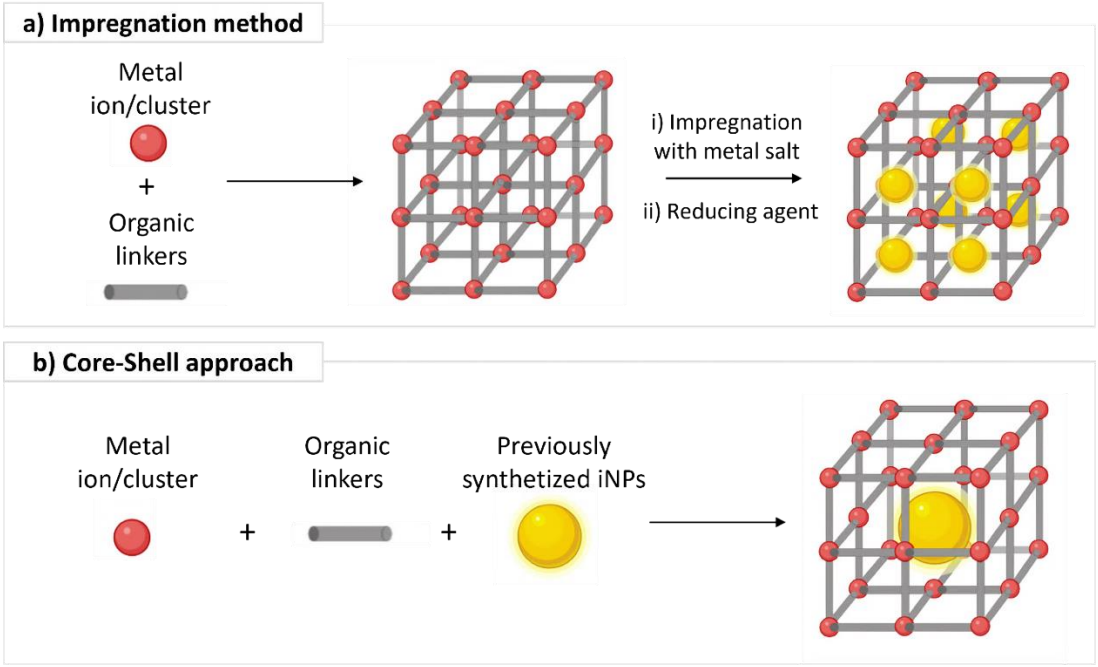

Figure 1.1.5. Schematic representation of different approaches to produce iNPs@NMOFs nanocomposites.

1.1.6. Cargo Loading inside MOF´s pores.

One of the main advantages of the MOFs is the high and permanent porosity that can be used to load cargoes of different nature, *i.e.*, size, charge, or polarity. Therefore, NMOFs can host a wide variety of guests or reagents, such as proteins, carbohydrates, drugs, or nucleic acids.[51,52] The incorporation of APIs inside the NMOFs´ pores offers a solution to some of the main problems related to the systemic administration of free drugs or biomolecules, like the fast biodegradation, side effects or the difficulties of some agents crossing the cell membrane.[52] The incorporation of biomacromolecules or other pharmaceutical agents in the MOFs can be achieved by three approaches: encapsulation, post-synthesis strategies and direct assembly.[53] Last method refers to the use of the selected cargo or a prodrug as ligands in the synthesis of NMOFs, via coordination bonds between the cargo and the SBU. However, next part will focus mainly on the first two strategies (Figure 1.1.6.).[54]

1.1.6.1. Post-synthesis encapsulation

This approach involves the loading of the selected cargoes via noncovalent or covalent interactions, and lately has been successfully performed for the encapsulation of chemotherapeutic drugs, DNA, or enzymes (Figure 1.1.6.a).[54] The pore and the cargo size play a key role in this approach, as it is necessary to fit these agents inside the MOF´s structure. MOFs´ pore sizes can be tailored from micropore (<2 nm) to mesopore (2-50 nm).[55] This way, larger pores would allow the encapsulation of larger cargoes and a higher loading capability.[54] However, it is critical to ensure the stability of the loading inside the structure to avoid uncontrolled cargo release. To achieve this stable loading, there are some strategies such as the MOF´s amorphization via heating or ball-milling treatments, or the further functionalization of the structure's surface to block the pores of the MOFs.[18,56]

The most used post-synthesis encapsulation approach is based on the infiltration of the selected agents. Here, the loading is achieved by free diffusion of the functional guest molecules

through the pore aperture of the pre-synthetized MOFs. This way, the agents will be filling the pores typically with high loading efficiency. One of the main advantages of this method is that the loading can be carried out in mild conditions, enabling the incorporation of sensitive cargoes such as enzymes, that may be degraded under synthetic conditions.[55] Furthermore, when entrapped inside the MOFs, enzymes can maintain their activity in harsh conditions such as high temperatures or organic solvents.[57] For example, Wang *et al.* recently reported a new Zr-based NMOFs (NU-1000 and PCN-222) for the delivery of insulin as model protein.[56] Insulin was loaded via infiltration by mixing the particles with an insulin (0.4 $mg \cdot mL^{-1}$) solution in bis-tris-propane buffer (BTP, pH = 7). The results showed high loading capabilities of the NMOFs with values of 34 and 63 wt % of insulin for NU-1000 and PCN-222 NMOFs, respectively. This strategy can be applied also for the loading of other relevant active molecules such as photosensitizers (PS). For example, Lou *et al.* showed the encapsulation of zinc-phthalocyanine (ZnP) PSs inside a Hf-Ir NMOF for highly efficient photodynamic therapy (PDT).[58] The loading was achieved by simply mixing the NMOFs with the ZnP in DMF at 70°C for 24h, resulting in loadings of 13.6 wt% of ZnP. The encapsulated cargo presented high light absorption with reduced aggregation-induced quenching and an improvement of $^1O_2$ generation. Additionally, the samples were tested in mouse models and showed great efficiency to eradicated and reduced colorectal cancer.[58]

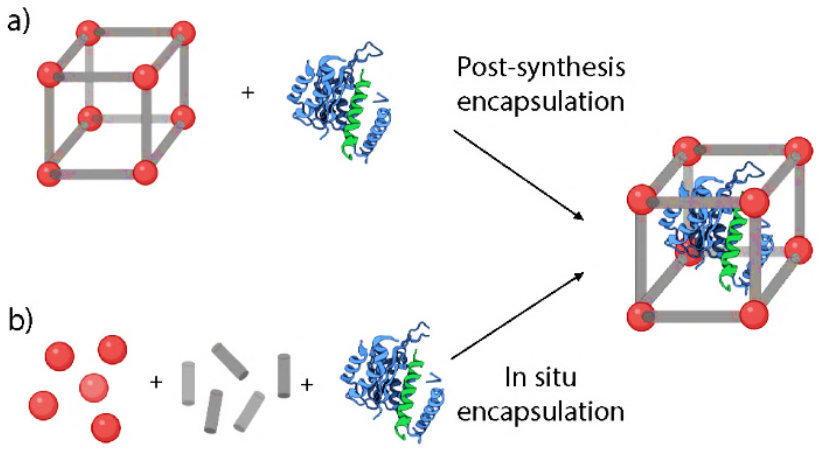

Figure 1.1.6. Schematic representation of a) post-synthesis encapsulation and b) In situ encapsulation methods.

In some other cases, the post-synthesis encapsulation has been employed for the loading of fluorescent probes. As a proof of concept, a dye molecule was loaded inside the pore of ZIF-8-gold nanostars (AuNSs) nanocomposites (NCs) to study the controlled release of the cargo.[18] Bisbenzimide compound Hoechst H 33258 (HOE) was selected as bioactive cargo, a blue fluorescent dye typically used for DNA staining in molecular biology. The loading was performed by immersion of the NCs in a HOE solution in methanol, achieving an average loading of 2.9 x 10^5 HOE/NC.

However, this method presents some drawbacks as there is a size limitation for the selected loadings that need to diffuse through the pore aperture of the MOFs. This also can lead to some problems such as the leaking of the guest molecules that are smaller than the pore size.

USC
UNIVERSIDADE DE SANTIAGO DE COMPOSTELA

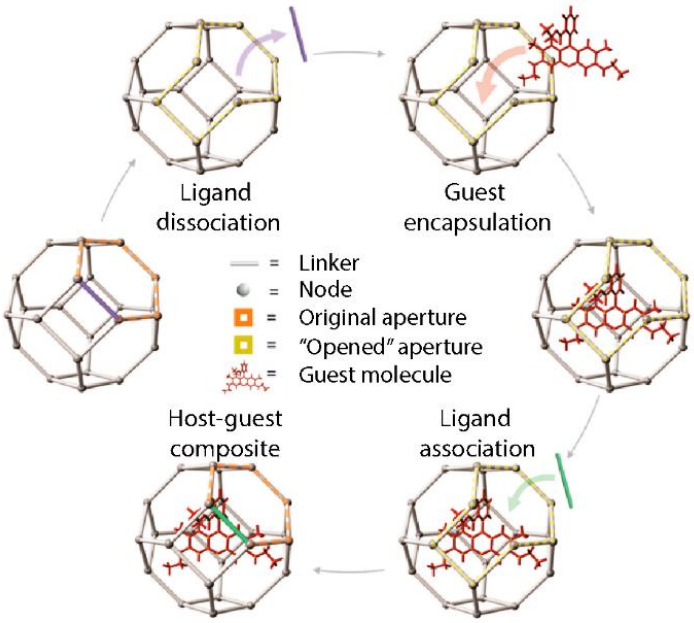

Figure 1.1.7. Schematic representation of the post-synthesis encapsulation of a guest molecule taking advantage of the ligand exchange reactions. Adapted with permission from Morabito et al.[59] Copyright 2014, Journal of the American Chemical Society.

As a solution to this problem, Morabito *et al*. reported a new approach for the encapsulation of larger guest molecules inside the MOFs by taking advantage of ligand exchange reactions that lead to the "opening" of part of the external framework of the pre-synthesized MOF (Figure 1.1.7.).[59] This ligand exchange is based on the fact that coordinative-saturated metallic centers make the dissociation easier providing the MOFs with temporary vacancies. These vacancies would temporarily expand the pore aperture allowing larger molecules to diffuse inside the NMOFs without interfering with the crystalline structure and morphology. Then, the dissociated linkers can be restored so that the cargo is trapped inside the pores. In 2018, the application of this method was reported for the encapsulation of catalysts inside the structure of robust MOFs such as the UiO-66.[60] The encapsulation of two molecules was considered, *i.e.*, a fluorescent molecule, Rhodamine 6G (R6G), and a ruthenium complex as a catalyst. The encapsulation process was analyzed under different conditions and proved that the R6G loading was highest at elevated temperatures in polar protic solvents (*e.g.*, methanol), whereas the dye leaking was reduced in aprotic solvents compared to protic solvents. The experiments were repeated in similar conditions for the encapsulation of the ruthenium complex showing coherent results and proving the potential of the method for the encapsulation of transition metal complexes within MOF based on a solvent-dependent, aperture-opening events occurring from dissociative linker exchange reactions in MOFs.

1.1.6.2. In situ encapsulation

This method, also called *de novo* approach, involves the encapsulation of guest molecules inside the pores during the MOF growth process (Figure 1.1.6.b.). The main advantage of this method is the high loading efficiency independently of the pore size.[55] Some recent works have studied the encapsulation of enzymes using this approach and proved the reduction of structural changes that usually lead to protein unfolding.[61,62] Furthermore, this method can also be applied for the encapsulation of a wide variety of metalorganic compounds and

organometallic complexes.[63] As an example, Liao *et al*. employed this method to prove the maintenance of the biological function of enzymes under a wide variety of conditions.[61] They reported the encapsulation of catalase inside ZIF-90 and ZIF-8 MOFs. The loading was performed via a water-based mild *de novo* approach where a zinc nitrate solution was mixed with an aqueous solution containing appropriate amounts of imidazolate-2-carboxaldehyde (ICA), catalase, and capping agent. The results showed loadings up to 6.0 wt % and the encapsulated catalase showed higher stability and kept its enzymatic activity even under harsh conditions such as urea treatment. Alsaiari *et al*. reported the first successful encapsulation of CRISPR/Cas9 inside ZIF-8 NMOFs (CC-ZIFs) for its intracellular delivery.[64] The co-encapsulation of Cas9 protein and sgRNA was performed via *de novo* approach, by mixing the Cas9 and sgRNA in a phosphate buffer saline (PBS) solution with the ZIF-8 precursors in water. The NMOFs´ size was characterized by electron microscopy and dynamic light scattering (DLS), presenting sizes of *ca.* 100 nm. The loading capability was estimated to be 1.2 wt % of the Cas9/sgRNA with an efficiency of 17%. Furthermore, the particles showed improved endosomal escape abilities, with a decrease of up to 37% of the gene expression over 4 days. This way, they proved the potential of this ZIF-8 NMOFs as an efficient delivery method, where the imidazole-based framework at endosomal pH provokes the endosomal escape and improve the nuclei delivery. However, this encapsulation strategy presents some drawbacks as it requires the stability of the selected guest molecules in the synthetic conditions, that in some MOFs involve organic solvents or high temperatures that can lead to their degradation.

Overall, guest immobilization techniques still need to be improved to achieve higher loading rates and increased stability of cargo and loaded MOFs for their applications in biomedicine. Some of the main problems to be addressed are related to: i) the microporosity of the structures which avoid the incorporation of macromolecules as enzymes, ii) the synthetic conditions that are not biocompatible with the integrity of some cargo (i.e., chemical stability, or maintenance of structure and function of proteins) or, iii) the stability of the cargo once it is encapsulated.[55] Therefore, it is necessary to develop new strategies so that these systems can be used in clinics.

1.1.7. Surface modification

Besides their chemical stability and their ability to encapsulate different cargoes, another relevant characteristic of NMOFs is the possibility of suffering external surface functionalization. These post-synthetic modifications allow the improvement of their colloidal stability, cellular uptake, control drug release, or prolong their circulation time.[65] When it comes to targeting, discerning between cancerous and normal cells poses significant challenges in cancer treatment. Unwanted off-target effects can result in adverse side effects and harm to healthy cells, complicating the therapeutic process. Functionalizing the surface of NMOFs can provide recognition abilities by their modification through specific interactions with molecules such as peptides, antibodies, or saccharides, capable to interact with cells via specific ligand-receptor recognition. In this context, utilizing the variances in cellular processes and surface markers between cancerous and healthy cells offers significant potential (Figure 1.1.8.). This can pose some challenges, as the external surface modification agent and process must effectively meet several critical objectives as preserving the integrity of the MOF structure, enhancing the material's stability in biological environments, and ensuring no interference with the entrapped molecule.[66]

There are two main strategies for the surface functionalization of NMOFs. The first one is based on the modification during the NMOF´s self-assembly where, as an example, the organic

linker can be modified to introduce functional groups to change the final NMOF surface. This method presents an important limitation as the potential of organic molecules that can be introduced as linkers are limited.[67,68] The other one is the so-called post-synthetic modification (PSM) that allows the surface functionalization of already synthesized particles. In this case, it is critical to use specific reaction conditions to avoid NMOFs´ degradation and losses of crystallinity and porosity.[67] Within this second method, one can find four main approaches (Figure 1.1.9.): i) the attachment of new molecules via coordination to free metal sites (Coordinative PSM), ii) the formation of covalent interactions at reactive sites (Covalent PSM), iii) "core-shell" strategies based on the NMOF coating with polymers or silica and iv) cell membrane coating.[68,69]

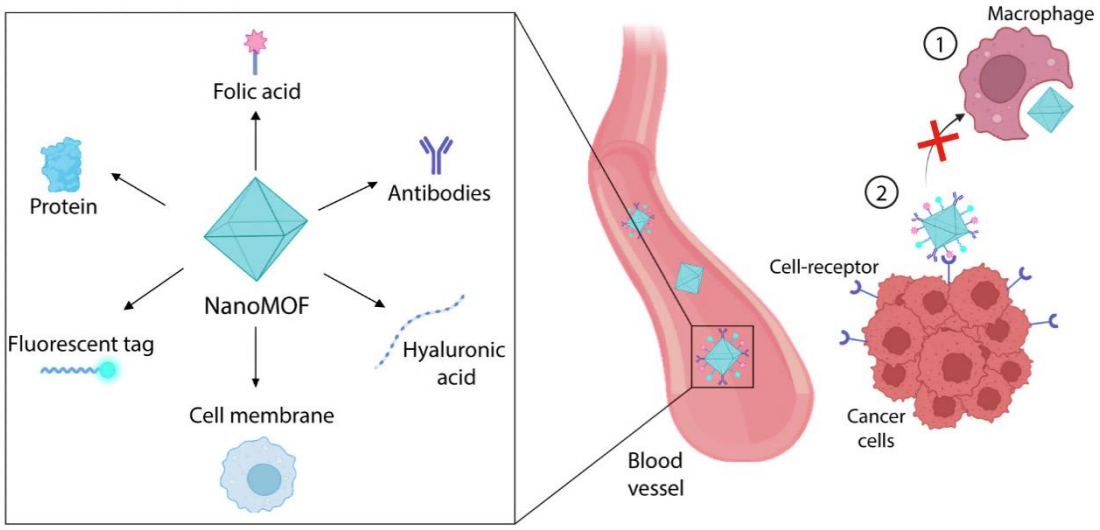

Figure 1.1.8. Possible surface functionalization techniques in NMOF delivery and distribution encompass strategies designed to (1) evade macrophagocytic clearance and (2) enhance cell selectivity and targeting for improved efficacy.[66]

1.1.7.1. Coordinative PSM

This type of PSM takes advantage of the free metal sites present on the superficial SBUs of NMOFs due to structural defects to add new functionalities via coordination chemistry. The most used molecules are chelating molecules such as carboxylates or phosphates. This way, the surface of the NMOFs can be selectively modified while maintaining the porosity and crystallinity of the structure.[70] Using this method, NMOFs can be easily functionalized with biomacromolecules modified with coordinative groups. In the context of biomedical systems, one of the main challenges is the intracellular delivery of biomacromolecules such as proteins or peptides.[71] Wang *et al.* reported the functionalization of the Zr-based NMOF NU-1000 via coordinative PSM with nucleic acids.[72] For that, they employed terminal phosphate-modified oligonucleotides achieving a homogenous and effective coating that increased the NMOF´s stability and cellular uptake. Similarly, Chen *et al.* used the free positions in the Zr present in PCN-222 NMOFs to functionalize their surface with a phosphate functionalized PEG (5kDa MeO-PEG-PO_3) to increase the stability and delay the release of the encapsulated drug.[73]

1.1.7.2. Covalent PSM

The post-synthetic covalent modification of NMOFs´ surface includes two main strategies: i) the addition of functionalities that do not fit inside the pores of the structure and ii) the use of

USC UNIVERSIDADE DE SANTIAGO DE COMPOSTELA

reactive moieties in the outer part of the particles to add new functionalities.[70] To work, this strategy requires that the selected ligands have specific chemical functionalities that do not interfere in the MOF´s structure and allow the modification of the outer and internal surfaces of the MOF.[71,74] This MOF functionalization approach can improve the colloidal, chemical and thermal stability of the particles.[61,62] Some modifications include N-alkylation, click chemistry or protonation.[70] Besides the improvement of the colloidal stability, one of the main purposes of the surface modification of NMOFs in the context of bioapplications is the increment of the blood circulation time of the NPs (stealthiness). Usually, different polymers can be employed for this purpose, such as PEG, which is one of the most typical and common coatings used for nanomaterials.[71] As a representative example, Zimpel *et al.* reported the functionalization of the MOF MIL-100 (Fe) with amino-PEG by the conjugation of the amino group with the NMOF surface groups, achieving increased stability of the NMOFs.[75]

1.1.7.3. "Core-shell" strategies

The creation of core-shell structures is an approach widely used for stabilizing colloidal inorganic NPs. Now, this methodology is also being used to stabilize NMOFs increasing their biocompatibility.[70,71] This method is based on the NMOF´s core coating with a dense shell. Silica coatings are typical examples of these core-shell strategies, which provide protection to the NMOF against decomposition and can act as a support for further functionalization. The use of organic shells is a very extended strategy to create core-shell systems. Polymers such as poly(vinylpyrrolidone) (PVP) or PEG are widely used to fabricate core-shell nanosystems. To create shells using polymers, amphiphilic polymers such as poly- [isobutylene-alt-maleic anhydride]-graft-dodecyl (PMA) can be used to stabilize NPs of different materials, shapes and sizes.[43,76] MOFs such as ZIF-8 have been coated with this polymer, showing an increased water stability and reduced leaking of the cargo. Besides this, polymers could be modified with functional groups to act as an anchoring point for the further addition of new functionalities. Other examples of this coating strategy include the lipid bilayer coating or the cell membrane coating, which are usually employed to improve the stability of the particles in biological media and achieve immune evading capacities, leading to the increment in the blood circulation time.[71]

1.1.7.4. Cell membrane coating

The use of cellular membranes to coat colloidal nanomaterials can endow these systems with new properties. Coating of nanomaterials has been carried out using different cell lines including platelets, mesenchymal stem cells, red blood cells, immune cells or cancer cells.[77] Final properties of the nanomaterials will be highly influenced by the cellular coating providing them with lymphocyte and dendritic cell activation, tumor targeting, immune scape abilities, endothelial adhesion or homotypic targeting, respectively.[78][79][80][81] One of the most commonly used approaches in the used of membranes derived from cancer cells, this coating provides NMOFs homotypic targeting abilities, which is the ability of self-recognition of cancer cells for its cell lineage or the evasion of the immune system.[82][83] Therefore, this strategy offers great advantages for its use in areas such as cancer therapy or vaccination. Whereas NMOFs had been coated before with liposomes or exosomes, this strategy is relatively new, with few examples available.[84] [85] Recently, Alyami et al. have developed biomimetic cancer cell coated ZIFs for cell targeting and specific delivery of CRISPR/Cas9, following its previous results (see section 1.4).[86] They coated the CRISPR/Cas9-loaded ZIF-8 NMOFs (CC-ZIF-8) with human breast adenocarcinoma cells (MCF-7) membranes to improve cell-targeting by the inherent homotypic targeting of tumoral cells. The uptake of CC-ZIF-8 was studied in different

cancer cell lines and healthy cells, showing higher uptake for MCF-7 cells and negligible uptake for the healthy ones. This proved the efficiency of this biomimetic approach increasing NMOFs selectivity and overcoming one of the main problems in DDSs.

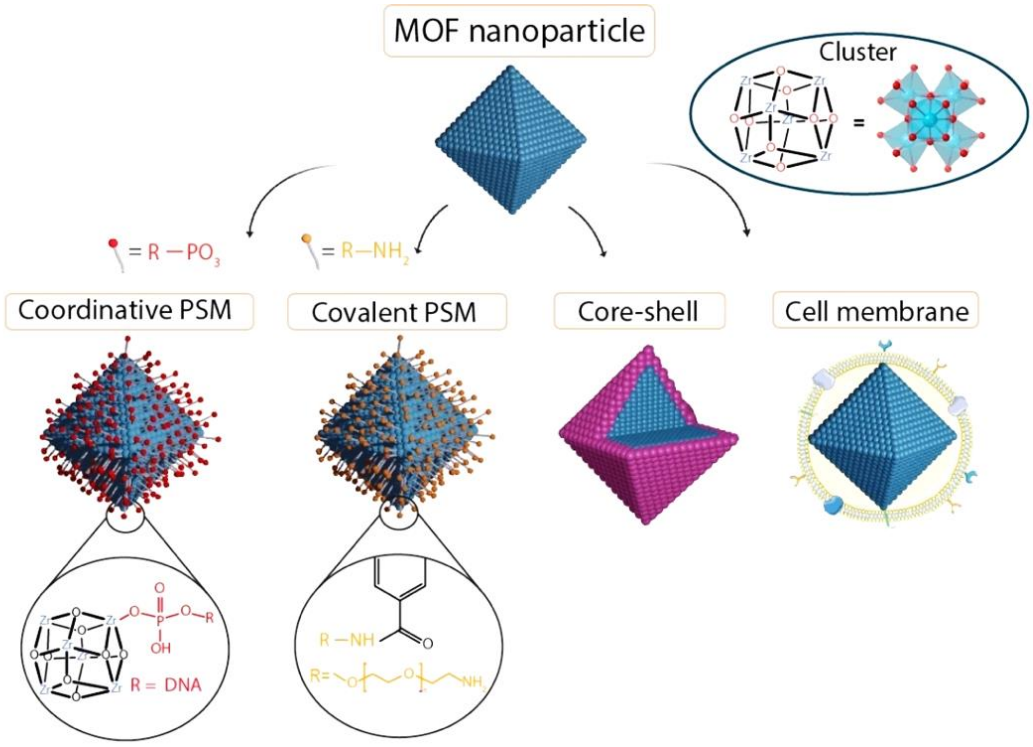

Figure 1.1.9. Schematic representation of different PSM approaches to achieve surface modification in MOFs.

1.1.8. Stability

MOFs stability should be carefully assessed for their application, especially in biomedicine, where the degradation of the particles can cause the loose of their functionalities and may lead to different toxicity results.[87] The surface of the nanocrystals constitutes the most reactive domain of the structure and is where the interaction with the components of the surrounding media occurs. As previously mentioned, engineering the surface of NMOFs is critical to determine aspect such as the colloidal stability of the NMOFs in biological media, the formation of the protein corona or the targeting abilities.[88] For this reason, it is important to study all the possible interactions on the bio-interface (aggregation, biodistribution, or elimination) to develop stable systems.[89] The stability of NMOFs can be divided into colloidal and chemical stability.

1.1.8.1. Colloidal stability

Colloidal stability refers to the capacity of the particles to remain suspended at equilibrium in a solution. Therefore, the lack of colloidal stability would lead to limiting the possible administration routes and/or issues related to uncontrolled early drug delivery.[90] For this reason, it is critical to consider the colloidal stability at the long-term storage and further resuspension in solution before their administration.[90] Moreover, it is important to analyze the behavior of the particles in physiological environments. This behavior is partially governed by electrostatic interactions. So, when the surface charge of NMOFs is close to neutrality, the repulsion between the particles will be reduced and they will tend to aggregate. Likewise, if the

surface charge increases, the colloidal stability will be improved. However, this feature depends on the media where the particles are placed and the interaction with the components of this media, for example, proteins tend to adsorb non-specifically forming the so-called protein corona or biocorona which can lead to uncontrolled aggregation processes.[91]

1.1.8.2. Chemical stability

On the other hand, the chemical stability of MOFs has received considerable attention during the past years. Several studies have been performed to understand the decomposition pathways and the stability of the particles in different media.[87] Ideally, the chemical stability of NMOFs should synchronize *in vivo* degradation with the expected functional therapy for a given biomedical application.[88] Generally, the chemical stability of MOFs is referred to their ability to keep their structural features after being exposed to chemicals, high temperatures, and mechanical forces.[92] This stability depends on several factors such as thermodynamic, kinetic, or the presence of other elements present in the environment surrounding the particles, all influencing the design of stable framework structures. [93,94]

Thermodynamic stability: The stability of the MOFs is related to their resistance to chemical treatments (such as water, acid, or salt solutions) to maintain the structure and porosity.[95] This stability is mainly related to the strength of the metal-ligand (M-L) coordination bond, which may be predicted by Pearson's (HSAB, hard soft acid-base) theory. This theory considers ligands with relatively high pKa (*e.g.*, azoles like imidazolates or pyrazolates) as soft bases producing robust frameworks with low-valent metal ions (Zn^{2+}, Cu^{2+}, Ni^{2+} or Mn^{2+}) which can be considered as borderline soft acids. The most typical example of this is the ZIF-8 built by the coordination of Zn^{2+} metal ions and imidazolates. On the other hand, ligands with relatively low pKa (*e.g.*, carboxylic acids) are considered as hard bases and form high stable MOFs by preferentially binding to high-valent metal ions (Ti^{4+}, Zr^{4+}, Al^{3+}, Fe^{3+}, and Cr^{3+}) which are hard acids.[93,95] The Zr^{4+} MOFs such as UiO-66 ($[Zr_6O_4(OH)_4$ $((OOCC_6H_4COO_{12}])$ have shown high stability features. Zr^{4+} has a high charge density, which creates a strong affinity when the Zr^{4+} ions interact with carboxylate groups, generating strong Zr-O bonds. The combination of $[Zr_6O_4(OH)_4]$ or $[M_3OX(CO_2)_6]$ (M = Al^{3+}, Cr^{3+}, or Fe^{3+}; X = OH^-, F^-, or Cl^-) clusters with carboxylate linkers with different topologies give rise to a wide diversity of MOFs with great stability, as UiO-66, PCN-222, MIL101(Cr), MOF-808.[95]

Kinetic stability: The kinetic factors constitute other key points affecting the stability of the MOFs and depend mainly on the rigidity of the linker. The elongation of the ligand has the advantage of the enlargement of the pores, but at the same time, it weakens the framework structure.[95] The reason is that the length of the ligand is related to the activation energy of the MOFs dissociation process and, therefore, it affects its degradation.[92] As an illustrative example, the UiO isoreticular family of MOFs (UiO-66, UiO-67, and UiO-68) have the same cluster but they differ in the linker length. The coordination bond strength should be equal in the three cases based on the previously explained HSAB theory and the chemical stability should be the same. However, it has been proven a decrease in the stability while increasing the linker length directly correlated to its rigidity.[87] Dense and rigid frameworks formed by rigid and highly connected building blocks (metal ions/clusters and ligands) generally show higher stability against partial lattice collapse. Another kinetic factor affecting structural stability is the linker hydrophobicity. When the surface of the particle is mainly hydrophobic, the structure tends to be more stable in aqueous media as it avoids the adsorption of water in the pores or its condensation around metal clusters.[93] The incorporation of functional groups within the MOFs structure will be likely to reduce the pore size and cause the condensation of water vapor at

decreased pressures.[87] For example, in ZIF-8 the methyl groups on the imidazolates can serve as blocking agents preventing water molecules from approaching the ZnN_4 node leading to increased stability.[92]

Additionally, by selectively designing hydrophobic surfaces or interfaces, water and other guest molecules can be excluded from approaching metal ions.[87] The addition of functional groups capable to repel water from the metal clusters' surroundings can act as a defense against the weak coordination bonds improving the water stability.[93] Furthermore, the structural stability of the particles can be improved by using post-synthetic strategies including post-synthesis exchange, post-synthesis modification or hydrophobic surface treatments.[93] Some examples of typical coatings to improve the colloidal and chemical stability of the particles in biological media are polymers, polysaccharides, or phospholipids, where the hydrophobic part can coat homogeneously the outer surface of the NMOFs that would impede the permeation of ions and protect the weak coordination bonds against phosphates present in the medium.[90]

Despite the community efforts, the assessment of the chemical stability in biological relevance media is still not completely addressed. This is a consequence of the high number of variables that should be considered, such as the type of components of the media, their concentration, or the temperature of the solution, among others.[92]

1.1.9. NMOFs in biological media

During the past few years, several studies have proven MOFs to be promising materials for their biomedical applications as DDSs, contrast agents or photothermal therapy (PTT) agents.[88] However, there are still some important issues concerning these materials that need to be assessed for their clinical applications, such as their toxicity and immunological impact,[96] which remains relatively unknown. The toxicity of NMOFs, as it happens for other NPs, depends on different parameters that can affect their interaction with living organisms, including chemical composition, structure, size, morphology, and surface properties.[88] These materials can be easily internalized into cells and subcellular compartments.[96]

NPs routes of entry inside the cells are determined by their interaction with elements in the extracellular matrix and the outer plasma membrane. Generally, the entry process occurs via endocytosis, where the particles are internalized in the cells via engulfment processes followed by the generation of endocytic vesicles and transported to the particular intracellular compartment.[97] Very generally, one can distinguish among five types of endocytosis: phagocytosis, clathrin-mediated endocytosis, caveolin-mediated endocytosis, clathrin/caveolae-independent endocytosis, and micropinocytosis.[98] Clathrin and caveolin-mediated endocytosis constitute the two main mechanisms of NPs uptake.[98] These interactions are highly affected by the physicochemical properties of NPs, as the size, shape, surface charge, surface chemistry or chemical stability (Figure 1.1.10.).[98,99]

USC UNIVERSIDADE DE SANTIAGO DE COMPOSTELA

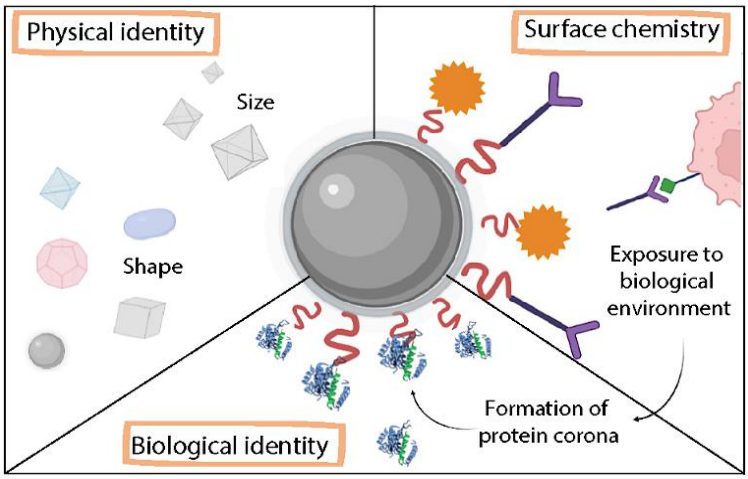

Figure 1.1.10. Schematic representation of factors that determine toxicity of nanoparticles.

1.1.9.1. Size and agglomeration

The size of the NPs plays a key role in the cellular uptake and toxicity of the NPs.[98,99] NPs can induce toxicity as their size becomes comparable to the size of the molecular components, their ability to penetrate physiological barriers increases, inducing the interruption of physiological functions and sometimes causing cell death. Furthermore, as mentioned above, when reducing the size of a material to the nanoscale, there is a high increase in the surface area but also its reactivity. This determine their stability as there is a higher exposure to the surrounding media that can lead to the degradation of the particle into smaller fragments. Like the dimension effects, the agglomeration state of the NPs in biological fluids also affects toxicity. In most cases, the interaction of NMOFs with biological media components leads to an uncontrolled aggregation that produces the formation of bigger agglomerates that changes their biological behavior.

1.1.9.2. Surface chemistry

As previously mentioned, surface of NMOFs is their most reactive part. The correct surface engineering can contribute to the stability of the NPs in biological media and to minimize undesired interactions with the surrounding biological environment.[88] One important factor is the surface charge of the particles. For example, charge affects the electrostatic interaction between the NMOFs and cellular membranes, having a great impact on the cellular uptake. Some studies have shown that charged particles, either negative or positive, showed higher uptake than neutral counterparts, due to the attractive/repulsive forces among the cationic/anionic NPs and the negatively charged cell membrane.[100]

The hydrophobicity will affect the interactions with proteins and the protein corona formation and therefore the way the interact with cells.[74] As previously discussed, NMOFs can be functionalized to target specific receptors or molecules by the addition of peptides, antibodies, or proteins.[96,98] At the same time, several strategies have been developed to increase the chemical stability and minimize the adsorption of biomolecules as proteins or lipids, as well as to target the NPs, *i.e.*, PEGylation. Nevertheless, it is worth noticing that despite the surface functionalization of NMOFs, their properties will experiment changes when placed in biological media that can be difficult to predict, and these interactions in the bio-interface will define the fate of the NMOFs, and hence, their toxicity.[96]

1.1.9.3. Biological chemical stability

The stability under biorelevant conditions is also an important feature to consider before evaluating the final toxicity. MOFs can undergo different degradation processes in biological media. Depending on the nature of MOFs components (i.e., metal cations, SBUs or linkers), they will be processed by the organism in a different way and may generate higher toxicity rates. For that, it is important to evaluate both the stability of the structure, choosing MOFs with strong coordination bonds between the metal and the ligand, and the toxicity of the individual components *i.e.*, the toxicity of the free metal, metal clusters or linkers. Following the concepts discussed in the previous section, for a more acidic environment, it would be convenient to use NMOFs with 'hard´ constituents to avoid the competition between metal ions and protons from the media. However in more basic surrounding these MOFs will likely degrade due to the exchange of organic ligands by OH^- groups present in the media.[96] Depending on the components, the toxicity of the NMOFs would be classified as less toxic for those containing Ca^{2+}, Bi^{3+} or Eu^{3+}, followed by those with Ti^{4+}, Fe^{2+}, Fe^{3+}, Co^{3+}, Al^{3+}, and Cr^{3+}, and followed by Zr^{4+}, Mg^{2+}, Gd^{3+}, Ni^{3+}, and Zn^{2+}, whereas those with Cu^{2+} and Mn^{2+} can be considered the most toxic. Moreover, the hydrophobicity of the linker also plays an important role in the final toxicity of the particles. As an example, hydrophobic ligands interact easily with lipid droplets in the lysosomes, so it takes more time to remove them from the organism, whereas hydrophilic linkers are cleared faster.[97] Therefore, the engineering of the particle surface constitutes a key factor for the improvement of the stability, as it would avoid the degradation of the particle and the biodistribution would be mainly influenced by the properties of the MOF (size, surface chemistry, etc.) and not its constituents. The higher the degradation of the MOF, the higher release potential toxic substances.

To assess the biocompatibility of NMOFs, their behavior must be studied carefully. First step will cover testing their stability and degradation in different biological media, such as PBS or cell culture media, at their corresponding pH. These studies will facilitate the prediction of the *in vitro* behavior of the NPs before performing further toxicity tests.

After confirming the stability along time in complex biological media, *in vitro* studies should be carried out. However, cytotoxicity studies *in vitro* are generally conducted in cancer lines to prove their potential as cancer treatments, whereas there are only few studies in healthy cells.[74] For these studies, the particles are normally incubated for 24h to 72h at different dose rates, and cell viability is evaluated. The parameter evaluated is called IC50, which corresponds to the concentration (in mM or $mg \cdot mL^{-1}$) of the particles that cause 50% inhibition of cell growth.[96]

1.2. METALLIC NANOPARTICLES FOR NMOFs COMPOSITES

1.2.1. Plasmonic nanoparticles

Plasmonic nanoparticles have been widely used in biomedical applications due to some of their features as their high chemical and physical stability or high biocompatibility. But mainly they have great interest due to its ability to interact with electromagnetic radiation thanks to its optical properties.[101]

Localized surface plasmons (LSPs) are charge density oscillations confined to metallic nanoparticles (sometimes referred to as metal clusters) and metallic nanostructures. Excitation of LSPs by an electric field $\vec{E}_0$ (light) at an incident wavelength where resonance occurs results in strong light scattering, in the appearance of intense surface plasmon (SP) absorption bands,

and an enhancement of the local electromagnetic fields.[102] This is called Localized Surface Plasmon Resonance (LSPR), which occurs when free electrons on the metallic surface are excited by the electric component of electromagnetic radiation, generating a coherent oscillation of conduction electrons around the particle at a resonant frequency that produces a localized electromagnetic field (Figure 1.2.1.).[6] In metallic nanoparticles such as gold, silver, copper, among others, the frequency of LSPR is found in the visible spectrum region, leading to intense absorption and scattering of light in that region, accounting for the vibrant colors displayed by their colloidal dispersions.[103,104]

The LSPR concentrates the electric field of light on the particle's surface, amplifying it by several orders of magnitude.[105] This electromagnetic field gradually weakens as it moves away from the NP's surface. The spectral characteristics of the LSPR depend on the size, geometry, composition, and refractive index of the NP's environment.[106,107] Therefore, controlling these properties is essential for their application in various fields. For instance, light absorption and scattering can be adjusted by modifying the shape and size of plasmonic NPs, allowing the tuning of their absorption spectrum to different wavelengths.[107]

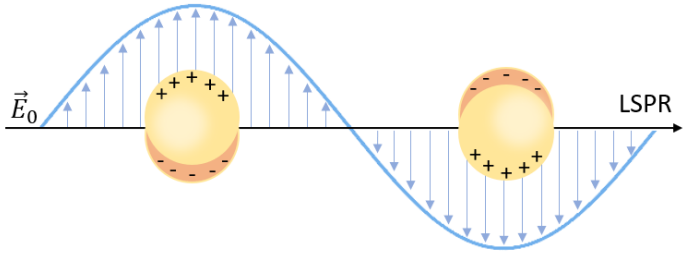

Figure 1.2.1. Localized Surface Plasmon Resonance in plasmonic nanomaterials produced when the electrical field of an electromagnetic wave interacts with its electronic free cloud.

Gustav Mie's theory was proposed in 1908, an states that when metallic nanoparticles are exposed to light with the same wavelength as the collective oscillation of the conduction-band electrons, the phenomenon of resonance occurs (LSPR).[108] Mie's theory provides a comprehensive framework for understanding and predicting how metallic NPs interact with light. It is based on Maxwell's equations and provides a mathematical framework to calculate the scattering and absorption efficiency, taking into account factors such as particle composition, size, and refractive index of both the particle and the surrounding medium.

The surface plasmon oscillation can be described by the polarizability α of the dipolar mode:

$$\alpha = 3\varepsilon_0 V \left(\frac{\varepsilon-\varepsilon_m}{\varepsilon+\chi\varepsilon_m}\right) \quad [1]$$

where ε_0 is the vacuum permittivity, V is the volume of the particle, ε_m is the permittivity of the medium, χ is a constant ($\chi = 2$ for spherical nanoparticles) and ε(ω) is the complex dielectric function of the metal frequency dependent ($\varepsilon(\omega)=\varepsilon_r(\omega) + i\varepsilon_i(\omega)$). This equation shows there is a strong resonance when $\varepsilon=-2\varepsilon_m$, which coincides with the SPR frequency of the nanoparticle. This corresponds to the maximum peak of absorption at the plasmon frequency, which for gold and silver nanoparticles occurs at visible-NIR light. LSPR is highly affected by factors that influence the density of electrons on the particle surface, such as size, shape, composition, dielectric properties of metal, and the surrounding medium.[109] Therefore,

USC UNIVERSIDADE DE SANTIAGO DE COMPOSTELA

these factors are responsible for the absorption and scattering properties of plasmonic nanoparticles.

The plasmon resonance effect results in a strong enhancement of radiative properties of the NPs, such as scattering and absorption, and may even lead to the generation of energetic (hot) electrons that can largely influence chemical reactions.[110] However, the persistence of plasmonic oscillation is limited in time by energy losses. This can be understood with the complex permittivity of the material, where the real part describes the frequency of resonance, and the imaginary part describes the losses.[104] The energy loss of the electromagnetic wave after interacting with matter is due to two principal contributions: absorption and scattering processes, which reflect the observed colour of the colloidal metal nanoparticle solution.[109,111] The absorption phenomenon occurs when the incident light is dispersed via inelastic processes, whereas scattering takes place when the incident light is scattered either with the same wavelength as the initial light (Rayleigh scattering) or with shifted frequency (Raman scattering).

The cross sections of these processes (absorption or scattering) are highly dependent on the size and shape of the NPs. For smaller particles, as 20 nm gold spheres, absorption constitutes the main energy losses and the ones due to scattering are negligible. When the size of the particles increases (40-80 nm), the scattering effects become significant and both types of losses must be considered.[111] Besides the size of the particles, the shape can play a key role in the optical properties. For example, smaller gold nanorods with a higher aspect ratio are the best photo-absorbers, whereas those with a larger volume and higher aspect ratio are the best scattering contrast agents.[109] Moreover, plasmonic nanoparticles undergo non-radiative processes alongside radiative ones, finding applications in bioapplications such as photoemission, electrical doping, and local heating. When excited at resonant wavelengths, these nanoparticles experience relaxation processes, leading to the generation of hot electrons. These hot electrons transfer energy to the metallic lattice, causing thermal dispersion and a substantial temperature increase of tens of degrees (photothermal effect) (Figure 1.2.2.). Eventually, both the lattice and excited electrons cool down, returning the system to its ground state.[109]

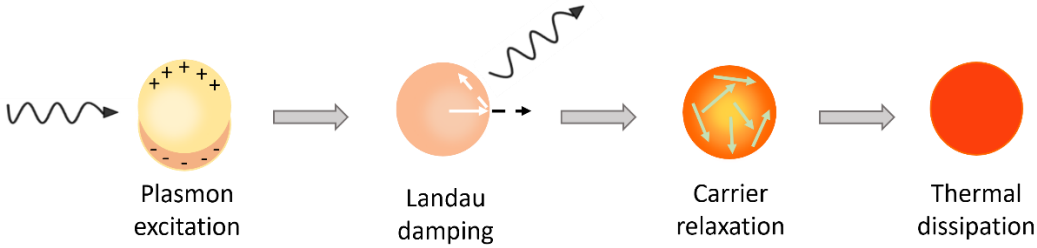

Figure 1.2.2. The stages of energy relaxation of excited plasmon: i) The incident electric field excites the surface plasmon, ii) the plasmon quasi-particles lose their energies by different scattering processes to excite hot carriers, iii) Hot carriers undergo redistribution through electron-electron and other scattering mechanisms, gradually thermalizing over a period of one to hundreds of picoseconds, iv) cooling processes take place, and energy is transferred to the substrate via phonon and geometry-assisted scattering processes, leading to the relaxation of the hot carrier distribution towards equilibrium.[112]

In most biomedical applications where plasmonic nanoparticles are employed, visible or NIR light is mainly used. NIR light (650–900 nm) is within what is called “biological window”, which means it can deeply penetrate the body due to the low absorption or scattering of photons by biological tissues (e.g., blood, water, melanin, and fat). For this reason, gold, silver, and

USC DE COMPOSTELA

copper are the preferred materials employed for biomedical applications based on their optical properties as their LSPR can be easily tuned to cover most of the visible and NIR spectra. Among them, gold is the most suitable due to its high stability, biocompatibility, and the wide possibility of surface modifications. Moreover, it is a promising material for some applications as PTT, as its absorption rates can achieve high ratios of absorption versus extinction so that there is a maximum conversion light to heat. Regarding these conditions, the NIR-responsive metallic NPs, including nanorods, nanoshells, and nanocages, are considered promising materials for the photothermal effect-based biomedical applications. This photothermal effect, or hyperthermia effect, is defined as the therapeutic technique where temperature rise in specific tissues over physiological conditions and can provoke cell death. Generally, this technique is applied for the targeted heating of cancer cells, which are more sensitive to the temperature than normal tissues due to their low pH (lower thermotolerance).[113] Over 41-46ºC the tumour cells survival is substantially reduced, whereas healthy cells can cool down and have higher viability.

The coating of plasmonic nanoparticles with shells composed by other materials as NMOFs (AuNPs@NMOF), can be the solution for the design of new nanosystems that combine both the properties of the plasmonic NPs with the features and the protection of the NMOFs, giving rise to outstanding drug delivery vehicles.

1.2.2. Catalytic nanoparticles

Over the past few years, metal nanoparticles (MNPs), have shown great potential for their application in catalysis.[114] MNPs have special physicochemical and biological properties that could be employed to improve the catalytic activity. These qualities, as their high catalytic efficacy, make them outstanding candidates for biorthogonal catalysis.[115] Nevertheless, some features such as the high surface areas imply high surface energies and, thus, the easy aggregation of the NPs in biological environments. Therefore, for their application in biomedicine it is necessary to develop effective supports that protect the NPs from this agglomeration so that they maintain the catalytic activity.[116] Some of the most typical transition metal catalysts (TMCs) include Cu, Au, Pt, Pd, Ru, Ag, Co and Ni.

During the past few years, copper nanoparticles (CuNPs) have attracted increased attention due to its favourable features for different applications in life sciences, as their high availability, low cost, or high biocompatibility.[114] Lately, some studies have shown the potential of CuNPs for different copper-catalyzed organic reactions, like Suzuki or click reactions. As a common biorthogonal reaction, the Cu(I)-catalyzed azide–alkyne cycloaddition (CuAAC) reaction has been employed for bioconjugation and coupling functional groups and molecules with high yields in biological conditions.[117,118] This type of reaction has been used for several applications as in materials science and pharmaceutical industry.[119] The main advantages of CuAAC reactions are the high specificity among the azide and alkyne groups, the efficiency of the reaction in biological environment conditions and the stability of the triazole product.[119] However, the cytotoxicity of Cu(I) ions can damage normal cells and healthy tissues and provoke various side effects, restraining its application in biological scenarios.[117]

Palladium is one of the most polyvalent metals for TMC-driven chemistry, as it can mediate both bond forming and bond cleavage reactions in an efficient way.[115] The use of palladium in biological environments is very appealing because of the well-demonstrated catalytic power of many palladium complexes, even in aqueous environments.[114] Palladium nanoparticles (PdNPs) have outstanding properties as high thermal and chemical stability or high photocatalytic activity, besides their associated low cost.[120] Furthermore, they can be easily

USC DE COMPOSTELA

functionalized with different biomolecules or polymers to increase their biocompatibility and achieve specific new properties. These particles can be widely employed in PTT, photoacoustic imaging (PAI), antibacterial therapy or gene and drug delivery, among others. However, they have interesting properties for their application as catalysts in biorthogonal reactions. These reactions enable the formation of medical molecules as drugs inside the biological environment, achieving the activation of the toxic drug in the desired place and minimizing the side effects of the classical treatment.

Other example is Au nanoparticles. In the case of gold, it has been proved that decreasing the size of the particles to < 5 nm can generate very effective catalysts, due to the enhanced reactivity of low coordinated Au atoms in the nanoscale.[121] In parallel to enzyme catalysis, Au NPs can catalyse multiple reactions at room or low temperatures, what makes them suitable biocatalysts. Furthermore, as previously mentioned, Au NPs can be modified in size and shape to have thermoplasmonic effects in the NIR region. This way, they can be used to achieve thermal-promoted chemical reactions in biological environments.[20]

1.2.3. Magnetic nanoparticles

Magnetic nanoparticles (MNPs) constitute a type of nanomaterial that can be manipulated using an alternating current magnetic field.[122] MNPs are metal-based materials generally made of magnetic elements as iron, nickel, cobalt, and their oxides; and they have been employed for a wide variety of applications as magnetic energy storage, catalysis, or magnetic resonance imaging (MRI).[122,123]

These NPs can be synthesized with specific morphologies and may be easily functionalized to change their surface properties. Several studies have been carried out to improve the control over the composition, shape, size, surface charge and magnetic properties.[123] These particles have some main features that make them unique candidates for their use in biomedicine, such as MRI, hyperthermia cancer treatment, drug and gene delivery or biosensing.[113,122] Furthermore, their capability to be surface modified and respond to magnetic fields make MNPs promising materials for therapeutic and diagnostic applications. Incidentally, MNPs can be functionalized and coated with other materials to change their properties and increase their biocompatibility. This results in the multifunctionality of the particles, such as a synergic hyperthermia effect combined with drug delivery or multimodal imaging.[113]

There are several types of MNPs that can be classified into pure metals, metal oxides and magnetic nanocomposites.[123] The most common MNPs for biomedicine include Co, Fe, Ni, Ti, iron oxide and ferrites. However, the main type is the iron oxide MNPs, such as magnetite Fe_3O_4, due to its high chemical and colloidal stability, high biocompatibility, and low cost.[122] [124]. The main MNPs property is the magnetic moment (m). It can be defined as the product of the magnetization (M) and the particle volume (V).[125] This is highly influenced by the size and shape, and higher magnetic moments will lead to improved magnetic moment yields and bigger magnetic forces.[124,125] In the surface of the particles there is a lack of crystal symmetry that provides this layer with different features in comparison to the inner part, so that these particles can be viewed as core@shell structures.[124] This way, the inner part has aligned spins along the applied magnetic field while the ones in the surface are canted relative to the field (spin-canted effect). This effect affects the saturation magnetizations that will be critical for the different bioapplications.

The high magnetic moments and surface-area-to-volume ratios make MNPs suitable for hyperthermia therapy for cancer, targeted drug delivery or MRI.[113] Hyperthermia in MNPs

can be generated by the application of an alternating magnetic field (AMF). The heat is produced by the hysteresis loss in the magnetization cycles due to the multi-magnetic domains present in ferromagnetic materials (Weiss domains). These domains align with the AMF and when it stops, the magnetization doesn't go back to the initial condition. Then, an opposite magnetic field is applied to restore the magnetization and the hysteresis loop represent the energy converted to heat.[113] This way, the particles can generate the hyperthermia effect widely used for the targeted therapeutic heating of tumour cells. Furthermore, MNPs have the potential to act as drug delivery vehicles, as they can be localized in a desired spot just by employing an external magnetic field before their activation.[113] These properties also allow the combination of targeted drug delivery with hyperthermia effects.

The addition of a NMOF shell to MNPs can improve the properties of this materials while maintaining the main advantages and therapeutic effects, acting in synergy with MOFs features and generating complex systems with high potential in biomedicine.

1.3. NMOFS FOR BIOAPPLICATIONS

As discussed before, NMOF´s unique properties such as the wide variety, their reusability, controllable degradation, the high surface areas, controllable loading capabilities of biological cargoes, or the good biocompatibility of the structures are being appreciated for their application in biomedicine.[12] Therefore, they are being used as nanocarriers for the delivery of drugs, imaging agents, biomolecules, etc.; contrast agents for imaging; or for different therapies such as chemotherapy, PTT, or PDT.[126] Furthermore, NMOFs constitute a promising material for catalysis in biomedicine, as they can act as heterogeneous catalyst due to the activity of their metallic centers or by synergistically combined with catalytic NPs (Au, Pt, Pd, *etc*.) forming composites.[127] The formation of active composites using NMOFs as host carriers allow the incorporation of other functional materials, such as NPs or polymers, creating nanocomposites with improved features with respect to the pristine NMOFs.[128] Some typical NPs encapsulated inside NMOFs structures are catalytic NPs (Au, Pt, Pd, Cu), magnetic NPs (Fe_3O_4) or quantum dots. These composites combine both the crystalline and highly porous structures of the NMOFs with the unique properties of the NPs, composing new promising materials for biocatalytic applications, drug delivery, bio-imaging or detoxifying agents (Figure 1.3.1.).[128]

1.3.1. Drug delivery: Stimuli-responsive NMOF-based DDS.

NP drug delivery systems (NDDSs) can be defined as nanosystems capable to carry and to deliver an API to a specific target in the body.[8] These systems should be designed to overcome the main problems associated to conventional treatments, as the poor stability of the drugs or their low specificity. Therefore, the development of DDSs with targeting capabilities and controlled release features, would assess the problem of side effects and improve the effectiveness of the treatments.[129] However, whereas the targeting functionalities are widely considered and explored, the controlled release in DDSs is still in its infancy. Until now, some systems have shown efficient and controlled drug release features in response to external stimuli.

USC UNIVERSIDADE DE SANTIAGO DE COMPOSTELA

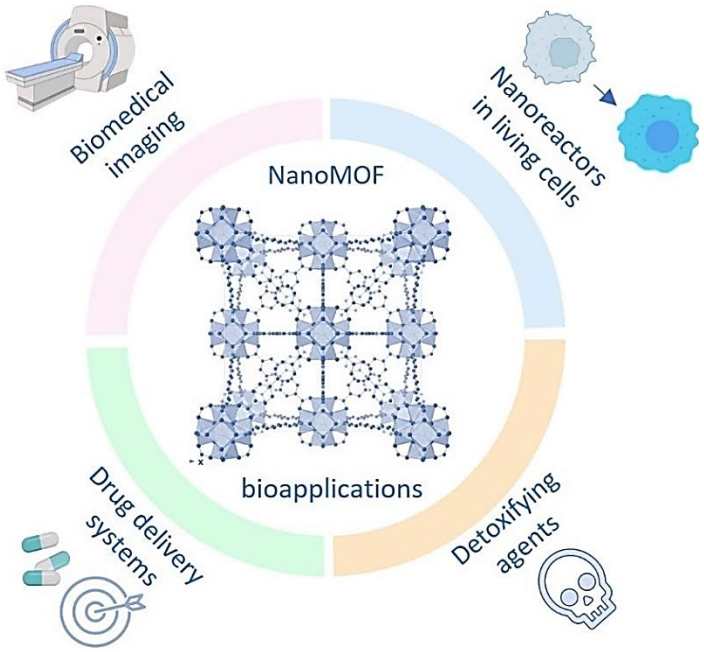

Figure 1.3.1. Representative biomedical applications of NMOFs i) in biomedical imaging, ii) in drug delivery, iii) as nanoreactor in living cells and iv) as detoxifying agents.

As DDSs, NMOFs provide intrinsic features as high loading capabilities or the easily tunable external surface of the particles. Meanwhile, they can also be designed as stimuli-responsive systems for the triggered intracellular release of their cargo.[130] During the past few years, different cargoes were studied for drug delivery applications of NMOFs. Especially, they have been studied as anticancer treatment based on the delivery of chemotherapeutic drugs (*i.e.*, doxorubicin, cisplatin or topotecan), siRNA, PS, or light-absorbing dyes.[131] On the other hand, NMOFs have been recently explored for the delivery of biomolecules with important roles in biological processes, such as nucleic acids, proteins, lipids, or carbohydrates.[126]

While there are many possible therapeutic agents that can be efficiently loaded into the pores of NMOFs,[132] the high loading capabilities are not enough to create a functional system. For that, it is necessary to control the cargo release to prevent off-target effects and increased cytotoxicity. Stimuli-responsive NMOFs could be a solution to address these problems. Especially responding to given stimulus such as pH, light, magnetic fields, redox, ions, ultrasounds, *etc*. These systems can suffer conformational changes under a determined stimulus that will lead to the release of the cargo.[88]

1.3.1.1. PH responsive NMOFs

PH-responsive NMOFs are the most studied stimuli-responsive systems considering the acidic microenvironment of tumor cells, lysosomes, or endosomes (pH varying from 4.5-7.8). These acidic media can lead to the degradation of some MOFs with acidic response as Zn-MOF, Fe-MOF or pH-sensitive bonds as amine or imide, leading to the release of the cargo.[9,133] Among them, ZIF-8 and MIL-10x MOFs are widely employed for this purpose due to their pH sensitivity (pH 5.0-6.0).[133] Cabrera-García *et al.* recently reported the design of novel pH-responsive DDSs based on amine-functionalized MIL-100 (Fe) y MIL-101(Fe) NMOFs loaded with the cytotoxic molecule 20-(S)-camptothecin (CPT).[134] The system showed high stability at physiological pH conditions with no release, whereas when the particles are internalized by

USC DE SANTIAGO DE COMPOSTELA

the lysosomes, the acidic pH (pH 5) boosted the drug release. This way, they achieved the delivery of the cytotoxic CPT while minimizing the side effects.

1.3.1.2. Magnetic responsive NMOFs

Magnetic responsive NMOFs are capable to interact with an external magnetic field showing a synergic effect both triggering a controlled drug release while allowing the accumulation of the particles in a target location. This approach is also referred as magnetophoretic therapy. Furthermore, these systems may be used for MRI, where can lead to enhanced contrast in T_2*- weighted images.[13,135] Some systems might combine magnetic stimuli-response with other stimuli-responsive features, as in the work reported by Chen *et al.* where they designed magnetic nanocomposites combining magnetic hyperthermia and chemotherapy treatments.[136] They designed a system composed of a Fe_3O_4@PDA (polydopamine) core and a ZIF-90 NMOF shell (Fe_3O_4@PDA@ZIF-90) with an average overall size of 200 nm. The Fe_3O_4 NPs served as magnetic heating platforms under excitation with alternating magnetic field, whereas the ZIF-90 shell act as protective layer and as a drug container to load doxorubicin (DOX) which release was triggered in a pH-responsive way. After cell, the DOX-loaded Fe_3O_4@PDA@ZIF-90 nanocomposites showed an excellent efficacy to kill tumor cells due to the synergic effect of the magnetic hyperthermia and pH-triggered drug release.

1.3.1.3. Light-mediated therapy, or phototherapy

Light-mediated therapy, or phototherapy, also represents a promising strategy for therapeutics and diagnosis as it is non-invasive, and involves high spatial precision.[132] Light-responsive NMOFs DDSs aim to control the cargo release via induced conformational changes, chemical bonds cleavage, or photothermal conversion of the molecules/materials under illumination.[9] Phototherapy aims to cell-killing treatment employing therapeutic systems that react under light irradiation. This approach can be divided very generally into two strategies: one based in the *in-situ* generation of ROS, called PDT; and another based in heat generation and temperature increase, called PTT (Figure 1.3.2.). In both cases one can differentiate between intrinsic photo-responsive MOFs and MOF composites among the phototherapeutic agents (PTAs) used. PDT constitutes a non-invasive approach for cancer treatment due to the oxidation capabilities of ROS to nucleic acids, enzymes, proteins, and cellular membranes in cancer cells.[137] In particular, NMOFs can be used for this type of therapy as a result of the easy diffusion of singlet oxygen and preventable self—quenching.[137] Among the different intrinsic photodynamic MOFs used for PDT, porphyrin-based MOFs constitute the most explored structures. In this case, the photo-response of the NMOFs can be tuned by using different porphyrin linkers. Recently, Kan *et al*. reported a UiO-66 NMOF based PS (UiO-66-TPP-SH) for PDT.[138] NMOFs are based on an S-ethylthiol ester monosubstituted metal-free porphyrin (TPP-SH) incorporated via post-synthetic modifications. The particles, with sizes around 150 nm, were further functionalized with porphyrinic PS that besides maintaining the MOF crystallinity, allowed the effective singlet oxygen generation. This way, they produced efficient nanosystems for PDT tumor treatment.

On the other hand, PTT is based on the conversion of near infra-red (NIR) light to heat, known as photothermal effect, with high precision and efficacy. PTT have the advantage of being non-invasive and easily implemented besides other treatments.[137] PTT can further cause the anti-tumor immune response, provoking irreversible cellular damage and subsequent tumor death.[139] The main advantage of NIR light-responsive systems versus visible light response

USC
DE SANTIAGO
DE COMPOSTELA

underlies into the biological window. The biological window(s) corresponds to the light range(s) where light penetration into biological tissues reaches a maximum, *i.e.*, expected penetration depth of 1000-1100 nm. First biological window comprises wavelengths from 700 nm to 950 nm.[140] For this reason, developing systems with strong absorption in the NIR and with high photothermal conversion efficiency is a great strategy to produce PTT platforms. Photothermal MOFs can be fabricated by the encapsulation of PTAs inside the structures.[141] Noble metal NPs are excellent materials that fulfill the required features for PTAs and have been widely studied for this application. These materials include Au, Ag, Pt and Pd and can be excited with light to efficiently produce heat through non-radiative decay processes. However, among these, Au-based NPs are the most used agents for PTT. Spherical Au NPs have their LSPR centered around 520 nm, but LSPR can be red-shifted to the NIR by changing the shape and size of the particles, producing *i.e.*, nanorods, nanostars, nanoplates, nanobipyramids, *etc*.[142] Nanocomposites based on MOFs and AuNPs have a promising future for drug delivery as they combine the advantages of both systems. On one hand, they have the great AuNPs features such as excellent tunable photothermal properties and good stability in biological environments. On the other hand, the high porosity, highly tunable surface functionalities, and the ability to host a wide variety of APIs of the MOFs. These composites have been employed for optical sensing, therapeutics, theragnosis, and heterogeneous catalysis with encouraging results.[12,18] However, due to the aqueous instability of most of these systems, their application as DDSs should still be optimized.

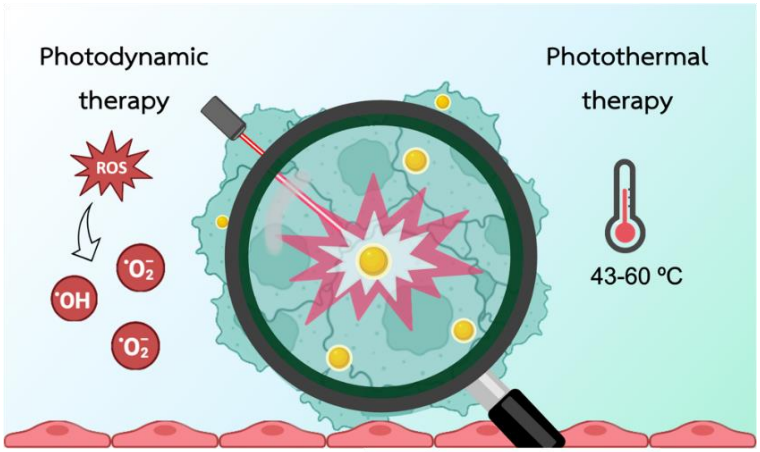

Figure 1.3.2. Phototherapy based nanosystems divided in i) photodynamic therapy and ii) photothermal therapy.

Recently, Zhou *et al*. reported the design of a MOF composite that applies the synergic effect of both PDT and PTT.[137] To achieve this, they synthesized a porphyrinic NMOF (PCN-222) shell with a core of plasmonic AuNRs. The singlet oxygen ($^1O_2$) generation by the PCN-222 shell was analysed after the exposure of the particles to LED light (640 nm, 20 mW cm^{-2}). by using a fluorescent $^1O_2$ indicator. Results showed an increase in the fluorescence correlated with longer irradiation times. Then, the photothermal activity of the NRs of the composite was evaluated by irradiation with a NIR 808 nm laser at different power values. This led to an increment of the temperature during the first 3 minutes, followed by a plateau after 5 minutes. The plateau temperatures varying from 35 to 60 °C depended on the laser power, confirming the efficient thermal conversion of light (*ca*. 22.2% conversion efficiency). Finally, the composites were incubated with breast cancer cells and in 4T1 breast tumor-bearing mice proving the potential for enhanced tumor treatment based on the combination of PDT and PTT.

Furthermore, these systems can be loaded with functional molecules for application in drug delivery or catalysis.

A colloidally stable thermoresponsive carrier composed by a core of a AuNSs coated with a NMOF ZIF-8 shell was developed in 2019, having LSPR centered around 800 nm. Transmission electron microscopy (TEM) showed a well-defined core–shell nanocomposite with a single AuNS core and a MOF shell of an average size of 218 nm. To address the problem of the aqueous instability of the ZIF-8 they functionalized the NMOFs with PMA providing the system with stability up to 7 days in aqueous and biological media. To perform *in vitro* studies and analyze the potential of the systems as drug carriers, they employed the bioactive cargo HOE, a blue-fluorescent dye typically used for DNA staining. Interestingly, the final nanocomposites showed an excellent response to NIR laser illumination inside living cells and high chemical stability with no cargo leakage after the PMA-coating. Furthermore, after the comparison between the response of the system with and without the irradiation under the NIR laser, they were able to prove the efficient triggered release of the loading (Figure 1.3.3.).

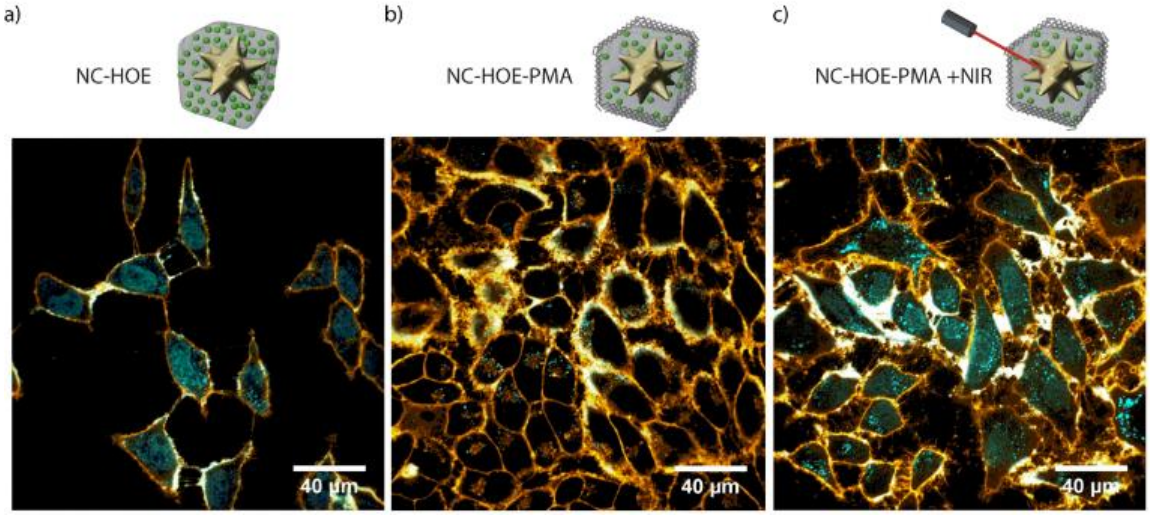

Figure 1.3.3. Confocal microscopy image of HeLa cells incubated with NC-HOE (a), NC-HOE-PMA (b), and NC-HOE-PMA after NIR treatment (c). Blue and orange colours represent HOE and cell membrane staining (CellMaskTM Deep Red), respectively. Scale bars correspond to 40 µm. Adapted with permission from Carrillo-Carrión. Copyright 2019, Angewandte Chemie.

1.3.2. NMOFs platforms as nanoreactors in living cells

In biomedicine and biotechnology, enzymes pay an important role to perform the basic reactions required for cell functions and cell survival.[143] The replacement of natural enzymes by synthetic catalysts to perform unnatural reactions in a living organism could imply the evolution of medicinal chemistry in several ways. Some of the possible candidates for this purpose are homogeneous transition metal catalysts. However, these catalysts suffer from some limitations for their direct application in biomedicine. The required characteristics of a catalyst to be active in biological media are: i) high activity even at low concentrations, ii) good solubility, iii) high stability in biological media, and at physiological pH, and iv) little or virtually no toxicity.[144,145] The interest in the possibility of performing controlled reactions inside living cells has increased during the past few years. One reason is the potential of producing bioactive molecules as anticancer drugs at intracellular locations, minimizing the secondary effects associated with conventional treatments. Moreover, the development of systems capable of transporting the precursors directly inside the cells may overcome the

drawbacks related to the low uptake of large molecules.[144] However, some of these transformations can be accomplished by performing abiotic catalysis within living cells using homogeneous transition metals catalysts. These catalysts promote controlled biorthogonal reactions. Defining biorthogonal reactions as reactions that take place in aqueous or biologically complex media, usually occurring with high chemo-selectivity and bio-compatibility, with minimized off-target reactions.[145,146]

Transition metal-catalysed reactions have been widely performed inside living cells for the past decade. Before their application, several studies were carried out to solve some of the main problems associated to these materials, as the poor biocompatibility, the low cellular uptake, or the deactivation of the catalyst in biological media. The main solution to these issues is the use of heterogeneous catalysts such as NPs, *i.e.*, Pd NPs.[147] However, some transition-metal NPs´ functionalization and stabilization are difficult and when placed in biological media the NPs tend to aggregate. Also, the high concentration of biomolecules containing thiols or amines can strongly impair the catalytic activity of the particles.[19] Beside, if NPs are stabilized with organic coatings the catalytic activity is highly reduced and the particles lose their functionality.[147] Another key challenge associated with these materials is their synthesis, often carried out in organic solvents, leading to eventual deactivation of their active surfaces. Hence, there is an imperative to develop novel systems that can effectively address these limitations.

Due to the metal centers, high porosities, and very high surface areas, the NMOFs constitute great candidates for their application as catalyst carriers. They can act as catalysts themselves by using the free metal sites in their surfaces or in synergy with catalytic NPs encapsulated inside the structure as metal and semiconductor oxide NPs.[148] However, NMOFs have been mainly studied for biocatalysis due to their ability to load biomolecules, mainly enzymes, where the MOF structure acts as protection avoiding the biological degradation of the biomolecule in harsh conditions, as high temperatures or extreme pH. The combination of activity of loaded catalytic biomolecules with the free metal sites of the NMOFs allows for the improvement of biological activities.[149] Furthermore, the easily external modification, stimuli-responsiveness, and some enzyme-mimicking features of MOFs allow their application with enzymes for smart catalysis, as well as their use as versatile nanoplatforms for enzyme delivery and catalytic nanomedicine. Li et al. reported the efficient immobilization of the enzyme lactate dehydrogenase (LDH) in different selected NU-100x MOF structures for their use as a cell-free biosynthetic catalytic system.[60] With this work they demonstrate the potential of MOF as enzyme carriers, as the prepared systems were water stable and showed high enzyme loadings and coenzyme accessibility, making these materials suitable for industrial applications.

Nevertheless, the development of non-natural catalytic reactors that can perform reactions inside living organisms could constitute a new important achievement in the biomedical field. Among different materials, catalytical metal NPs are great candidates, *i.e.*, Au, Pd or Pt NPs. However, as mentioned above, NPs with high surface energy have higher instability and tend to aggregate in biological media losing their catalytic activity.[19] In this scenario, NMOFs would act as protective structures to immobilize NPs preventing their aggregation for their use in catalytic processes.[148] This is combined with the high external surface areas and porosity of the structure of the NMOF that allows the diffusion of substrates and products minimizing the mass-transfer limit.[127] Therefore, the formation of new nanocomposites built of by a metal NP encapsulated inside a NMOF structures would produce platforms with improved features for catalysis.[148,150]

USC UNIVERSIDADE DE SANTIAGO DE COMPOSTELA

Recently, several NP@MOFs composites have been studied for their application in catalysis. One possibility includes the impregnation of NPs through the pores of the structure of the NMOFs. However, due to the small size of the pores, the diffusion of the particles can be difficult. Another effective procedure is called “bottle around the ship” where the MOF is synthesized around the NP, which acts as a nucleation site for the building of the structure, forming the NP@MOF composite. This approach would limit the adsorption of undesired species of the biological milieu to the NP surface, allowing the selective adsorption of substrates.[91,148] However, this method has been achieved only with a few MOFs as ZIF-8 or some Zr MOFs.[127]

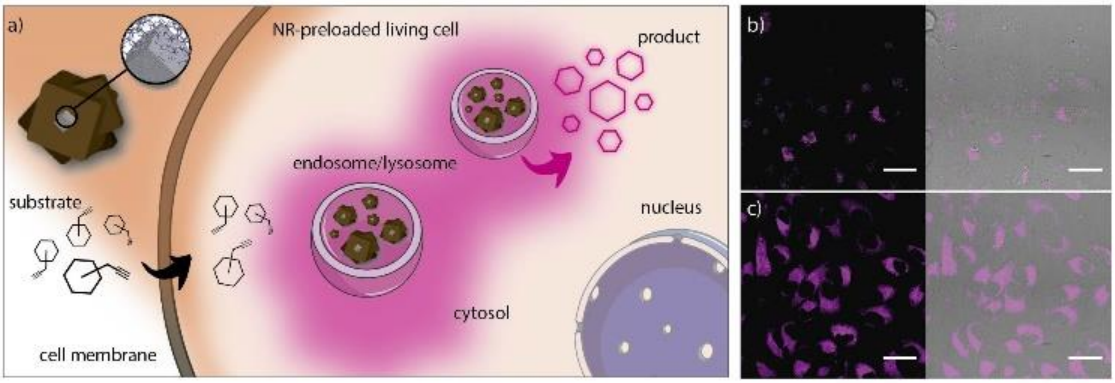

Figure 1.3.4. a) Pd-NCs coated by a porous ZIF-8/PMA shell NRs. The NRs tend to accumulate in cytosolic compartments (endosomes/lysosomes) and work as heterogeneous palladium-based NRs capable of processing substrates. b) Confocal microscopy images (60x) after incubation of NR-preloaded cells with different concentrations of substrate 5 (top: 2.5 mM; down: 10 mM; the fluorescence corresponds to the intracellular production of cresyl violet). Scale bars correspond to 40 μm. Adapted with permission from ref [19]. Copyright 2019, Cell Reports Physical Science.

Recently, an innovative water-compatible system based on the core-shell Pd@ZIF-8 nanocomposites that can act as long-lasting bio-orthogonal nanoreactors (NR) was reported.[19] The nanocomposite is formed by a Pd-nanocube (PdNC) that acts as catalyst, surrounded by a ZIF-8 shell that protects the PdNC to avoid aggregation or deactivation, and serves as a platform for the diffusion of the reactants. Simultaneously, the ZIF shell acts as a filter for the adsorption of larger biomolecules that would inactivate the Pd. They studied different reacting probes that generate fluorescent products after the removal of the propargylic groups, a reaction which is catalyzed by Pd (Figure 1.3.4.). Interestingly, the results showed the efficacy of the NRs to perform catalytic reactions inside living cells, both in 2D monolayers and 3D tumor spheroids, and their reusability by the simple addition of new reactants due to their storage in cytosolic vesicles. These results show the potential of intracellular recurrent NRs and the possible applicability as “catalytic cellular or tissular nanoimplants”.

This strategy still has some potential limitations due to the intrinsic reactivity of the reactants or the toxicity problems associated with some metal-based reagents. To avoid this, thermal-driven reactions can serve as alternative processes. Thermal-driven reactions can be triggered by temperature stimulus. However, there are some restrictions when applying this in living organisms, as cells cannot be heated over. A NR based on ZIF-8 NMOFs with a core of AuNSs (AuNS@ZIF-8) that could overcome these challenges was reported in 2018.[20] In this case, the plasmonic AuNSs would act as NIR responsive thermal transducers, achieving localized heating around the AuNSs and addressing the problem of the cells overheating.

Simultaneously, the ZIF-8 shell would act as protection avoiding the adsorption of undesired biomolecules such as proteins in the surface of the AuNSs. In this work, they presented a thermal-promoted intramolecular chemical reaction (thermocyclization) performed inside living cells. The ZIF-8 shell of the nanocomposite allows the diffusion of the reactants through the pores of the crystal, close to the AuNSs heating source under NIR irradiation. Furthermore, the thermal conductivity of the ZIF-8 is rather low, so it avoids the temperature increase in the surrounding media of the NMOFs. The selection of the substrates/nanocomposites pairs was based on the purposes of demonstrating that it is possible to carry out abiotic nucleophilic substitutions in biological media and inside living cells; that the reaction needs heating to be performed and that a cyclic fluorogenic product can be formed using these NRs. The nanocomposites were tested in mammalian cells with different substrates with two different set-up a collimated laser or a laser pointer in both cases showing a good level of transformation in living cells. This improvement in the performance of the NSs when the ZIF-8 shell is present was explain because it facilitates the access of the substrates to the AuNSs core while providing protection and control in the flow of reactants and products. This example opens a new avenue of intracellular reactions promoted by light that has many potential applications.

1.3.3. Metal organic frameworks for biomedical imaging

Biomedical imaging is a key to the improvement in the diagnosis and treatment of different diseases. NMOFs represent a new promising category of NPs for biomedical imaging, as their unique chemical features and versatility enable their use in various imaging modalities as MR (magnetic resonance), CT (Computed tomography) or PET (positron emission tomography), among others.[131,151-153]

MR imaging is one of the main techniques used for diagnosis, as it can provide morphological and functional information besides being a non-invasive technique[151]. However, it requires the use of contrast agents due to the low contrast-to-noise ratio, which implies a considerable reduction in the resolution. Moreover, the conventional clinic contrast agents (i.e., Gd^{3+}-based complexes) suffer from a lack of sensitivity, toxicity, and undesired side effects.[154]

Some Gd-based NMOFs have been developed to overcome these limitations. In 2006, Lin et al. were the first to report Gd^{3+}-containing NMOFs with improved relaxation times compared to clinical molecules.[155] However, the toxicity related to free Gd^{3+} ions that leach from the structure makes these systems not suitable for clinical use. To solve this, non-Gd^{3+}-based NMOFs have been developed.[154] Lin et al. reported a system based on Fe_3O_4 NPs assembled into responsive ZIF-8 NMOFs, generating T_1-T_2 changing contrast agents.[156] They synthesized 6 nm Fe_3O_4 NPs that exhibit a T_1 contrast enhancement, whereas while embedded in the ZIF-8 (forming an assembly), they show a T_2 contrast effect. When the Fe_3O_4@ZIF-8 nanosystems reach the tumor environment (acidic conditions), the pH and glutathione (GSH) trigger the Fe_3O_4 NPs disassembly recovering the individual NP behaviour as T_1 contrast agents. In vivo T_1 weighted images (mice liver) showed darkening contrast improvement, while it exhibits brightening contrast in the tumor sites. This proved the efficiency of this synergic systems to easily distinguish between normal and tumor tissues.

CT imaging is a non-invasive 3D technique used in diagnosis based in X-ray attenuation by contrast agents. It provides high resolution images of 3D biological tissues depending on their Xray absorption abilities. This is applied to visualize mainly bone structures as this technique requires materials with high atomic numbers.[151] Lately, Zhang et al. reported the

USC DE COMPOSTELA

design of UiO-PDT NMOFs as contrast agents for CT imaging.[157] They first synthesized UiO-66 NMOFs and then they exchanged the organic ligand with a diiodide-substituted monocarboxylfunctionalized BODIPYs (I2-BDP) to obtain UiO-PDT. The resulting NPs, of around 70 nm in size, were tested as CT contrast agents using a Micro CT at 80 KVp, presenting an excellent X-rays attenuate performance. Moreover, the biocompatibility both in vitro and in vivo of these NMOFs was studied showing no cytotoxicity at high concentrations and a clear accumulation in the tumor site, proving the potential of these systems as CT contrast agent for solid tumors.

PET constitute another important imaging technique, based in the emission of positrons by radionuclides accumulating in the target organs. When a positron and an electron encounter, annihilation occurs, generating gamma rays that are captured by detector panels, reconstructing the origin source, and forming 3D images.[151],[154] Chen *et al*. reported the design of an intrinsic radioactive UiO-66 NMOF with the incorporation of positron-emitting isotope zirconium-89 (^{89}Zr) for in vivo PET.[152] In this work, they incorporate the PET isotope zirconium-89 (^{89}Zr, $t_{1/2}$ = 78.4 h) during the synthesis of UiO-66, achieving NMOFs of 90 nm. Then, the particles were functionalized with PEG and a peptide to increase their stability and provide them with tumor targeting capabilities, respectively. Moreover, the NMOFs were loaded with DOX, used as a model anticancer drug and a fluorophore to track these nanosystems. In vivo results showed the potential of these systems as image-guidable, tumorselective cargo delivery nanoplatforms.

However, besides these promising results, NMOFs for biomedical imaging are still in their infancy and further studies need to be performed to address several aspects of NMOFs in this field.

1.3.4. Metal−Organic Frameworks as Efficient Oral Detoxifying Agents

Poisoning and intoxication via ingestion are considered major public health problem.[158,159] The lack of effective treatments for poisoning implies serious harsh effects and limits their use as efficient agents. Some typical detoxification methods are activated charcoal, gastric lavage or antidotes, but all of them involve low efficacy rates, low affinity for toxins and severe side effects.[159] The first method is employed for the removal of non-adsorbed drugs from the gastrointestinal system, so it presents some drawbacks as it should be administrated before the drug is adsorbed by the body. Gastric lavage also may be responsible for hypoxia results or gastrointestinal perforations.[160] In the case of antidotes, despite the higher efficacy with respect to the other two, their use is restricted to a small number of toxins. For this reason, it is necessary to develop new systems capable of capturing drugs or toxins.[158]

Recently, a few types of NPs, such as liposomes or microemulsions, have been employed for this purpose due to their versatility and a wide variety of possible functionalizations.[158,160] Although few studies have been made, NMOFs represent a promising alternative for detoxifying materials due to some of its features as the high porosity, which make them suitable for selective adsorption and elimination of toxic agents with low *in vivo* toxicity.[158,161]

USC UNIVERSIDADE DE SANTIAGO DE COMPOSTELA

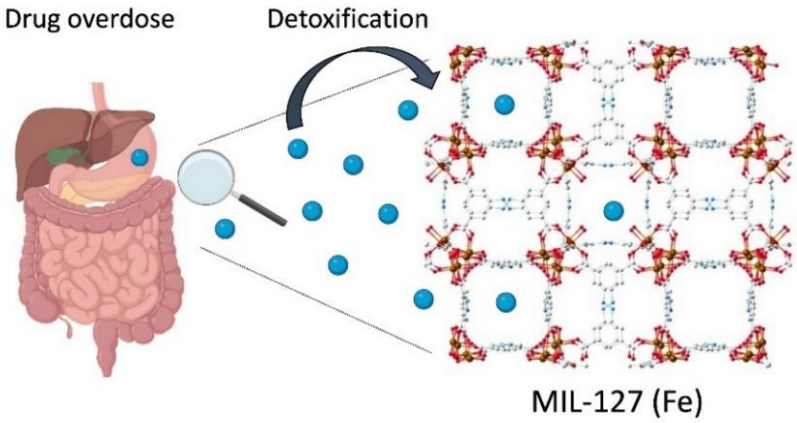

Figure 1.3.5. MOFs as efficient oral detoxifying agents. Adapted with permission from ref [158]. Copyright 2018, Journal of American Chemical Society.

Lately, Rojas *et al.* reported the pioneering design of a new detoxifying agent based on a single biocompatible MOF for its application for decontamination of drugs, generally related to voluntary poisoning (Figure 1.3.5.).[158] The studied MOF was the MIL-127 structure, based on octahedral iron (III) trimers and 3,3′,5,5′-azobenzenetetracarboxylate anions ($TazBz^{4-}$). The results of this work showed good biocompatibility, high porosity (1400 $m^2 \cdot g^{-1}$) with high adsorption capacities and high chemical stability at different pH values. However, to prevent the intestinal crossing and potential toxicity, the systems were prepared in the micrometer scale (~20 μm). As a model of overdose pain medication, they used the salicylate derivative aspirin (acetylsalicylic acid, ASA), which is classified among the nine pediatric poisons that can cause death in enfants at small doses, and that has no specific antidote. They studied the chemical stability and the adsorption capabilities of the systems both *in vitro* and *in vivo*. *In vitro* results showed high stability and high adsorption capabilities of the MOF, which could reach a maximum ASA loading of 0.14 $g \cdot g^{-1}$ (grams of ASA per grams of MIL-127). Furthermore, after the encapsulation there were no release of the drug, demonstrating the great affinity of the aspirin for the MOF. *In vivo* results revealed the decrease of the silicates intestinal absorption by over 40-fold. Therefore, this report showed the first experiments concerning the *in vivo* toxicity and biodistribution of a MOF via oral administration, specifically upon salicylate overdose, with a high reduction of salicylate gastrointestinal absorption and toxicity with outstanding gastrointestinal stability.[103] However, the development of a MOF in the nanoscale was not reported until next year, in 2019, in the work by Rojas *et al.*,[102b] where they presented a Ti-based NMOF (MIL-125-NH_2) as drug overload detoxifying agent. The selected NMOF was the tetragonal titanium (IV) aminoterephthalate MIL-125-NH_2 ($Ti_8O_8(OH)_4(O_2C{-}C_6H_3NH_2{-}\ CO_2)_6$). The NMOFs presented properties that made them suitable as oral detoxifying agents: the system is based on titanium, which is regarded as one of the most biocompatible metals; it showed very low absorption when orally administered, and it presented high porosity that made the structure an ideal candidate for the encapsulation of drugs. Furthermore, it could be synthesized at the nanoscale, which also opens the window for their further application as drug delivery agents. The studied drug was again the widely used anti-inflammatory and analgesic ASA. For the experiments, they have employed the same quantity (mass) of adsorbent and the same ASA initial concentration under simulated gastrointestinal (GI) conditions. Despite the efficiency of ASA removal of the NMOF, the resulting detoxifying action is relatively low with respect to the commercial treatment (2−13% using stable MOFs vs 97% using Norit@activated carbon). However, the MIL-125-NH_2

presented the important advantage of allowing a low release after the drug adsorption, which is one of the main problems associated to conventional treatments. To confirm the results, the MIL-125-NH_2 was compared to other common MOFs (MIL-53(Fe), MIL-53(Fe)-$(OH)_2$, MIL-100- (Fe), UiO-66(Zr), UiO-66(Zr)−NH_2, and ZIF-8(Zn)). *In vitro* results showed high ASA adsorption capacity of the MIL-125-NH_2 NMOF (2.59 and 1.64 $mol \cdot mol^{-1}$ at ASA/adsorbent ratio = 1:0.5 and 1:2, respectively) after 24 h. After *in vitro* and *in vivo* studies, MIL-125-NH_2 was demonstrated to be the only MOF capable of resisting intestinal conditions, being an efficient detoxifying agent with the ability to twofold reduce the salicylate concentration peak in blood, whereas keeping intact their structure and proving good biocompatibility.

USC
UNIVERSIDADE DE SANTIAGO DE COMPOSTELA

1.4. OBJECTIVES

The main objective of this PhD thesis is the design and utilization of innovative nanosystems based on metal-organic frameworks (MOFs) for a wide range of biomedical applications. Despite extensive research on the physicochemical properties of MOFs in fields like energy storage and gas separation, their potential in biomedicine remains largely unexplored. This research aims to fill this gap by showing the unique characteristics of MOFs to address the current limitations of drug delivery systems.

MOFs possess inherent features, such as exceptional porosity for encapsulating diverse biomolecules and easily modifiable targeting capabilities, making them promising candidates for applications in nanomedicine, as mentioned earlier. Additionally, the combination of MOFs with other nanomaterials, like gold nanoparticles, enables the creation of core@shell nanocomposites with photothermal capabilities and therapeutic NIR activation abilities.

This thesis, structured into three main chapters, seeks to explore various encapsulation techniques, surface engineering methods for MOFs, and the development of novel core@shell nanocomposites. Furthermore, fundamental studies into MOF-cell interactions will be conducted to underscore the potential of these materials in advancing nanomedicine. Through interdisciplinary investigations, the goal is to demonstrate the transformative impact of MOFs in revolutionizing nanomedicine.

1.4.1. Chapter 1

The main objective of Chapter 1 is to introduce a versatile, clickable surface coating using an amphiphilic polymer derivatized with dibenzo cyclooctyne groups as a universal post-synthetic modification. To prove its universality NMOFs of UiO-67, NU-1000, PCN-222 and ZIF-8 were produced with high monodispersity and uniformity and were coated with an amphiphilic polymer to improve the final colloidal and structural stability in different biologically relevant media. NMOFs were synthetized and characterized from a physical, chemical, and biological perspective: their hydrodynamic size, stability and morphology have been investigated.

For comparative purposes, two size-equivalent (150 nm) NMOFs were selected, ZIF-8 and UiO-67, which were functionalized with a library of biologically relevant azide-derivatized (macro)molecules, including polyethylene glycol, mannose, a cell-penetrating peptide, or a fluorescence probe (Cy5) using a biorthogonal reaction. Additionally, the selected NMOFs were loaded with cresyl violet (CV), a common histological stain and lysosomal marker. Preliminary cargo encapsulation/release studies were then performed to assess functionalized MOFS' ability to retain loaded cargos and to release them inside living cells.

The internalization process of these derivatized NMOFs into cancer cells has been investigated with the aim of identifying the differences in the uptake as a result of their distinct surface functionalization and demonstrating the efficiency and versatility of the proposed coating approach.

USC UNIVERSIDADE DE SANTIAGO DE COMPOSTELA

1.4.2. Chapter 2

Chapter 2 primarily focuses on investigating the introduction of an innovative post-synthesis modification (PSM) of the surface of various Zr-based NMOFs. Before initiating the functionalization, a thorough examination of particle concentration was conducted utilizing two distinct methodologies: Nanoparticle Tracking Analysis (NTA) and flow cytometry. This involved a comparative analysis between the two techniques. Then, a new approach for PSM is studied for three Zr-MOFs (UiO-67, NU-1000 and PCN-222), involving a combination of coordinative modification using modified DNA and PEG molecules with phosphate groups, along with a novel approach for protein immobilization on the surface of DNA-functionalized NMOFs.

The initial phase of the study involved coordinative surface modification of UiO-67, NU-1000, and PCN-222 NMOFs synthesized in the preceding chapter. DNA and PEG molecules, previously modified with phosphate (PO_3) groups, were chosen for this purpose. This strategy relies on the coordination of PO_3 groups to the free Zr present on the outer surface of the NMOFs, forming strong bonds and creating a uniform coating that enhances stability.

Further investigations were conducted using UiO-67 as a model from the Zr family of NMOFs. Initially, particles were loaded with calcein for fluorescence tracking *in vitro* and, then, functionalized with DNA. Subsequently, a new functionalization approach was developed by hybridizing new azide-modified DNA strains complementary to those on the surface of the MOFs, leaving free azide groups on the particle surface. Finally, utilizing these as anchor points, BSA protein modified with DBCO groups was attached to the surface via click chemistry reactions, enabling protein coating of the UiO-67. The effects of surface functionalization on the structural and functional properties of MOFs were thoroughly analyzed, alongside in vitro experiments, providing insights into their enhanced performance and potential applications.

1.4.3. Chapter 3

The main objective of Chapter 3 is to study the integration of light-responsive nanoantennas into NMOFs to enhance their application as smart drug delivery nanosystems. By integrating gold bipyramid nanoantennas within ZIF-8 and NU-1000 NMOFs, the creation of core@shell nanosystems with photothermal capabilities was explored.

Initial investigations focused on examining the loading and release dynamics to evaluate the nanosystems capacity to retain loaded cargos and release them upon NIR light stimulation within living cells. This feature is employed for the loading of CV, selected as a model drug, with the aim of proving the controlled drug release under near-infrared (NIR) light stimulation. Subsequent photothermal release studies were conducted within living cells to assess the potential of these nanocomposites for targeted, light-activated drug delivery with precise spatiotemporal control.

Further evaluation of the NU-1000 nanocomposite loaded with chemotherapeutics ─Doxorubicin, Carboplatin, and Oxaliplatin─ in both 2D and 3D cell cultures, was carried out to study the nanosystem effectiveness in cell internalization and therapeutic NIR activation. The potential of the drug loaded nanocomposites as stimuli responsive drug delivery systems

USC DE COMPOSTELA

were thoroughly analyzed through in vitro experiments, providing insights into their enhanced performance and future clinical applications.

USC
UNIVERSIDADE
DE SANTIAGO
DE COMPOSTELA

USC
UNIVERSIDADE
DE SANTIAGO
DE COMPOSTELA

2. Materials and methods

USC
UNIVERSIDADE
DE SANTIAGO
DE COMPOSTELA

USC
UNIVERSIDADE
DE SANTIAGO
DE COMPOSTELA

GENERAL CONSIDERATIONS: All glassware was first cleaned with detergent followed by aqua regia, which oxidizes and dissolves residual organic and inorganic impurities, and then carefully rinsed with Milli-Q water and acetone to guarantee an extremely cleaned glass surface. Aqua regia solution is prepared by mixing 3 volume parts of hydrochloric acid (HCl) with 1 volume part of nitric acid (HNO_3) and should be used fresh. Aqua regia is a corrosive and strong oxidizing agent that should be prepared with care in a well-ventilated fume cupboard with protective clothing, goggles, and gloves. Reagents were used as received without further purification or modification unless specifically specified. Reagents were purchased from Sigma-Aldrich (reference codes are provided in the following) unless otherwise specified.

2.1. REAGENTS

Silver nitrate ($AgNO_3$, ≥99.0%); phosphorus oxychloride ($POCl_3$, 99%); poly(ethylene glycol) methyl ether thiol (MeO-PEG-SH, 2 kDa); triethylamine (≥99.5); L-Ascorbic acid ($C_6H_8O_6$, ≥99%); sodium borohydride ($NaBH_4$, ≥98.0%); citric acid (≥ 99.5%); cetyltrimethylammonium chloride (CTAC, 25 wt% in H_2O); Zinc nitrate hexahydrate ($Zn(NO_3)_2 \cdot 6H_2O$; Sigma Aldrich #96482), 2-methylimidazole (MeIm; Sigma Aldrich #M50850), zirconyl chloride octahydrate ($ZrOCl_2 \cdot 8H_2O$ 98%, Sigma Aldrich, #224316); zirconium (IV) n-butoxide (80 wt% in 1-butanol,Sigma-Aldrich); 4,4'-Biphenyldicarboxylic acid ($C_{14}H_{10}O_4$, 98%, BPDC, ACROS Organics, #A0420549); tetrakis(p-benzoate)pyrene (TBAPy), Tetrakis(4-carboxyphenyl) porphyrin (TCPP), N,N-dimethylformamide (DMF, ≥99.8%, Fisher Scientific); chloroform ($CHCl_3$, ≥99.8%, Fisher Scientific); Hydrogen tetrachloroaurate (III) hydrate ($HAuCl_4$, Au≥49%, Thermo Scientific); dichloromethane (DCM, ≥99.8%, Thermo Scientific); hydrochloric acid (HCl, 37%, Thermo Scientific); hexadecyltrimethylammonium bromide (CTAB, ≥98%), Poly(isobutylene-alt-maleic anhydride) (average Mw ~6,000, 12-200 mesh 85%); acetic acid glacial (CH_3COOH, 99.7%, Fisher Scientific), benzoic acid (≥99.5%, Sigma-Aldrich); Cresyl violet acetate (CV, ACROS ORGANICS), poly(ethylene glycol) methyl ether (MeO-PEG, M_n=5000, Sigma-Aldrich), Mannose-azide (≥99%, Sigma-Aldrich, Man-N_3), Methoxypolyethylene glycol azide (M_n=5000, MeO-PEG- N_3), Dyn-Pro (CPP-N_3), Cyanine5 azide (Cy5-N_3, Lumiprobe). Doxorubicin hydrochloride ($C_{27}H_{29}NO_{11}$ HCl, 98.0-102.0% HPLC); Oxaliplatin ($C_8H_{14}N2O_4Pt$) and carboplatin ($C_6H_{12}N_2O_4Pt$, >98%) were provided by TCI chemicals. Cresyl violet acetate ($C_{18}H_{15}N_3O_3$) was provided by Alfa Aesar. 1,3,6,8-Tetra(4'-carboxyphenyl)pyrene) (H_4TBAPy) ($C_{44}H_{26}O_8$, 95%) was provided by Alfachem; and methanol (MeOH) were used as purchased without any purification.

2.2. SYNTHESIS OF GOLD NANOBIPYRAMIDS (AuBy)

2.2.1. Synthesis of penta-twinned seeds

Within a 20 mL glass vial, initial seeds were prepared by combining 8.639 mL of water with 0.661 mL of a CTAC solution and 0.100 mL of 25mM $HAuCl_4$ (in water) under vigorous magnetic stirring (1000 rpm) for 5 min. Subsequently, 0.1 mL of 0.5 M citric acid (in water) was introduced into the reaction mixture, followed immediately by two consecutive doses of 0.25 mL of freshly prepared $NaBH_4$ 25 mM (in water). The solution presented a color change from pale yellow to a brownish solution, indicating the formation of gold seeds. After 2 mins of stirring, the vial was sealed, and the seeds were subjected to heating in a block at 80 °C for 90 min under gentle stirring (300 rpm). Ultimately, the solution color transitioned from brown to red, meaning the successful creation of penta-twinned defects through the aging process.

USC UNIVERSIDADE DE SANTIAGO DE COMPOSTELA

2.2.2. Gold bipyramids (AuBy) synthesis

Within a 600 mL glass bottle, the growth solution for AuBy was formulated by introducing, under magnetic stirring (500 rpm), 275 mL of water, 250 mL of 0.2 M CTAB, 10 mL of 25 mM $HAuCl_4$, 5 mL of 10 mM $AgNO_3$, 0.833 mL of HCl, and 4 mL of 0.1 M ascorbic acid (all in water). Following the color transition from orange-yellow to colorless upon the addition of ascorbic acid, 12 mL of pentatwinned seeds were incorporated. The reaction mixture was maintained at 30 °C for 2 h. Subsequently, the nanoparticles were washed three times with water to eliminate excess CTAB and were then retained in a final volume of 10 mL of water.

2.2.3. PEGylation and phase transfer of gold bipyramids (AuBy)

In the absence of excess CTAB, AuBy exhibits a LSPR at approximately 808 nm, with an absorption molar coefficient of 3.63 x 10^{10} $M^{-1}\cdot cm^{-1}$ at this wavelength. For PEGylation, 500,000 MeO-PEG-SH (2 kDa) chains were utilized per particle. For the PEGylation,10 mL of a 15 nM solution of AuBy was used. A 1% fraction of the total PEG quantity selected (5,000 chains) was introduced into the colloidal dispersion of AuBy, corresponding to the addition of 75 µL of 20 $mg\cdot mL^{-1}$ MeO-PEG-SH solution to the 10 mL of 15 nM AuBy in water. In a separate tube, 150 mg of MeO-PEG-SH, corresponding to 500,000 chains per particle, were dissolved in chloroform. The NPs in water and the MeO-PEG-SH solution in chloroform were combined in a separation funnel, vigorously shaken, and followed by the addition of 10 mL of methanol to initiate phase transfer from the aqueous to the organic phase. The resulting emulsion was disrupted with the addition of more water. Once AuBy were transferred to the organic phase, they were collected, dried under rotary evaporation, and subsequently redispersed in the same volume of DMF as the initial volume.

2.3. NMOFS SYNTHESIS

2.3.1. ZIF-8

Nanosized ZIF-8 particles were prepared in water at room temperature (RT) using $Zn(NO_3)_2\cdot 6H_2O$; and MeIm as zinc and organic ligand sources, respectively, and CTAB as size-controlling and structural-directing agent. The molar ratio of ligand to zinc ion ($MeIm/Zn^{2+}$) in the reaction mixture was fixed at 54.

Synthesis of pristine ZIF-8 particles: 5 mL of 1.3 M MeIm aqueous solution was placed in a glass vial under magnetic stirring at room temperature (RT). Then, 5 mL of 0.025 M $Zn(NO_3)_2\cdot 6H_2O$ aqueous solution was added, and immediately after, 5 mL of 5×10^{-4} M CTAB aqueous solution was added. The mixture was stirred for 5 min and left undisturbed for 3 h at RT, being observed during this time the gradually appearance of whitish turbidity, which indicated the formation of the ZIF-8 particles. Finally, the particles were collected by centrifugation (7100 RCF, 10 min), washed twice with methanol (MeOH) and finally, redispersed in 1 mL of MeOH.

2.3.2. UiO-67

Nanosized UiO-67 particles were prepared in DMF solution using $ZrOCl_2\cdot 8H_2O$ and BPDC as Zr and organic ligand sources, respectively, and AA as modulator. All the reagents were used as received. For the synthesis, 51 mg of $ZrOCl_2\cdot 8H_2O$ and 72.5 mg of BPDC were weighted in two separated 50 mL falcons and redispersed in 25 mL of DMF each. Then, a heating plate and the adaptor for the 50 mL round flask were prepared at 120 °C. When the temperature is reached, 5 mL of $ZrOCl_2\cdot 8H_2O$ and 5 mL of BPDC were added into a 50 mL

round flask and the mixture was sonicated for 30 seconds. Then, 0.4 mL of acetic acid is added to the solution. After sonication for other 30 s, the round flask was placed in a heating plate and left at 120 °C overnight. Finally, the sample was collected by centrifugation (10 min, 7100 rcf). Then, it is washed 3 times in DMF, 3 in methanol and 1 in acetone. The final product is redispersed in 1 mL of acetone and placed in a 1.5 mL Eppendorf.

2.3.3. NU-1000

Nanosized NU-1000 particles were prepared in DMF at 90ºC using $ZrOCl_2 \cdot 8H_2O$ and H_4TBAPy as Zr and organic ligand sources, respectively, and acetic acid as modulator. All the reagents were used as received. For the synthesis, $ZrOCl_2 \cdot 8H_2O$ was directly weighted in a 20 mL vial (64 mg), followed by the addition of H_4TBAPy (10 mg). The powder was dissolved in 10 mL of DMF, and then 2 mL of AA and 1 mL of Milli Q water were added. Then, the vial was sealed and placed in an adaptor at 90ºC for 30 min without stirring. The sample was collected by centrifugation (10 min, 10000 rcf), washed twice in DMF and twice in acetone. The final product is redispersed in 1 mL of acetone and placed in a 1.5 mL Eppendorf.

2.3.4. PCN-222

2.3.4.1. Zr cluster

100 mL of 1-propanol and 5 mL of Zr (IV) n-butoxide (80 wt%) were mixed and stirred for 10 min. Then, 33 g of benzoic acid were added, and the mixture was ultrasonicated for 20 min. After that, it was heated at reflux and stirred overnight. Next day, it was evaporated, and the solid product washed 3 times with 1-propanol and centrifuged for 10 min at 7000 rcf. The final product was dried under vacuum at RT.

2.3.4.2. PCN-222 synthesis

Nanosized PCN-222 particles were prepared in DMF solution using the Zr_6O SBU previously synthetized and TCPP as Zr and organic ligand sources, respectively, and TFA as modulator. For the synthesis, 22.5 mg of TCPP (28.5 µmol) were weighted directly in a 20 mL glass vial and 8 mL of DMF were added using a 10 mL syringe and sonicate. Then, 38 mg of the cluster (14.2 µmol) and 230 µL of TFA were added to the solution under magnetic stirring. The reaction vial was sealed and left in a block heater at 120ºC under magnetic stirring for 5 h. Finally, the sample was collected by centrifugation (35 min, 7100 rcf) and washed 3 times in DMF, 3 in ethanol and redispersed in 1 mL of ethanol.

2.4. SYNTHESIS OF AuBy@NMOFS COMPOSITES

2.4.1. AuBy@ZIF-8

CTAB-stabilized AuBy served as seeds for the growth of a ZIF-8 shell. In a 5 mL glass vial, under magnetic stirring at room temperature, a solution mixture was created by combining 1 mL of a 1.3 M aqueous solution of 2-MeIm, 1 mL of a 0.025 M aqueous solution of zinc nitrate hexahydrate, and 1 mL of a 1.5 nM AuBy dispersed in a 0.16 $mg \cdot mL^{-1}$ CTAB aqueous solution. The mixture was stirred for 5 min and left to stand for 3 h at room temperature. The development of purple turbidity involved the formation of AuBy@ZIF-8. Subsequently, the particles were washed by centrifugation at 7200 rcf for 10 min and were rinsed twice with methanol.

USC UNIVERSIDADE DE SANTIAGO DE COMPOSTELA

2.4.2. AuBy@NU-1000

In a 20 mL glass vial, a mixture was prepared by dissolving 64 mg of $ZrOCl_2 \cdot 8H_2O$ and 10 mg of H_4TBAPy in 9 mL of DMF. Subsequently, 1 mL of PEGylated AuBy at a concentration of 10 nM was introduced into the solution, followed by the addition of 2 mL of acetic acid and 1 mL of water. The vial was sealed and subjected to heating at 90 ºC for 30 min. Following this, the resulting product was centrifuged at 7200 rcf for 10 min, with three subsequent washing steps using DMF and other three with acetone. The product was then dried under vacuum for subsequent characterizations.

2.4.3. AuBy@PCN-224

In a glass vial, 20 mg of Zr_6 cluster were added together with 0.8 mL of acetic acid and 0.2 mL of DMF. In an Eppendorf tube, 10 mg of TCPP linker were weighed and dissolved in 1 mL of DMF or in 1 mL of AuBy DMF solution using ultrasonication. The mixture in the vial was stirred with a magnetic bar at 300 rpm and then, the solution of the Eppendorf tube was added. The reaction was carried out at RT for 1 h. The resulting solution was sonicated and collected in a 2 mL Eppendorf tube and centrifugated at 10000 rcf for 10 min. It was washed 3 times with 1 mL of DMF and 3 more with 1 mL of MeOH, centrifugated each time (10 min, 10000 rcf). Finally, the product was redispersed in 1 mL of MeOH.

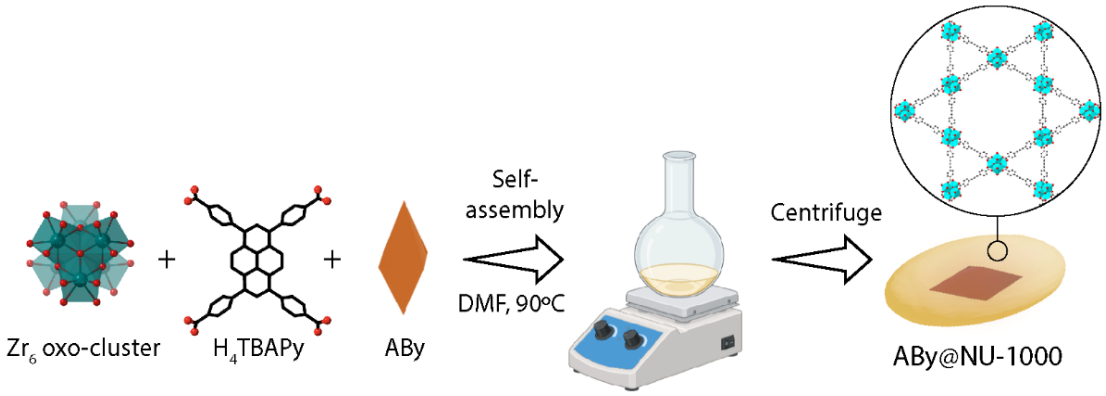

Figure 2.4.1. Schematic representation of the AuBy@NU-1000 solvothermal synthesis.

2.5. CARGO ENCAPSULATION

2.5.1. Cresyl violet (CV)

ZIF-8 nanoparticles: CV (Figure 2.5.1.-2.5.2.a) was loaded in ZIF-8 NMOFs via *in situ* encapsulation. For the ZIF-8(CV), the synthetic and purification protocol was equivalent to the one previously described for pristine ZIF-8 particles, but the cargo molecule (CV) was included in the CTAB solution in a volume relation 1:4.75. In this case, the appearance of reddish/violet turbidity was gradually observed during the formation of ZIF-8. The resulting nanoparticles were redispersed in 1 mL of MeOH.

Zr NMOFs family: Zr MOFs as dispersed in acetone (200 µL, 1 $mg \cdot mL^{-1}$) were mixed with a solution of CV in MeOH (200 µL, 2 $mg \cdot mL^{-1}$) in a weight relation 1:2 (NMOF:CV). The mixture was incubated for 3 days under stirring at 60ºC to ensure that the maximum loading was reached regardless of the diffusion kinetic of the dye molecules through the UiO-67 pores. Particles were collected by centrifugation (10000 rcf, 10 min) and washed three times (10000

rcf, 10 min). For further PMA functionalization, particles were redispersed in acetone, whereas for DNA and PEG coating, the pellet was directly redispersed in a prepared solution of these molecules in water.

AuBy@MOFs: Dispersions of AuBy@NU-1000, AuBy@ZIF-8 and AuBy@PCN-224 nanocomposites, comprising 200 µL with a solid concentration of 1 mg·mL^{-1}, were combined with a 200 µL solution of CV in MeOH at a concentration of 2 mg·mL^{-1}. The resultant mixture was kept overnight incubation at RT with continuous shaking. Post-incubation, NCs were separated from the solution through centrifugation at 7100 rcf for 10 mins.

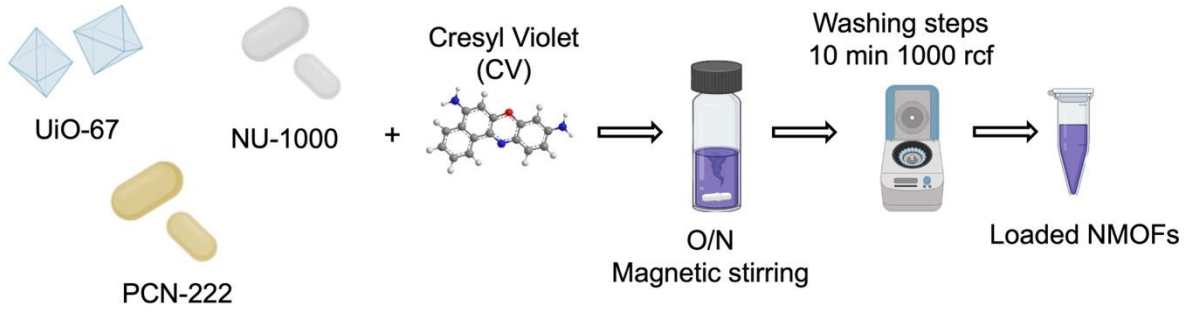

Figure 2.5.1. Post-synthesis Cresyl Violet (CV) encapsulation in Zr NMOFs.

2.5.2. Calcein

UiO-67 as dispersed in acetone (200 µL, 1 mg·mL^{-1}) was mixed with a solution of calcein (Calc) (Figure 2.5.2.b) in MeOH (200 µL, 2 mg·mL^{-1}) in a weight relation 1:2 (NMOF:Calc). The mixture was incubated for 3 days under stirring at 60ºC to ensure that the maximum loading was reached regardless of the diffusion kinetic of the dye molecules through the UiO-67 pores. Particles were collected by centrifugation (10000 rcf, 10 min), washed twice with acetone and redispersed directly in a solution of DNA or PEG in water.

2.5.3. Drug loading

The selected drugs were doxorubicin (DOX), Carboplatin (CbPt) and Oxaliplatin (OXA) (Figure 2.5.2.c-e). The loading procedure followed was analogous to the dye encapsulation.

AuBy@NU-1000 nanoparticles were mixed with a molar excess of the selected drug molecule (relation 3:1) and left overnight. Samples were collected by centrifugation (10000 rcf, 10 min) and the pellet was directly resuspended in aPEG-PO_3 dilution in order to perform the PEGylation.

USC UNIVERSIDADE DE SANTIAGO DE COMPOSTELA

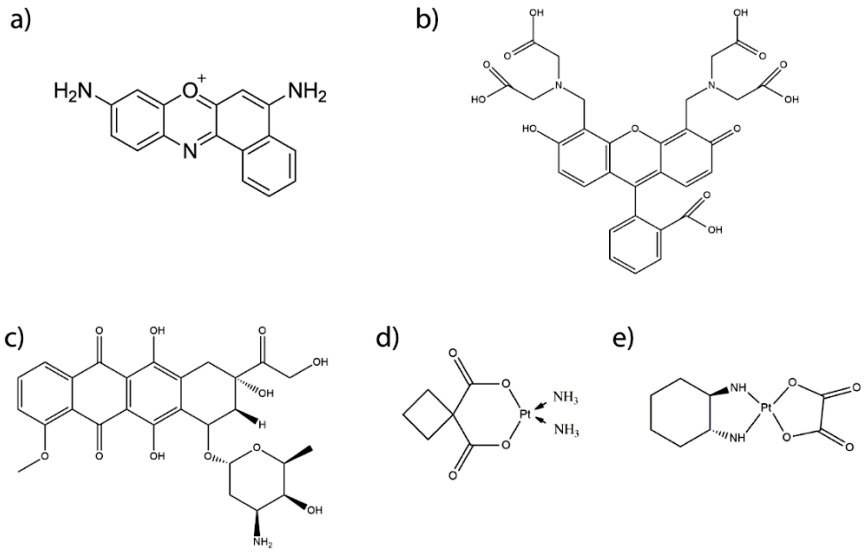

Figure 2.5.2. a) Cresyl Violet acetate, b) Calcein, c) Doxorubicin, d) Carboplatin and e) Oxaliplatin.

2.6. SURFACE FUNCTIONALIZATION

2.6.1. PMA functionalization procedure

2.6.1.1. PMA synthesis

PMA-based amphiphilic polymer (i.e., poly [isobutylene– alt–maleic anhydride]–graft–dodecyl) was synthetized following a protocol previously described by W. Parak et al.[162] In a 50 mL round flask, 20 mmol (3.08 g) of poly (isobutylene-alt-maleic anhydride) and 15 mmol (2.78 g) of dodecylamine (DDA) were mixed in 40 mL of tetrahydrofuran (THF). The solution was kept under magnetic stirring (350 rpm) and reflux (65 °C) overnight. Then, the THF was evaporated under vacuum using a rotary evaporator and the dried polymer was redispersed in 10 mL of chloroform. To purify the polymer and remove the excess of unreacted DDA, 50 mL of hexane were added to the solution and left for 2 h in the freezer (-4ºC). The sample was centrifuged (2 min, 7100 rcf) to remove the hexane and dried under vacuum. The final powder was weight to obtain a final monomer (MW = 154 g·mol^{-1}) concentration of 0.5 M (Figure 2.6.1.)

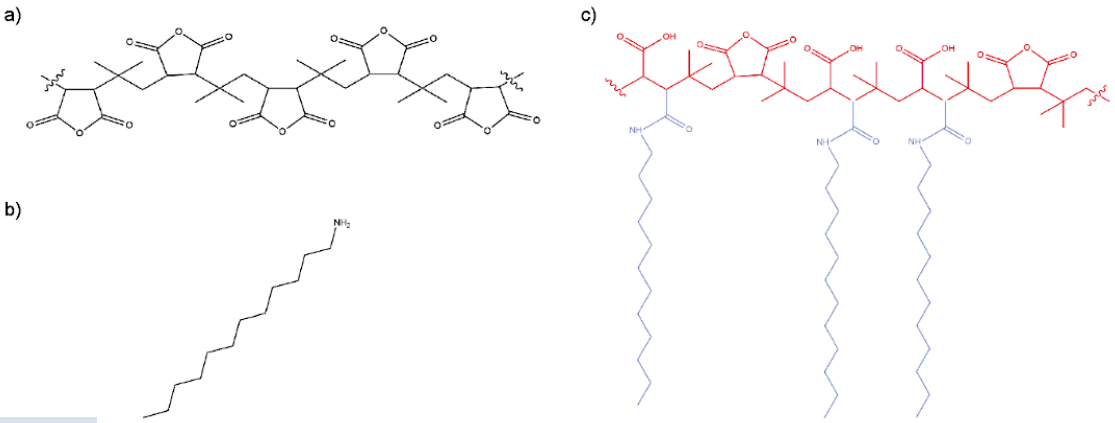

Figure 2.6.1 a) Poly (isobutylene-alt-maleic anhydride), b) DDA and c) PMA-based amphiphilic polymer

2.6.1.2. PMA modification

PMA modification with DBCO: The molar percentage employed was 2 %. For the reaction, 20 mmol (3.08 g) of poly (isobutylene-alt-maleic anhydride), 15 mmol (2.78 g) of DDA and 0.4 mmol (110 mg) of DBCO were mixed in 40 mL of THF. The solution was kept under magnetic stirring (350 rpm) and reflux (65 °C) overnight. Then, the THF was evaporated under vacuum using a rotary evaporator and the dried polymer was redispersed in 10 mL of chloroform. To purify the polymer and remove the excess of unreacted DDA, 50 mL of hexane were added to the solution and left for 2 h in the freezer (-4ºC). The sample was centrifuged (2 min, 7100 rcf) to remove the hexane and dried under vacuum. The powder was weighed to prepare a final solution in chloroform of monomer (MW= 154 $g \cdot mol^{-1}$) concentration of 0.5 M.

PMA modification with fluorescein-amine: The PMA was modified with fluorescein amine (FAM) molecules to provide the polymer with fluorescence. The molar percentage employed was 2 %. For the reaction, 20 mmol (3.08 g) of poly (isobutylene-alt-maleic anhydride), 15 mmol (2.78 g) of DDA and 0.4 mmol (138 mg) of FAM-amine were mixed in 40 mL of THF. The solution was kept under magnetic stirring (350 rpm) and reflux (65 °C) overnight. Then, the THF was evaporated under vacuum using a rotary evaporator and the dried polymer was redispersed in 10 mL of chloroform. To purify the polymer and remove the excess of unreacted DDA, 50 mL of hexane were added to the solution and left for 2 h in the freezer (-4ºC). The sample was centrifuged (2 min, 7100 rcf) to remove the hexane and dried under vacuum. The powder was weighed to prepare a final solution in chloroform of monomer (MW= 154 $g \cdot mol^{-1}$) concentration of 0.5 M.

2.6.1.3. PMA functionalization

PMA coating of Zr NMOFs family: All Zr MOFs were mixed with PMA in chloroform solution (300 monomers per nm^2 surface area of NP) and were slowly evaporated in a rotary evaporator. Then the dried product was resuspended by adding ca. 0.5 mL of sodium hydroxide (0.001 M, pH 11) aided by sonication (3 min). The resulting nanoparticles, NMOFs@PMA, were collected by centrifugation (10000 rcf, 10 min), washed twice with sodium hydroxide 0.1 mM, and finally redispersed in water (Figure 2.6.2.).

DBCO modified PMA coating of ZIF-8 and ZIF-8(CV): NMOFs as dispersed in MeOH were mixed with PMA in chloroform solution (600 monomers per nm^2 surface area of NP, assuming a spherical particle of diameter 150 nm in the case of the ZIF-8/ZIF-8(CV) and was slowly evaporated in a rotary evaporator. Then, the dried product was resuspended by adding ca. 0.5 mL of sodium hydroxide (0.1 M, pH 13), aided by sonication (1 min). The resulting nanoparticles (ZIF-8/ZIF-8(CV)@PMA) were collected by centrifugation (7100 rcf, 10 min), washed twice with sodium hydroxide 0.01 M, and finally redispersed in water.

DBCO modified PMA coating of UiO-67 and UiO-67(CV): NMOFs as as dispersed in acetone were mixed with PMA in chloroform solution (300 monomers per nm^2 surface area of NP, assuming a spherical particle of diameter 150 nm and the solvent was slowly evaporated in a rotary evaporator. Then, the dried product was resuspended by adding ca. 0.5 mL of sodium hydroxide (0.001 M, pH 11), aided by sonication (1 min). The resulting nanoparticles (UiO-67 (CV)@PMA) were collected by centrifugation (7100 rcf, 10 min), washed twice with sodium hydroxide 0.01 M, and finally redispersed in water.

USC UNIVERSIDADE DE SANTIAGO DE COMPOSTELA

FAM modified PMA coating of AuBy@ZIF-8(CV) PMA coating: NCs dispersed in MeOH were mixed with PMA in chloroform solution (600 monomers per nm^2 surface area of NP, considering for the calculations a sphere with the same NC diameter, and the solvent was slowly evaporated in a rotary evaporator. Then, the dried product was resuspended by adding ca. 0.5 mL of sodium hydroxide (0.1 M, pH 13), aided by sonication (1 min). The resulting nanoparticles (AuBy@ZIF-8(CV)@PMA) were collected by centrifugation (7100 rcf, 10 min), washed twice with sodium hydroxide (0.01 M, pH 12), and finally redispersed in water.

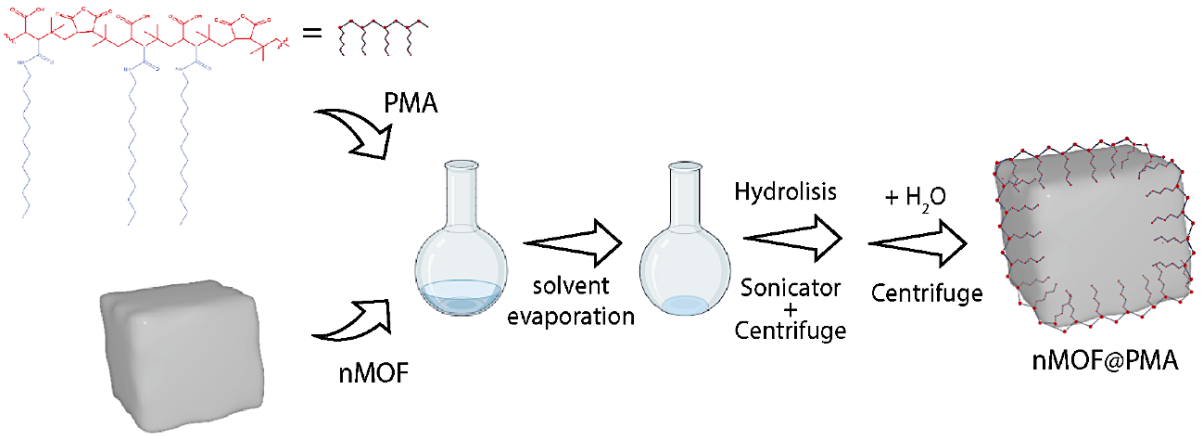

Figure 2.6.2. Schematic representation of the PMA coating method for all the NMOFs

2.6.1.4. Click chemistry.

After PMA coating, ZIF-8/ZIF-8(CV)@PMA and UiO-67/UiO-67(CV)@PMA were further surface functionalized via copper-free click chemistry reactions. As previously mentioned, PMA was modified with a DBCO group (representing a molar percentage of 2% of the total polymer). Typically, 100 µL of PMA-modified NMOFs redispersed in water were mixed with the selected azide functionalized molecules (see Figure 2.6.3. and Table 2.6.1.) at 37ºC for 30 min. Then, samples were washed twice with MilliQ water (10 min, 10000 rcf) and redispersed in 100 µL of MilliQ water.

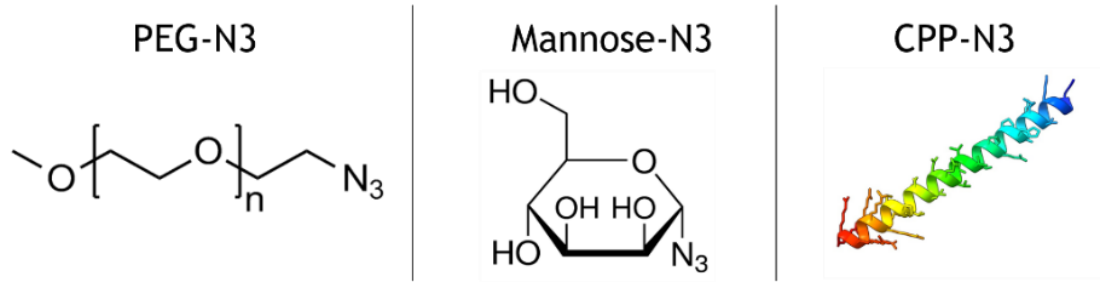

Figure 2.6.3. Selected azide-functionalized biomolecules for the functionalization of the NMOFs

Table 2.6.1. Selected azide-functionalized molecules and corresponding MW and employed molecules/MOF.

Molecule	MW (g/mol)	Molecules/MOF
MeO-PEG-N_3	5000	10000
Mannose-N_3	430.3	17000
TAMRA-CPP-N_3	3907	4000
Cy5-N_3	601.22	1000

2.6.2. PEGylation

2.6.2.1. MeO-PEG-PO_3 synthesis

MeO-PEG-PO_3 was synthesized through a modified adaptation of a previously documented procedure.[73] The synthesis was made in a two-neck flask, being initiated with the addition of 50 mmol of $POCl_3$ dissolved in 5 mL of DCM. Subsequently, 150 mmol of triethylamine was introduced at 0 °C. After 30 min, 15 mmol of MeO-PEG (5 kDa) was incorporated into the mixture in 50 mL of DCM. The resulting solution was stirred at room temperature for 10 h. After stirring, 20 mL of water was introduced to the reaction mixture and allowed to react for additional 3 h. Following this, the DCM solvent was removed under vacuum using a rotavapor, and the crude product was purified through dialysis, employing a dialysis membrane with a molecular weight cutoff of 3500 Da. Ultimately, the remaining water content was eliminated through lyophilization, resulting in the production of MeO-PEG-PO_3 in the form of a white solid. The obtained product was characterized using NMR (Figure 2.6.4.).

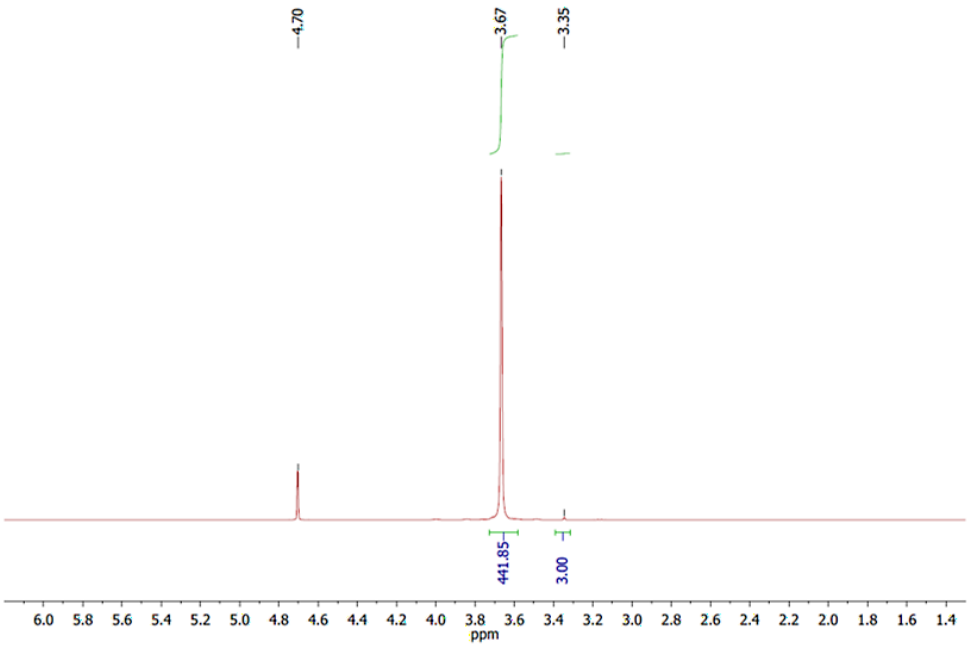

Figure 2.6.4. ^{1}H NMR spectrum of MeO-PEG-PO_3.

2.6.2.2. MeO-PEG-PO_3 functionalization procedure

Zr NMOFs PEGylation: For this, the product from a synthesis was centrifuged and the pellet was combined with 2.5 mL of a 10 $mg \cdot mL^{-1}$ aqueous solution of MeO-PEG-PO_3. The resulting mixture was stirred using a magnetic bar at 500 rpm for 3 h. Subsequently, the coated material was washed three times with water by centrifugation at 10000 rcf for 10 min, and finally redispersed in 1 mL of Milli Q water.

AuBy@NU-1000(CV) PEGylation: Surface modification of AuBy@NU-1000(CV) was also done using the MeO-PEG-PO_3 polymer. For this, the product from a synthesis previously loaded with CV AuBy@NU-1000(CV) in water was combined with 2.5 mL of a 10 $mg \cdot mL^{-1}$ aqueous solution of MeO-PEG-PO_3. The resulting mixture was stirred using a magnetic bar at 500 rpm for 3 h. Subsequently, the coated material was washed three times with water by centrifugation at 10000 rcf for 10 min.

2.6.3. DNA based functionalization

2.6.3.1. DNA-PO_3 functionalization of Zr MOFs

For this procedure, 250 mmol of oligo DNA-PO_3 (NanoTag_PO_3, 5' cac aca cac aca cac ttt ttt ttt ttt ttt 3' - PO_3) were added into the pellet of the centrifuged Zr MOFs (1 mL, 5 $mg \cdot mL^{-1}$), (in a 50:1 mmol DNA:mg MOF relation). The reaction was left under stirring at room temperature for 16 h and collected via centrifugation (10000 rcf, 10 min) to remove the unreacted DNA-PO_3, washed 3 times and finally redispersed in 1mL of Milli Q water to obtain UiO-67(Calc)@DNA.

2.6.3.2. DNA-N_3 Hybridization

The functionalized UiO-67(Calc) with NanoTag_PO_3 (UiO-67(Calc)@DNA) was mixed with cNanoTag_Azide (tttgtgtgtgtgtgtgtg) using the same quantity as the one used in the previous step (NanoTag_PO_3, relation 1:1). The reaction was left for 1 h at 26ºC to achieve the hybridization of the DNA. The final product (UIO-67(Calc)@DNAds) was washed twice and left in 1 mL of MQ water.

2.6.4. Protein functionalization

2.6.4.1. BSA functionalization with Cy5-NHS

BSA was marked with Cy5-NHS in a molar relation 1:25. To do it, 10 mg of the protein were weighted in an Eppendorf and diluted in 1 mL of water. Then, 20 µL of the Cy5-NHS stock solution (100 $mg \cdot mL^{-1}$, MeOH) was added to the protein solution and incubated at room temperature for 60 min. To stop the reaction, Tris (10 µL, 100 mM in water) was added to quench the unreacted Cy5-NHS ester and incubated for 15 min. The next day, to purify the sample, PD10 columns were used to remove the excess of the dye and collect the marked proteins. The final product was left in 100 µL of PBS. The concentration of the protein was calculated by a calibration curve using a BSA solution with a known concentration (Figure 2.6.5.). The measurements were performed using a BCA Protein Assay.

USC UNIVERSIDADE DE SANTIAGO DE COMPOSTELA

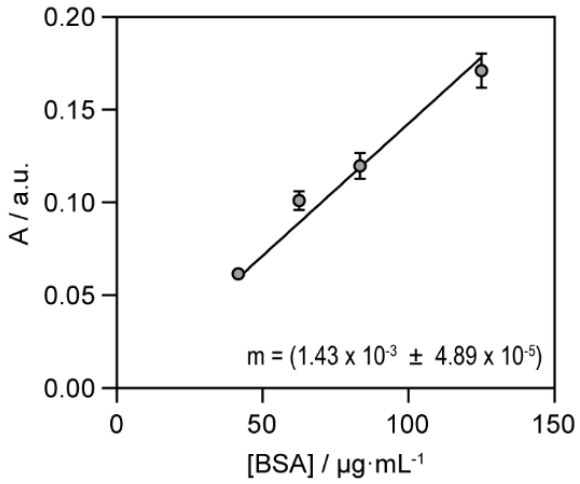

Figure 2.6.5. BSA calibration curves (Absorbance measured at λ=570 nm).

2.6.4.2. BSA-Cy5 functionalization with DBCO-NHS

400 µL of modified BSA-Cy5 were mixed with 6.6 µL of 20-fold molar excess of DBCO-NHS ester dissolved in DMSO (10 mM) and incubated at room temperature for 60 min. To stop the reaction, Tris (10 µL, 100 mM in water) was added to quench the unreacted DBCO-NHS ester and incubated for 15 min. Finally, the unreacted DBCO was removed using a PD10 column and the marked protein was collected and left in PBS.

2.6.4.3. UiO-67(Calc)@DNA functionalization with BSA

UiO-67(Calc)@DNAds NMOFs were functionalized with the as-prepared BSA-Cy5-DBCO. A mixture of 100 µL of UiO-67(Calc)@DNAds with the modified BSA was added in a molar ratio 2:1 (BSA:MOFs). The mixture was left overnight at 4 ºC to enable the click chemistry reaction between the DBCO groups present in the protein and the N_3 free groups on the surface of the NMOFs. The sample was washed twice with Milli Q Water and left in 50 µL of water.

2.6.5. NIR laser irradiation experiments

In lasers experiments, to control the spot size as well as irradiate cells homogeneously, an 808 nm laser (Lasing, #FC-W-808A) with a zoom fiber collimator (Thorlabs, #ZC618SMA-B) was used. To determine the intensity of the laser irradiation received by the cells, a power energy meter (Thorlabs, #PM100D) equipped with a thermal powerhead (10 W, 25 mm, Thorlabs, #S425C) was employed to measure the output power. The spot size was determined by using a viewing card (Thorlabs, #VRC4) to visualize the spot, and ImageJ software was utilized to measure its dimensions. Since the beam was collimated, a uniform spot distribution was assumed, allowing the intensity to be calculated by dividing the power (7.85 W) by the surface area (0.785 cm^2) of the spot giving an irradiance of 10 $W \cdot cm^{-2}$. Various experimental conditions involving different time intervals and power densities were investigated, as specified in each individual experiment.

USC UNIVERSIDADE DE SANTIAGO DE COMPOSTELA

2.7. CHARACTERIZATION TECHNIQUES

2.7.1. Thermogravimetric analysis (TGA)

TGA of powder samples was performed using a TA Instruments Inc. Q5000 operating in nitrogen with sample purge gas flow of 25 mL·min^{-1}, or air, and samples scanned at a heating rate of 10 °C·min^{-1} from 30 to 800 °C.

Considering the evaporation of water and remaining solvents within the porosity T<150 °C, the recalculation of the inorganic and organic content (% wt = weight percentage) of the samples in section 3.1. (*i.e.*, ZIF-8, ZIF-8(CV), ZIF-8@PMA, ZIF-8(CV)@PMA and the UiO-67 equivalents), is described below.

- CV wt% NMOFs: considering the inorganic content (Zn) remains constant:

$$\text{Organic wt\% NMOF}_{\text{equivalent}} = \frac{\text{Inorganic wt\% NMOF(CV)}}{\text{Inorganic wt\% NMOF}} \text{x Organic wt\% NMOF} \quad (1)$$

$$\text{CV \%} = \text{Total organic wt\% NMOF(CV)} - \text{Organic wt\% NMOF(CV)}_{\text{equivalent}} \quad (2)$$

- PMA wt% in NMOFs-PMA**:** considering the inorganic content (Zn) remains constant:

$$\text{Organic wt\% NMOF@PMA}_{\text{equivalent}} = \frac{\text{Inorganic wt\% NMOF@PMA}}{\text{Inorganic wt\% NMOF}} \text{x Organic wt\% NMOF} \quad (3)$$

$$\text{PMA wt \%} = \text{Total organic wt\% NMOF@PMA} - \text{Organic wt\% NMOF@PMA}_{\text{equivalent}} \quad (4)$$

- CV & PMA wt% in NMOFs(CV)@PMA: considering the inorganic content remains constant and taking the values obtained from fluorescence measurements as the % of CV that remains inside after PMA functionalization:

$$\text{Organic wt\% NMOF(CV)@PMA}_{\text{equivalent}} = \frac{\text{Inorganic wt\% NMOF(CV)@PMA}}{\text{Inorganic wt\% NMOF}} \text{x Organic wt\% NMOF} \quad (5)$$

$$(\text{PMA} + \text{CV})\text{wt \%} = \text{Total organic wt\% NMOF(CV)@PMA} - \text{Organic wt\% NMOF(CV)@PMA}_{\text{equivalent}} \quad (6)$$

$$\text{CV wt \%} = (\%CV\ fluo)\frac{\text{Inorganic wt\% NMOF(CV)@PMA}}{\text{Inorganic wt\% NMOF}} \text{x CV wt\% in NMOF(CV)} \quad (7)$$

$$\text{PMA wt \%} = (\text{PMA} + \text{CV})\ \text{wt\%} - \text{CV wt\%} \quad (8)$$

USC UNIVERSIDADE DE SANTIAGO DE COMPOSTELA

2.7.2. Optical characterization (UV-Vis)

UV-visible absorption spectra were recorded using an Agilent UV-Vis Cary 3500 spectrophotometer. The measurements were performed using a 1 cm quartz cell at a controlled temperature of 25 ºC to minimize variability. Data acquisition was carried out over a wavelength range of 200 to 1000 nm to capture the entire extinction profile.

2.7.3. Fourier transform infrared spectroscopy (FTIR)

FTIR of powder samples was performed using a Perkin-Elmer Two equipped with ATR; samples were scanned from 550–3500 cm^{-1}.

2.7.4. Dynamic light scattering (DLS) and ζ-potential

NMOFs hydrodynamic size and polydispersity index (PDI) were determined by dynamic light scattering (DLS) using a Malvern Zetasizer Nano ZSP. equipped with a 10 mW He–Ne laser operating at a wavelength of 633 nm and fixed scattering angle of 173˚. The ζ-potential was measured with laser Doppler anemometry (LDA) by the same Malvern Zetasizer Nano ZSP instrument.

2.7.5. Nanoparticle tracking analysis (NTA)

NP tracking analysis was used to characterize the colloidal properties of the NMOFs and determine the particle concentration in solution. All the samples were analyzed by using a NanoSight NS300 (Malvern Instruments, UK) equipped with a 488 nm laser module, a sCMOS camera and a syringe pump was used for all NTA measurements. All measurements were carried out at 24 ºC. NMOFs were diluted in filtered MilliQ water to a final volume of 1 mL and loaded in the measurement chamber with a flow rate of 100 $\mu L \cdot min^{-1}$. Flow mode measurements were obtained recording 3 videos of 60 s for each measurement. The NanoSight NS300 software was used to analyze the sample (10-100 particles per frame).

2.7.6. Quantification by Fluorescence Measurements

The amount of cargo molecules loaded into the NMOFs was quantified measuring the fluorescence signal by using a Microplate reader (TECAN, Infinite® 200 PRO) equipped with monochromator-based optics and wavelength selection between 280 and 850 nm. In Table 2.7.1, the $\lambda_{exc}/\lambda_{em}$ ranges used for the different fluorescent molecule are reported. The number of fluorescent molecules loaded into NMOFs was quantified by fluorescence indirectly, by measuring the fluorescence remaining in the supernatants after centrifugation and washing steps. The cargo concentration in the supernatant was determined by interpolation of the measured fluorescence intensity (I) to previously constructed analytical calibration curves (Figure 2.7.1.- 2.7.2.).

USC UNIVERSIDADE DE SANTIAGO DE COMPOSTELA

Table 1.7.1. Excitation and emission wavelengths of the employed fluorescent molecules

Fluorescent molecule	$\lambda_{exc}/\lambda_{em}$
Cresyl Violet	590 / 620
Cy5	650 / 670
FITC	491 / 516
Calcein	495 / 515
Doxorubicin	470 / 560

2.7.7. Scanning electron microscopy (SEM)

SEM micrographs were obtained using a ZEISS FE-SEM ULTRA Plus after the deposition of a drop of diluted sample onto a piece of clean silicon wafer.

2.7.8. Inductively coupled plasma-optical emission spectrometry *(ICP-OES)*

The elemental analysis was performed using an Agilent 5800 Inductively Coupled Plasma Optical Emission Spectrometer (ICP-OES). Prior to analysis, the samples underwent acid digestion through Anton Paar Multiwave GO Plus microwave heating system. Calibration curves ranging from 0 to 10 ppm were constructed for all the analyzed elements (Zr, Zn, Pt and Au). Additionally, Mn and Se were added at known concentrations as internal standards. For each element, the concentration was extrapolated from two atomic emission lines: Zr at 339.198 nm and 343.823 nm, Zn at 202.548 nm and 213.857 nm, Pt at 203.646 nm and 214.424 nm, Au at 242.794 nm and 267.594 nm, Mn at 257.610 nm and 259.372 nm, Se at 196.026 and 203.985 nm.

2.7.9. Powder X-Ray diffraction (PXRD)

X-ray diffractometer Phillips was used to study the crystalline powder of samples; the samples were examined in the range of 2θ between 2° and 75°, with a passage of 0.02° and a time by step of 2s.

2.7.10. N_2 adsorption–desorption analysis

N_2 sorption isotherms at 77 K were measured on a Micromeritics 3Flex Adsorption Analyzer. The samples (about 20–30 mg) were activated overnight under a high vacuum at 90 °C prior to analysis. The specific surface area was extrapolated within the relative pressure (P/P_0, where P_0 is the saturation pressure) interval of 0.05–0.3 by applying the Brunauer, Emmett & Teller (BET) equation. The data were analyzed using the 3Flex V5.03 software (Micromeritics Instrument Corp., Norcross, GA, United States).

2.7.11. Colloidal stability tests

DLS measurements at different times were carried out in different media: MilliQ water and cell culture medium (DMEM with phenol red, 4.5 g L1D-glucose, L-glutamine and pyruvate (DMEM Gibco, Thermo Fisher Scientific, Massachusetts, USA) supplemented with 10% FBS

(Gibco, Thermo Fisher, Massachusetts, USA) and 1% penicillin/streptomycin (P/S, Gibco, Thermo Fisher Scientific, Massachusetts, USA)).

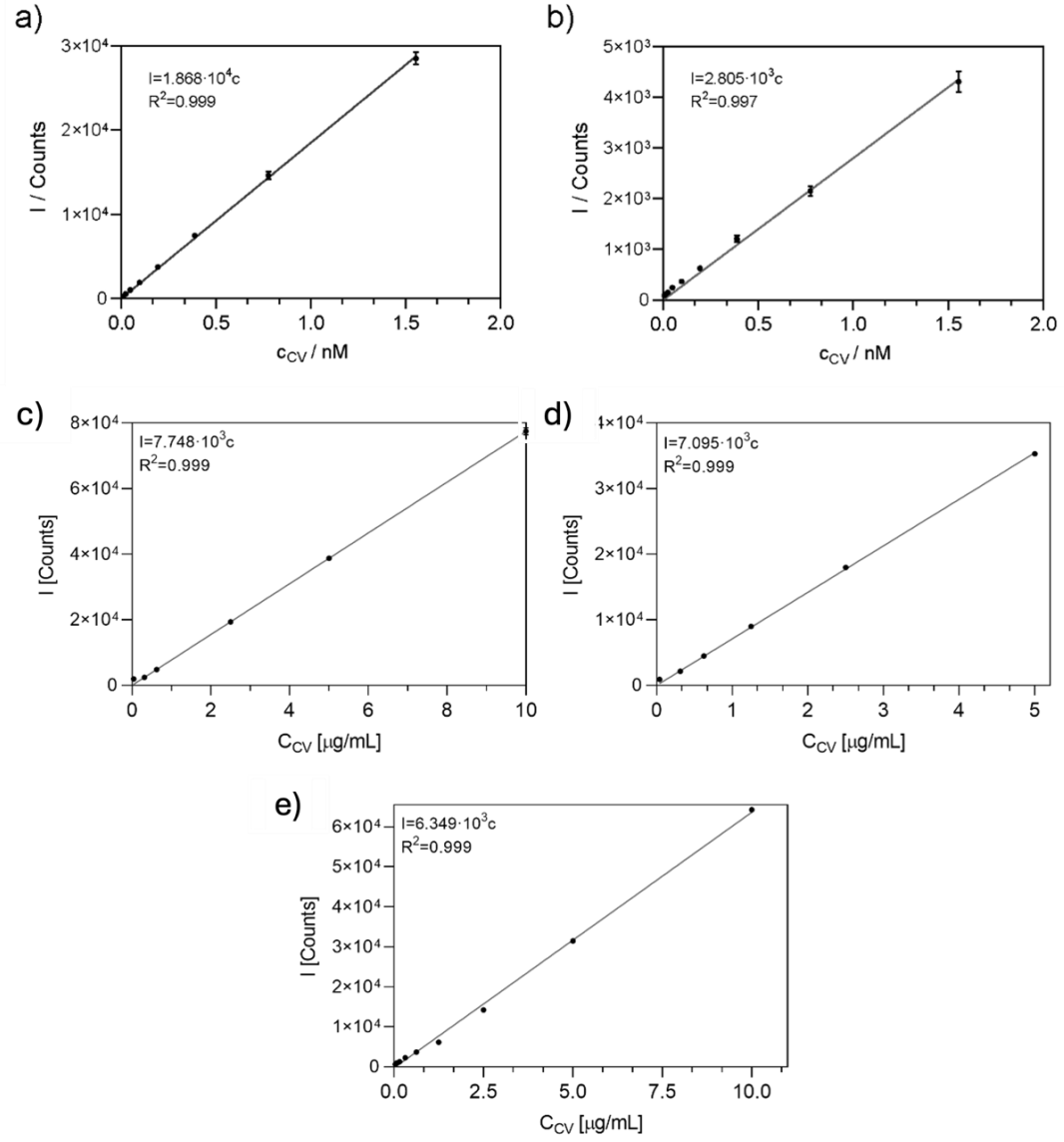

Figure 2.7.1. Calibration curves of CV in a) Water, b) MeOH, c) PSF, d) DMEM and e) PBS.

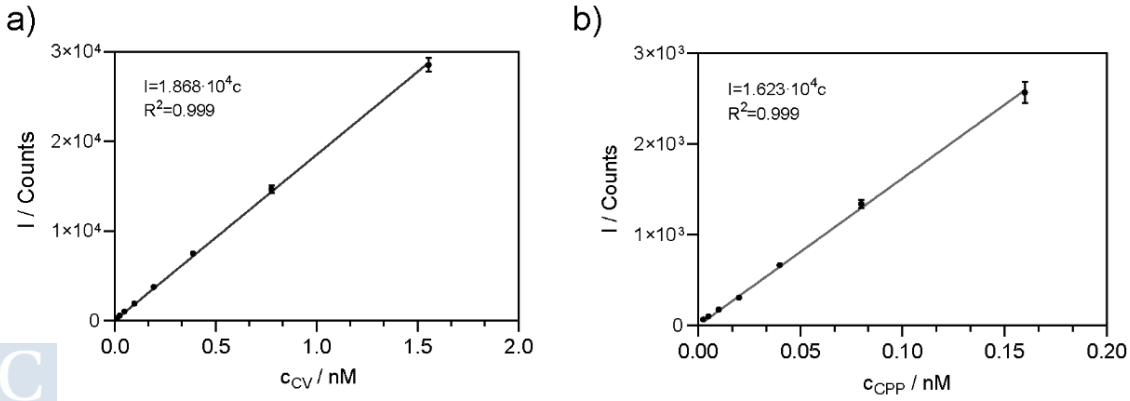

Figure 2.7.2. Calibration curves in water for a) Cy5-N_3 and b) Tamra-CPP-N_3

2.7.12. High performance liquid chromatography (HPLC):

The potential linker release (BPDC) from the MOF structure was determined using a reverse phase HPLC Jasco LC-4000 series system, equipped with a photodiode array (PDA) detector MD-4015 and a multisampler AS-4150 controlled by ChromNav software (Jasco Inc, Japan). For the quantification, isocratic conditions were used through a Purple ODS reverse phase column (C18, 5 µm, 4.6 x 150 mm, Análisis Vínicos, Spain) with a flow rate of 1 mL·min^{-1}. The column temperature was fixed at 25°C and the injection volume was 30 µL. The mobile phase was based on a mixture of 95:5 phosphate buffered solution (pH = 9): MeOH. Retention time and maximum adsorption (λ) for BPDC were 7.6 min and 278 nm respectively.

2.7.13. Cargo loading stability.

Cargo stability tests were performed at different times (t = 0, 4, 8, 24, 48, 120 and 240 h) in different media: MilliQ water, DMEM, PBS (1×, pH = 7.4) and PSF (pH = 5; PSF (100 mL): 114 mM sodium phosphate dibasic anhydrous, 114 mM sodium chloride, 0.5 mM sodium sulphate anhydrous, 0.2 mM calcium chloride dihydrate, 6 mM glycine and 20 mM potassium hydrogen phthalate). For the analysis, 100 µL of the samples were centrifuged and the pellets were redispersed in 2 mL of the corresponding media for the analysis. At each time point, 100 µL (x3) of each sample.

2.8. IN VITRO STUDIES

2.8.1. Cell culture

The A549 (human lung carcinoma) cell line was maintained in culture in Dulbecco's Modified Eagle Medium with phenol red, 4.5 g L-1D-glucose, L-glutamine and pyruvate (DMEM Gibco, Thermo Fisher Scientific, Massachusetts, USA) supplemented with 10% (v/v) fetal bovine serum (Gibco, Thermo Fisher, Massachusetts, USA) and 1% penicillin/streptomycin (P/S, Gibco, Thermo Fisher Scientific, Massachusetts, USA) (cDMEM). Cells were cultured at 37 °C under a 5% CO_2 atmosphere and kept under humid conditions. After reaching 80% confluency, the cells were washed with Dulbecco's phosphate buffered saline (PBS, Thermo Fisher #14190169) and passaged after incubation with 0.25% Trypsin–EDTA (Gibco, Thermo Fisher Scientific, Massachusetts, USA).

2.8.2. MTT toxicity assay

MTT (3-[4,5-dimethylthiazol-2-yl]-2,5-diphenyltetrazolium bromide) assay was performed to study cells viability after NCs exposure. A549 cells were seeded in 96-well plates (7500 cells/well in 100 µL of cDMEM). After 24 hours, the medium was removed and 100 µL of NCs solution diluted in fresh cDMEM were added. After the selected incubation time (24 h or 72 h), each well was rinsed once with 1X PBS and 100 µL of freshly prepared MTT solution diluted in cDMEM was added. 96-well plates were left 3 hours at 37 ºC and 5% CO_2, then MTT solution was removed and 50 µL of DMSO were added to each well to dissolve the formazan crystals. After 10 mins at 37 ºC and 5% CO_2, absorbance was measured with a plate reader (TECAN, Infinite® 200 PRO) at 540 nm. The absorbance value of each well provided by the instrument is an average of nine consecutive measures in the same well. Final absorbance value for control cells (Ac) (untreated), is an average of, at least, nine different well values. Final absorbance values for samples (As) are a mean of three independent well values. Cell viability value is calculated as follows: (As/Ac)×100.

USC UNIVERSIDADE DE SANTIAGO DE COMPOSTELA

2.8.3. Flow cytometry

A549 cells were seeded in 48-well plates at a density of 25000 cells·well^{-1} in 0.3 mL of cDMEM. After 24 h, cDMEM was replaced with NMOFs solutions diluted in fresh cDMEM. Experiments were performed by exposing cells to NMOFs dispersions at 0.25 pM, 0.5 pM and 1 pM for 1 hour. Then, cells were rinsed once with 1X PBS and were harvested after trypsinization for 2 min with 0.070 mL 0.25% Trypsin-EDTA. 0.15 mL of PBS were added to each well to recover the cells. Fluorescence intensity was measured using a flow cytometry (Beckman Coulter Cytoflex S B-R-V-Y Series, C02947) equipped with a 532 nm green laser coupled with a 620/50 filter, according to CV emission spectrum. Results are reported as the mean of cell fluorescence intensity, provided by the measurement of 3 wells (MFI).

2.8.3.1. Concentration calculations of NMOFs

Typically, 200 µL of a dilution of NMOFs in water is placed in a 96 multi well plate. The plate is run on a flow cytometer adjusting the instrument settings to visualize the nanoparticles on a fluorescence intensity of the NMOFs vs. violet side scatter. In the case of non-fluorescent UiO-67, the NMOFs are visualized using violet side scatter vs side scatter. After the measurement, gating strategies are used to identify NMOFs population and directly measure events per mL, corresponding to particles·mL^{-1}.

2.8.3.2. VitroCheck NanoParticle Reference Kit: concentration calculation

Typically, 200 µL of a dilution of NMOFs in water is placed in a 96 multi well plate. Then, 50 µL of the 100 nm VitroCheck reference beads suspension is added to each sample. The plate is run on a flow cytometer adjusting the instrument settings to visualize the nanoparticles on a fluorescence intensity of the beads vs. fluorescence intensity of the NMOFs (NU-1000 and PCN-222). In the case of UiO-67, the NMOFs are visualized using violet side scatter. After the measurement, gating strategies are used to identify beads and NMOFs population. Using the count statistics from the sample and reference beads gates, the original sample concentration can be determined.

2.8.4. Microscopy imaging

A549 cells were initially seeded onto µ-slide 8 well-IbiTreat chambers, with each well providing a surface area of 1 cm^2. The seeding density employed was 20000 cells per well, cultured in complete Dulbecco's Modified Eagle Medium (cDMEM) for 24 h. After the incubation, the cDMEM was replaced with freshly prepared solutions of the NMOFs at the selected concentrations diluted in cDMEM. Following the chosen time exposure to these particles, the cells underwent a single rinse with 1X PBS. This step aimed to eliminate any non-internalized particles that might have remained dispersed in the cDMEM prior to the subsequent image acquisition. Fluorescence images of the cells were captured using a Leica Microscope type DMI8, equipped with a Leica DFC9000 camera, and maintained in an incubator at a temperature of 37 °C under a 5% CO_2 atmosphere. Cells were observed in the brightfield channel, the CV channel (wavelengths: excitation range 542-566 nm; emission range 578-610 nm), Calcein and Fluorescein channel (excitation range 462-496 nm; emission range 506-632 nm), NU-1000 fluorescence channel (excitation range 375-407 nm; emission range 420-450 nm), Cy5 and Lysotraker Deep-red channel (excitation range 622-654 nm; emission range 666-724 nm).

USC DE COMPOSTELA

To analyze the images, ImageJ software was utilized for image processing and data extraction. NIR irradiation of the samples was performed using Leica infinity scanner installed in the microscope that allows the scanning of the selected ROIs with a NIR laser using LASX software.

To study the PDT effect of the AuBy@PCN-224(CV)@PEG, samples were excited with a 405 nm laser in a confocal microscope. The experiments were performed using an Andor Dragonfly spinning disk confocal system mounted on a Nikon TiE microscope equipped with a Zyla 4.2 PLUS camera (Andor, Oxford Instruments) and an OKO-lab incubator to keep cells at 37°C under a 5% CO_2 atmosphere during the whole experiment. Samples were irradiated for 2 and 5 min. To study the viability, a live-dead assay employing calcein-AM and propidium iodide was employed as reporters for viable and apoptotic cells, respectively. All the images were processed with ImageJ.

2.8.5. Spheroids

A549 cell lines were used to obtain the 3D spheroids. 100 mL of suspension of 50000 cells·mL^{-1} were transferred to a 96 multi-well plate previously treated with agarose as follows: a 1-1.5% agarose solution was prepared in filtered PBS 1X and heated up to 100 °C; 50 µL of agarose solution were used to cover the bottom of the wells. The plate was let to cool at RT in sterile conditions without the lid for at least 30 min before seeding the cells. The 3D spheroids were grown at 37 °C in a humidified 5% CO_2 atmosphere, with 100 µL of fresh complete media gently added every day, for 3 days in order to obtain spheroids with a ~ 0.5 µm diameter. On the fourth day, the spheroids were washed with PBS 1X twice, carefully avoiding displacing them from the wells. The spheroids were incubated with a 200 µL solution of the NCs. After 24 h, the NCs solution was removed, and the spheroids were washed twice with PBS 1X. After that, the consecutive irradiation experiments were performed.

2.8.6. LIVE/DEAD assay

Each spheroid was individually transferred into the 96 multi well plate without agarose. Then, they were harvested after trypsinization for 2 min with 0.05 mL of 0.25% Trypsin-EDTA. 0.2 mL of cDMEM was added to recover the cells, which were transferred to a 96 multi well V-bottom plate. The cells were collected after centrifugation at 500 g for 5 min. The cell pellets were resuspended in 0.2 mL of PBS 1X at 0.1 µM calcein AM and 3 µM Propidium Iodide. The cells were incubated for 15-20 min at room temperature in the dark. After the incubation period, the stained cells were analyzed by flow cytometry (Beckman Coulter Cytoflex S B-R-V-Y Series, C02947) using a 488 nm excitation and measuring green fluorescence emission of calcein (*i.e.*, 530/30 bandpass) and red fluorescence emission of the propidium iodide (*i.e.*, 610/20 bandpass). Results were analyzed using BD FlowJo 10.10.0.

2.8.7. Statistical analysis

All data are presented as the mean and standard deviation (SD). Two-way ANOVA was used to test the differences between groups. Statistical significance was set at $p<0.05$. All statistical analysis were conducted using GraphPad Prism 8.0.1.

USC UNIVERSIDADE DE SANTIAGO DE COMPOSTELA

3. Results and discussion

USC
UNIVERSIDADE
DE SANTIAGO
DE COMPOSTELA

USC
UNIVERSIDADE
DE SANTIAGO
DE COMPOSTELA

3.1. CLICKABLE POLYMER-BASED FOR CUSTOMIZING THE INTERACTION OF NMOFS WITH LIVING CELLS

MOFs have been extensively explored for various applications, such as catalysis, gas storage, and sensing. Due to their large pore volumes, well-defined tunable structures, and permanent porosities, they are also considered ideal candidates for drug delivery vehicles.[13]

The microporous nature of ZIF-8 has made it a popular choice for drug delivery due to its ability to accommodate a wide range of challenging drugs. However, a significant limitation lies in the rapid release kinetics associated with these NMOFs, with up to 80-90% release occurring within the first 10 h in physiological media. This drawback hampers their application in biomedicine, primarily stemming from the instability of ZIF-8 in aqueous environments, which is influenced by factors such as pH and concentration. This degradation is related to the action of dissolved carbon dioxide which can replace imidazolate linkers leading to the degradation of the nano-ZIF-8.[163,164] Alternatively, the UiO family of Zr-MOFs, which feature $Zr_6(OH)_4O_4^{12+}$ clusters, are known for their exceptional stability and a high tolerance for structural defects. Among the members of this prolific family is the isoreticular UiO-67, with 4,4′-biphenyl dicarboxylate (BPDC) linkers. UiO-67 features relatively large voids (1 nm), and high thermal and chemical stability due to its $[Zr_6O_4(OH)_4(BPDC)_{12}]$ brick structure, making it a high-potential candidate for biomedical applications. However, conflicting conclusions about UiO-67's stability against exposure to aqueous settings have been reported in multiple articles, as well as apparently contradictory findings for other $Zr_6(OH)_4O_4^{12+}$-based MOFs, including NU-1000, PCN-222 or MOF-808.[65,165] In addition, if MOF-based nanocarriers are to be developed for their use in physiological environments, they must withstand the relatively high endogenous phosphate concentrations (1-10 mM) in biological settings, at least to some extent. This may pose challenges, particularly for group 4-based MOFs,[166] due to the strong coordinating nature of phosphate ions.[167] Moreover, NMOFs should remain colloidally stable in the presence of crowded media such as blood, serum, or cytosolic media of cells.[168,169]

Because of the need to ensure NMOFs' stability and provide them with recognition abilities, one of the primary interests of NMOFs in the context of biological applications is their potential for external surface functionalization.[170] Post-synthetic modifications, in particular, can improve colloidal stability, cellular uptake, drug release control, or prolong circulation time.[169,171] Furthermore, active targeting through specific interactions between homing molecules such as peptides, antibodies, or saccharides can enhance the targeting performance of these systems.[172]

Polymers such as polyethylene glycol (PEG) stand out as one of the most utilized macromolecules for stabilizing nanomaterials. PEG’s widespread use is attributed to its antifouling properties, which partially prevent opsonic interaction and macrophage uptake, thereby promoting prolonged blood circulation.[73,173] On the other hand, carbohydrates are also extensively employed as biomolecule-based coatings, garnering attention for their capacity to enhance cell recognition, stability, and biocompatibility.[174] Among carbohydrate-functionalized nanomaterials, mannose-conjugated nanoparticles provide new advances in targeted delivery because of the lectins with mannose-binding ability, which are predominantly expressed on various cancer cells, enabling cancer treatment targeting.[175,176] Mannose is a membrane carbohydrate capable of binding to glycolipids and glycoproteins, playing a crucial role in cell-cell recognition and enzyme triggering processes.[177] Surface functionalization of nanoparticles with mannose molecules can enhance target binding and selectivity of DDSs, as several tumor cell lines overexpress the mannose receptor (MR).[175,178] Similarly, cell-

penetrating peptides (CPPs) are widely used as a biomimetic, virus-inspired approach for delivering a broad range of cargoes across cellular membranes.[179,180] CPPs belong to a class of peptides that have the potential to act as carriers for covalently or non-covalently attached cargoes of various sizes, ranging from small molecules to peptides, nucleic acids, proteins, and even particles.[181,182] These peptides facilitate the translocation of certain proteins across the plasma membrane, enabling them to overcome cellular transport mechanisms such as endocytosis, which can impede the cytosolic delivery of hydrophilic particles with high molecular weight.[181,183,184] CPPs find applications in diverse fields, including gene delivery, liposome functionalization, nanoparticle decoration, and therapeutic protein delivery.[180]

Numerous strategies have surfaced for post-synthesis functionalization of NMOFs, known as post-synthesis modification methods (PSMs). Covalent PSM entails surface functionalization achieved by forming covalent bonds between chosen functionalities and the moieties present in the linkers on the outer surface of the NMOFs. This method includes various covalent modifications, including N-alkylation, click chemistry, or protonation, as mentioned previously. Among these, click chemistry stands out as a series of chemical reactions offering distinct advantages over traditional methods. [70][185][186]

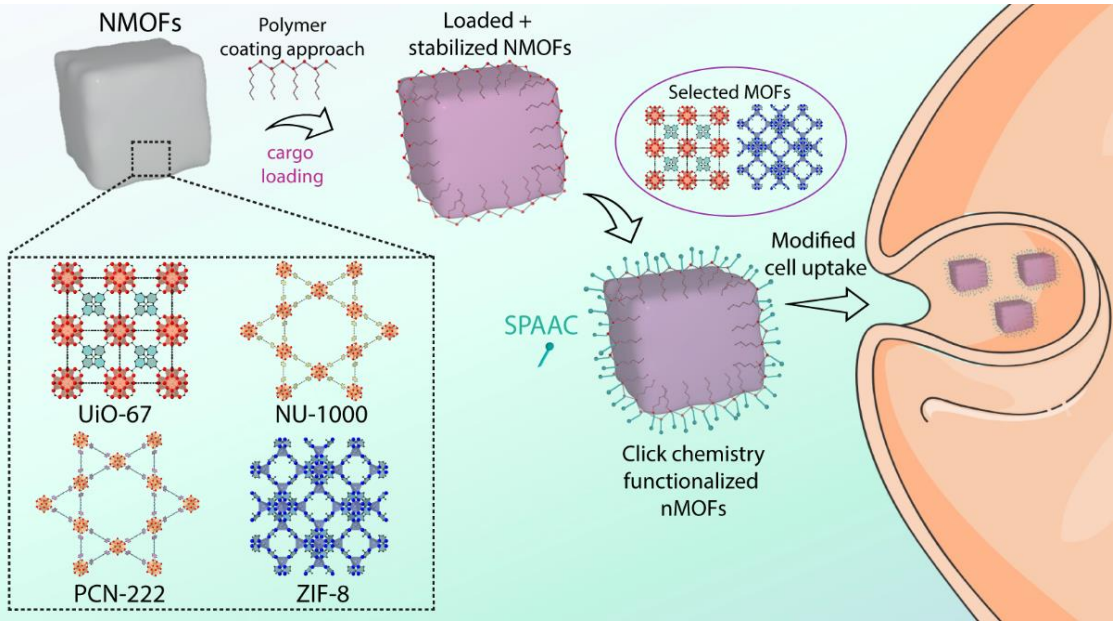

Figure 3.1.1. Scheme of the proposed polymer functionalization approach.

Click chemistry is characterized by several compelling advantages, including high yields, broad applicability, minimal generation of cytotoxic byproducts, high stereospecificity, and straightforward reaction conditions.[187] Additionally, it exhibits compatibility with a range of functional groups such as azides, amines, and carboxylic acids, rendering it a versatile tool for surface modification of NMOFs in biomedical applications. Copper-free click chemistry involves the reaction between a diarylcyclooctyne moiety (DBCO or ADIBO) and an azide-labeled reaction partner.[188] This reaction, known as strain-promoted alkyne azide cycloaddition (SPAAC), offers significant advantages.[189] Notably, these copper-free reactions exhibit rapid kinetics at room temperature and can be conducted within living cells without inducing cytotoxicity associated with copper ions. This is particularly advantageous as traditional Cu(I)-catalyzed reactions may cause damage to normal cells and healthy tissues.[190] However, despite its advantages, click chemistry also presents certain drawbacks, particularly

the requirement for ligand modification to incorporate the necessary functional groups, a process that may not be universally applicable across all types of NMOFs.[169]

To address this challenge, herein a hybrid approach that combines the strengths of both strategies is proposed. Specifically, the selected polymer was PMA, which can be modified to include free groups serving as anchor points for the covalent attachment of other biomolecules via click chemistry. This innovative approach offers the potential to overcome the limitations associated with click chemistry alone, expanding the scope of surface functionalization possibilities for NMOFs in biomedical applications (Figure 3.1.1.).

3.1.1. Synthesis and characterization of NMOFs

Herein, NMOFs were synthetized, Zn- and Zr-based, including PCN-222, NU-1000, UiO-67 and ZIF-8, using relatively mild conditions and short times (Figure 3.1.2.).

To control the size and morphology while producing nanoparticles (NPs) is critical for biological applications. Typical syntheses to produce Zr-based MOFs are based on solvothermal methods which employ high boiling temperatures solvents such as DMF or DMSO to dissolve the metal salt(s) and ligand(s) in a vial or closed vessel, allowing for heating during long periods (i.e., 12 h or longer). Generally, organic acids (i.e., acetic acid, formic acid, trifluoroacetic acid, benzoic acid, etc.) are used as modulators to control the particle size. These modulators act as competitors with the organic linkers for the available Zr sites, preventing the growth of the particles.[191-193] For the synthesis of the selected Zr-MOFs, the experimental protocol described by Ceballos et al. was modified.[194] In this protocol, DMF was used as a solvent and acetic acid as modulator, except for PCN-222 where TFA and a preformed Zr-cluster as source of Zr were used.

To produce UiO-67, $ZrOCl_2 \cdot 8H_2O$, H_2BPDC and AA were used as Zr source, ligand, and modulator, respectively, at a molar ratio of 1:2:220, as shown in the Experimental Section. The resulting UiO-67 nanoparticles were characterized using scanning electron microscopy (SEM), presenting an octahedral morphology with an average edge size of (80 ± 5) nm (Figure 3.1.3.) and a surface charge of (10 ± 1) mV.

For NU-1000, $ZrOCl_2 \cdot 8H_2O$, TBAPy and AA were used as Zr source, ligand, and modulator, respectively, at a molar ratio of 1:2:220, following previous procedures.[195] The resulting NU-1000 nanoparticles were characterized using SEM, presenting an octahedral morphology with an average size of (151 ± 16 nm) (Figure 3.1.4.) and a surface charge of (40 ± 1) mV.

Nanosized PCN-222 particles were prepared in DMF solution using a Zr_6O cluster previously synthesized and TCPP as Zr and organic ligand sources, respectively, while TFA was used as a modulator, using molar ratio of ligand to cluster of 2:1 (Figure 3.1.5.).[73] The resulting PCN-222 nanoparticles presented a seed morphology with an average size of (134 ± 13) nm and a surface charge of (17 ± 1) mV, respectively.

On the other hand, ZIF-8 was selected as a widely employed and representative example of the ZIF family, containing Zn as metal nodes and 2-methylimidazole (MeIM) as organic linkers, using a molar ratio of ligand to zinc ion ($MeIm/Zn^{2+}$) of 54 (Figure 3.1.6.). Nanosized ZIF-8 particles were prepared following a method previously reported.[20] Resulting ZIF-8 NMOFs are cubes of (140 ± 8) nm and surface charge of (35 ± 1) mV, respectively.

USC UNIVERSIDADE DE SANTIAGO DE COMPOSTELA

The size obtained using SEM images was confirmed using DLS measurements, obtaining intensity mean values of the hydrodynamic diameters of $d_{h,\ UiO\text{-}67}$ = (255 ± 71) nm (Figure 3.1.3.b), $d_{h,\ NU\text{-}1000}$ = (184 ± 8) nm (Figure 3.1.4.e), $d_{h,\ PCN\text{-}222}$ = (250 ± 35) nm (Figure 3.1.5.e) and $d_{h,\ ZIF\text{-}8}$ = (170 ± 3) nm (Figure 3.1.6.b). These results confirm the nanometric size and the successful synthesis of the NMOFs in similar size ranges in all case.

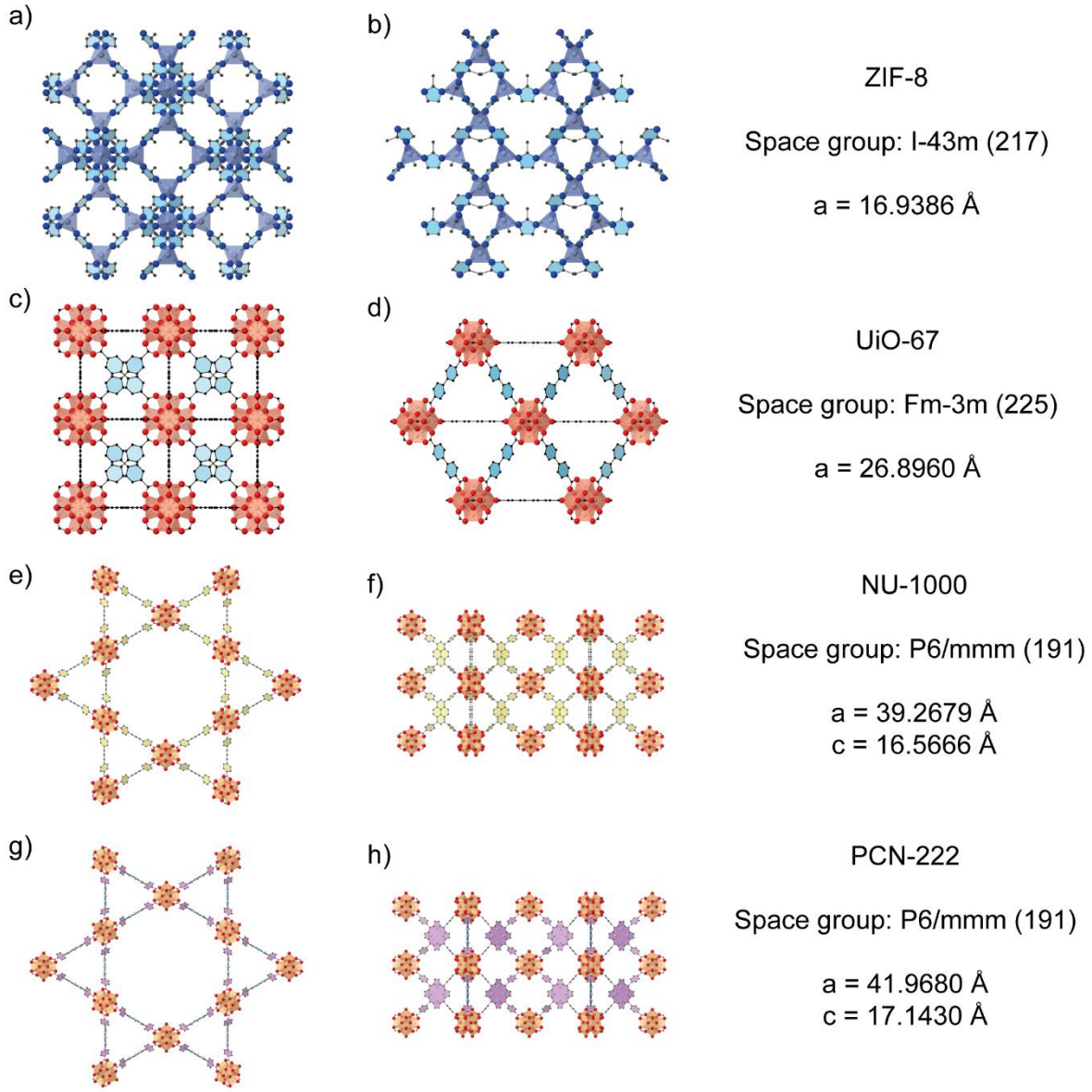

Figure 3.1.2. Crystal structure of the selected NMOFs: a) ZIF-8 a-axis oriented, b) ZIF-8 [110] oriented, c) UiO-67 a-axis oriented, d) UiO-67 [110] oriented, e) NU-1000 c-axis oriented, f) NU-1000 a-axis oriented, g) PCN-222 c-axis oriented, h) PCN-222 a-axis oriented.

USC UNIVERSIDADE DE SANTIAGO DE COMPOSTELA

3.1.2. PMA surface functionalization

To study the effect of the surface functionalization of the particles, an amphiphilic polymer (poly- [isobutylene-alt-maleic anhydride]-graft-dodecyl, PMA) was selected and a core-shell strategy based on the coating of the NMOFs with a dense shell of the selected polymer was followed.[163] This polymer has been used to stabilize NPs of different materials, shapes, and sizes.[196] PMA was already studied as a stabilizing and capping agent to ensure the stability of the loaded cargo inside NMOFs voids. In this case, a quantity of 300 monomers of PMA per nm^2 of Zr NMOFs was optimized to achieve a homogeneous coating of the surface in all cases, whereas for ZIF-8 an average of 600 monomers per nm^2 of NMOFs were employed.

After the functionalization and redispersion in water, the purified NMOFs (UiO-67@PMA, NU-1000@PMA, PCN-222@PMA and ZIF-8@PMA), did not present any significant changes in the morphology nor the d_h measured by SEM and DLS, respectively (Figure 3.1.3-3.1.6, Table 3.1.1). UV-Vis spectra also confirm there are no differences among the samples before and after the functionalization (Figure 3.1.7.a-d), whereas ζ-potential values revealed a clear decrease in the surface charge in all cases, which changed from positive values in all cases to highly negative results (between -20 and -40 mV) due to the free carboxylic acid groups following the hydrolysis of remaining maleic acid rings of PMA (Figure 3.1.7.e-h, Table 3.1.1.). The reduction in the ζ potential values indicates the successful PMA functionalization of the NMOFs particles.

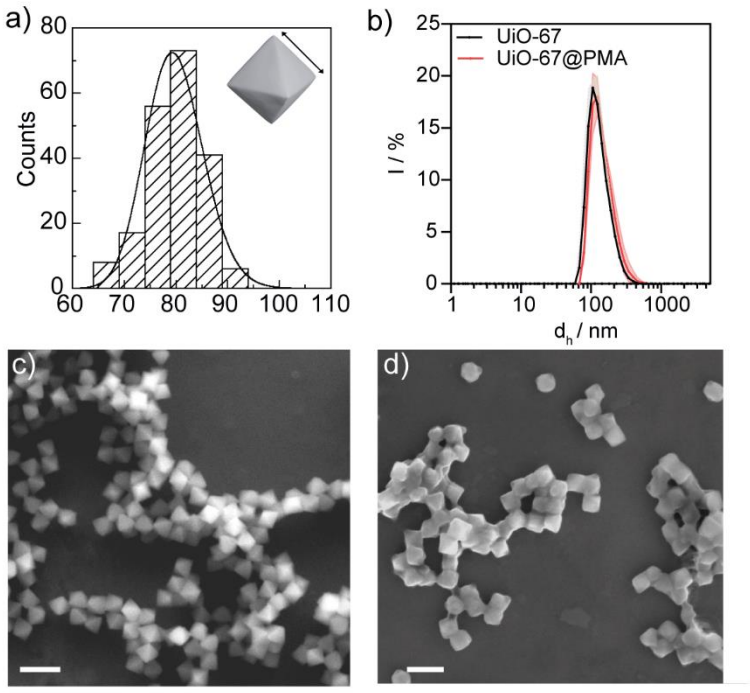

Figure 3.1.3. a) Histogram distribution of the UiO-67 hydrodynamic diameter based on microscopy images, b) Number distribution of the d_h measured by DLS, c) FE-SEM images of the as synthetized UiO-67 and d) UiO-67@PMA. Scale bars 200 nm.

USC UNIVERSIDADE DE SANTIAGO DE COMPOSTELA

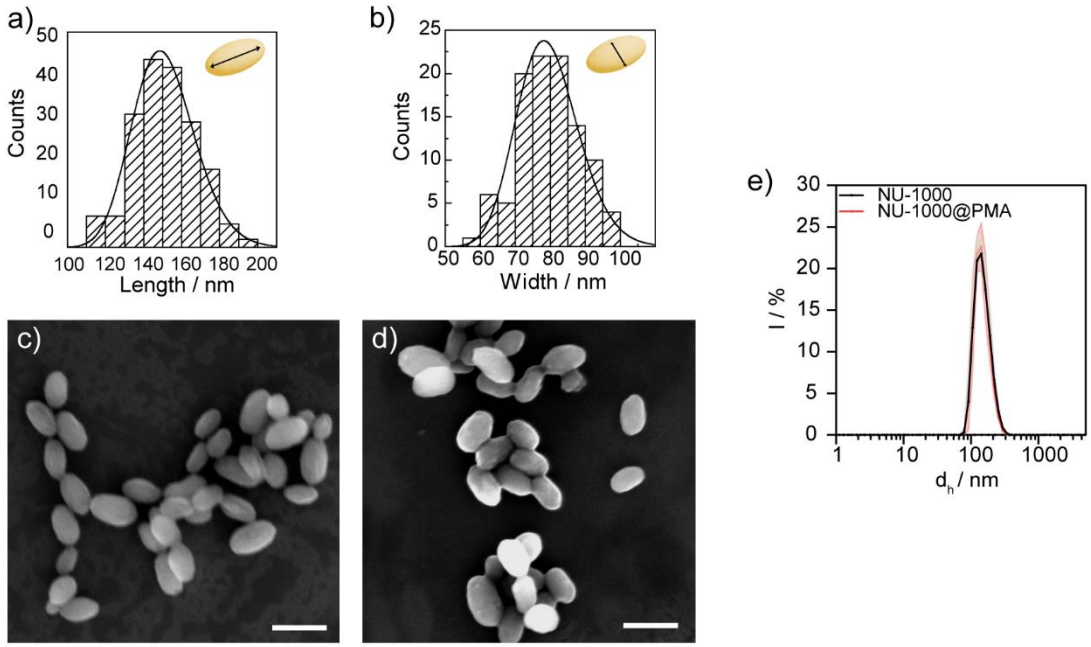

Figure 3.1.4. a) Histogram distribution of the NU-1000 a) length and b) width based on microscopy images, c) FE-SEM images of the as synthetized NU-1000 and d) NU-1000@PMA, e) Number distribution of the d_h measured by DLS. Scale bars 200 nm.

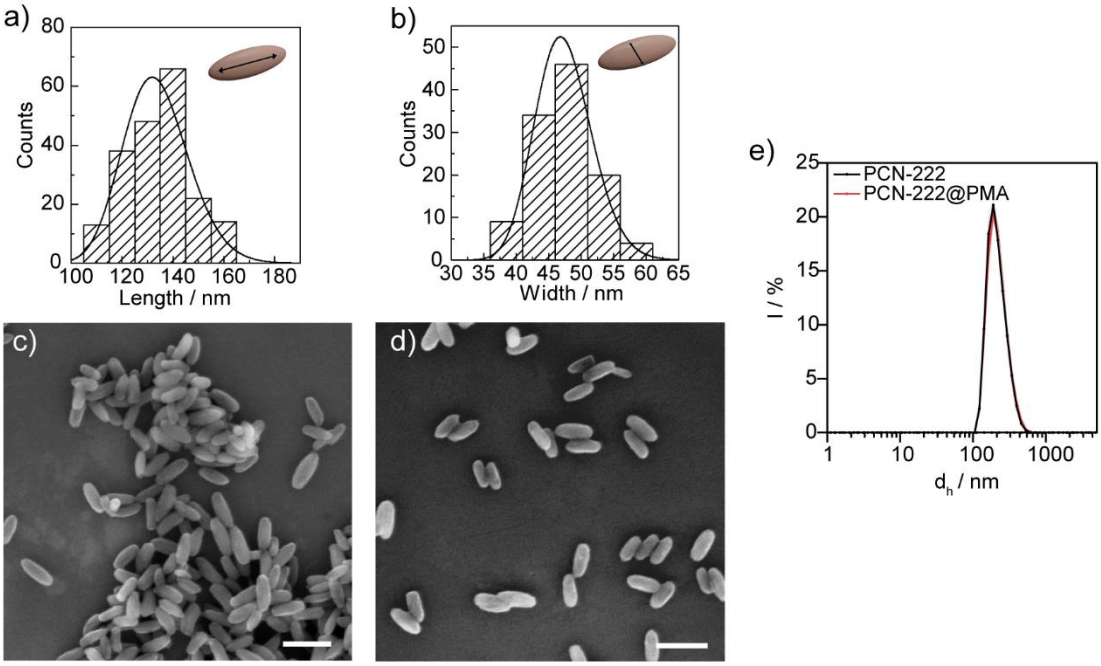

Figure 3.1.5. a) Histogram distribution of the PCN-222 a) length and b) width based on microscopy images, c) FE-SEM images of the as synthetized PCN-222 and d) PCN-222@PMA, e) Number distribution of the d_h measured by DLS. Scale bars 200 nm.

USC
UNIVERSIDADE DE SANTIAGO DE COMPOSTELA

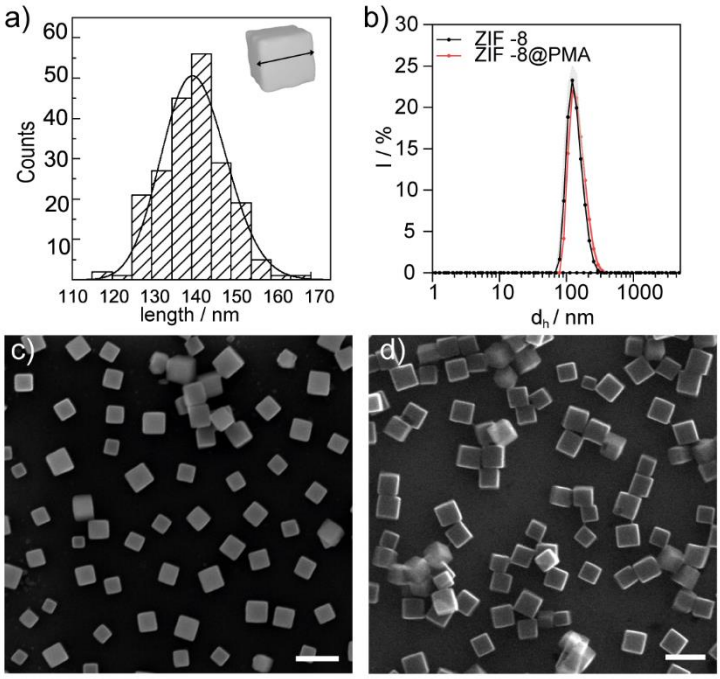

Figure 3.1.6. a) Histogram distribution of the ZIF-8 hydrodynamic diameter based on microscopy images, b) Number distribution of the d_h measured by DLS, c) FE-SEM images of the as synthetized ZIF-8 and d) ZIF-8@PMA. Scale bars 200 nm.

Table 3.1.1. DLS and Zeta potential results for all NMOFs without and with PMA

Sample	$d_{h,N}$ ± sd	$d_{h,I}$ ± sd	$d_{h,V}$ ± sd	PDI	ζ pot / mV
UiO-67	174 ± 7	255 ± 71	391 ± 25	0.17	10 ± 1
UiO-67@PMA	189 ± 18	275 ± 91	293 ± 41	0.14	-36 ± 1
NU-1000	150 ± 12	184 ± 8	181 ± 9	0.12	40 ± 1
NU-1000@PMA	199 ± 10	210 ± 9	211 ± 10	0.21	-22 ± 1
PCN-222	145 ± 10	250 ± 35	223 ± 33	0.20	17 ± 1
PCN-222@PMA	206 ± 8	261 ± 4	267 ± 5	0.16	-27 ± 1
ZIF-8	140 ± 6	170 ± 3	166 ± 1	0.04	35 ± 1
ZIF-8@PMA	154 ± 7	188 ± 4	187 ± 4	0.05	-30 ± 1

USC UNIVERSIDADE DE SANTIAGO DE COMPOSTELA

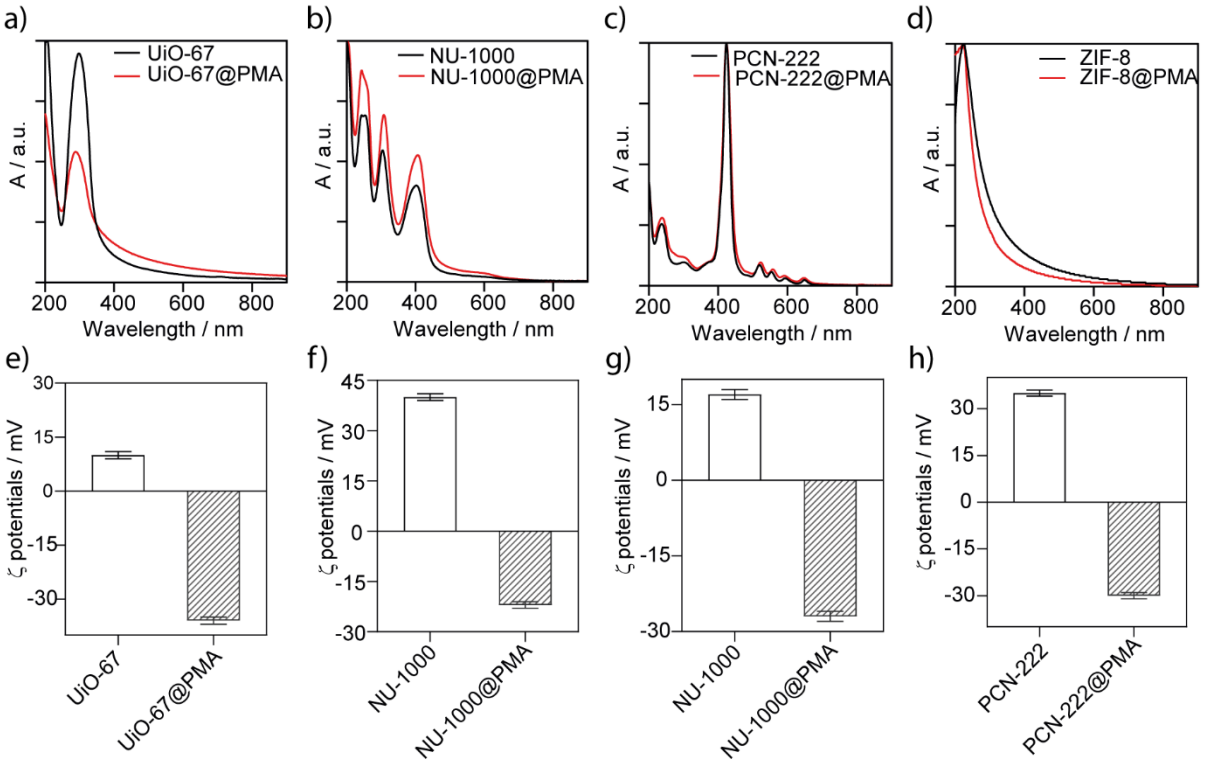

Figure 3.1.7. UV-Vis spectra of the synthetized NMOFs before and after the PMA functionalization a) UiO-67, b) NU-1000, c) PCN-222 and d) ZIF-8; ζ-potentials of the same particles e) UiO-67, f) NU-1000, g) PCN-222 and h) ZIF-8.

The crystallinity of the samples was also studied before and after the addition of the polymer. In order to make PXRD the Zr MOFs samples were activated with acetone for 5 days before performing the measurement. After the addition of PMA and redispersion in water, samples where freeze-dried before the analysis. All the samples exhibited the characteristic Bragg peaks of the corresponding bare MOFs, proving the functionalization with the polymer do not affect the crystalline structure (Figure 3.1.8.). These results indicate the importance of the described PMA coating procedure, as we have proved it can assess one of the main problems related to these MOFs for their use in biomedical applications, as the presence of the PMA provides the necessary stability in aqueous media both colloidal and structural. PXRD data for UiO-67@PMA samples placed in water show three main peaks at 2ϑ = 5.7º, 6.51º and 9.34º, corresponding to crystalline planes (111), (200) and (220), indicating the crystallinity of the NMOFs is unaffected in aqueous media due to the PMA protection. For NU-1000@PMA PXRD pattern, the four first peaks also correspond to the simulated pattern, at 2ϑ = 5.1º, 7.5º and 10.3º corresponding to the crystalline planes (020), (120) and (040), respectively, whereas in the case of PCN-222@PMA, the Bragg peaks at 2ϑ = 4.77º, 7.09º, 8.27º, 9.60º and 9.8º correspond to (020), (201), (400) and (421) planes. Again, these Zr NMOFs can maintain the crystallinity in water due to the polymer functionalization. On the other hand, for ZIF-8@PMA, the first six peaks at 7.31º, 10.35º, 12.70º, 14.75º, 16.51º and 18.09º coincide with the simulated patterns, corresponding to the crystalline planes (110), (200), (211), (220), (310) and (222), respectively. These results indicate the clear preservation of the crystalline structure after the samples are placed in water, proving the high stability of the PMA coated NMOFs.

USC DE SANTIAGO DE COMPOSTELA

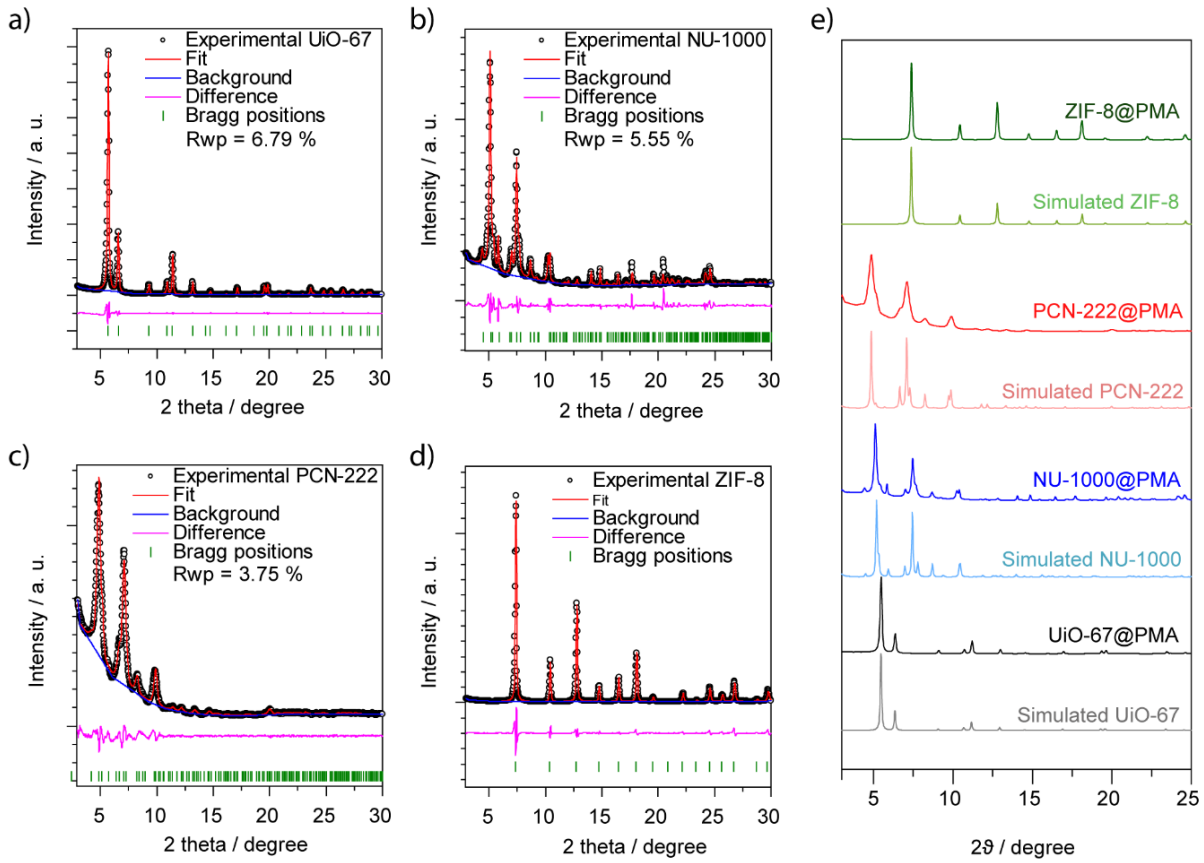

Figure 3.1.8. PXRD refinement of a) UiO-67, b) NU-1000, c) PCN-222 and d) ZIF-8, and e) obtained patterns of the samples with PMA compared to the simulated ones.

To study the thermal behavior of the NMOFs, thermogravimetric analysis (TGA) was performed under air (Figure 3.1.9.). All of them were stable up to 400°C. For UiO-67, NU-1000 and PCN-222 we can observe a final plateau representing the ZrO_2 residue left from the temperature treatment. The residual mass % for UiO-67 in this case is 35%, whereas for samples with PMA the inorganic % is reduced to 19%, indicating that a 16% of the total weight of the sample corresponds to the polymer. The presence of PMA is revealed by the higher weight loss before 400ºC, presented as a first mass loss (10 wt %) related to the PMA glass transition (150–250ºC) and a final loss (20 wt%) at around 250–350ºC. This behavior is repeated for the other MOFs. For NU-1000, MOFs show a residual mass of 26% and 9% for the samples without and with PMA, respectively. Therefore, the polymer % corresponds to 17% in this case, similar as the UiO-67. For PCN-222, non-coated MOFs presented an inorganic residue of 31% whereas the PMA-functionalized ones have a 7%, being this MOFs the one with higher percentage of polymer. For the ZIF-8, results are coherent with previous works.[197] The samples without PMA presented a pronounced weight loss (60-70 wt%) at around 400ºC associated with the entire combustion of 2-methylimidazole and the formation of inorganic residue of ZnO. The PMA samples follow the same tendency as the other MOFs, and the polymer weight loss is followed by the combustion of the 2-methylimidazole, as in non-PMA samples (~400ºC). Additionally, TGA results show missing-linker defects in the framework as shown in Figure 3.1.8. or UiO-67, the experimental results indicated a lower weight decomposition value

compared to the theoretical one, suggesting the existence of missing linker defects. Conversely, the theoretical 8-connected NU-1000 exhibited an excess of the linker. These variations could stem from various synthetic factors like the linker/cluster ratio, the used modulator, or the synthesis parameters as the temperature.[198] As for PCN-222, the reported TGA values matched the anticipated 8-connected Zr cluster, while for ZIF-8, the results were consistent with the expected Zn connectivity.

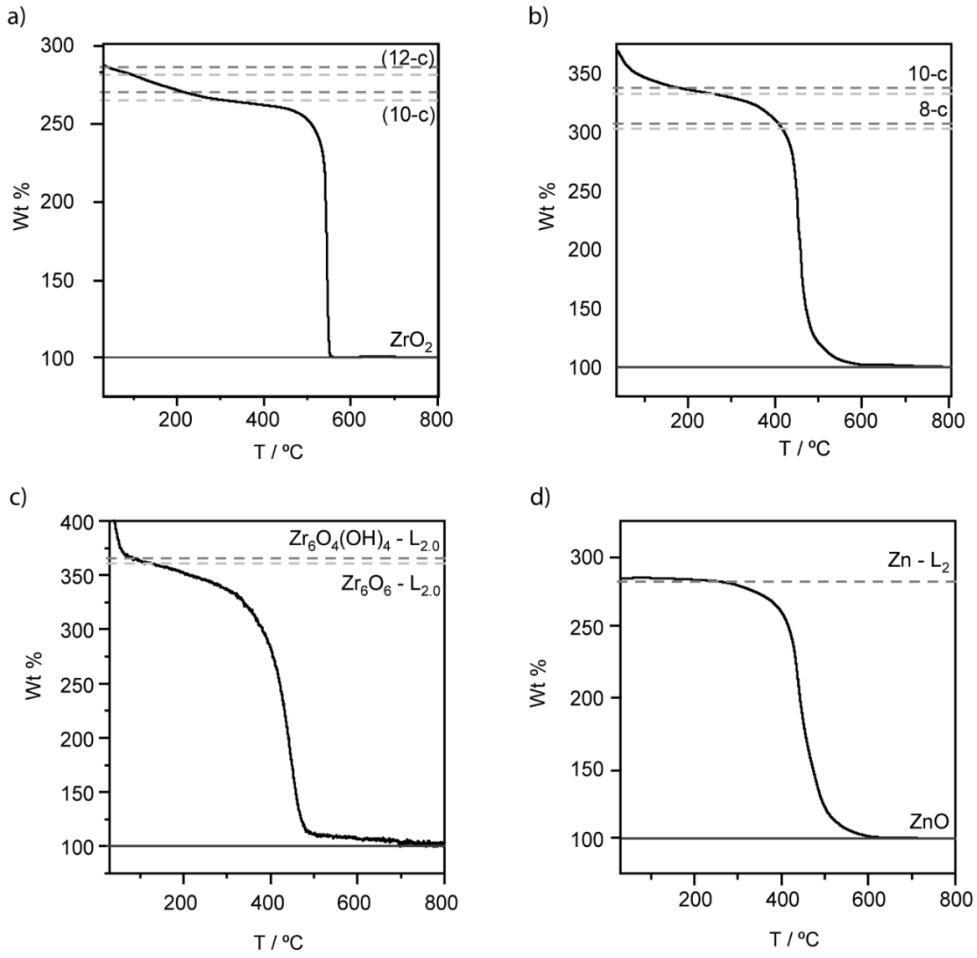

Figure 3.1.9. TGA measurements of the MOFs before and after the PMA coating a) UiO-67, b) NU-1000, c) PCN-222 and d) ZIF-8.

Colloidal stability in biological media is a key factor influencing the final fate of the particles. To analyze this property, different relevant biological media were selected such as water, complete cell media supplemented with serum (Dulbecco's Modified Eagle Medium (DMEM) with 10% (v/v) FBS), and phagolysosome simulated fluid (PSF, pH= 5) for 10 days using DLS (Figure 3.1.10.). As mentioned earlier, UiO-67 NMOFs showed no significant differences in d_h upon PMA coating, while a change in the ζ-potential value was observed from positive potential (10 ± 1) mV to negative, (-36 ± 1) mV, Stability assays showed an improved stability over time for the PMA-coated UiO-67 (Figure 3.1.10.a). This is especially relevant for cell media, in which a slight increment in size is observed due to the non-specific adsorption of proteins but size was kept unaltered for the analyzed time. Similarly, NU-1000 and PCN-222 present a high colloidal stability after functionalization, where the surface charges are reduced

from (40 ± 1) mV to (-22 ± 1) mV and (17 ± 1) mV to (-27 ± 1) mV, respectively. However, bare particles showed a tendency to aggregation specially in PSF and cell media, where after 6 h there is a clear increase in the measured particle size (Figure 3.1.10.b,c). On the other hand, for ZIF-8 (Figure 3.1.10.d) there is a decrease in the hydrodynamic diameter after 5 h both in cell media and PSF, which is a consequence of the poor stability and degradation of the structure in aqueous media and low pH environments.[197] After PMA coating, samples presented a great colloidal stability for 10 days in all the media.

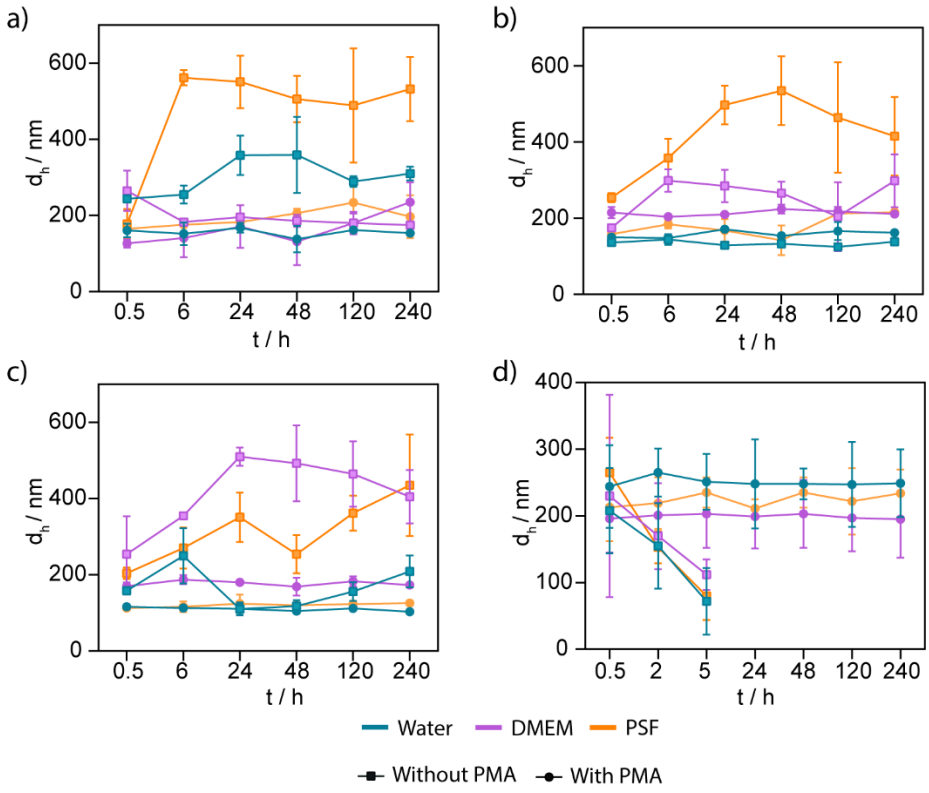

Figure 3.1.10. Colloidal stability of a) UiO-67, b) NU-1000, c) PCN-222 and d) ZIF-8 over time in water DMEM and PSF media, as determined by DLS. Experiments were carried out using n = 3. Error bars represent standard deviation.

SEM analyses were carried out to evaluate morphological changes (Figure 3.1.11.). Zr NMOFs are expected to degrade easily in the presence of phosphate groups (biological media) due to the competition between the phosphate and the COOH groups of the linkers to coordinate with the Zr, leading to a breakage of the structure. For this reason, PSF medium was selected to study the morphological changes of the NMOFs, as it simulates the biological environment after cell internalization of the particles. The Zr MOFs and ZIF-8 with and without PMA were placed in PSF for 7 days and then washed and prepared for SEM analysis. Images show no significant variations in the appearance of the structures after the 7 days. This contrasts with crystalline instability of the NMOFs, where only when the samples are coated with the polymer the crystal structure is preserved in aqueous media. On the other hand, as expected from DLS measurements, ZIF-8 structure was clearly degraded after 5 h (Figure 3.1.11.d), whereas the PMA coated ZIF-8 did not present any changes or degradation after 7 days (Figure 3.1.11.h).

USC UNIVERSIDADE DE SANTIAGO DE COMPOSTELA

To complement the stability tests, UiO-67 was specifically chosen to assess the release of the linker from the empty MOFs in water and PSF over different time intervals. Figure 3.1.12 illustrates the degradation patterns observed in both media at 0 h, 24 h, and 7 days. The findings demonstrate a higher degree of stability in PSF compared to water for the non-functionalized NMOF. This difference in structural stability can be attributed to the increased acidic character of the PSF medium, which is known to favor the stability of MOFs based on carboxylates (with a favored stability range around p_{ka}=3-5). However, the presence of PMA in both media significantly enhances stability. The polymer coating on the MOF surface acts as a protective barrier, effectively mitigating premature degradation in both solvents.

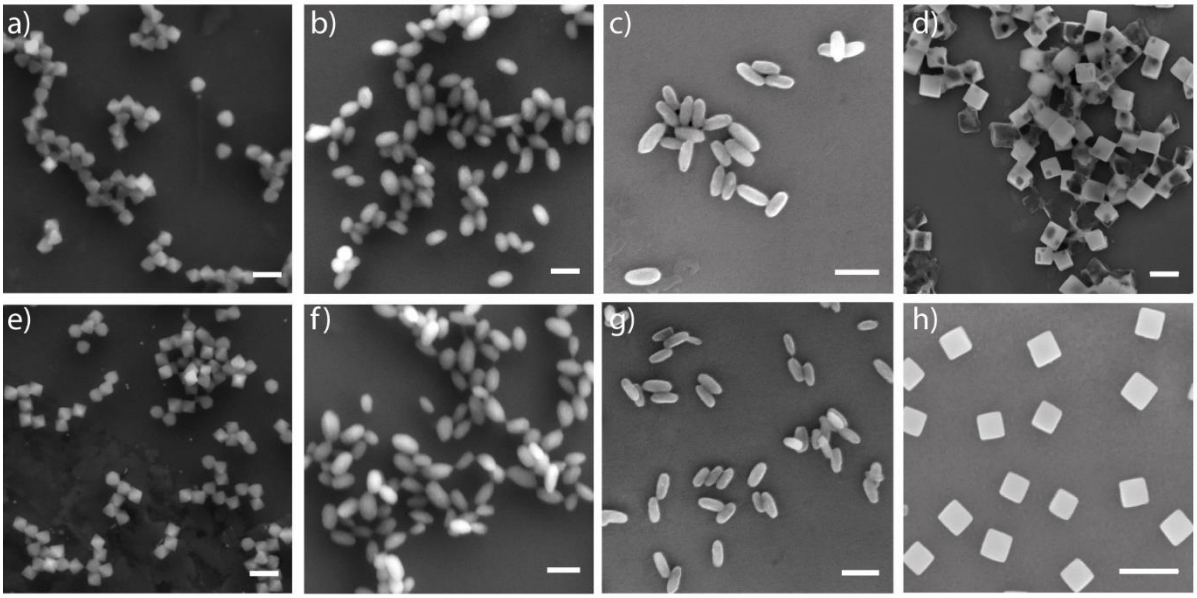

Figure 3.1.11. SEM images of the samples placed in PSF for 7 days: a) UiO-67, b) NU-1000 c) PCN-222 d) ZIF-8 (after 5h) and PMA coated samples after 7 days in PSF: e) UiO-67@PMA, f) NU-1000@PMA, g) PCN-222@PMA, h) ZIF-8@PMA.

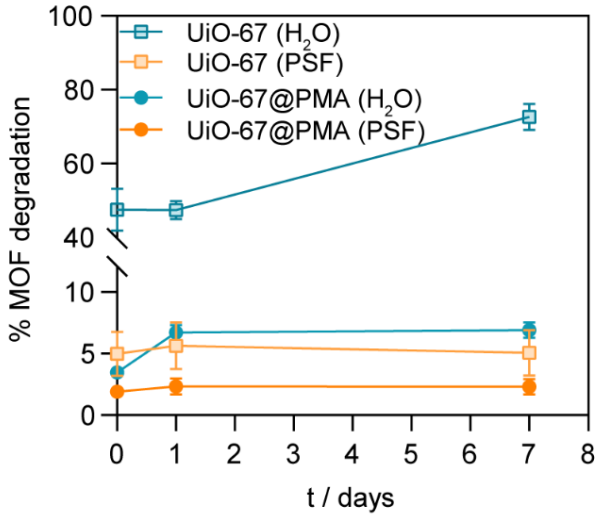

Figure 3.1.12. UiO-67 linker release for samples with and without PMA in water (Blue) and PSF (orange). Experiments were carried out using n = 3. Error bars represent standard deviation.

3.1.3. Cresyl violet cargo encapsulation

After proving the efficiency and generality of the PMA surface functionalization approach, the encapsulation and loading capabilities of each MOF was studied, as well as the combination with the PMA coating.

For the initial loading capability analysis, the fluorescent molecule Cresyl Violet (CV) was employed. CV is a well-known fluorescent dye often used as a lysosomal marker in molecular biology, chosen for its favorable properties compared to other probes.[199] The encapsulation of CV entailed immersing the particles in a CV aqueous solution for one day under stirring, utilizing a weight ratio of 1:3 MOF:CV (post-synthesis encapsulation) as detailed in the chapter 2 (Figure 3.1.13.). For UiO-67, wherein the length of the CV molecule (1.2 nm) surpasses the pore aperture of the MOF (~8 Å), loading was performed at 60ºC, following the protocol outlined by Morabito et al.[59] This elevated temperature promotes the expansion of the MOF's linker pore apertures, facilitating the entry of the selected cargo into the structure's voids. Conversely, for PCN-222 and NU-1000, encapsulation was conducted at room temperature owing to their larger window apertures, enabling direct immersion of CV.[173] The harsh synthesis conditions of these NMOFs render in-situ encapsulation of certain biomolecules unsuitable. Nonetheless, the selected post-synthesis loading method proves highly efficient and water-compatible, offering mild loading conditions for various biomolecules such as proteins or nucleic acids.

In contrast, the encapsulation of CV within the pores of ZIF-8 (ZIF-8(CV)) was achieved by incorporating the dye during synthesis (see section 2). The resulting NMOFs exhibited morphology and size similar to bare ZIF-8, with an average diameter (d_h) of (137 ± 7) nm (Figure 3.1.13.d). This in-situ encapsulation method enhances the binding between the loaded molecule and the MOF, thereby minimizing CV leaching. Furthermore, it enables the encapsulation of molecules larger than the pore aperture, expanding its applicability. Considering ZIF-8's pore aperture of 3.4 Å and CV's length of 1.2 nm, this approach proves suitable for accommodating guest biomolecules like enzymes or large drugs for various bioapplications. However, its applicability is subject to specific MOF properties; for instance, certain Zr MOFs may have synthetic parameters (e.g., temperature, pH, ligand/metal precursors) that could compromise the activity of selected active molecules. ZIF-8, in particular, is favored for biomolecule encapsulation due to its biocompatible synthesis conditions (room temperature, mild pH).[165] The CV-loaded MOFs were further functionalized with PMA following the previous protocol developed for bare MOFs. After purification, particles did not present any significant changes in the hydrodynamic diameter or the morphology as confirmed by DLS and SEM images, respectively (Figure 3.1.13.e-h, Table 3.1.2.). UV-Vis spectra analysis reveal consistent profiles between pre- and post-functionalized samples. Notably, a clear peak around $\lambda \approx 590$ nm, characteristic of CV, appears in all samples, albeit with varying intensity levels (Figure 3.1.14.a-d). The observed variation can be attributed to losses of CV during the coating processes.

ζ-potential measurements of the CV-unloaded and -loaded MOFs exhibit an increase possibly attributed to acetate ions from CV binding to the surface (Figure 3.1.14.e-h, Table 3.1.2.). A more significant change is observed when the loaded NMOFs are coated with PMA, resulting in negative ζ-potential in all cases (ranging from -17 to -26 mV), indicative of free

carboxylic acid groups following the hydrolysis of remaining maleic acid rings. To further corroborate the size of the particles and measure the concentration (particles·mL^{-1}), NTA measurements were carried (Figure 3.1.15.). In Figure 3.1.15.d, NTA results for ZIF-8(CV) are not presented due to the instability of this NMOFs in aqueous media that leads to its degradation when placed in water to perform the measurements.

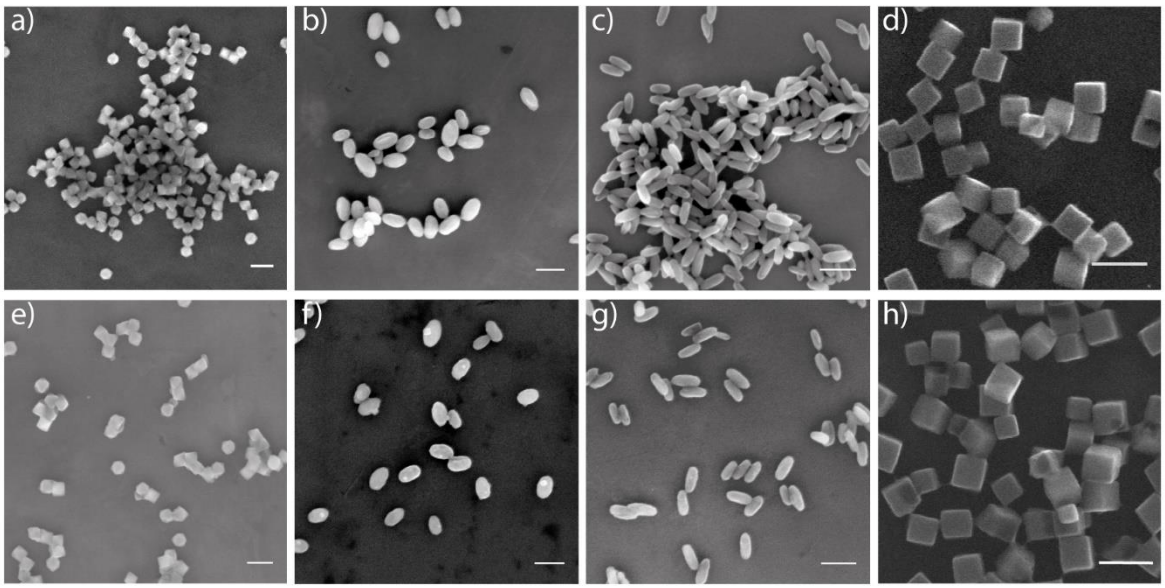

Figure 3.1.13. SEM images of the samples after the CV encapsulation a) UiO-67(CV), b) NU-1000(CV) c) PCN-222(CV) d) ZIF-8(CV) and after the consecutive PMA functionalization: e) UiO-67(CV)@PMA, f) NU-1000(CV)@PMA, g) PCN-222(CV)@PMA, h) ZIF-8(CV)@PMA. Scale bars of 200 nm.

Table 3.1.2. Number and intensity distribution of the d_h, PDI and Zeta potentials of the samples with CV and PMA.

Sample	$d_{h,N}$ ± sd	$d_{h,I}$ ± sd	PDI	ζ pot / mV
UiO-67(CV)	196 ± 34	285 ± 71	0.17 ± 0.07	15 ± 1
UiO-67(CV)@PMA	161 ± 15	275 ± 91	0.14 ± 0.09	-24 ± 1
NU-1000(CV)	136 ± 6	158 ± 24	0.30 ± 0.03	26 ± 1
NU-1000(CV)@PMA	160 ± 12	216 ± 8	0.12 ± 0.06	-26 ± 1
PCN-222(CV)	158 ± 2	250 ± 56	0.18 ± 0.01	27 ± 1
PCN-222(CV)@PMA	132 ± 13	180 ± 8	0.11 ± 0.01	-17 ± 3
ZIF-8(CV)	138 ± 3	163 ± 2	0.04 ± 0.04	28 ± 1
ZIF-8(CV)@PMA	158 ± 6	194 ± 7	0.05 ± 0.03	-23 ± 1

USC UNIVERSIDADE DE SANTIAGO DE COMPOSTELA

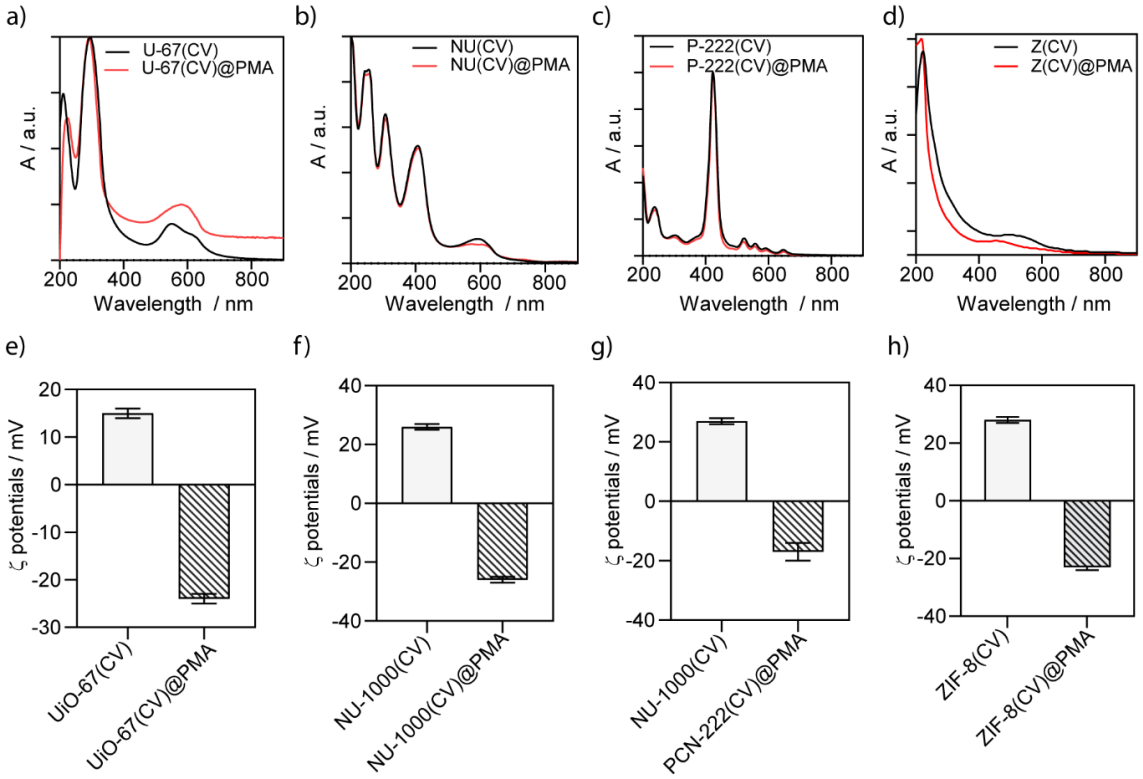

Figure 3.1.14. UV-Vis spectra of the loaded and PMA coated a) UiO-67, b) NU-1000, c) PCN-222, d) ZIF-8; ζ potentials after the CV loading and the PMA coating of e) UiO-67, f) NU-1000, g) PCN-222 and h) ZIF-8. Experiments were carried out using n = 3. Error bars represent standard deviation.

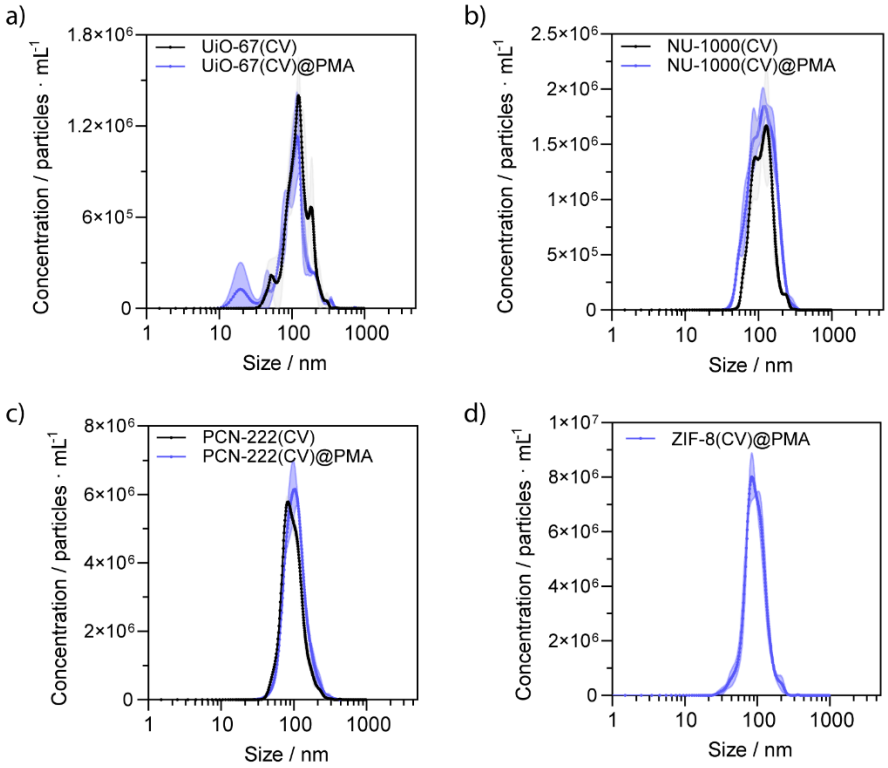

Figure 3.1.15. NTA measurements of the NMOFs concentration after the CV encapsulation and further polymer coating.

The quantification of CV encapsulation was performed by measuring fluorescence in the supernatants (SN) after washing steps. CV encapsulated per MOF was calculated by comparing SN fluorescence to calibration curves in MeOH and water. UiO-67 results showed 6.68 x 10^5 ± 2.34 × 10^2 CV/UiO-67 (21 wt%) after the CV addition, whereas it decreased to 18 wt% (CV/UiO-67) after the polymer coating. On the other hand, NU-1000 and PCN-222 presented CV loadings of 18 wt% and 14 wt%, respectively, while the polymer addition reduced these quantities to 8 wt% and 6 wt%, respectively. ZIF-8 presented an average of 1.73 × 10^5 ± 4.34 ×10^2 CV/ZIF-8 (11 wt%), whereas after the PMA-coating, this quantity decreased to 8 wt% (CV/ZIF-8). This reduction implies that the polymer could infiltrate the pores, displacing the CV, consistent with findings from previous studies.[200]

Regarding the design of efficient DDSs, it is critical to develop new nanosystems capable of retaining the selected drug until it reaches its target. The chosen coating is anticipated to block the pores of the structure, thereby mitigating cargo leakage over time. To validate this, the stability of the loaded CV was assessed along various durations, up to 10 days before and after the addition of PMA. Different biologically relevant media, including water, PSF, complete DMEM, and PBS, were employed for this investigation. In this case, CV encapsulated per MOF was calculated by comparing SN fluorescence to calibration curves in the selected media (Figure 3.1.16.).

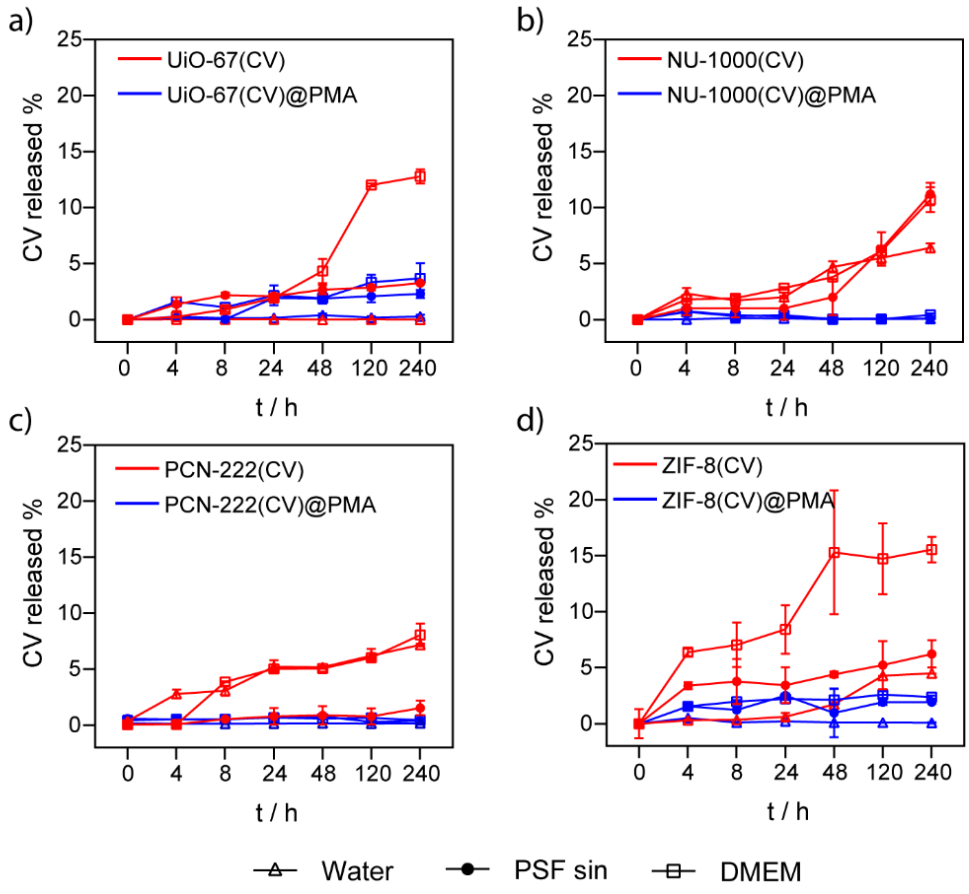

Figure 3.1.16. %CV released with respect to the loaded quantity measured by fluorescent measurements of the SN both in PSF (round colored dots) and cell media (empty squares) up to 10 days for e) ZIF-8 and f) UiO-67 with and without PMA. Experiments were carried out using n = 3. Error bars represent standard deviation.

For non-coated UiO-67, the CV encapsulated was stable in MilliQ water with no significant release in any case (Figure 3.1.16.a). However, for PSF, DMEM and PBS, after 10 days there is a notable release over 7% of the encapsulated CV, especially in DMEM, where it goes up to 13%. The PMA-coated nanoparticles, however, showed reduced leaking in all cases, with notable effect in DMEM (up to 3%) in comparison to the non-coated NPs. Results for NU-1000 and PCN-222 exhibit a similar trend. While the initial release of non-coated particles is relatively low, the addition of different coatings significantly enhances the stability of CV (Figure 3.1.16.b-c). The results for ZIF-8 revealed a significant reduction in CV release following PMA coating, particularly evident in PSF and DMEM. In these media, values decreased from 5% to 2% and from 13% to 2% of the total loaded CV, respectively (Figure 3.1.16.d). This decrease can be attributed to the low stability of ZIF-8 in aqueous media, leading to structural degradation and subsequent cargo release. Hence, PMA coating emerges as an effective strategy for enhancing cargo stability within the structure, resulting in significantly reduced release. These findings demonstrate that PMA not only enhances nanoparticle stability but also effectively covers the pores of the NMOF structure, minimizing cargo leakage.

ZIF-8 and UiO-67 were selected as the two representative MOFs for further functionalization studies. Therefore, the following characterization will mainly focus on these two NMOFs.

The adsorption capacities of the ZIF-8 and UiO-67 were assessed through N_2 adsorption isotherms, as illustrated in Figure 3.1.17. Figure 3.1.17.a shows the adsorption isotherm of ZIF-8 NMOFs. The Type I isotherm shape is preserved post-loading with CV, although with reduced uptake, decreasing from 413 $cm^3 \cdot g^{-1}$ before loading to 375 $cm^3 \cdot g^{-1}$ after the loading (at 0.8 P/P_0) (Table 3.1.3.). Previous investigations have revealed the inherent flexibility of ZIF-8 structures, allowing them to open their windows and accommodate larger molecules than their nominal window size, typically around 3.4 Å.[201,202] However, after the PMA coating it decreases to 82 $cm^3 \cdot g^{-1}$. This reduction can be attributed to the pores being filled with alkyl chains from PMA and the hindrance of N_2 diffusion into the pores caused by the coating, resulting in a significant loss of the microporous region.

On the other hand, UiO-67 exhibited a type I isotherm, demonstrating an uptake of 386 $cm^3\ g^{-1}$ at 0.8 P/P_0 (Figure 3.1.17.b). Upon loading with CV, there was a reduction to 248 $cm^3 \cdot g^{-1}$ attributed to pore occupation. PMA coating of the CV-loaded samples led to a further decrease in uptake to 39 $cm^3 \cdot g^{-1}$ (Table 3.1.3). This result indicates a loss of the porosity as PMA molecules get into the UiO-67 structure, causing a near-complete loss of micropores.

USC UNIVERSIDADE DE SANTIAGO DE COMPOSTELA

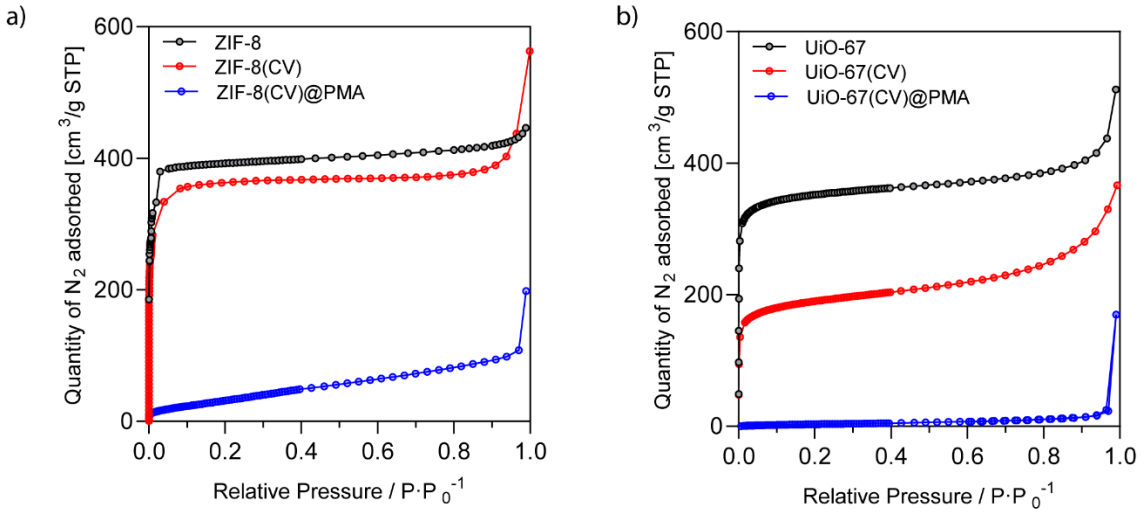

Figure 3.1.17. N_2 adsorption isotherms of a) ZIF-8 and b) UiO-67 samples.

Table 2.1.3. CV encapsulation quantification measured via fluorescence of the SN and TGA, and S_{BET} area calculated from BET analysis.

Sample	CV wt % (Fluo)	CV wt % (TGA)	S_{BET} ($m^2 \cdot g^{-1}$)
ZIF-8(CV)	11	9.5	1431
ZIF-8(CV)@PMA	8	4.9	72
UiO-67(CV)	21	23.9	721
UiO-67(CV)@PMA	18	3.9	39

PXRD was also studied for the ZIF-8 and UiO-67 NMOFs before and after the loading of CV and PMA (Figure 3.1.18.a-b). Results show the prevalence of the main Bragg peaks analogous to previous results after adding the PMA. Therefore, the selected method for the CV encapsulation do not affect the crystalline structure of the MOFs. Furthermore, the PMA coating of the CV loaded nanoparticles did not affect the crystallinity and provides structural stability in water.

TGA was further repeated with the CV encapsulated ZIF-8 and UiO-67 (Figure 3.1.18.c-d). The performed analysis was analogous as for the non-loaded MOFs. The different inorganic residues for the CV-loaded and PMA-coated NMOFs allowed to estimate the relative content of PMA and CV in the samples (See chapter 2, Table 3.1.4-3.1.5.). These findings are consistent with the data from CV fluorescence measurements. In the case of ZIF-8(CV), the TGA-derived value of 9.5 wt% for CV closely aligns with the 11 wt% determined through fluorescence. Regarding UiO-67(CV), the TGA analysis now yields a percentage of 23.9 wt%, compared to the previously obtained 21 wt%.

USC
UNIVERSIDADE DE SANTIAGO DE COMPOSTELA

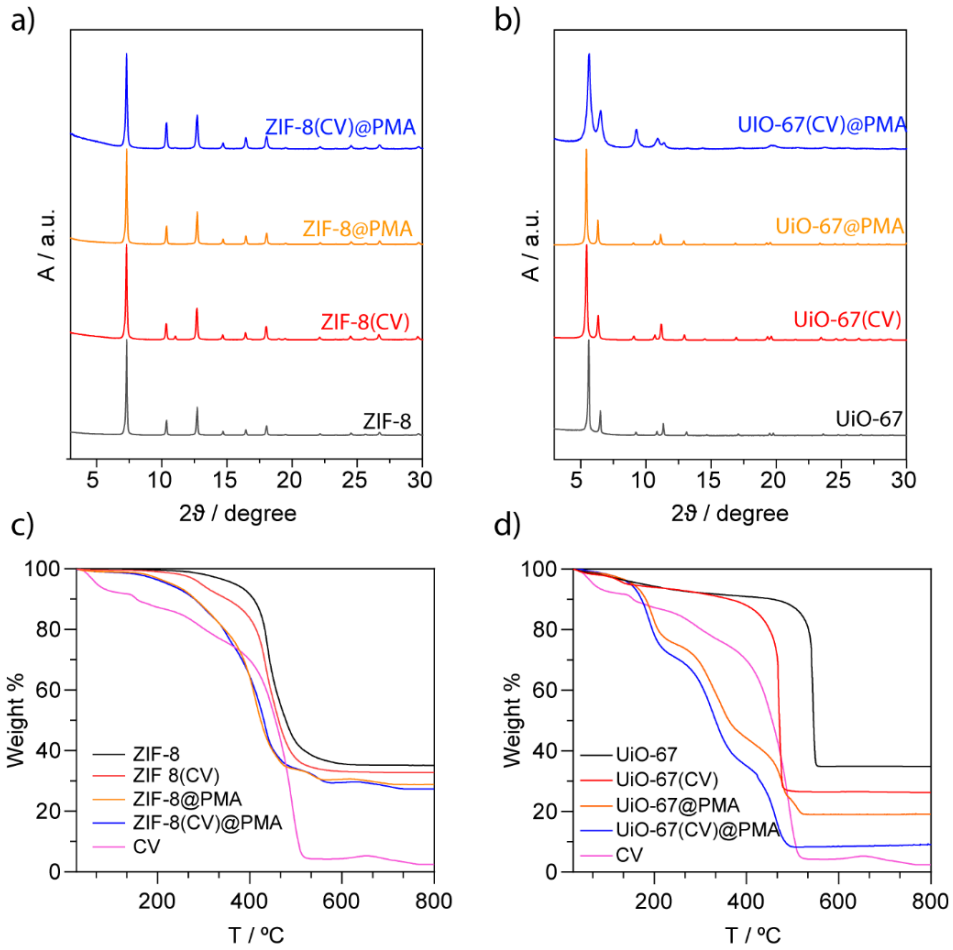

Figure 3.1.18. PXRD diffraction patterns of a) ZIF-8 and b) UiO-67 samples and the corresponding TGA measurements of c) ZIF-8 and d) UiO-67 before and after the CV loading and PMA functionalization.

Table 3.1.4. TGA Measurements of ZIF-8 NMOFs

	% Inorganic	% Organic	wt % (CV)	wt % (PMA)
ZIF-8	35.2	64.8	n/a	n/a
ZIF-8@PMA	28.8	71.2	n/a	12.9
ZIF-8(CV)	30.38	69.62	9.5	n/a
ZIF-8(CV)@PMA	25.38	74.62	-	-
CV	2.42	97.58	n/a	n/a

USC UNIVERSIDADE DE SANTIAGO DE COMPOSTELA

Table 3.1.5. TGA Measurements of UiO-67 NMOFs

	% Inorganic	% Organic	wt % (CV)	wt % (PMA)
UiO-67	34.80	65.20	n/a	n/a
UiO-67@PMA	19.10	80.90	n/a	36.5
UiO-67(CV)	23.89	76.11	23.9	n/a
UiO-67(CV)@PMA	6.64	93.36	-	-
CV	2.42	97.58	n/a	n/a

Next, the interaction of all the selected NMOFs with cells was evaluated in 2D cell cultures of A549 adenocarcinoma cells. The biocompatibility was assessed by determining the cellular metabolic activity using a 3-[4,5-dimethylthiazol-2-yl]-2,5-diphenyltetrazolium bromide (MTT) assay. This study confirmed the high viability related to the NMOFs at different concentrations. Values of up to 100 pM in all cases were used, as calculated from NTA, corresponding to about 20-40 $\mu g \cdot mL^{-1}$ of Zr for UiO-67, NU-1000 and PCN-222 and 40 $\mu g \cdot mL^{-1}$ of Zn for ZIF-8, as calculated using ICP-OES. Figure 3.1.19. show the toxicity results after 24 h on incubation for each MOF.

Non-loaded UiO-67, NU-1000 and PCN-222 showed no significant toxicity at any concentration after 24 h of incubation, related to the high biocompatibility of these Zr MOFs.[173] A significant increase in toxicity is observed in CV-loaded UiO-67 and ZIF-8 samples prior to the introduction of PMA, particularly at concentrations exceeding 10 pM. This increase in toxicity is attributed to the leakage of CV associated with these MOFs, as evidenced in previous CV stability tests in cell media and the related toxicity of the CV (Figure 3.1.19.e). However, post-functionalization with PMA demonstrates a notable enhancement in viability, evidencing its efficacy in impeding cargo release. In contrast, both NU-1000 and PCN-222 consistently exhibit high viability across all conditions, owing to their minimal cargo release properties.

This confirms that the selected Zr MOFs and ZIF-8 exhibit no toxicity at concentrations up to 100 pM after PMA addition. Therefore, the selected polymer for surface functionalization of NMOFs demonstrates remarkable efficacy in retaining loaded cargo, effectively mitigating any potential leakage. These results highlight the considerable promise of these nanosystems as highly effective DDSs.

USC UNIVERSIDADE DE SANTIAGO DE COMPOSTELA

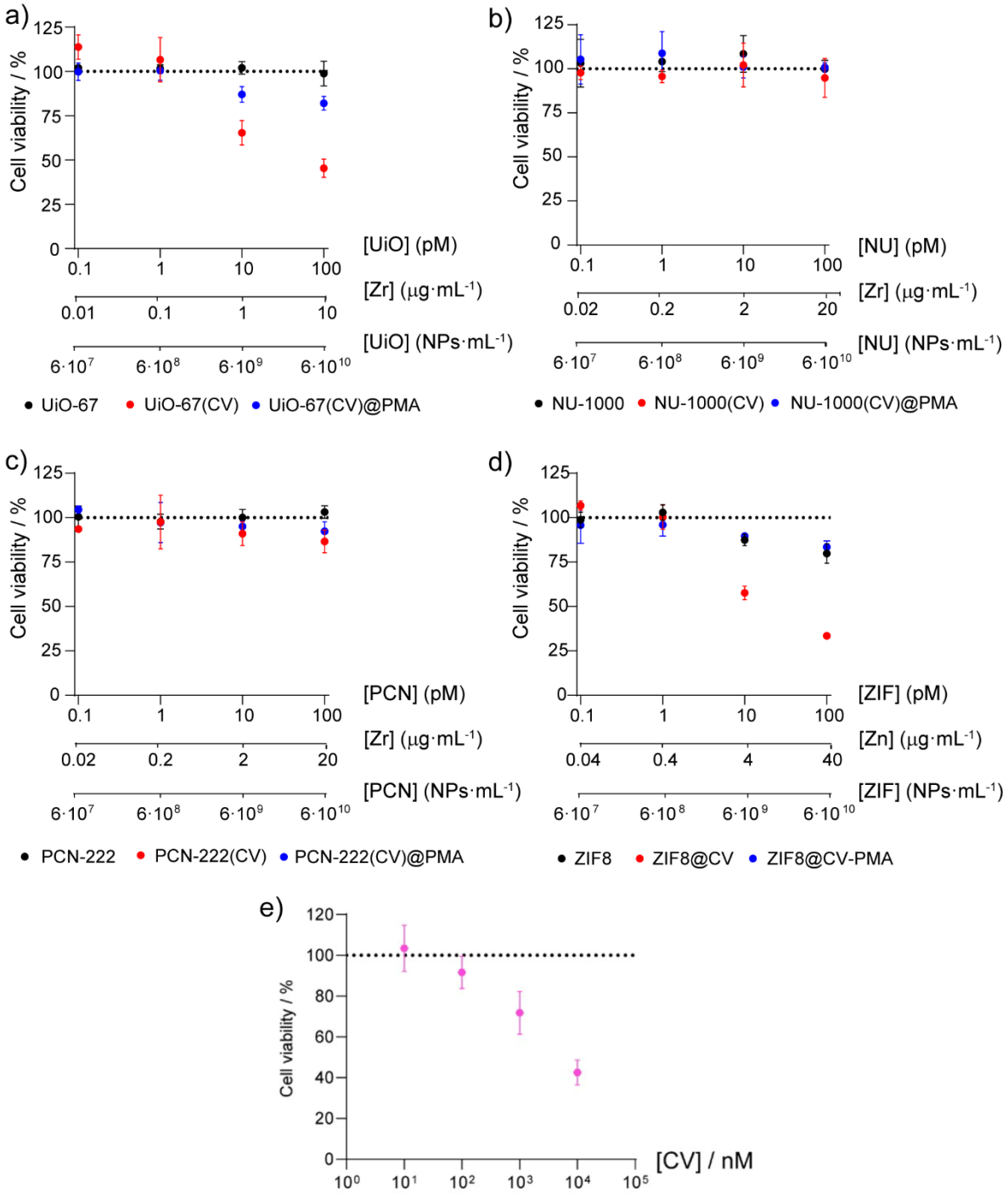

Figure 3.1.19. Cell viability of A549 cells incubated with a) UiO-67, b) NU-1000, c) PCN-222, d) ZIF-8 nanoparticles and e) free CV for 24 h, assessed by MTT assay. Experiments were carried out using n = 3. Error bars represent standard deviation.

To further demonstrate the polymer's efficacy in retaining cargo and reducing CV release to enhance cell viability, toxicity studies were conducted on UiO-67 (as a model) loaded with CV, with and without PMA. Two concentrations (10 and 100 pM) of particles were incubated for three different durations (24, 48, and 120 h). Microscopy analysis of cells after 120 h (Figure 3.1.20.) revealed a significant decrease in cell population due to CV-induced cell death in the

USC DE SANTIAGO DE COMPOSTELA

uncoated structures. Conversely, PMA-coated particles showed comparable cell growth to the control, suggesting no associated toxicity even at high exposure durations.

Furthermore, MTT assay was employed to quantify toxicity at the three different time points. As depicted in Figure 3.1.21., cell viability significantly decreased when incubated with non-coated NMOFs, whereas viability remained above 80% in the coated particles even after 5 days.

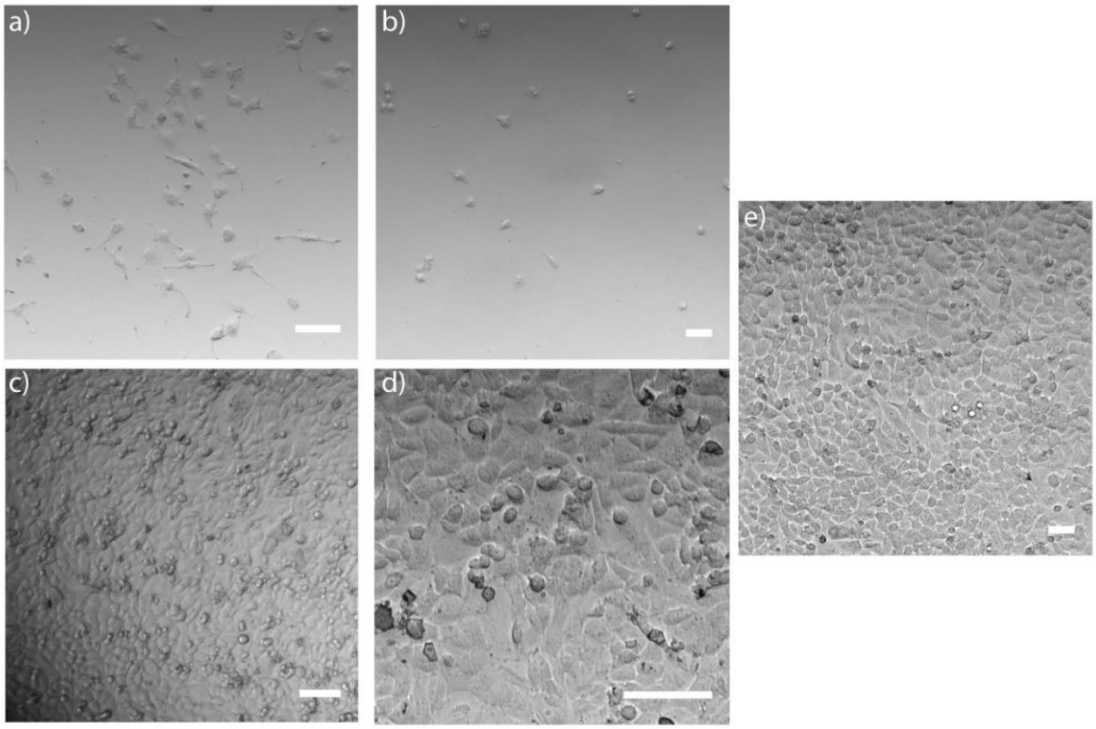

Figure 3.1.20. Microscopy images of A459 cells incubated for 5 days with a) UiO-67(CV) 10 pM, b) UiO-67(CV) 100 pM, c) UiO-67(CV)@PMA 10 pM and d) UiO-67(CV)@PMA 100 pM and e) Control cells.

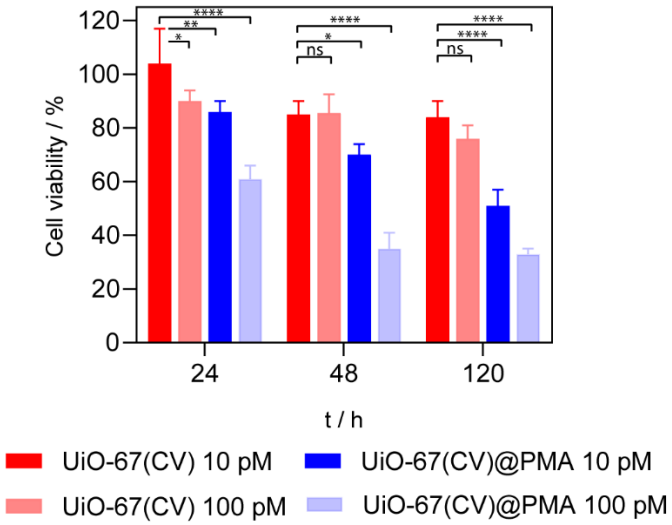

Figure 3.1.21. Cell viability of A459 cells incubated with UiO-67(CV) and UiO-67(CV)@PMA by MTT assay.

USC UNIVERSIDADE DE SANTIAGO DE COMPOSTELA

3.1.4. Click chemistry-based surface functionalization.

As previously discussed, the selectivity and targeting capabilities are crucial factors in the design of DDSs. While the stability issues in aqueous media were already addressed for the proposed NMOFs, these systems must be further modified to impart affinity towards specific targets. In the last part of this chapter, the covalent addition of directionality to ZIF-8 and UiO-67 NMOFs was explored through the incorporation of DBCO molecules into the PMA, which can react via click chemistry with various selected azide-modified molecules (Figure 3.1.22.).

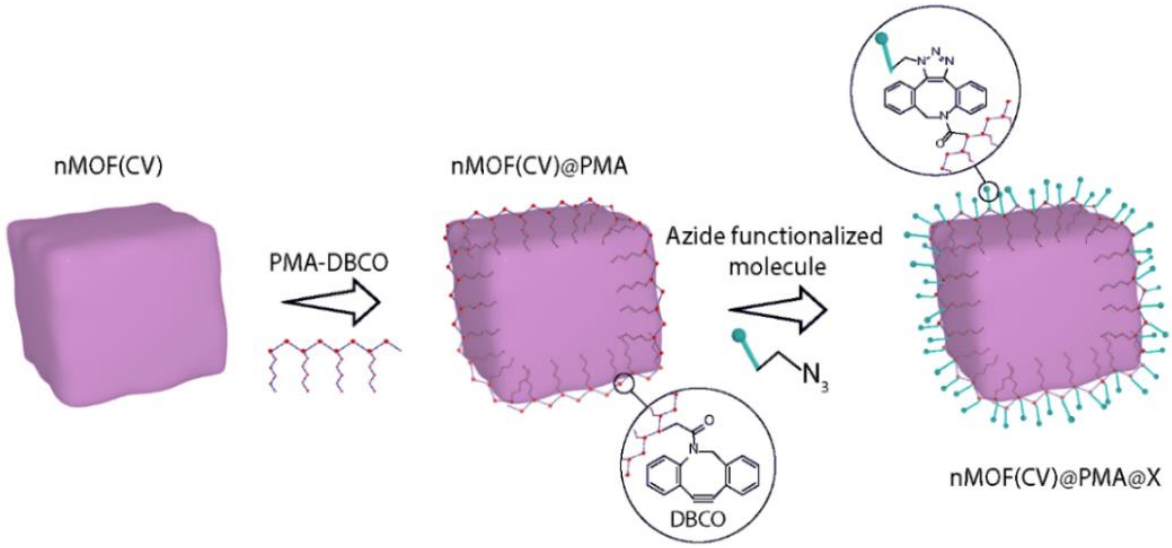

Figure 3.1.22. Schematic representation of the click chemistry functionalization.

The investigation was initialized with PEG due to its widespread application in surface shielding of nanomaterials. Its ability to hinder rapid cellular uptake by the mononuclear phagocyte system (MPS) ensures prolonged blood circulation. Specifically, methoxy PEG-azide (MeO-PEG-N_3, Mn = 5 kDa) was utilized using a molar relation of 10000 PEG per NMOF, following optimization findings reported by Shunzhi Wang et al.[203] Next, based on previous studies for the coating of inorganic NPs,[204] an azide-modified Cell-Penetrating Peptide (CPP) was used is a molar relation of 4000 CPPs per NMOFs. The studied CPP is a DynPro (dynein-propelled), derived from the product of the E183L gene of the African swine fever virus (p54).[204] DynPro was specifically selected due to its potential utility in facilitating cellular uptake. The primary amine moieties of lysine residues were utilized for fluorescent labeling with 5-carboxytetramethylrhodamine (TAMRA). Lastly, the functionalization was studied with an azide-functionalized mannose, specifically targeting the A549 lung epithelial cancer cell line, which is known to overexpress the MR.[205] In this case, a molar relation of 17000 mannoses per NMOFs was employed.

Additionally, beyond the CV-loaded nanoparticles, this approach was corroborated with bare ZIF-8 NMOFs. To facilitate *in vitro* experiments, it was essential to label the samples with fluorescence. For this purpose, the fluorescent molecule Cy5-N_3 was added to the particles in a molar relation of 1000 Cy5 per NMOF. This dye is modified with an azide group, allowing for its attachment to the surface of the NMOFs using a procedure analogous to the previous click chemistry reactions.

USC DE COMPOSTELA

In a typical experiment, the selected ligands (see Chapter 2) were reacted with the nanoparticles in water for 30 min at 37ªC and washed three times in water. The chosen quantities were determined based on preliminary results aimed at achieving homogeneous coatings and comparable final fluorescence intensities, facilitating subsequent comparative analysis. Following functionalization and redispersion in water, the hydrodynamic diameter measured using DLS and NTA in all cases remained consistent with the original NMOFs (Figure 3.1.23, Figure 3.1.24, Table 3.1.6-3.1.8). Changes in ζ-potential values indicated successful particle functionalization, with a notable reduction observed in the absolute value of the initial surface charge. This reduction can be attributed to the chosen molecules being either neutral (e.g., PEG and Mannose) or positively charged (e.g., CPP or Cy5) (Figure 3.1.23.c-d).

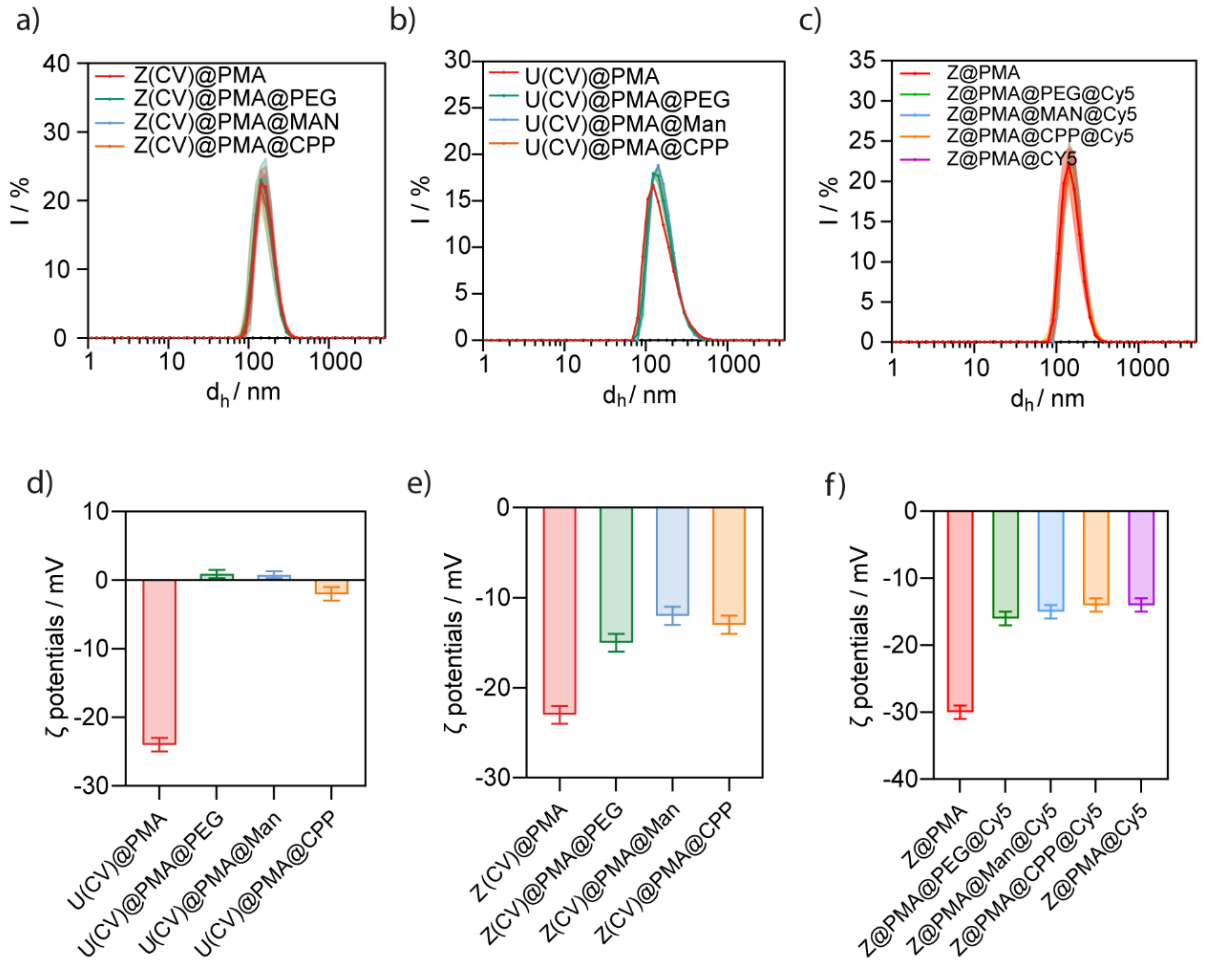

Figure 3.1.23. Sample characterization after the click-chemistry based functionalization of the surface using DLS for a) CV loaded ZIF-8, b) UiO-67, c) non-CV loaded ZIF-8 samples, and ζ potential measurements for d) CV loaded ZIF-8, e) UiO-67, f) non-CV loaded ZIF-8.

USC UNIVERSIDADE DE SANTIAGO DE COMPOSTELA

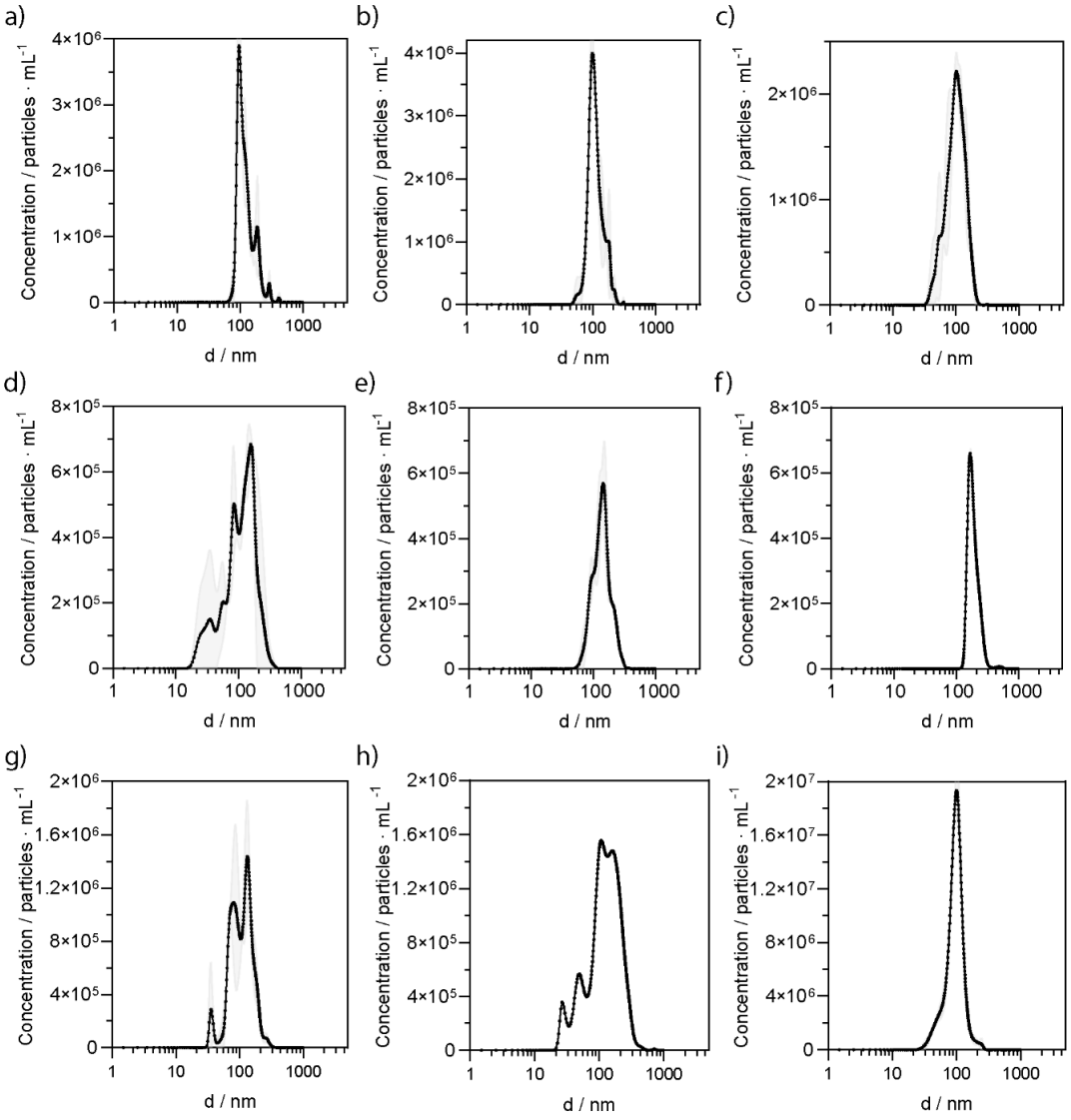

Figure 3.1.24. NTA measurements for a) ZIF-8(CV)@PMA b) ZIF-8(CV)@PMA@PEG, c) ZIF-8(CV)@PMA@Man, d) ZIF-8(CV)@PMA@CPP, e) UiO-67(CV), f) UiO-67(CV)@PMA, g) UiO-67(CV)@PMA@PEG, h) UiO-67(CV)@PMA@Man, i) UiO-67(CV)@PMA@PEG.

Table 3.1.6. DLS and ζ potential results for ZIF-8(CV) samples.

Sample	$d_{h,N}$ ± sd	$d_{h,I}$ ± sd	$d_{h,V}$ ± sd	PDI	ζ pot / mV
ZIF-8(CV)	138 ± 3	166 ± 1	163 ± 2	0.04	28 ± 1
ZIF-8(CV)@PMA	158 ± 6	195 ± 7	194 ± 7	0.05	-23 ± 1
ZIF-8(CV)@PMA @PEG	155 ± 8	184 ± 5	183 ± 5	0.05	-12 ± 1
ZIF-8(CV)@PMA@Man	154 ± 14	203 ± 19	202 ± 21	0.20	-15 ± 1
ZIF-8(CV)@PMA@CPP	162 ± 6	199 ± 10	198 ± 6	0.08	-23 ± 1

USC UNIVERSIDADE DE SANTIAGO DE COMPOSTELA

Table 3.1.7. DLS and ζ potential results for UiO-67(CV) samples.

Sample	$d_{h,N}$ ± sd	$d_{h,I}$ ± sd	$d_{h,V}$ ± sd	PDI	ζ pot / mV
UiO-67(CV)	196 ± 34	285 ± 71	263 ± 2	0.02	15 ± 1
UiO-67(CV)@PMA	162 ± 9	195 ± 7	194 ± 7	0.05	-24 ± 1
UiO-67(CV)@PMA@PEG	169 ± 7	196 ± 7	190 ± 5	0.02	-1 ± 1
UiO-67(CV)@PMA@Man	159 ± 10	187 ± 3	186 ± 4	0.05	-1 ± 1
UiO-67(CV)@PMA@CPP	163 ± 6	192 ± 10	192 ± 7	0.02	-2 ± 1

Table 3.1.8. DLS and ζ potential results for ZIF-8-Cy5 samples.

Sample	$d_{h,N}$ ± sd	$d_{h,I}$ ± sd	$d_{h,V}$ ± sd	PDI	ζ pot / mV
ZIF-8	140 ± 6	170 ± 3	166 ± 1	0.04	35 ± 1
ZIF-8@PMA	154 ± 7	188 ± 4	187 ± 4	0.05	-30 ± 1
ZIF-8@PMA@PEG-Cy5	160 ± 1	191 ± 6	190 ± 6	0.06	-16 ± 1
ZIF-8@PMA@Man-Cy5	167 ± 1	196 ± 5	196 ± 5	0.04	-15 ± 1
ZIF-8@PMA@CPP-Cy5	159 ± 10	196 ± 13	195 ± 13	0.10	-14 ± 1
ZIF-8@PMA@Cy5	165 ± 4	192 ± 6	192 ± 6	0.02	-14 ± 2

3.1.5. Cell studies

Subsequently, the interaction between the NMOFs and cells was assessed in 2D cell cultures of A549 lung adenocarcinoma cells. Having confirmed the low toxicity of the NMOFs, the cellular uptake of CV-loaded ZIF-8 and UiO-67 was investigated using fluorescence microscopy and flow cytometry.

Quantitative analysis of sample uptake was performed for CV loaded NMOFs using flow cytometry. As depicted in Figure 3.1.25.a, the internalization of ZIF-8(CV)@PMA@CPP notably surpasses that of other samples, while the lowest uptake is observed with PEGylated particles. These results align with expectations as CPPs are known to enhance cell recognition, thereby promoting increased cellular internalization of CPP-functionalized particles. Conversely, ZIF-8(CV)@PMA@PEG samples exhibit reduced uptake compared to non-functionalized particles, highlighting the shielding potential of PEG polymer in diminishing cell recognition. Mannose-labeled samples, although showing higher uptake than PEGylated ones, demonstrate lower values than non-functionalized NMOFs. This discrepancy may arise

from the highly negative charge of PMA polymer, which could modify cell recognition. Furthermore, despite the higher quantity of mannose compared to PEG or CPP, its small size might limit its efficacy in functionalizing NMOFs, resulting in less pronounced effects compared to other molecules. To verify the retention of cargo within the particles, the uptake of free CV alongside CV-encapsulated within the NMOFs was examined, using equivalent quantities based on fluorescence measurements. The uptake of free CV is substantially reduced when it is not encapsulated within the MOFs, indicating both the efficient internalization of the MOFs and the successful retention of the cargo. Additionally, considering that CPP emits fluorescence (TAMRA), colocalization of the TAMRA and CV signals after internalization in samples containing both CPP and CV was expected. However, the fluorescence of TAMRA was too faint to detect, and TAMRA signals were not observed.

The uptake pattern observed in UiO-67(CV) closely resembles that of ZIF-8(CV) (Figure 3.1.25.b). Specifically, CPP-functionalized UiO-67(CV) exhibited increased uptake, while PEGylated particles showed decreased uptake compared to the control (UiO-67(CV)@PMA). However, the uptake of mannose-labeled samples was slightly higher in this case. This discrepancy may arise from the differing features of UiO-67 and ZIF-8, such as morphology or surface characteristics, which could influence the efficacy of coating small molecules like mannose onto the NMOFs.

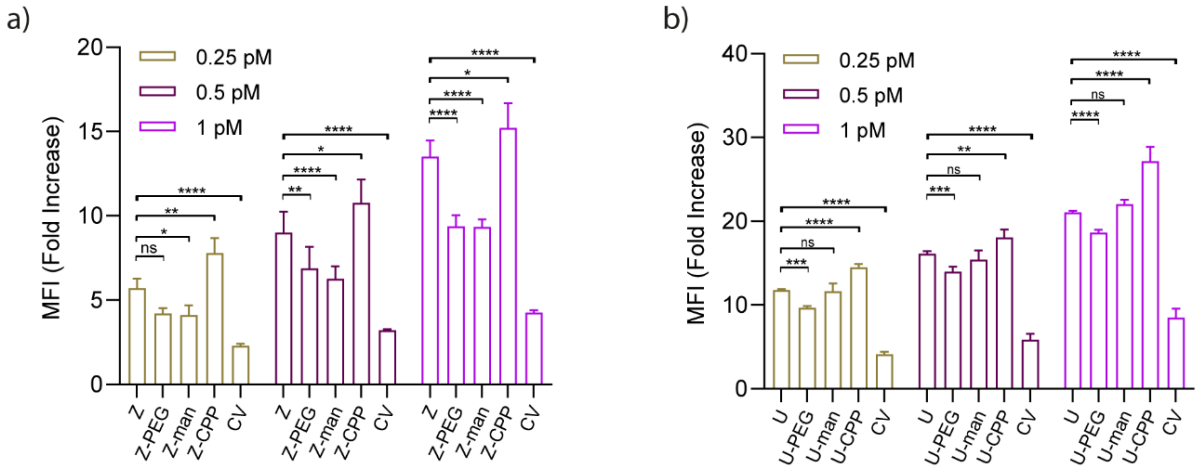

Figure 3.1.25. Flow cytometry measurements of the particle uptake for a) ZIF8 (where (Z=ZIF-8(CV)@PMA) and b) UiO-67 samples (where (U=UiO-67(CV)@PMA). Experiments were carried out using n = 3. Error bars represent standard deviation. Statistical analysis was assessed by two-way ANOVA test (***p = 0.0018, ****p < 0.0001, ns = no significant difference).

Confocal microscopy imaging experiments were conducted to qualitatively confirm the uptake results. NMOFs were incubated for 3 h at a concentration of 0.5 pM. The images clearly depicted the intracellular localization of all CV-NMOFs in the perinuclear region, consistent with expectations (Figure 3.1.26.).[194,206] The microscopy results are in line with the flow cytometry findings in both ZIF-8 (Figure 3.1.26.a) and UiO-67 samples (Figure 3.1.26.b). CPP significantly enhances cell recognition of both NMOFs, resulting in increased uptake, whereas PEG serves to shield the particles, thereby reducing the internalization. Interestingly, there is a subtle discrepancy between the effects of mannose and bare PMA on the NMOF surface, with the latter showing slightly higher uptake.

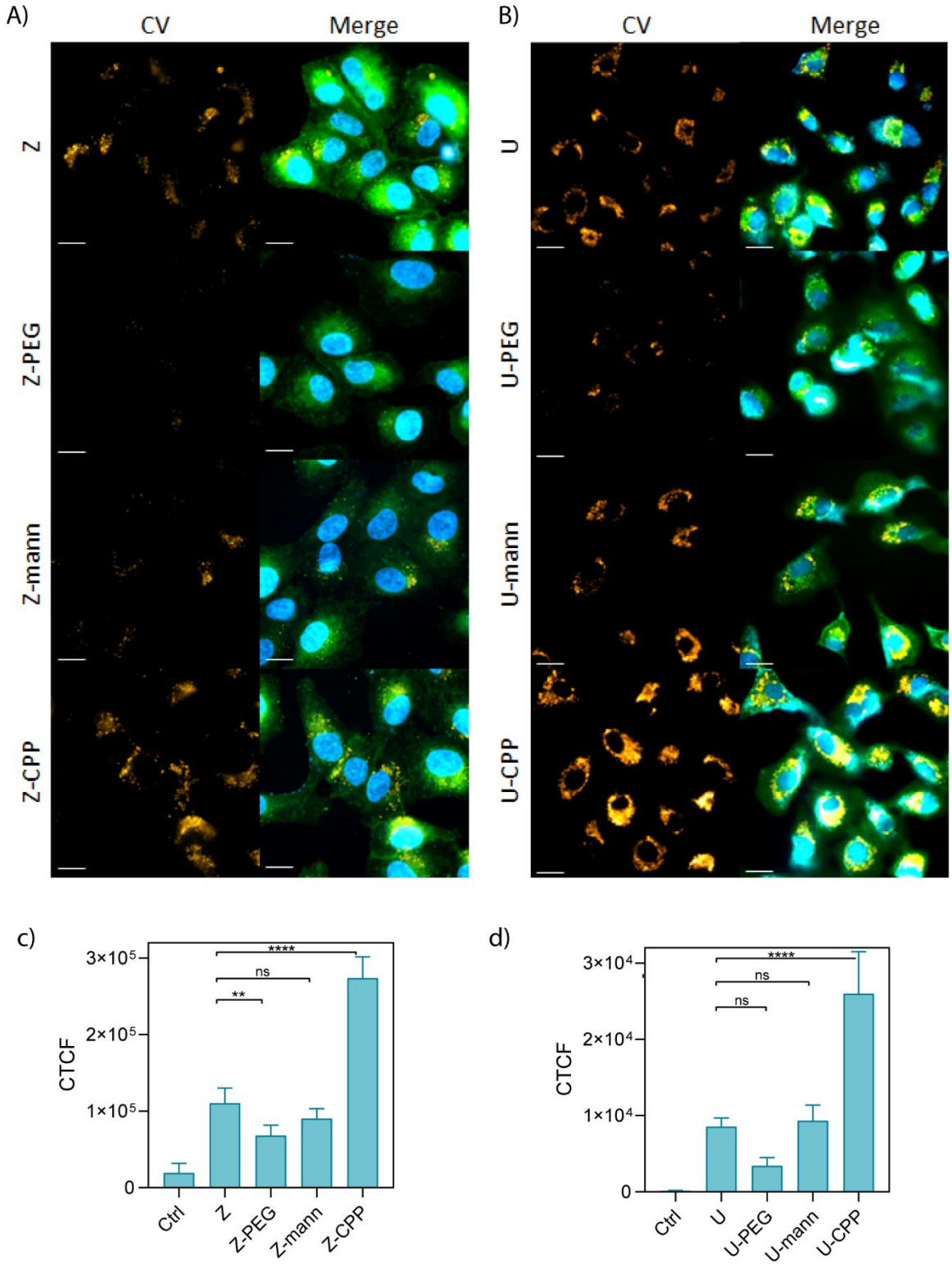

Figure 3.1.26. a) Microscopy images of cells incubates with ZIF-8 samples where Z=ZIF-8(CV)@PMA and b) UiO-67 where U=UiO-67(CV)@PMA samples for 3h at a concentration of 0.5 pM. Corrected total cell fluorescence (CTCF) calculated from microscopy images for c) ZIF-8 samples and d) UiO-67 samples. Experiments were carried out using n = 5. Error bars represent standard deviation. Statistical analysis was assessed by two-way ANOVA test (***p = 0.0018, ****p < 0.0001, ns = no significant difference).

USC UNIVERSIDADE DE SANTIAGO DE COMPOSTELA

To further confirm these observations, qualitative microscopy experiments were conducted using Cy5-functionalized ZIF-8 (Figure 3.1.27.). Cy5 was selected to functionalize the surface of CV-free NMOFs due to its ability to target functional mitochondria.[207] However, the intracellular localization of the particles suggests that Cy5 remains on the surface of the NMOFs, as staining of mitochondria is not visible. The uptake trend observed with the Cy5-functionalized particles differs from that of the CV-loaded particles. In this case, while PEG-functionalized particles exhibit reduced internalization, CPP does not significantly impact final uptake. Additionally, mannose-functionalized samples show higher uptake compared to previous experiments. This could be attributed to a synergistic effect resulting from the combination of Cy5 and mannose on the particle surface, potentially enhancing cell recognition.

However, it's important to acknowledge that these results are not entirely conclusive. The presence of Cy5 may compete with the selected biomolecules to bind to the free DBCO groups in the PMA, leading to variability in the final distribution of PEG, mannose, CPP, and Cy5 on the particle surface across different samples. Furthermore, despite PMA effectively blocks the pores of ZIF-8, some molecules may still penetrate the structure in the absence of loaded cargo.

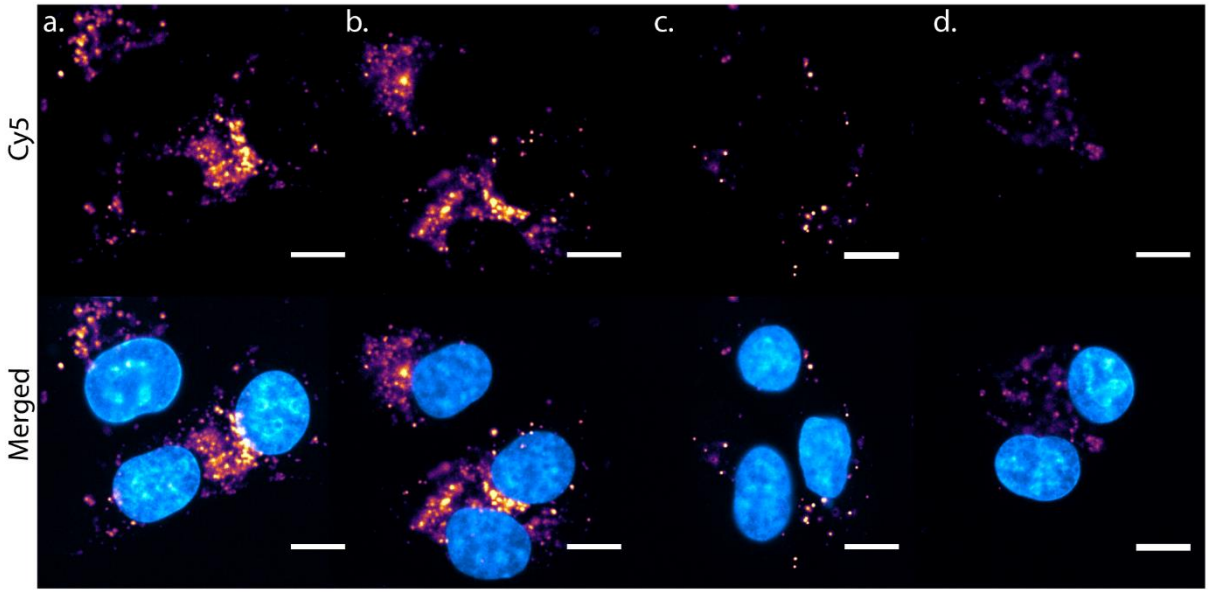

Figure 3.1.27. Microscopy images of cells incubated with ZIF-8-Cy5 samples for 3h at a concentration of 0.5 pM: a) ZIF-8@PMA-Cy5, b) ZIF-8@PMA-Mann-Cy5, c) ZIF-8@PMA-CPP-Cy5 and d) ZIF-8@PMA-PEG-Cy5. For each panel, from up to bottom, images show the fluorescence signal of Cy5 (in magenta) and merged of the Cy5 and DAPI (in blue) signals.

Therefore, with this method, not only the particles showed higher colloidal stability in different biological-relevant media, but the DBCO group on their surface allowed rapid functionalization via click chemistry with azide-containing molecules. Moreover, this approach revealed that the NMOFs were efficiently internalized by living cells without impairing cell viability and with a clear dependency on the ligands exposed on their surfaces.

USC
UNIVERSIDADE DE SANTIAGO DE COMPOSTELA

USC
UNIVERSIDADE
DE SANTIAGO
DE COMPOSTELA

3.2. POST-SYNTHESIS SURFACE MODIFICATION OF Zr NMOFs

Delivering drugs within the body involves navigating through various physiological barriers. Consequently, surface modifications of NMOFs are essential to overcome these obstacles effectively. NMOFs possess a rich structure and unique porosity, rendering them easily modifiable. These characteristics facilitate the functionalization of NMOFs to achieve specific objectives.[208] Post-synthesis modification of NMOF materials primarily involves two approaches based on physical and chemical modifications. In the last case one can distinguish between two main strategies: covalent and coordinative PSM. The first one involves the formation of covalent bonds with organic ligands, while the other entails the formation of coordination bonds with metal centers. In recent years, there has been a growing trend towards chemically modifying biomaterials on the surface of NMOFs to enhance drug delivery.[208] Specifically, coordinative PSM has emerged as a leading method for surface functionalization of MOF nanoparticles.[171,209] It relies on the presence of coordinatively unsaturated (open) metal sites (CUS), a unique feature of NMOFs that primarily originates from metal-coordinated solvents during the solvothermal process. This approach provides precise control over surface chemistry while preserving the crystalline structure, making it highly appealing for a variety of applications. By using free metal sites on the superficial SBUs, coordinative PSM allows for selective modification of MOF surfaces with specific functional groups.[169]

Concerning the interaction of DDSs with cells, the cell membrane, also known as the plasma membrane or cytoplasmic membrane, serves as a natural barrier, regulating the movement of substances in and out of cells. Large molecules, including nanoparticles, can enter cells through processes like endocytosis, which can be divided into phagocytosis and pinocytosis.[66,210] Endocytosis is the cellular process that forms small, membrane-bound vesicles, typically sized between 50 to 150 nm. These vesicles act as transporters, shuttling various substances within the cell to different destinations. This mechanism holds particular importance in the context of NMOF internalization and drug delivery applications. The journey of these vesicles involves traversing different cellular compartments, including early and late endosomes, recycling endosomes, autophagosomes, lysosomes, and the Golgi apparatus.[66] Notably, these pathways serve as the primary means for the uptake of nanomaterials into cells. While a variety of endocytic pathways exist in eukaryotic cells, the most extensively studied include clathrin-mediated, caveolae-mediated, clathrin-independent, caveolin-independent, macropinocytosis, and phagocytosis. This understanding is essential in assessing NMOF data.

One promising approach for surface functionalization NMOFs involves the use of DNA molecules. DNA possesses water solubility, allowing for chemical modifications in aqueous environments, with common sites including the 5' phosphate and 3' hydroxyl groups. Its biodegradability, mediated by nucleases, yields harmless metabolites, rendering it biocompatible. These properties make DNA an excellent candidate for nanomaterial construction, surpassing other polymers in precision and accuracy.[211] However, when discussing the cellular uptake, the negatively charged nature of DNA often results in strong electrostatic repulsion between DNA molecules and the negatively charged cell membrane. [212] Consequently, unmodified DNA oligonucleotides typically struggle to efficiently enter cells without the aid of transfection agents, making passive uptake of DNA nanostructures by cells unlikely. However, recently, spherical nucleic acid (SNA)-nanoparticle conjugates have

garnered considerable attention. These structures feature a nanoparticle core encased within a dense shell of oligonucleotides. They represent promising architectures with diverse biological applications, going from gene regulation to immunomodulation and intracellular detection.[213,214] These applications are made possible by the enhanced cellular uptake and improved physiological stability of SNAs in comparison to their individual components.[213] In 2013, Mirkin *et al.* demonstrated the enhanced cellular uptake of SNAs across 50 cell lines, independently of the nature of the nanoparticle core or the specific sequences of the surface oligonucleotides. This was attributed to the 3D arrangement of the oligonucleotides, which facilitated enhanced interaction with cell surface receptors present on the surfaces of most cells compared to linear oligonucleotides.[213,215]

Enhancing MOFs with nucleic acids (e.g., ssDNA and aptamers) and amino acids (proteins, peptides, amino acids) holds significant promise for a range of biologically relevant applications. This bio-functionalization imparts high biocompatibility and bioactivity to MOFs, leveraging the unique properties of biomolecules.[216] However, there has been limited exploration into the advantages and distinct applications of MOFs functionalized with nucleic acids and amino acids. Recent efforts have primarily provided a summary of the rational synthesis of MOF biocomposites for sensing applications, leaving ample opportunity for further investigation and exploitation of their potential benefits.[216] Furthermore, densely arranging nucleic acids around a NMOF core to create a SNA architecture enhances cellular uptake, improves resistance to nuclease degradation, and boosts binding affinity to complementary targets.[212]

On the other hand, peptide and protein coatings play a crucial role in facilitating NP-based technologies by providing both biological and physical stability, altering interactions with host cells and circulating biomolecules to regulate tissue accumulation and ensure NP activity. Moreover, decorating particles with peptides or proteins capable of mediating transport or penetration represents a forefront approach to enable NP technologies to effectively reach their intended sites of action.[217] Specifically, the recognition of protein binding partners by cell-surface receptors is a fundamental aspect of biology, governing a multitude of intracellular interactions crucial for tissue formation and function. This interaction is central to numerous biological processes, involving hormones, growth factors, cytokines, and cell-signaling structures. Hence, protein-NP coatings have emerged as valuable tools for targeted delivery to specific areas of the body where specific receptors are overexpressed. By coating NPs with these structures, they can be directed to sites where their corresponding receptors are abundant, exemplifying their potential in delivering particles to precise locations. Bovine serum albumin (BSA) stands out as a popular choice for nanoparticle formulations owing to its purity, water solubility, accessibility, and cost-effectiveness. Its availability in a pure form makes it particularly advantageous for preparing nanoparticle dispersions.[218] Furthermore, BSA's structure boasts multiple binding sites, which enhance its ability to bind to a wide range of active molecules. In addition to BSA, other albumin variants like human serum albumin (HSA) and ovoalbumin have also been extensively studied for their applicability in nanoparticle formulations.[219]

Herein, a DNA-based coordinative PSM was studied in different Zr family MOFs. Before the functionalization, an exhaustive analysis of the concentration was performed using NTA

and flow cytometry. Then, coordinative PSM was studied. PSM can be easily applied to the Zr MOFs family, as the Zr lacking a complete coordination sphere in the surface of the structure offer free sites for the coordination of phosphate or carboxylate modified molecules.[73,195] The study was performed for the previously synthetized UiO-67, NU-1000 and PCN-222 Zr NMOFs. To provide comparation with a different coating, PEG was selected to perform similar functionalization studies. The subsequent functionalization of the DNA-coated surface was explored through the hybridization of complementary azide-modified DNA oligos, acting as anchoring points for click chemistry conjugation with bioactive molecules containing DBCO groups. This last investigation focused on calcein-loaded UiO-67 nanoparticles, with DBCO-modified BSA chosen for further bioactive functionalization.

3.2.1. Concentration analysis: NTA vs flow cytometry

Prior to investigating new functionalization approaches, it is crucial to accurately quantify the concentration of the particles. For the subsequent experiments, three previously synthesized Zr-based NMOFs were employed: UiO-67, NU-1000, and PCN-222. Accurate concentration quantification of nanoparticles plays a pivotal role in comprehending their interactions with cells. This underscores the necessity for robust methodologies to precisely measure the total concentration and size distribution of the NMOFs under examination.

Nanoparticle tracking analysis (NTA) constitute a rapid and highly sensitive method for visualizing and characterizing NPs in solution. Prior literature extensively details the principles underlying NTA, including comparative assessments with alternative methods for NP size and concentration determination.[220] Briefly, during NTA measurement, a solution of the particles is loaded into a sample chamber. While the liquid is passing through it, a laser beam illuminates the chamber, and the particles scatter the light that is collected by a 20x microscope objective and analyzed with a digital camera. The software allows to visualize a video of the particles moving under Brownian motion and analyses the hydrodynamic size individually using the Stokes-Einstein equation:

$$D = \frac{K_B T}{3\pi\eta d_h} \quad (1)$$

where D is the diffusion coefficient, K_B the Boltzmann constant, T the temperature, η the viscosity of the media and d_h the hydrodynamic diameter of the particles.[220] The flow rate in the video also allows the calculation of the particle concentration (in particles·mL^{-1}).[221] NTA offers several advantages that make it a valuable tool for nanoparticle characterization. Firstly, it provides high-resolution size measurements, allowing for precise determination of nanoparticle dimensions. Additionally, NTA enables count-based concentration determination, providing quantitative information about the number of nanoparticles present in a sample. Moreover, NTA does not require the use of fluorescent markers, simplifying sample preparation and analysis. However, despite its advantages, NTA has certain limitations as the long times needed for each measurement or the sensitivity of the technique to the type of nanomaterial being analyzed. Different nanoparticles may interact differently with the laser beam used in NTA, potentially leading to inaccurate size and concentration measurements. Additionally, the implementation of NTA requires specialized equipment, including a laser-based particle tracking system and associated software. This can pose logistical challenges for researchers without access to such equipment. Furthermore, the cost of acquiring and maintaining NTA

USC UNIVERSIDADE DE SANTIAGO DE COMPOSTELA

equipment can be prohibitive for some research groups, limiting the widespread adoption of this technique.

Flow cytometry constitute a possible alternative for nanoparticle concentration characterization.[222] Despite being intended for cell analysis, available in most biology laboratories, this instrument could also provide a qualitative and quantitative analysis of NPs size and concentration based on measurements of scattering and fluorescence. [222,223] The standard lower size detection limit for light scattering on conventional flow cytometers, which are widely accessible, typically ranges from 200 to 500 nm. However, fluorescence measurements tend to be more sensitive.[223]

Herein, taking advantage of the different nature of the selected Zr NMOFs (UiO-67, NU-1000 and PCN-222), a comparative analysis between NTA and flow cytometry experiments was carried out to calculate the concentration of the nanoparticles for its use in further in vitro experiments.

NTA measurements were performed for each NMOF to calculate the number of particles per mL using three dilutions of each sample. In order to obtain reliable results, the employed concentration range should be between 10^7 and 10^9 particles·mL^{-1}. Results are presented in Figure 3.2.1. and Table 3.2.1-3.2.3. The size distributions are coherent with previous DLS measurements, showing narrow peaks that demonstrate the monodispersity of the UiO-67 (Figure 3.2.1.a), NU-1000 (Figure 3.2.1.b) and PCN-222 (Figure 3.2.1.c). The initial sample concentration is determined by the slope of the linear fit shown in Figure 3.2.1.d-f. The results are consistent with each other, as they were anticipated to exhibit similar concentration values, in the range of ~10^{10} particles·mL^{-1}.

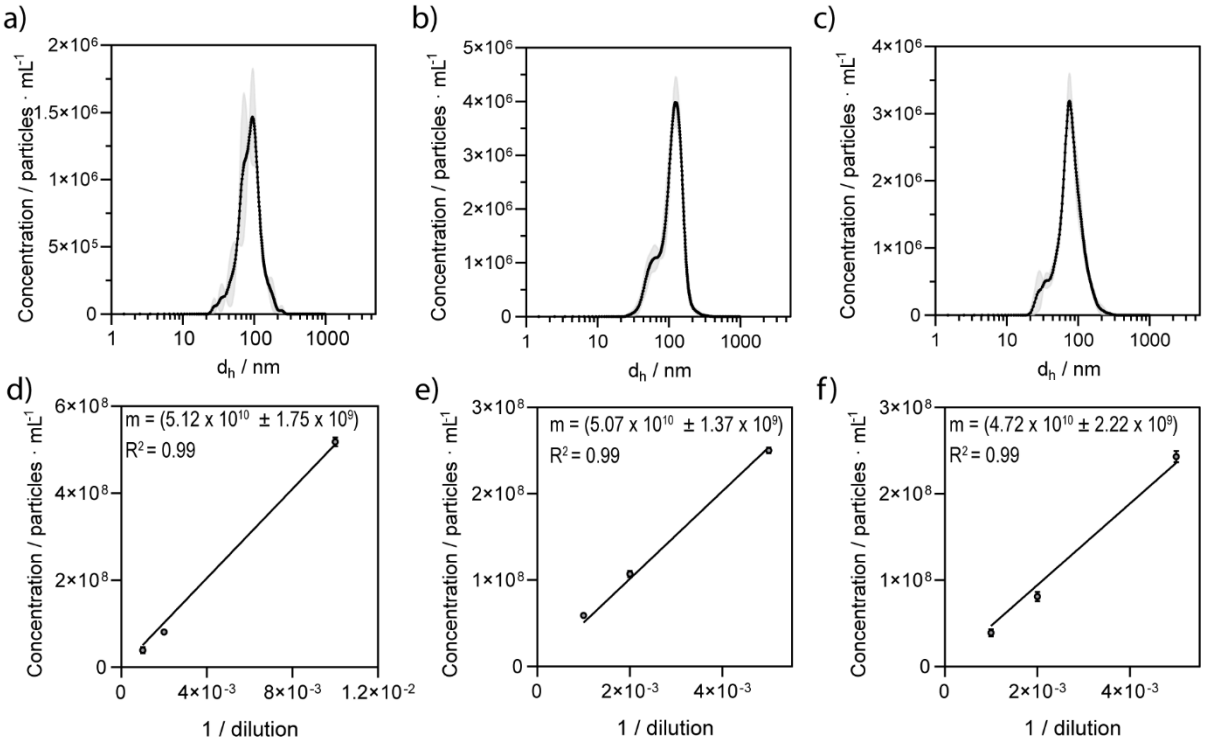

Figure 3.2.1. NTA measurements of the d_h for a) UiO-67, b) NU-1000 and c) PCN-222. Calibration curves calculated from NTA concentrations results and three different dilution of d) UiO-67, e) NU-1000 and f) PCN-222. Experiments were carried out using n = 3. Error bars represent standard deviation.

On the other hand, flow cytometry allows more precise measurements and lower particle concentrations for the studied dilution are needed. In this case, estimated concentrations between 10^3 and 10^6 particles·mL^{-1} can be precisely measured. Before performing the measurements, it is crucial when counting nanoparticles or submicron particles to have low background and a relatively high particle concentration. Ensuring a clear distinction between sample events and background is essential for accurate nanoparticle quantification. Therefore, it is a key factor to minimize background counts in the sheath fluid to prevent any interference with the absolute nanoparticle count.

Measurements were performed in a 96 multi well plate using 200 μL of sample in each case. Additionally, VitroCheck nanoparticle Reference Kit was added to dilutions to further confirm the concentration and size of the MOFs. The employed beads were 100 nm FITC-like beads excited using the green laser (λ = 488 nm).

When optimizing the settings for analysis, it is crucial to consider the optical properties of each NMOF. Although UiO-67 possesses high scattering, which means it can strongly scatter incident light, it does not exhibit fluorescence properties. Therefore, UiO-67 particle population was checked with high angle (SSC-A) scattering area events distribution.

On the other hand, NU-1000 and PCN-222 have intrinsic fluorescence due to the nature of their linkers. These photoluminescent properties allow to track them using fluorescence. The emission profiles of both NU-1000 and PCN-222 are presented in figure 3.2.2. NU-1000 exhibit an emission band at λ=450 nm using an excitation wavelength of λ = 380 nm (based on previous absorption spectra), whereas PCN-222 shows two main emission peaks at λ = 650 and 750 nm when exciting at 515 nm. NMOFs fluorescence (vertical axis) and high angle (violet SSC-A) scattering area event distributions were recorded (Figure 3.2.3.). The population fluorescence signal allows to easily distinguish the particle population from the background.

UiO-67 particle distribution can be observed in the different dilutions, with each event corresponding to one NMOF (Figure 3.2.3.a-c). However, the obtained distributions indicate high background signal that may lead to unreliable values of the concentration. Mean concentration calculated from NTA measurements give a value of (5.12 ± 0.18) x 10^{10} particles·mL^{-1} (Figure 3.2.1.d), whereas using flow cytometry it results in (1.77 ± 0.04) x 10^{11} particles·mL^{-1} (Figure 3.2.3.j). This difference may be due to the high background signal present in the flow cytometry experiments, that might lead to overestimation of the concentration.

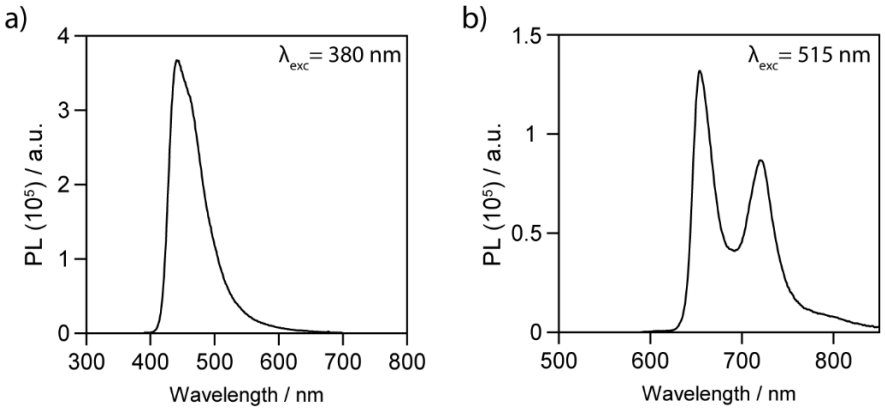

Figure 3.2.2. PL emission spectra of a) NU-1000 (excitation at 380 nm) and b) PCN-222 (excitation at 515 nm).

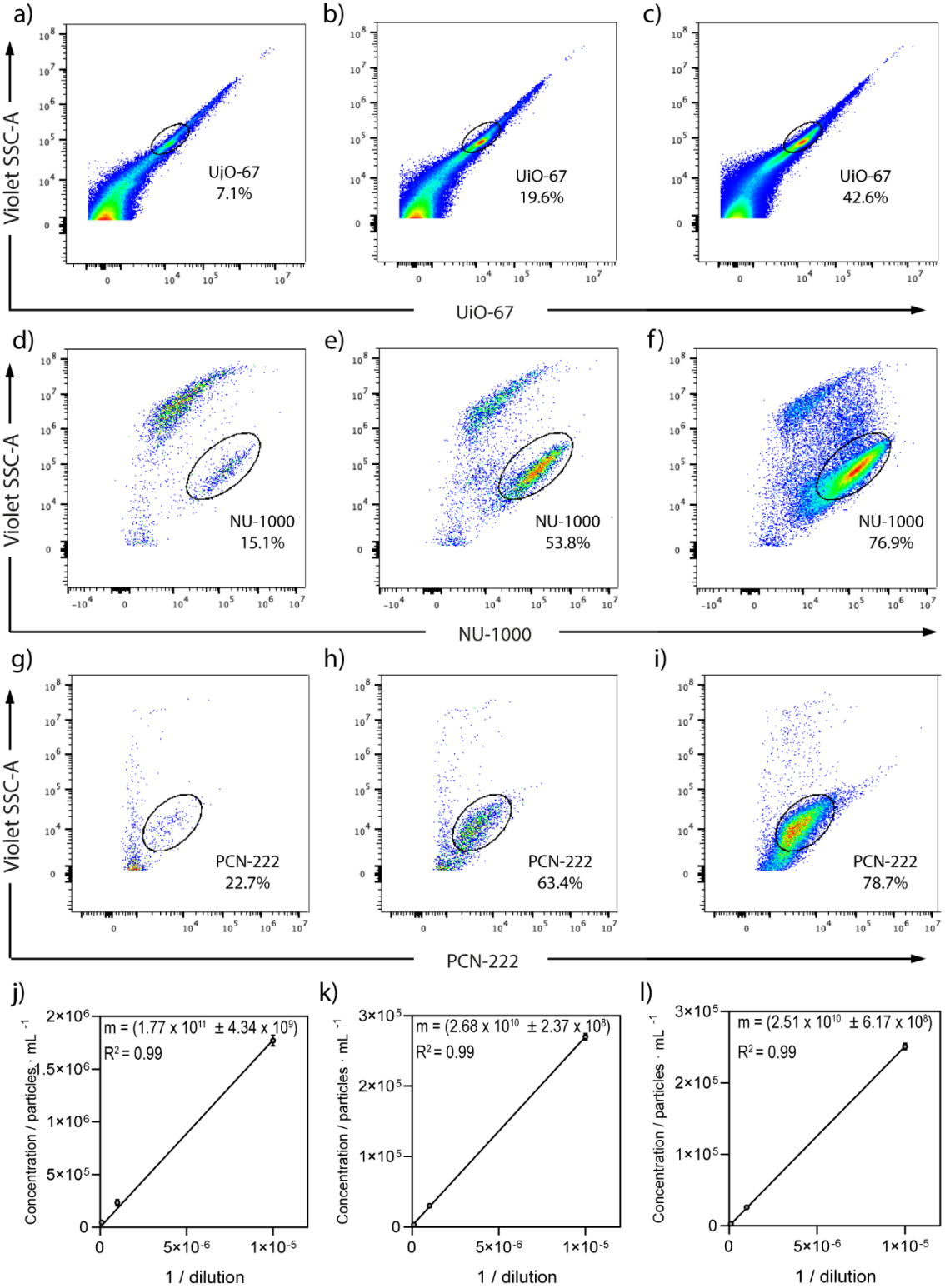

Figure 3.2.3. Flow cytometry particle distribution for each NMOF at three different dilutions from the initial sample a) Dilution 1:10^7 UiO-67, b) Dilution 1:10^6 UiO-67, c) Dilution 1:10^5 UiO-67; d) Dilution 1:10^7 NU-1000, e) Dilution 1:10^6 NU-1000, f) Dilution 1:10^5 NU-1000; d) Dilution 1:10^7 PCN-222, e) Dilution 1:10^6 PCN-222, f) Dilution 1:10^5 PCN-222; Concentration calibration curves based on cytometry results for j) UiO-67, k) NU-1000 and l) PCN-222. Experiments were carried out using n = 3. Error bars represent standard deviation.

USC
UNIVERSIDADE DE SANTIAGO DE COMPOSTELA

Table 3.2.1. UiO-67 concentration results measured by NTA and Flow cytometry experiments.

UiO-67	Dilution	Particles·mL^{-1}
NTA	1000	(3.90 ± 0.73) x 10^7
	500	(8.10 ± 0.42) x 10^7
	100	(5.18 ± 0.10) x 10^8
Flow Cytometry	1 x 10^7	(4.62 ± 0.09) x 10^4
	1 x 10^6	(2.32 ± 0.02) x 10^5
	1 x 10^5	(1.77 ± 0.01) x 10^6

Table 3.2.2. NU-1000 concentration results measured by NTA and Flow cytometry experiments.

NU-1000	Dilution	Particles·mL^{-1}
NTA	1000	(5.90 ± 0.24) x 10^7
	500	(1.07 ± 0.04) x 10^8
	100	(5.18 ± 0.03) x 10^8
Flow Cytometry	1 x 10^7	(3.49 ± 0.92) x 10^3
	1 x 10^6	(3.02 ± 0.26) x 10^4
	1 x 10^5	(2.70 ± 0.05) x 10^5

Table 3.2.3. PCN-222 concentration results measured by NTA and Flow cytometry experiments.

PCN-222	Dilution	Particles·mL^{-1}
NTA	1000	(3.9 ± 0.43) x 10^7
	500	(8.1 ± 0.54) x 10^7
	100	(2.43 ± 0.07) x 10^8
Flow Cytometry	1 x 10^7	(2.88 ± 0.81) x 10^3
	1 x 10^6	(2.59 ± 0.21) x 10^4
	1 x 10^5	(2.51 ± 0.05) x 10^5

USC UNIVERSIDADE DE SANTIAGO DE COMPOSTELA

Analysis of NU-1000 concentration presented in Table 3.2.2. reveals a significant correlation among the three dilutions utilized, demonstrating strong consistency with NTA values. Mean concentration calculated from NTA measurements give a value of (5.07 ± 0.17) x 10^{10} particles·mL^{-1} (Figure 3.2.1.e), whereas using flow cytometry it results in (2.68 ± 0.02) x 10^{10} particles·mL^{-1} (Figure 3.2.3.k).

On the other hand, PCN-222 concentration results are presented in Table 3.2.3., showing again high coherence among NTA and flow cytometry. In this case, mean concentration calculated from NTA measurements give a value of (4.72 ± 0.22) x 10^{10} particles·mL^{-1} (Figure 3.2.1.g), whereas using flow cytometry it results in (2.51 ± 0.06) x 10^{10} particles·mL^{-1} (Figure 3.2.3.l). In both cases (NU-1000 and PCN-222), the concentrations measured with NTA are consistently higher than those obtained with flow cytometry, albeit falling within the same range. This discrepancy may stem from potential errors in the NTA measurements, likely attributable to the instrument's sensitivity to the presence of aggregates, which can contribute to background noise. The differences between NTA and flow cytometry in each case are shown in Figure 3.2.4., where UiO-67 cytometry results manifest the previously mentioned overestimation in a six-fold concentration increase with respect to the NTA, whereas NU-1000 and PCN-222 do not present significant differences. Efforts to improve the accuracy of NTA measurements could involve optimizing sample preparation techniques to minimize aggregation and noise interference, thus enhancing the reliability of the results.

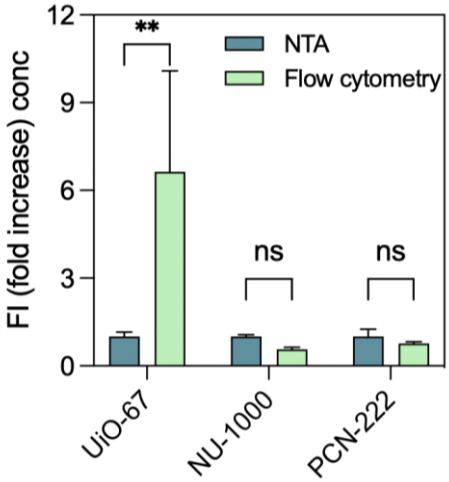

Figure 3.2.4. Fold increase of the concentration calculated using NTA and flow cytometry.

To validate these findings, 100 nm FITC-like beads were utilized. Figure 2.3.5. illustrates the particle population distribution of each sample based on FITC and the corresponding channel of each NMOF. A minor population showing positive FITC signals, corresponding to the beads (quadrant Q1), is evident. Considering the number of events in Q1 and the particles per µL obtained from Q3, the following equation:

$$\frac{NMOFs}{\mu L} = \frac{Sample\ count\ (Q3)\ x\ Ref\ Particle\ Vol\ (\mu L)}{Ref.Particle\ Count\ (Q1) x\ Sample\ Vol.(\mu L)}\ x\ Ref\ Particle\ conc\ \left(\frac{part}{\mu L}\right) \quad (2)$$

can be employed to calculate the total concentration of the NMOFs in each case. Results are shown in Table 3.2.4-3.2.6. Comparison among data calculated with and without beads leads to compatible results in most cases. For UiO-67, while the results for the first dilution may have

been overestimated, the particle concentrations for the second and third dilutions are consistent with previous measurements obtained through NTA and flow cytometry. Similarly, NU-1000 demonstrates coherence with previous values, except for the first dilution, mirroring the situation observed with UiO-67. However, PCN-222 exhibits higher concentration values when using beads compared to conventional cytometry measurements. This disparity could be attributed to experimental factors such as volume additions or errors in data analysis, such as the selection of the sample population.

However, these results manifest the great potential of flow cytometry for the study of nanoparticle concentration and size. Moreover, it proved some advantages with respect to NTA measurements, as the low concentration values and low volumes needed to perform the measure, as well as the high precision and rapid measurements.

Table 3.2.4. Calculated concentration of UiO-67 using 100 nm FITC-like beads.

Dilution	Sample count	Ref part V (µL)	Ref particle count	Sample V (µL)	Ref conc (part·µL^{-1})	Calculated conc MOF (part·mL^{-1})
1 x 10^{7}	10563	50	551	150	50	3,20E+05
1 x 10^{6}	27935	50	557	150	50	8,36E+05
1 x 10^{5}	180239	50	520	150	50	5,78E+06

Table 3.2.5. Calculated concentration of NU-1000 using 100 nm FITC-like beads.

Dilution	Sample count	Ref part V (µL)	Ref particle count	Sample V (µL)	Ref conc (part·µL^{-1})	Calculated conc MOF (part·mL^{-1})
1 x 10^{7}	19	50	24	150	50	1,32E+04
1 x 10^{6}	99	50	31	150	50	5,32E+04
1 x 10^{5}	1050	50	33	150	50	5,30E+05

Table 3.2.6. Calculated concentration of PCN-222 using 100 nm FITC-like beads.

Dilution	Sample count	Ref part V (µL)	Ref particle count	Sample V (µL)	Ref conc (part·µL^{-1})	Calculated conc MOF (part·mL^{-1})
1 x 10^{7}	69	50	34	150	50	3,38E+04
1 x 10^{6}	262	50	42	150	50	1,04E+05
1 x 10^{5}	2003	50	33	150	50	1,01E+06

USC UNIVERSIDADE DE SANTIAGO DE COMPOSTELA

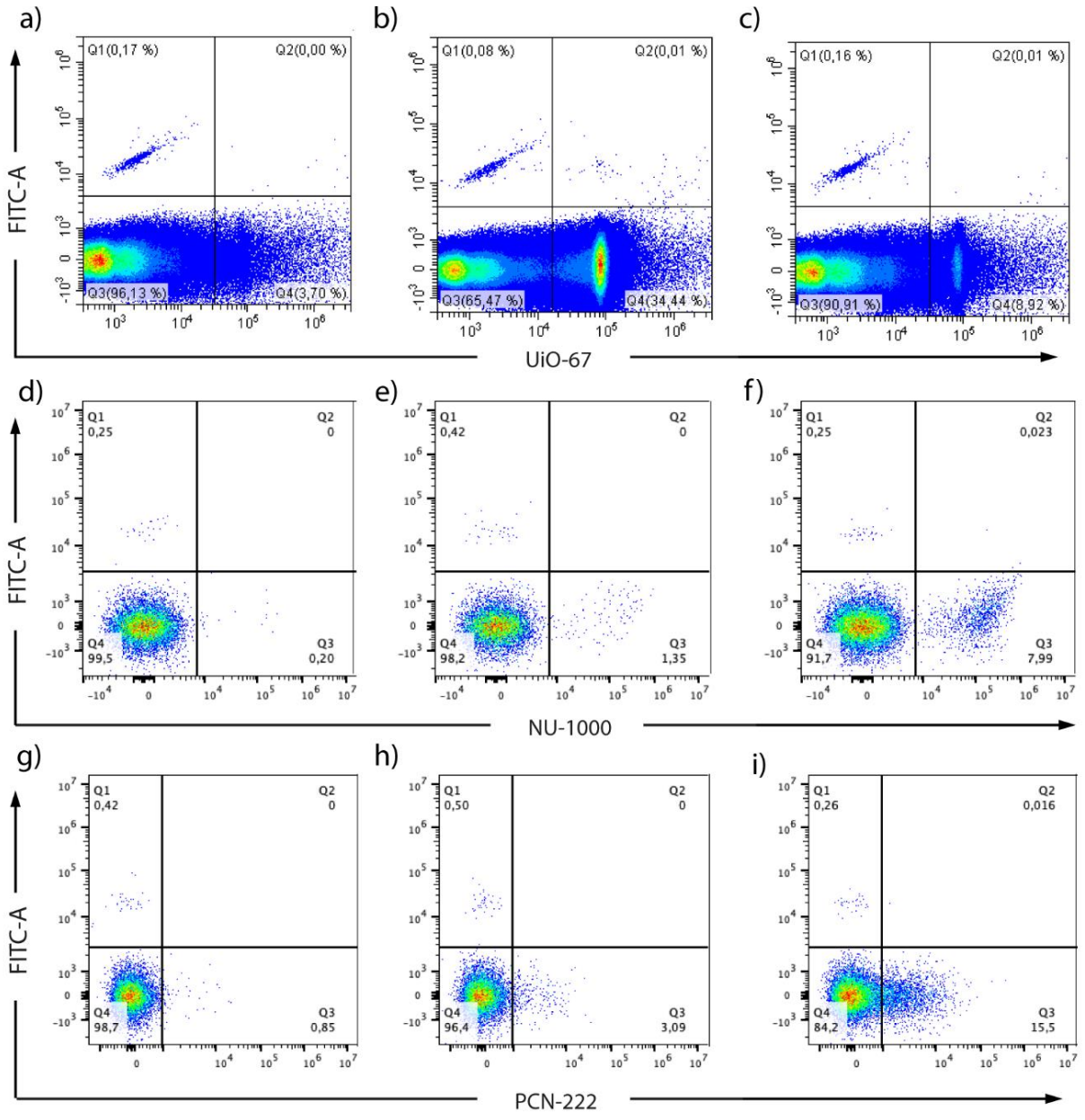

Figure 3.2.5. Flow cytometry particle distribution for each NMOF using 100 nm FITC-like beads at three different dilutions from the initial sample a) Dilution $1{:}10^7$ UiO-67, b) Dilution $1{:}10^6$ UiO-67, c) Dilution $1{:}10^5$ UiO-67; d) Dilution $1{:}10^7$ NU-1000, e) Dilution $1{:}10^6$ NU-1000, f) Dilution $1{:}10^5$ NU-1000; d) Dilution $1{:}10^7$ PCN-222, e) Dilution $1{:}10^6$ PCN-222, f) Dilution $1{:}10^5$ PCN-222.

USC UNIVERSIDADE DE SANTIAGO DE COMPOSTELA

3.2.2. Phosphate modified DNA and PEG coordinative PSM of Zr NNMOFs

Three previously synthesized Zr-based NMOFs: UiO-67, NU-1000, and PCN-222 were subjected to functionalization using phosphate-modified DNA[195] and PEG[73] molecules, following established protocols. The employed DNA sequence was previously modified with PO_3 groups at the 5' ends to allow phosphate groups to bind with Zr lacking a complete coordination sphere present on the particle surface. For DNA functionalization, the oligonucleotide was added to the NMOF pellet at a ratio of 50:1 (mmol DNA:mg MOF). On the other hand, PEG molecules modified with PO_3 groups (PEG-PO_3) were selected following the method reported by Chen et al.[73]. The Zr-MOFs were functionalized with phosphate-functionalized methoxy polyethylene glycol (MeO-PEG-PO_3, Mn = 5 kDa) groups, by adding it at a weight ratio of 3:1 (mg PEG:mg MOF). Due to the instability of bare Zr NMOFs in aqueous media, the nanoparticles were centrifuged before the experiments so that both the DNA and PEG water solutions were directly added to the pellet.

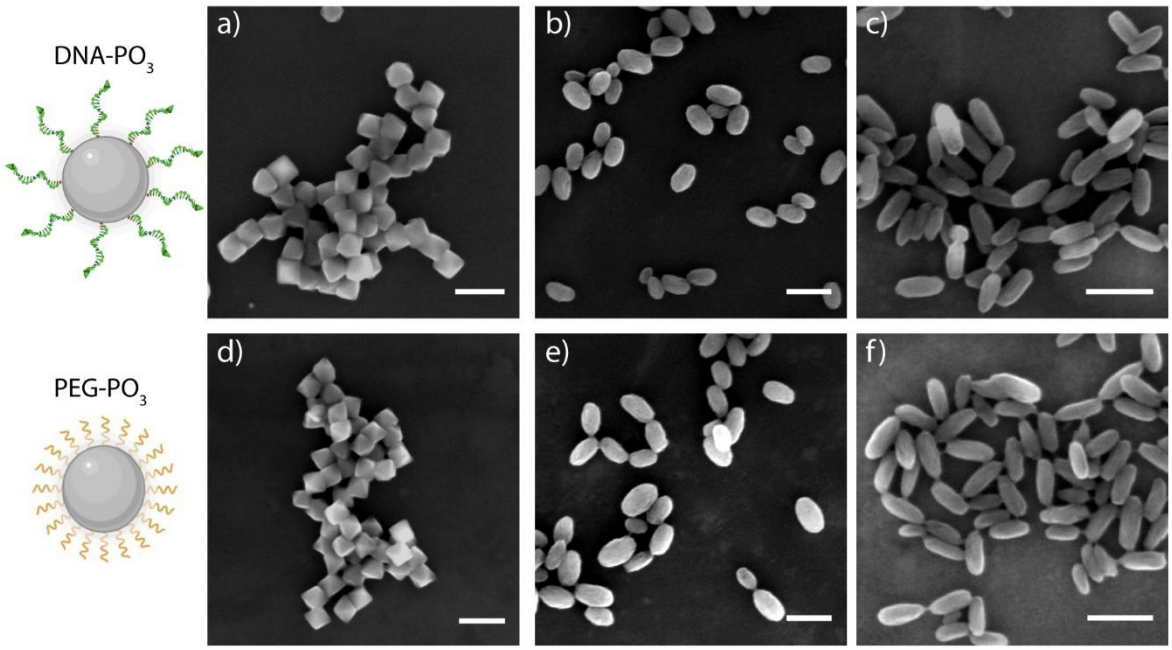

Figure 3.2.6. SEM micrographs of the different NMOFs after the DNA and PEG functionalizations: a) UiO-67@DNA, b) NU-1000@DNA, c) PCN-222@DNA, d) UiO-67@PEG, e) NU-1000@PEG, f) PCN-222@PEG. Scale bars correspond to 200 nm.

Particles were characterized after the functionalization and compared to the results obtained for non-coated particles shown in Section 3.1. SEM images after the coatings do not present any changes with respect to bare NMOFs in any of the cases (Figure 3.2.6). This is confirmed by DLS measurements (Figure 3.2.7.a-c**,** Tables 3.2.7-3.2.9), where the hydrodynamic diameter is compatible for all the samples, proving the particles do not aggregate after the functionalization. Furthermore, ζ-potential measurements prove the correct functionalization of the NMOFs, as there is a clear reduction in the total surface charge (Figure 3.2.7.d-f). All the bare particles possess a positive surface charge (10 ± 1) mV for UiO-67, (40 ± 1) mV for NU-1000, and (17 ± 1) mV in the case of PCN-222, respectively, due to the Zr defects of the surface that will facilitate the functionalization using PO_3 groups, leading to the formation of Zr−O−P coordination bonds. The incorporation of DNA resulted in a significant

USC DE COMPOSTELA

decrease in the total charge, rendering all samples negatively charged, changing to (-37 ± 2) mV for UiO-67, (-24 ± 2) mV for NU-1000 and (-20 ± 2) mV for PCN-222 (Tables 3.2.7-3.2.9). This change in charge is likely due to DNA's negative nature, suggesting that the NMOFs have been effectively coated. When PEG is added, the particles become neutral or slightly negative due to the methoxy groups at the free ends. The new ζ potential values are (-20 ± 1) mV, (12 ± 1) mV and (6 ± 2) mV for UiO-67, NU-1000 and PCN-222, respectively. Moreover, UV-Vis spectra confirm there are no significant differences between the samples before and after surface functionalization (Figure 3.2.7.g-i).

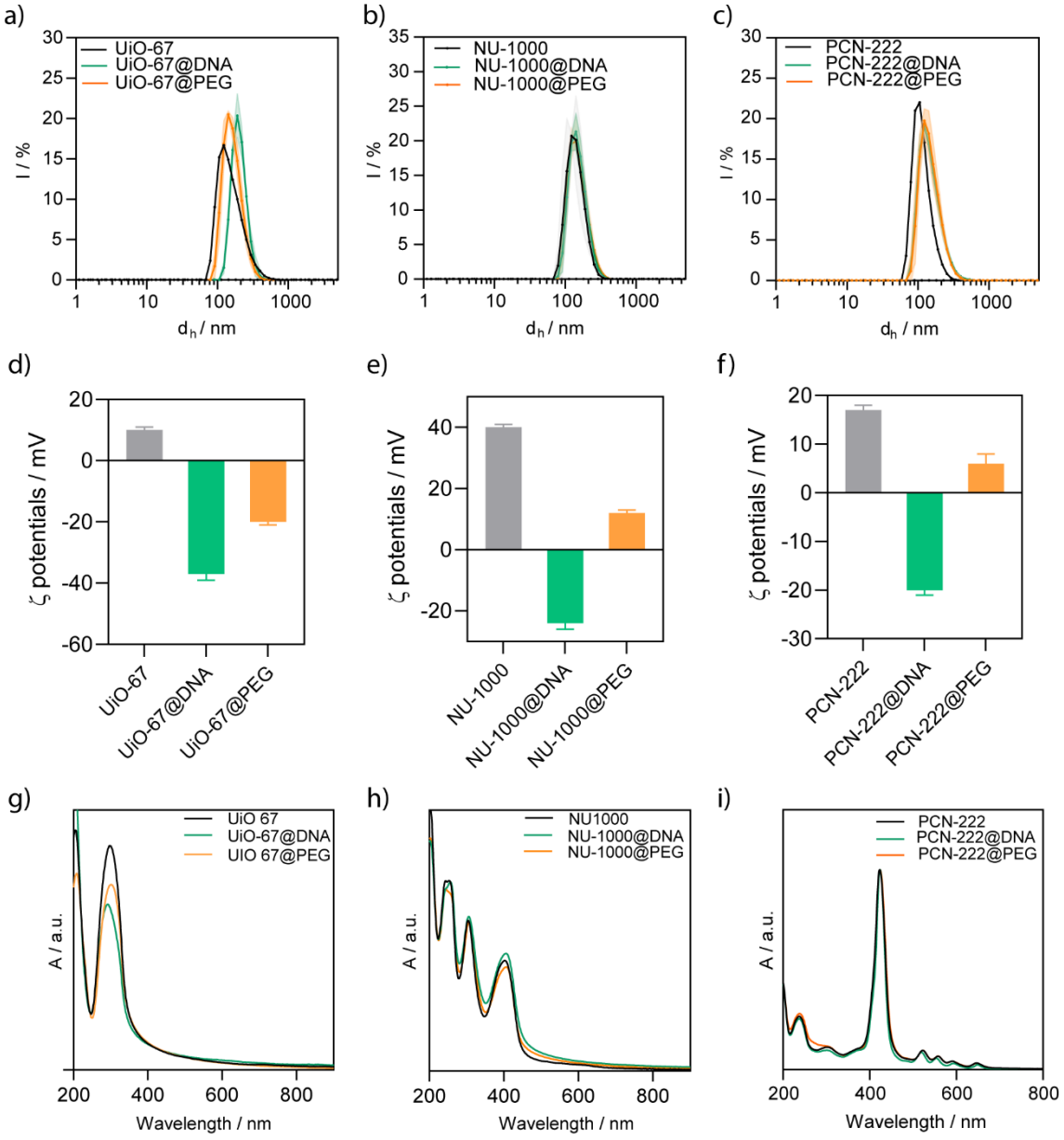

Figure 3.2.7. DLS measurements of the d_h number distributions of the samples before and after the functionalization with PEG and DNA a) UiO-67, b) NU-1000, c) PCN-222; ζ potentials of d) UiO-67, e) NU-1000 and f) PCN-22. Experiments were carried out using n = 3. Error bars represent standard deviation. UV-Vis spectra of g) UiO-67 (results are normalized to λ = 280 nm), h) NU-1000 (results are normalized to λ = 350 nm) and i) PCN-222 (results are normalized to λ = 350 nm).

Table 3.2.7. DLS measurements of the d_h number and intensity distributions, PDI and ζ-Potentials of the UiO-67 samples before and after the PEG and DNA functionalizations.

Sample	$d_{h,N}$ ± sd	$d_{h,I}$ ± sd	PDI	ζ-Pot / mV
UiO-67	165 ± 34	275 ± 71	0.17 ± 0.07	10 ± 1
UiO-67@DNA	144 ± 12	197 ± 22	0.14 ± 0.03	-37 ± 2
UiO-67@PEG	176 ± 16	240 ± 24	0.26 ± 0.10	-20 ± 1

Table 3.2.8. DLS measurements of the d_h number and intensity distributions, PDI and ζ-Potentials of the NU-1000 samples before and after the PEG and DNA functionalizations.

Sample	$d_{h,N}$ ± sd	$d_{h,I}$ ± sd	PDI	ζ-Pot / mV
NU-1000	136 ± 6	158 ± 24	0.30 ± 0.03	40 ± 1
NU-1000@DNA	146 ± 10	223 ± 58	0.22 ± 0.02	-24 ± 2
NU-1000@PEG	154 ± 5	205 ± 8	0.11 ± 0.02	12 ± 1

Table 3.2.9. DLS measurements of the d_h number and intensity distributions, PDI and ζ-Potentials of the PCN-222 samples before and after the PEG and DNA functionalizations.

Sample	$d_{h,N}$ ± sd	$d_{h,I}$ ± sd	PDI	ζ-Pot / mV
PCN-222	158 ± 2	250 ± 56	0.18 ± 0.01	17 ± 1
PCN-222@DNA	130 ± 15	179 ± 25	0.20 ± 0.06	-20 ± 1
PCN-222@PEG	174 ± 12	364 ± 80	0.29 ± 0.12	6 ± 2

Colloidal stability experiments were conducted in various relevant biological media, including water, DMEM, and PSF (pH= 5), over a period of 10 days using dynamic light scattering (DLS) (Figure 3.2.8-3.2.10). The stability assays revealed an enhanced stability over time for UiO-67 coated with PEG and DNA. This is particularly noteworthy in PSF, where a high increase in the size of non-coated NMOFs occurs due to the presence of salts leading to aggregation.

Similarly, NU-1000 and PCN-222 exhibit high colloidal stability after functionalization. However, bare particles show a tendency to agglomerate, especially in PSF and DMEM, where a noticeable increase in particle size is observed after 6 hours. Upon coating with PEG or DNA molecules, there is a clear stabilization, demonstrating the effectiveness of both coatings in

USC DE COMPOSTELA

enhancing the colloidal stability of NMOFs in biological media. This addresses one of the main challenges associated with these NMOFs.

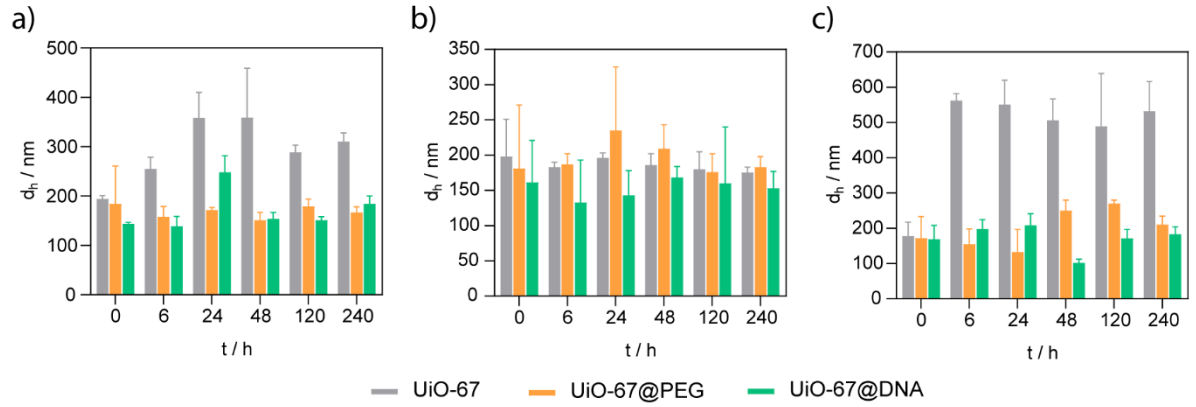

Figure 3.2.8. Colloidal stability of UiO-67 samples over time in a) water, b) DMEM and c) PSF media, as determined by DLS. Experiments were carried out using n = 3. Error bars represent standard deviation.

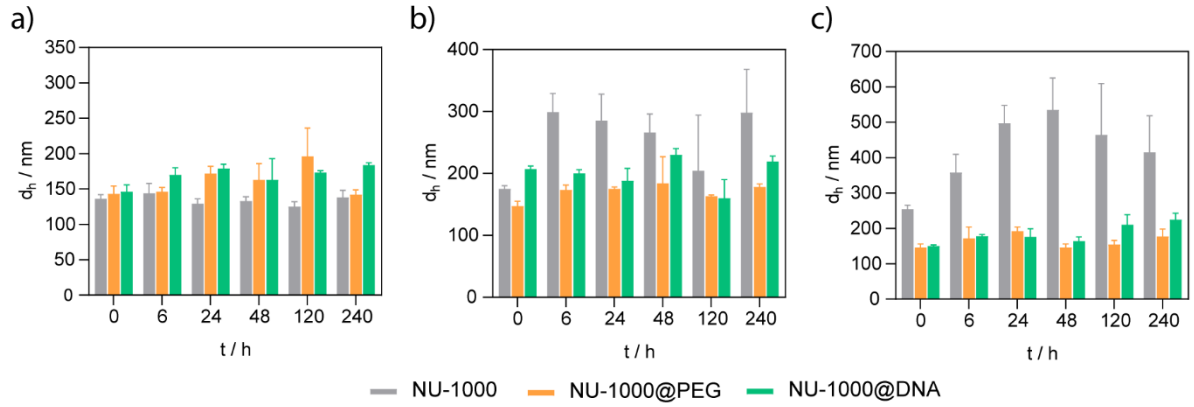

Figure 3.2.9. Colloidal stability of NU-1000 samples over time in a) water, b) DMEM and c) PSF media, as determined by DLS. Experiments were carried out using n = 3. Error bars represent standard deviation.

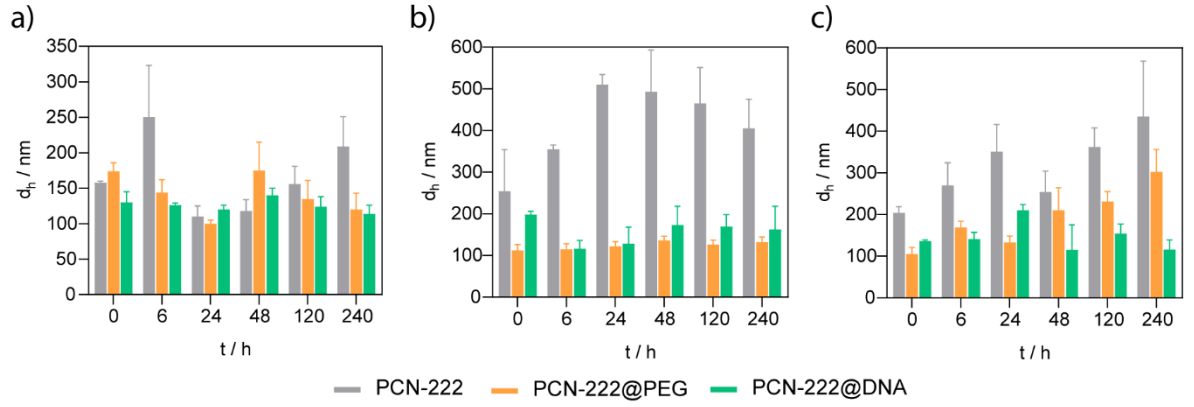

Figure 3.2.10. Colloidal stability of PCN-222 samples over time in a) water, b) DMEM and c) PSF media, as determined by DLS. Experiments were carried out using n = 3. Error bars represent standard deviation.

USC
UNIVERSIDADE DE SANTIAGO DE COMPOSTELA

Particles were further studied to check the efficiency of the coating by analyzing the presence of P by means of ICP. ICP measurements were performed for both the samples with PEG-PO_3 and DNA-PO_3 and the corresponding supernatant (SN) saved after the washing steps to study the relation between Zr and P. Tables 3.2.10 and Table 3.2.11. present the wt% of PEG or DNA for each sample. These results were obtained using the relation between the quantity of P in the stock and in the samples, measured using ICP.

Table 3.2.10. wt% and mol of DNA per MOF calculated from ICP measurements.

	wt% (DNA)	mol DNA/MOF
UiO-67@DNA	3.15 ± 1.13	5.98 x 10^2
NU-1000@DNA	4.15 ± 2.73	1.49 x 10^2
PCN-222@DNA	2.58 ± 1.54	3.92 x 10^2

Table 3.2.11. wt% and mol of PEG per MOF calculated from ICP measurements.

	wt% (PEG)	mol PEG/MOF
UiO-67@PEG	5.08 ± 3.42	1.34 x 10^3
NU-1000@PEG	5.31 ± 2.26	8.36 x 10^2
PCN-222@PEG	9.12 ± 2.31	6.95 x 10^2

3.2.3. Click chemistry protein functionalization of UiO-67

These results proved the successful functionalization of the Zr NMOFs family using phosphate modified biomolecules. However, the offer of biomolecules that can be modified with this terminal groups for this purpose are limited, and consequently, the coordinative PSM method. Therefore, further possibilities need to be explored to achieve the addition of specific moieties in the surface of the nanoparticles to provide them with needed targeting capabilities.

Specifically, the accumulation of NPs in cancer cells can take place via two different approaches due to the pathophysiological conditions of the tumor microenvironment (TME): passive and active targeting. [210][224] In the first case, the nanocarriers accumulate in the tumor due to the high permeability of vasculature in cancer tissue. This is called enhanced permeability retention (EPR) effect. The latter case is referred to the functionalization of the nanocarriers to achieve ligand-receptor interactions with high specificity towards targeted cells. In this case, NPs are generally functionalized with biomolecules as antibodies, proteins, or peptides. In particular, the use of proteins that generate cancer cell receptor responses have been widely studied for active drug delivery.[210] One of the most commonly used proteins with NMOFs is bovine serum albumin (BSA). With a molecular weight of 66.5 kDa and a length of 7.2 nm, BSA offers numerous advantages for its application in biomedicine. These include its

USC UNIVERSIDADE DE SANTIAGO DE COMPOSTELA

low cost, ease of preparation, aqueous solubility, high stability, good biocompatibility, and high biodegradability.[225] [224] Additionally, albumin receptors are overexpressed in several cancer cells, such as the secreted protein acidic and rich in cysteine (SPARC). Acting as a key transmembrane receptor for albumin, SPARC's overexpression can significantly enhance the cellular uptake of albumin-coated nanoparticles. Therefore, the use of this protein in NMOFs surface can actively target tumors through receptor-mediated endocytosis. [225][226]

Here, a novel approach for protein functionalization of NMOFs is presented. This method utilizes DNA chains as anchor points on the surface of the particles. In this study, calcein loaded UiO-67 NMOFs were selected as a model for the Zr-family.

3.2.3.1. Protein surface functionalization

BSA was provided with two functionalities before performing the next experiments. First, it was modified with DBCO-NHS-ester groups to generate DBCO groups as anchor points for click chemistry reactions. Additionally, it was modified with Cy5-NHS to provide it with fluorescence for later microscopy experiments. BSA was marked using reported protocols for the addition of antibodies or proteins.[227] This approach is based on the strong reactions between the NHS esters with the primary amino groups in a protein (amino terminus and ε-amino group of lysine) at pH 7.0–9.0.[228] Under these conditions, the reaction results in the formation of a stable amide bond between the primary amines and the NHS conjugate. The correct functionalization with DBCO and Cy5 molecules was proved using different characterization techniques. Initially, the concentration of BSA was determined using BCA assays, while the fluorescence properties were assessed through fluorescence measurements. Studies of Cy5 in the resulting protein were compared with a Cy5 calibration curve in PBS. This facilitated the quantification of Cy5 per protein, resulting in a molar relation of 5 mol of Cy5 per mol of BSA. Subsequently, the structure of the labeled protein was verified using circular dichroism (CD) spectra, corroborating the preservation of the alpha helix structure of BSA following both functionalization processes (Figure 3.2.11.a).[229]

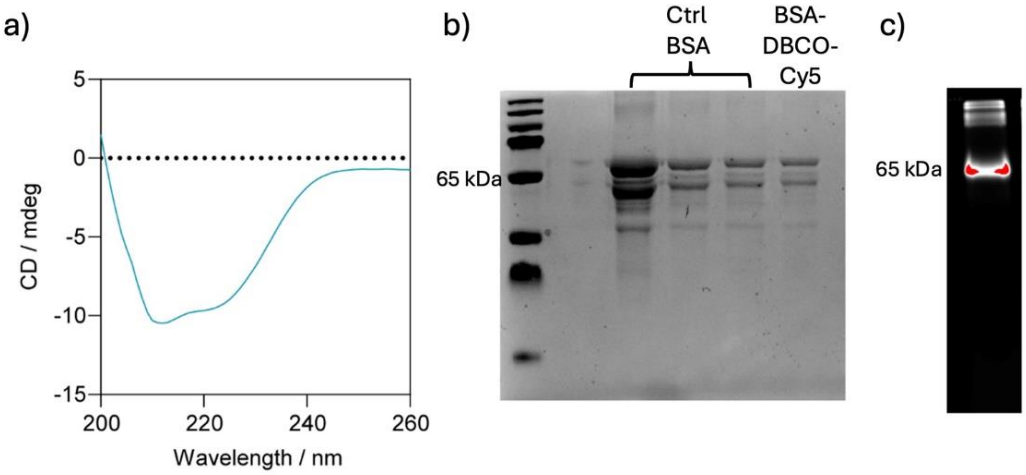

Figure 3.2.11. a) CD spectrum of BSA marked with DBCO and Cy5 molecules, b) Polyacrylamide gel electrophoresis of standard BSA samples at three different concentrations and modified BSA with DBCO and Cy5, c) Polyacrylamide gel electrophoresis of marked BSA with DBCO and Cy5 visualized in Cy5 channel.

USC UNIVERSIDADE DE SANTIAGO DE COMPOSTELA

Additionally, polyacrylamide gel electrophoresis was employed to assess the stability of BSA and detect any potential free Cy5 present in the sample. Figure 3.2.11.b shows a main band at 65 kDa confirming the size of the BSA (66 kDa). The gel also presents other bands due to impurities of the commercial protein. Figure 3.2.11.c corresponds to the Cy5 fluorescence that is clearly attached to the protein. The BSA structure can be observed in Figure 3.2.12.a-b.

After confirming the correct BSA labelling with DBCO and Cy5, a new approach for the surface functionalization of NMOFs was developed. From now on, BSA-DBCO-Cy5 will be referred as BSA for simplicity.

For this experiments, UiO-67 was selected as a model Zr family NMOF. To provide the particles with fluorescence for further *in vitro* experiments, calcein, a polyanionic fluorescein derivative, was utilized as a fluorescent probe and encapsulated within the pores of the structure to obtain UiO-67(Calc). Calcein exhibits fluorescence that is largely independent of pH within the range of 6.5 to 12. This green fluorophore is inherently impermeable to cells; therefore, its internalization can only be observed when it is transported using a carrier. The loading procedure followed the methodology previously employed for CV.

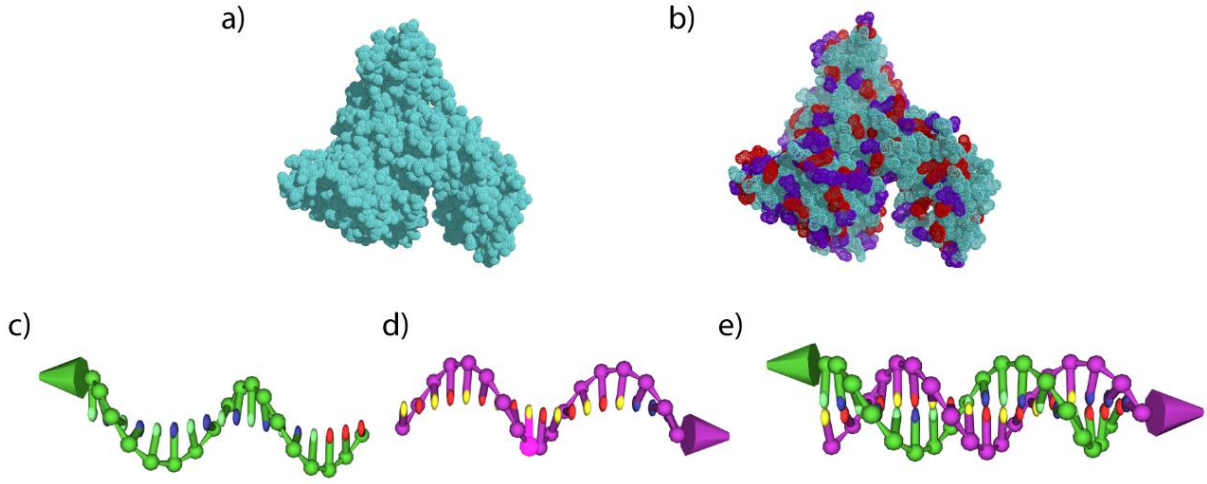

Figure 3.2.12. a) BSA structure and b) BSA structure showing the positive (red) and negative (purple) residues. Images obtained with PyMOL Molecular Graphics System, Version 1.2r3pre, Schrödinger, LLC. Selected oligos for surface functionalization c) NanoTag, d) cNanoTag, e) Hybridize Nanotag + cNanotag.Images obtained with oxView.[230,231]

The proposed surface functionalization was based on several steps. First, UiO-67(Calc) was functionalized with DNA-PO_3 following the previous protocol to obtain UiO-67(Calc)@DNA. Then, these chains in the surface of the MOFs were hybridized with complementary oligos modified with azide groups in the 5' ends (DNA-N_3), resulting in UiO-67(Calc)@DNAds. Using the free N_3 groups, click chemistry reactions were performed between the DBCO groups of the BSA and the N_3, enabling the addition of the protein to the system via covalent bonding (UiO-67(Calc)@DNA-BSA). Specifically, the followed protocol was:

i. *DNA-PO_3 coating* (see section 3.2.2.). For these experiments, DNA modified in the 5' end with the PO_3 group (nanotag_PO_3) was added to the structure allowing the coordination of PO_3 groups with Zr present on the surface of the UiO-67 (Figure 3.2.12.c., Table 3.2.12.).

USC UNIVERSIDADE DE SANTIAGO DE COMPOSTELA

ii. *DNA hybridization*: the complementary chain of the selected oligo for the previous step was modified with an azide group N_3 in the 5' (cNanoTag_N_3). The oligo was added in a ratio 1:1 to allow the hybridization and left for 1 h at 26ºC (Figure 3.2.12.d-e., Table 3.2.12.).[232,233]

iii. *BSA functionalization*. The selected protein (BSA) labelled with Cy5 and DBCO was added in molar excess to the DNA functionalized nanoparticles and left overnight at 4ºC to allow the click chemistry reaction between the DBCO groups attached to the protein and the azide groups on the surface of the UiO-67.

Table 3.2.12. DNA sequences employed.

Name	Sequence	End modification
NanoTag_PO_3	TTTCACACACACACACAC	5': Phosphate
cNanoTag_Azide	TTTGTGTGTGTGTGTGTG	5': Azide

Besides this functionalization, UiO-67(Calc) NMOFs were further functionalized in parallel with PEG-PO_3 as previously described, to obtain UiO-67(Calc)@PEG, to carry out comparison *in vitro* experiments.

3.2.3.2. Structural characterization

Scanning microscopy images (SEM) showed neither changes in the size nor in the morphology of the particles before and after the addition of the protein (Figure 3.2.13.). DLS measurements of the hydrodynamic diameter do not present any relevant changes, except a slight increment for the modified particles due to the functionalization of the surface. UiO-67(Calc) presents a d_h = (183 ± 7) nm, whereas after the DNA and the BSA coatings it changes to d_h = (188 ± 5) nm and d_h = (200 ± 8) nm, respectively (Figure 3.2.14.a). The addition of BSA presents an increment in particle size that may be attributed to the dimensions of the protein (~8 nm).[234] Moreover, BSA may partially penetrate into the DNA layers of the coated particles, resulting in repulsion of hydration water and, consequently, a denser coating layer than for UiO-67(Calc)@DNA.[235,236] On the other hand, ζ potential values after the functionalization present a clear decrease in the surface charge with respect to UiO-67(Calc). The calcein loaded MOFs show surface charge values of (15 ± 1) mV, whereas after for UiO-67(Calc)@DNA it is decreased to (-25 ± 1) mV. The addition of BSA slightly changes the total charge to (-25 ± 1) mV in UiO-67(Calc)@DNA-BSA due to the negative character of the protein. On the other hand, as shown in previous studies, the addition of PEG does reduce the total charge to (-6 ± 2) mV in UiO-67(Calc)@PEG due to the neutral character of the molecule (Figure 3.2.14.b).

The quantification of the attached protein to the surface of the NMOFs was characterized using fluorescence measurements. By measuring the Cy5 in the SN after the washing steps following the functionalization protocol, a quantity of (2,03 ± 0,01) wt% of BSA per UiO-67 was obtained, corresponding a molar relation of 600 BSA per particle. Assuming a size of 7.2 nm of the BSA and assuming a spherical shape of the UiO-67 particles with diameter of 180 nm, a maximum of 661 proteins per MOF's surface were estimated. Therefore, the obtained

USC UNIVERSIDADE DE SANTIAGO DE COMPOSTELA

value indicates a high yield of surface functionalization considering almost all the BSA is in the surface.

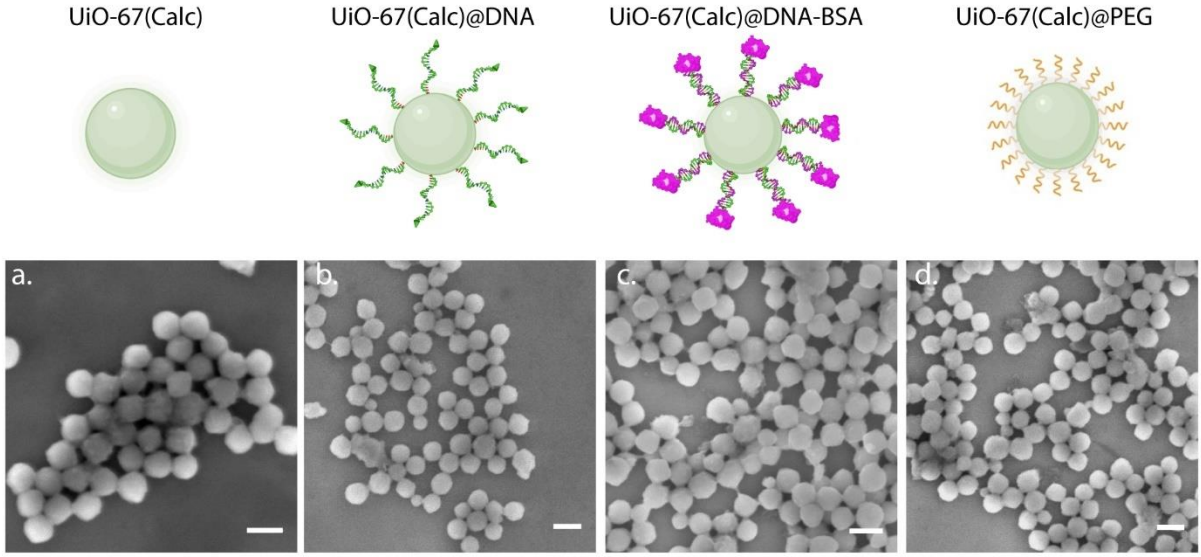

Figure 3.2.13. FE-SEM images of a) UiO-67(Calc), b) UiO-67(Calc)@DNA, c) UiO-67(Calc)@DNA-BSA and d) UiO-67(Calc)@PEG. Scale bars 200 nm.

UV-Vis spectra showed no significant changes among the samples. This can be due to the high signal generated by the UiO-67 at lower wavelengths, that "mask" the DNA and protein absorption spectrum. The peak corresponding to the calcein can be clearly observed for λ = 488 nm in all samples, proving the small calcein leakage after the functionalization. On the other hand, the presence of BSA is corroborated as the Cy5 signal is clearly appreciated by a band at λ = 630 nm (Figure 3.2.14.c).

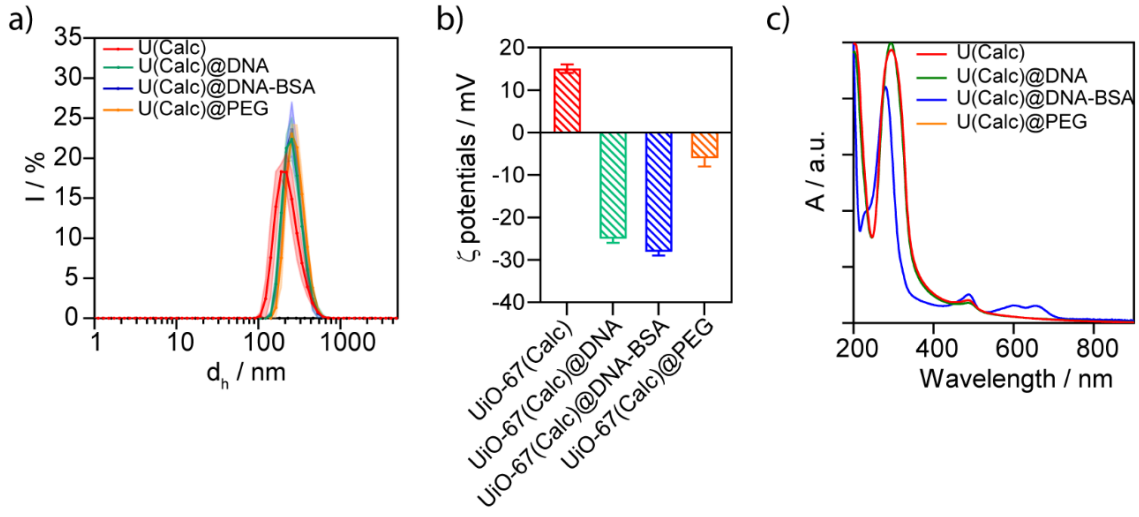

Figure 3.2.14. a) Number distribution of the d_h measured by DLS, b) ζ potentials and c) UV-Vis spectra of all the samples before and after the functionalization (normalized to λ = 300 nm). Experiments were carried out using n = 3. Error bars represent standard deviation.

NTA measurements were further performed to confirm the size of the particles as well as their concentration (Figure 3.2.15, Table 3.2.13.). To complement these values, ICP-OES measurements were analyzed to evaluate the concentration of Zr per mL of the particle solution.

This way, assuming particle size and morphology remains constant after functionalization (based on previous results), ICP, NTA and flow cytometry values can be combined to know the particle concentration in all cases (Table 3.2.13.).

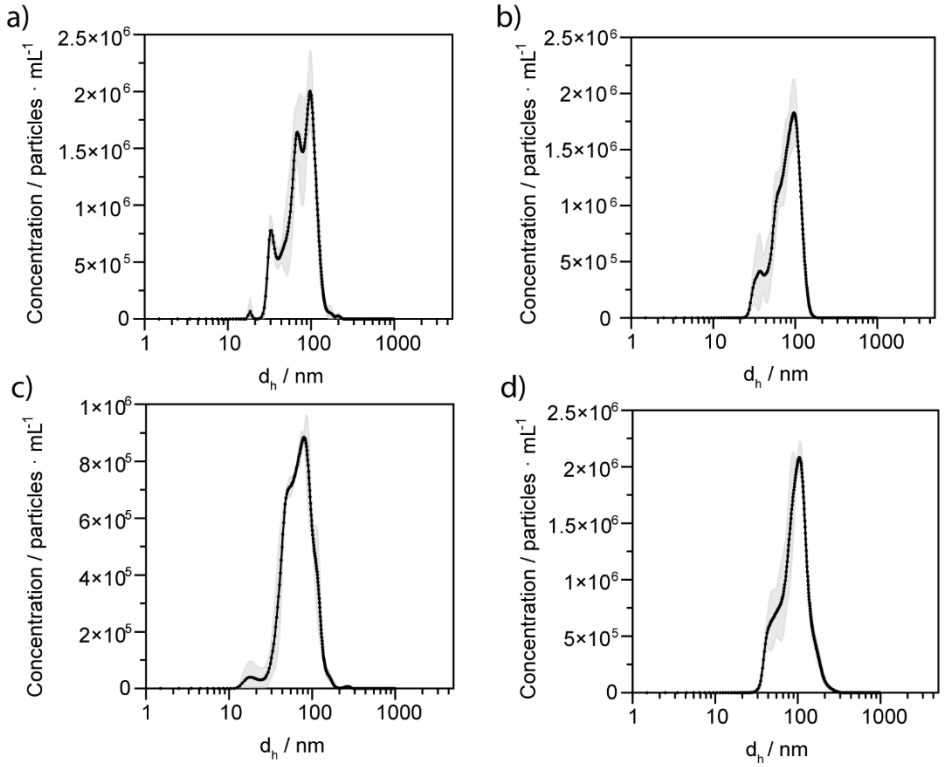

Figure 3.2.15. NTA measurements of a) UiO-67(Calc), b) UiO-67(Calc)@DNA, c) UiO-67(Calc)@DNA-BSA, d) UiO-67(Calc)@PEG. Experiments were carried out using n = 3. Error bars represent standard deviation.

Table 3.2.13. ICP measurements of Zr concentration and corresponding molarity and concentration in particles·mL^{-1} calculated from NTA measurements.

	mg·mL^{-1} Zr	nM	Particles·mL^{-1}
UiO-67(Calc)	3,75	8,63	5,20E+12
UiO-67(Calc)@DNA	2,75	6,33	3,81E+12
UiO-67(Calc)@DNA-BSA	1,50	3,45	2,08E+12
UiO-67(Calc)@PEG	2,81	6,44	3,88E+12

Additionally, fluorescence measurements of the particles in a same concentration were carried out using a plate reader. This way, the calcein signal in each sample was analyzed to normalize the final uptake results. Values are presented in Table 3.2.14., showing slight differences among the calcein cargo in each sample. All particles were expected to display similar calcein fluorescence intensities. However, variations arose in the overall fluorescence due to the presence of DNA and BSA, as well as differences in the washing procedures. In the

case of BSA-functionalized NMOFs, there is a higher reduction of the calcein signal that may be due to the losses of the dye when the protein is attached to the surface due to the extra washing steps and to the possible displacement of calcein molecules if BSA partially enters in the surface of the NMOFs. These results will be taken into consideration in further *in vitro* studies.

Table 3.2.14. Fluorescence measurements of each sample and corresponding correction factor calculated from the UiO-67(Calc)

	Fluo (intensity)	Correction factor
UiO-67(Calc)	2909	1
UiO-67(Calc)@DNA	2004	0.68
UiO-67(Calc)@DNA-BSA	1264	0.43
UiO-67(Calc)@PEG	3213	1.10

3.2.3.3. 2D cell culture experiments

Next, the interaction of the NMOFs with cells was evaluated in 2D cell cultures of A549 lung adenocarcinoma cells. Their biocompatibility was assessed using the MTT assay. The concentrations used were up to 200 pM, showing no significant toxicity for any of the samples (Figure 3.2.16.).

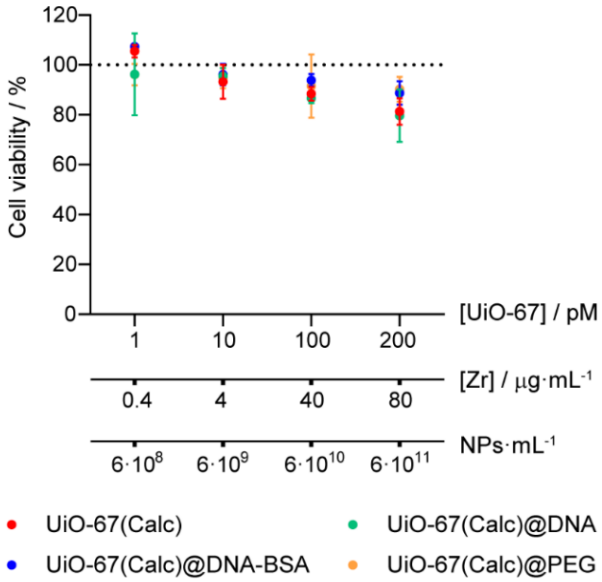

Figure 3.2.16. Cell viability results of the particles after 24 h incubation in A549 cells using MTT toxicity assay. Experiments were carried out using n = 3. Error bars represent standard deviation.

USC UNIVERSIDADE DE SANTIAGO DE COMPOSTELA

After confirming the low toxicity of the NMOFs, cell uptake studies were conducted using fluorescence microscopy and flow cytometry. Notably, since calcein molecules cannot permeate cell membranes unaided, the presence of green fluorescence within the cells in both cytometry and microscopy experiments would indicate successful dye encapsulation within the NMOFs.

Initially, the uptake of NMOFs was quantitatively assessed using flow cytometry with the A549 cell line. UiO-67 NMOFs were exposed to incubation periods of 0.5, 1, and 3 h at a concentration of 1 x 10^{10} particles·mL^{-1} (Figure 3.2.17.). Due to previous observed differences in the calcein signal of each sample, it was crucial to normalize the uptake values relative to the total fluorescence of the NMOFs using a correction factor (Table 3.2.14.). The four systems exhibited greater internalization with longer incubation times, as evident in Figure 3.2.17. As expected, the Cy5 signal was only detected in the UiO-67(Calc)@DNA-BSA sample, proving the successful functionalization of the particles with the protein. Following the application of the correction factor, Figure 3.2.18 illustrated a noticeable increase in the internalization rate of UiO-67(Calc)@DNA-BSA, contrasting sharply with the significantly reduced uptake observed for UiO-67(Calc)@PEG particles, as expected. Additionally, UiO-67(Calc)@DNA demonstrated improved cell recognition relative to bare UiO-67(Calc), indicating a notable enhancement in cellular uptake. This might be caused to the spherical arrangement of DNA (SNA) on the surface that increase cellular internalization in comparison to their individual components.

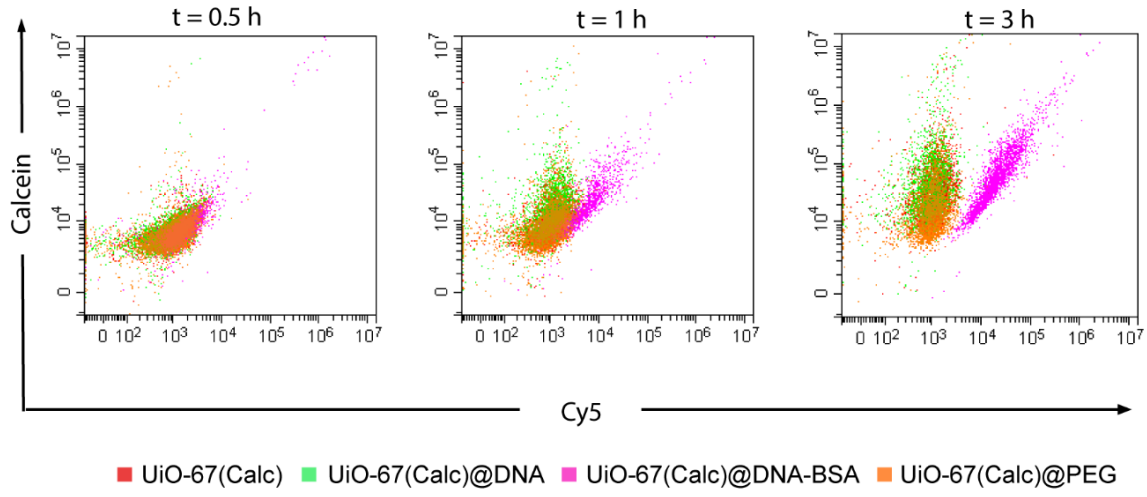

Figure 3.2.17. Flow cytometry uptake experiments conducted with UiO-67 samples in A549 cells at times 0.5, 1h and 3h.

USC UNIVERSIDADE DE SANTIAGO DE COMPOSTELA

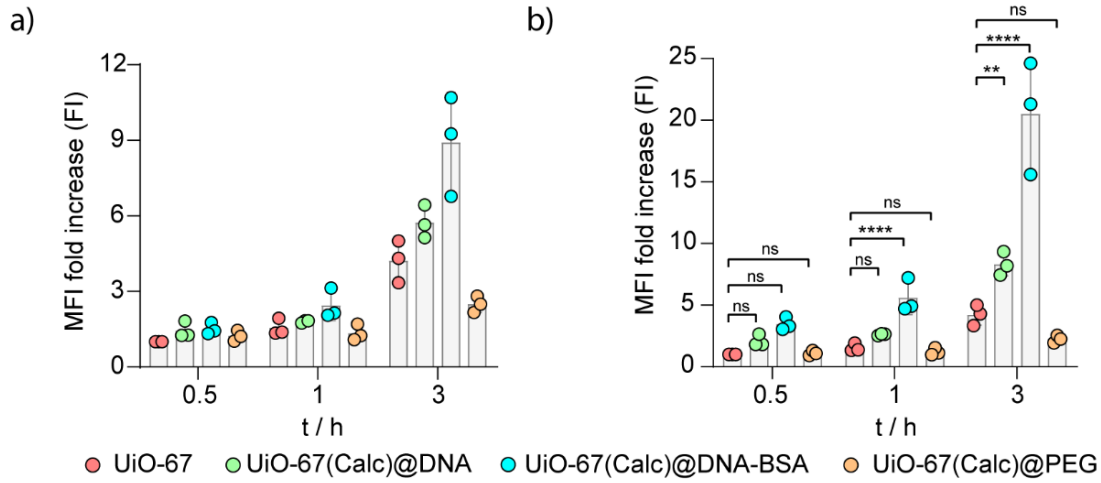

Figure 3.2.18. a) UiO-67 samples uptake in A549 cells and b) corrected values using correction factor obtained from fluorescence measurements. Experiments were carried out using n = 3. Error bars represent standard deviation.

Confocal microscopy imaging experiments were carried out to study the particle internalization and distribution inside A549 cells. The cellular uptake of NPs is influenced by their physicochemical properties, such as its composition, size, or surface functionalization. [210] When nanoparticles interact with the constituents of the plasma membrane, their principal route of entry into the cell is expected to be through endocytosis.[237] To elucidate the internalization process of the NMOFs, the colocalization of each sample with human transferrin (HT) endosome marker was investigated. After binding to its receptor on the cell surface, transferrin undergoes rapid internalization via the formation of clathrin-coated pits, leading to the formation of endocytic vesicles. Figure 3.2.19. shows the microscopy images of each sample after 3 h of incubation using a concentration of 1 x 10^{10} particles·mL^{-1}. Additionally, MemBrite and DAPI markers were employed to identify the cell membrane and the nucleus of the cells, respectively.

Confocal imaging illustrates the robust internalization of calcein-loaded nanoparticles, aligning with the trends observed in the flow cytometry analyses. As previously emphasized, the impermeability of calcein alone across cell membranes proves the efficient internalization mechanism facilitated by the NMOFs. The observed uptake of UiO-67(Calc) (Figure 3.2.19.a) and UiO-67(Calc)@DNA (Figure 3.2.19.b) presents similar tendencies, whereas UiO-67(calc)@PEG (Figure 3.2.19.c) shows a clear reduction in the total particle internalization. However, in the case of UiO-67(Calc)@DNA-BSA (Figure 3.2.19.d), there is a noticeable increase in the total calcein signal, alongside newly observed fluorescence in the Cy5 channel, indicating the presence of BSA, which aligns with the flow cytometry findings. Furthermore, the incorporation of an early endosome marker (HT) serves to validate the endocytic pathway involved in internalization. Across all observations, a clear colocalization between calcein and HT confirms the presence of the samples within endosomes, as hypothesized. Additionally, the colocalization of BSA (Cy5 channel) with both markers (Figure 3.2.19.d) suggests that the coating remains intact even after translocating into lysosomes. Hence, the proposed method has been demonstrated to be an effective strategy for surface modification, offering a broad range of possibilities for the attachment of biomolecules such as proteins, antigens, or peptides.

USC UNIVERSIDADE DE SANTIAGO DE COMPOSTELA

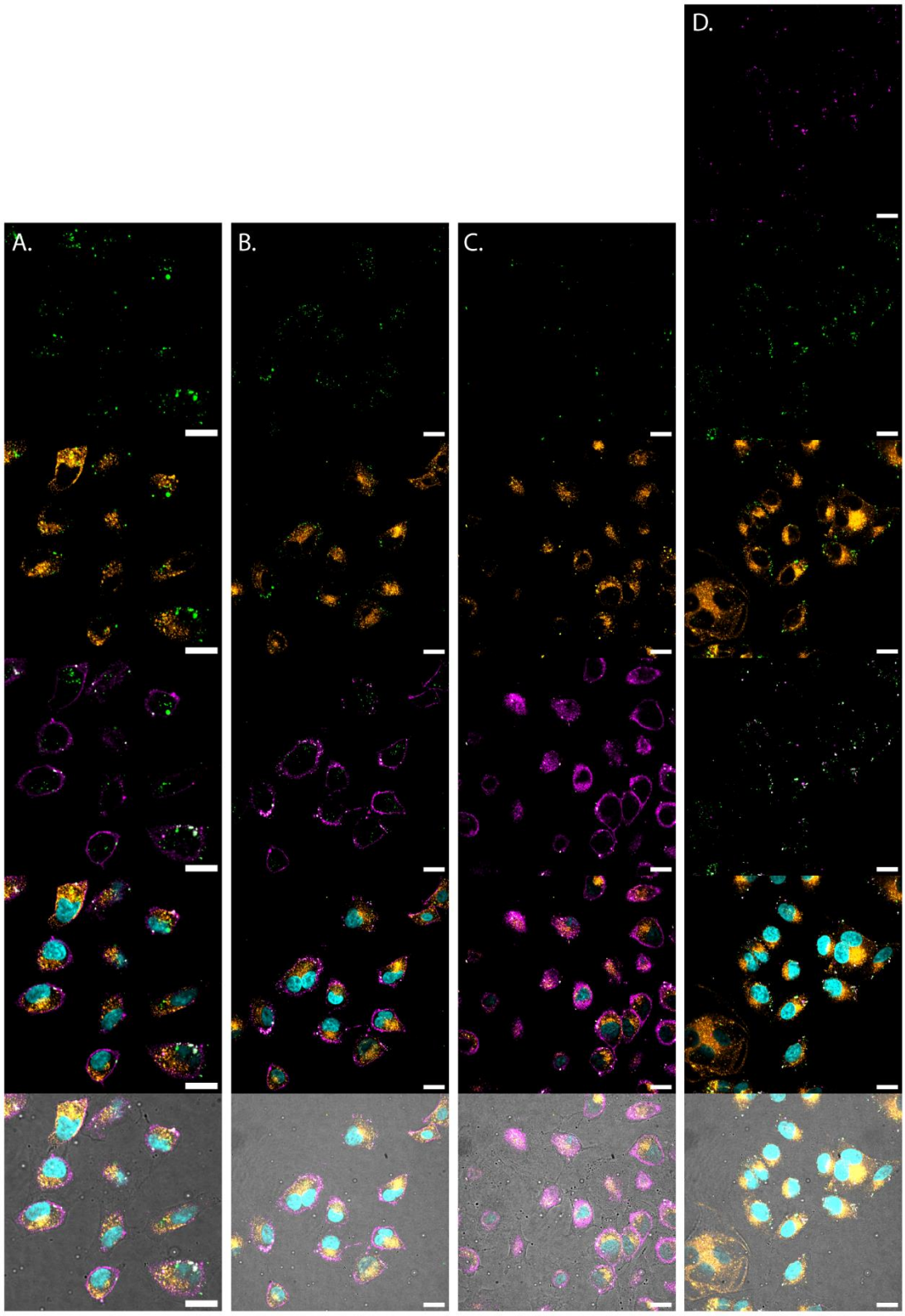

Figure 3.2.19. Confocal images of A549 cells incubated for 3 hours with a) UiO-67(Calc), b) UiO-67(Calc)@DNA, c) UiO-67(Calc)@PEG and d) UiO-67(Calc)@DNA-BSA. For each panel, from up to bottom, images show the fluorescence signal of Calcein (in green), CF®543 Human Transferrin (in orange), overlay of calcein and MemBrite® (in magenta) (except for d. that correspond to Cy5 marked BSA, calcein + cy5), merged of the three fluorescence signals and DAPI to mark the nucleus in cyan (green + orange + magenta + cyan) and merged + brightfield. Scale bars: 20 μm.

Moreover, this new approach for protein functionalization of NMOFs holds great potential to create a stable and biocompatible platform for vaccine delivery. This strategy can offer several advantages, including enhanced antigen stability, controlled release kinetics, and improved immune response modulation.

Furthermore, the precise control over the density and configuration of viral proteins on the NMOF surface might enable the design of highly efficient and specific vaccine formulations that closely mimic the natural infection process, thereby generating a potent immune response. [238]

Further research and development in this area have the potential to revolutionize vaccine technology, leading to the creation of more effective and accessible vaccines for a wide range of diseases.

USC
UNIVERSIDADE DE SANTIAGO DE COMPOSTELA

Part of the results presented in the following chapter are published in:

"Light-Responsive Nanoantennas Integrated into Nanoscale Metal-Organic Frameworks for Smart Drug Delivery". Small Science. (Published in **2024**)

Manuela Cedrún-Morales[1], Manuel Ceballos[1], Enrica Soprano[1], Giulia Zampini[1], Ester Polo[1], Beatriz Pelaz[1] and Pablo del Pino[1]

[1]*Center for Research in Biological Chemistry and Molecular Materials (CiQUS), University of Santiago de Compostela, 15705 Santiago de Compostela, Spain.*

Contributions: Preparation, optimization, and characterization of the materials, cell studies; writing – original draft.

Impact Factor: 12.7. Q1 in Nanoscience & Nanotechnology.

USC
UNIVERSIDADE DE SANTIAGO DE COMPOSTELA

3.3. LIGHT RESPONSIVE NANOANTENAS INTEGRATED INTO NMOFS FOR PHOTOTHERMAL DRUG DELIVERY

The pursuit of precision medicine—an approach where treatments are personalized based on an individual's genetic profile and environmental interactions—is increasingly becoming a tangible goal, propelled by breakthroughs in drug delivery technologies. Central to this progress is the innovative use of nanotechnology, particularly through the development of advanced nanocarriers, which promises to direct therapeutic agents to the site of pathology with unparalleled precision. The evolution of such advanced nanomedicines is set to transform treatment paradigms, making them not only more effective but also minimally invasive, thus offering fresh optimism in addressing longstanding healthcare challenges.

Among the various innovations in the field of drug delivery, the concept of controlled release stands out as a transformative approach. It aims to precisely manage the rate and location of drug administration, enhancing therapeutic effectiveness by maintaining optimal drug levels at the target site for the required duration. This approach is crucial in reducing side effects and improving patient compliance, especially in treatments like chemotherapy where the margin between effective and toxic doses is narrow.

The evolution of nanocarriers, including liposomes, solid lipid nanoparticles (NPs), dendrimers,[239] polymeric, and/or inorganic NPs, has been instrumental in advancing targeted therapy. Engineered to navigate the body's complex biological landscape, these nanoscale vehicles are designed to evade immune detection and accurately release their therapeutic payload directly at the site of the disease. The integration of these carriers with stimuli-responsive mechanisms marks a substantial advancement in drug delivery technology. The employment of NIR light for non-invasive targeting, alongside other stimuli like ultrasound, alternating magnetic fields, and uncaging chemistry, expands the horizon of therapeutic possibilities. These methods offer various mechanisms—mechanical, thermal, and chemical—for precise drug activation and release, showcasing the versatility and sophistication of smart drug delivery systems in meeting diverse therapeutic needs with high precision and efficiency.[129]

The rationale for choosing NIR light, specifically within the optical biological windows (650 to 1350 nm), is strategic for its deep tissue penetration and minimal absorption by water and hemoglobin, facilitating targeted intervention with reduced risk to surrounding non-targeted tissue. Recent studies underscore the potential of NIR light in enhancing the efficacy of drug delivery systems.[240,241] Similarly, significant advances on porous plasmonic nanosystems highlights the integration of thermoplasmonic effects with NIR light for remote delivery and/or activation of drugs in living cells.[20,197,242]

NMOFs serve as versatile platforms with remarkable porosities, allowing for the encapsulation of a diverse range of molecules. However, the development of precision drug delivery systems (DDSs) generally benefits of precise regulation of drug release to avoid lack of effectivity and undesirable side effects.[129] Stimuli-responsive NMOFs represent a promising solution to solve these problems, integrating the outstanding properties of these materials with the stimuli-controlled delivery of the encapsulated cargo.[169,206] The strategic combination of light-responsive agents with NMOFs allows the development of DDSs capable of controlled cargo release through conformational changes or photothermal conversion under illumination. Hence, the creation of new core-shell nanocomposites, featuring an Au NP core

USC UNIVERSIDADE DE SANTIAGO DE COMPOSTELA

within an NMOF, give rise to a synergistic effect between both components, presenting an excellent candidate for an advanced DDS.[197,206]

Herein the study is focused on the design of microporous plasmonic nanosystems based on ZIF-8 and NU-1000, that serve as nanoplatforms for encapsulating specific cargo with controlled triggered release employing NIR as external stimulus. Building upon previous work demonstrating enhanced stability in different NMOF structures after surface modification using polymers, ZIF-8 and NU-1000 NMOFs were selected for investigating their potential as NIR-controlled DDSs. The proposed nanocomposites (NCs) feature a plasmonic core, which consists of a light-responsive gold nanobipyramid (AuBy) that is encapsulated by a NMOF, creating a core-shell NC structure. These systems effectively combine the optical properties of the AuBy with the porosity and protective features of the NMOF shell. The NMOF shell serves as a support to load and retain the selected cargo molecule, while the NIR-responsive plasmonic core facilitates selective release upon resonant plasmonic excitation and photothermal heating.

3.3.1. NCs synthesis and characterization

AuBys were synthesized following a previously reported method,[243] utilizing penta-twinned seeds that facilitated the crystallization of pentagonal bipyramids with dimensions of 85.0 ± 5.6 nm in length and 30.9 ± 3.0 nm in width (Figure 3.3.1.a-d), which thanks to their aspect ratio possess a localized surface plasmon resonance (LSPR) at around 810 nm (with slight variations due to the dispersion media, Figure 3.3.1.e). The synthesis of AuBy@ZIF-8 NCs was carried out using a method that included multiple water washing steps and the subsequent redispersion of AuBys in CTAB at a concentration of 0.16 mg·mL^{-1}, as outlined in prior studies.[19,20,197] This surfactant facilitates the growth of ZIF-8 onto the surface of AuBy but does not support the growth of NU-1000, owing to differing synthesis requirements (see below).

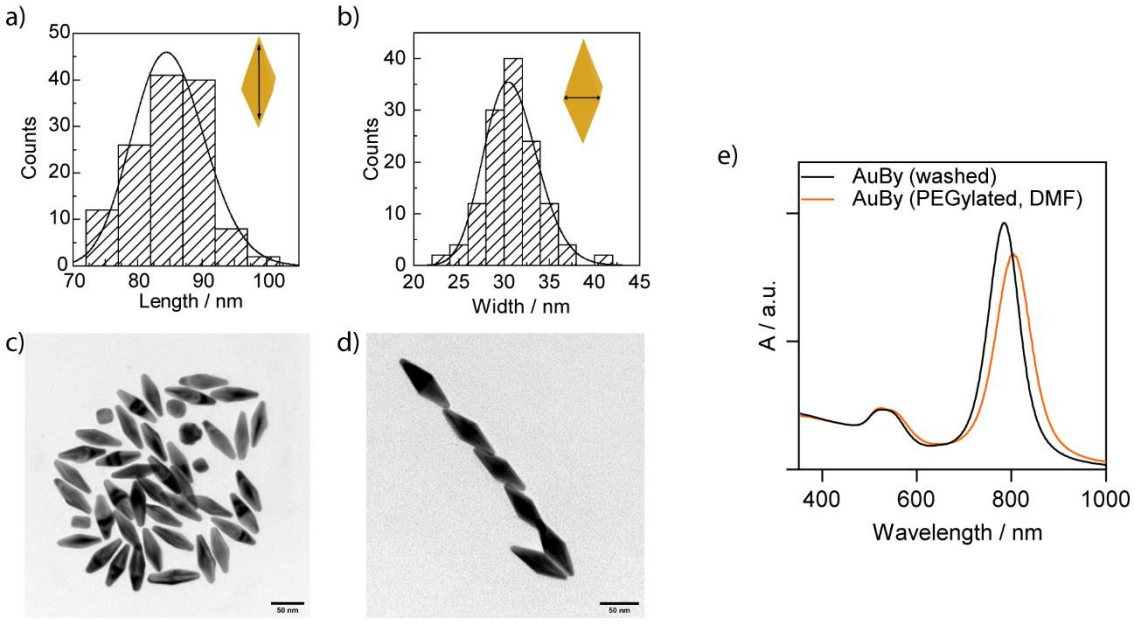

Figure 3.3.1. SEM analysis of AuBy. Size histograms corresponding to the a) length and b) width of the AuBy. SEM images of the c) Washed AuBys (used for AuBy@ZIF-8 synthesis) and d) PEGylated AuBys (used for AuBy@NU-1000 synthesis). e) UV-Vis spectra of the washed AuBys in water and after PEGylation and phase transfer to DMF. Scale bars correspond to 100 nm.

Figure 3.3.2.a-d shows the crystalline structure of the selected ZIF-8 and NU-1000 NMOFs. Field emission scanning electron microscopy images (FE-SEM) of AuBy@ZIF-8 NCs shows a cubic shape, each featuring one AuBy per NCs with a size around 160 ± 18 nm (Figure 3.3.2.e-3.3.3.a). This configuration arises from a seed growth crystallization mechanism that enables the formation of a polycrystalline ZIF-8 shell, facilitated by the presence of CTAB molecules on the AuBy's surface.[244] NCs were loaded with cresyl violet (CV) following a previously described post-encapsulation method (see Chapter 2). Moreover, NCs were functionalized with fluorescein-labelled poly [isobutylene– alt–maleic anhydride]–graft–dodecyl (in the following referred to as PMA) to enhance stability in water,[19,20,197] following previous studies. In Figure 3.3.2.f, FE-SEM images of AuBy@ZIF-8 NCs loaded with CV and coated with PMA reveal that the size and morphology of these functionalized NCs are consistent with those of the non-functionalized counterparts. This step is critical due to the rapid degradation of ZIF-8 when exposed to CO_2 dissolved in water, a process that typically unfolds within minutes.[245] Notably, the ZIF-8 within the PMA-coated NCs remained stable and did not convert into $ZnCO_3$, in contrast to the degradation observed in the non-PMA-coated NCs, as shown in Figure 3.3.4. Further comparison with the PMA-coated NCs (AuBy@ZIF-8(CV)@PMA NCs in Figure 3.3.4.c) confirms their enhanced stability in water, maintaining integrity for a minimum of 7 days.

In the case of AuBy@NU-1000 NCs, the synthetic protocol presents additional challenges owing to the specific conditions required to facilitate NU-1000 growth. These conditions involve the use of organic solvents such as DMF, monocarboxylic acids like acetic acid (HOAc) as modulators, and high temperatures (≥ 90 °C). The primary challenge was to identify an appropriate capping agent that would enable the transfer of AuBys into DMF media. Based on previous reports,[206] a polyethylene glycol linker HS-PEG-MeO (2 kDa) was chosen for the coating. After PEGylation, the AuBys were redispersed in DMF and utilized as seeds in the synthesis of AuBy@NU-1000 NCs. The PEG chains are aimed to attract Zr moieties, initiating the MOF-shell growth.[246] This process resulted in NCs with an average length of approximately 170 ± 16 nm, as illustrated in Figure 3.3.2.g and 3.3.3.b. To provide colloidal stability and prevent particle agglomeration, AuBy@NU-1000 NCs underwent functionalization with MeO-PEG-PO_3 after being loaded with CV (Figure 3.3.2.h).[73] NCs PEGylation preserved their morphology for at least 7 days (Figure 3.3.5.a,b).

The absorption spectra of AuBy@ZIF-8 NCs is shown in Figure 3.3.2.i both in MeOH and for the CV-loaded, PMA-coated variant. An observed red shift in the LSPR absorption band for AuBy near 800 nm can be ascribed to three main factors: i) the transition of the surrounding media from MeOH to water, ii) the incorporation of CV, evident around 600 nm, and iii) the effect of PMA functionalization. This functionalization alters the dielectric environment surrounding the NCs, consequently leading to the observed redshift in LSPR absorption.[247,248]

USC UNIVERSIDADE DE SANTIAGO DE COMPOSTELA

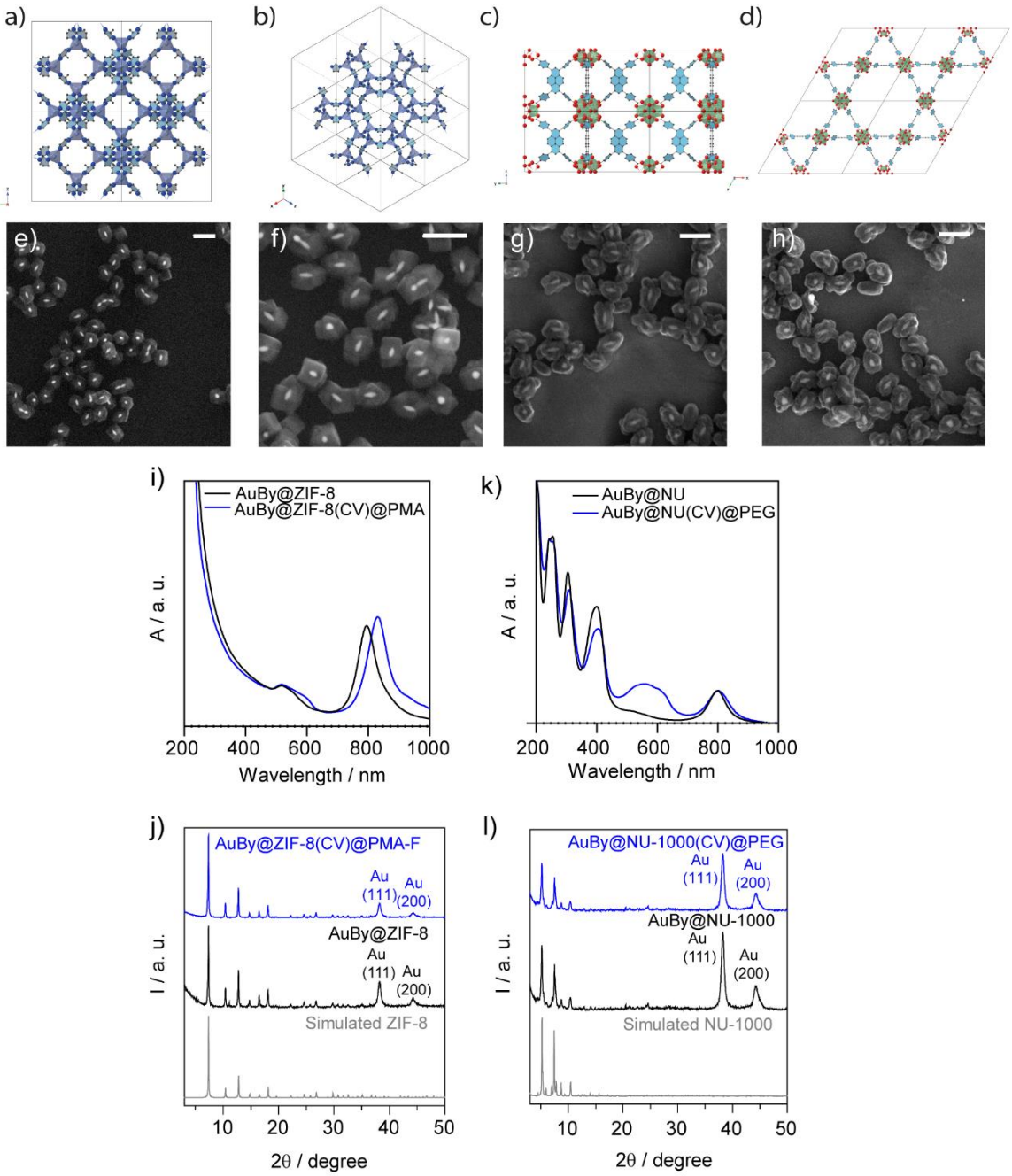

Figure 3.3.2. ZIF-8 and NU-1000 structures: a) from the x-axis and b) the [110] plane for ZIF-8; c) from the a-axis and d) the z-axis for NU-1000. FE-SEM images of e) AuBy@ZIF-8, f) AuBy@ZIF-8(CV)@PMA, g) AuBy@NU-1000, and h) AuBy@NU-1000(CV)@PEG. i) UV-Vis absorption spectra and j) PXRD diffractograms for ZIF-8 based NCs and k) UV-Vis absorption spectra and l) PXRD diffractograms for NU-1000 based NCs. Scale bars correspond to 200 nm.

USC UNIVERSIDADE DE SANTIAGO DE COMPOSTELA

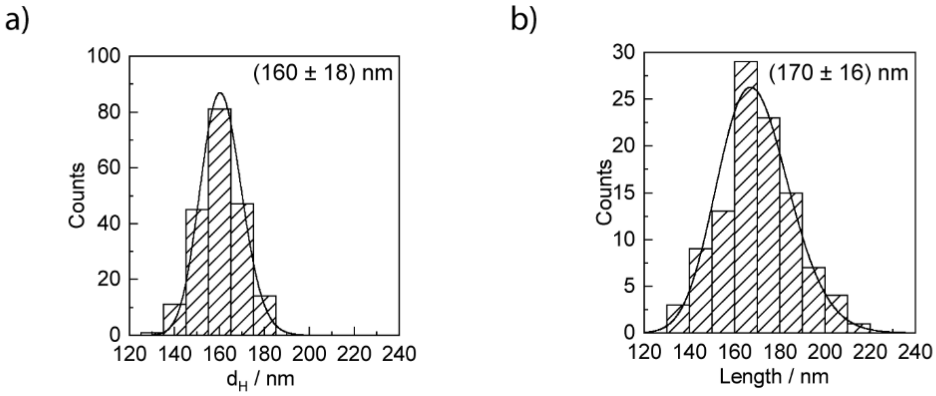

Figure 3.3.3. Size histograms of the synthetized nanocomposites a) AuBy@ZIF-8 and b) AuBy@NU-1000 based on microscopy images.

PXRD diffractograms for AuBy@ZIF-8 NCs and its PMA-coated variant demonstrate the structural stability of the NCs after PMA coating (Figure 3.3.2.j). The patterns align with the simulated PXRD pattern of bare ZIF-8, with the first two Au reflections corresponding to the (111) and (200) crystallographic planes at 38.1º and 44.2º 2θ degree, respectively.

The absorption spectra of AuBy@NU-1000 NCs before and after CV loading and PEGylation is illustrated in Figure 3.3.2.k, highlighting the presence of CV with an absorption band around 600 nm. Notably, no changes in the localized surface plasmon resonance (LSPR) absorption band were observed.

On the other hand, the PXRD diffractograms alongside the simulated pattern of NU-1000, revealing a match with the reflections of the NU-1000 reference at low angles (Figure 3.3.2.l). Furthermore, the first two reflections of Au (111) and (200), akin to the case of AuBy@ZIF-8, are evident. This comparison underlines the stable crystallinity of the NU-1000 structure, even after the processes of CV loading and PEGylation, demonstrating its stability in water for at least one week (Figure 3.3.5.c).

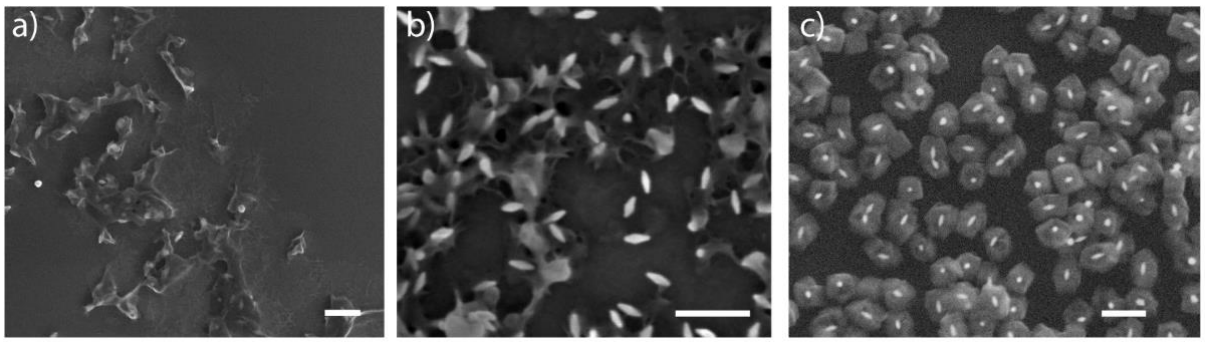

Figure 3.3.4. SEM images of the ZIF-8/NCs placed in water before the PMA coating for a) 5h, b) 24h, and after the PMA coating for c) 7 days.

USC
UNIVERSIDADE DE SANTIAGO DE COMPOSTELA

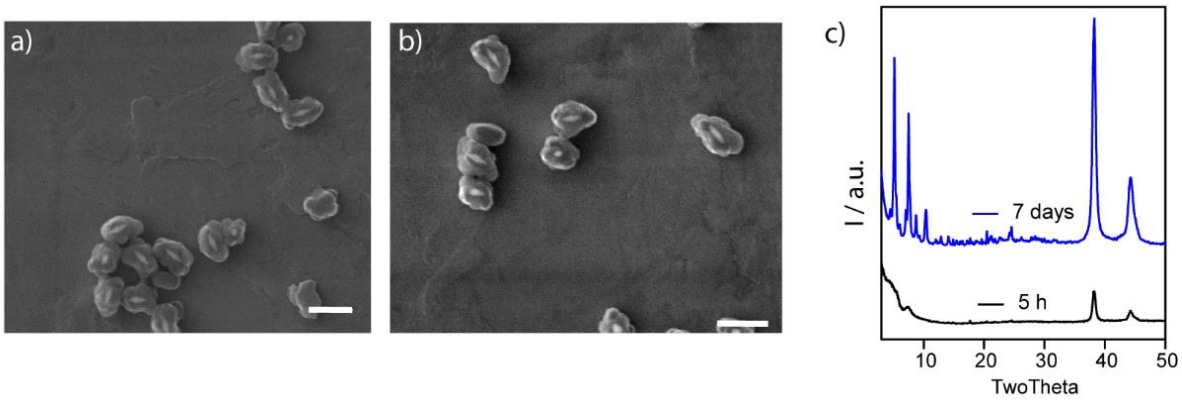

Figure 3.3.5. SEM images of the NU-1000/NCs placed in water a) before the PEG coating and b) after the PEG coating for 7 days, c) PXRD patterns of AuBy@NU-1000(CV)@PEG after 7 days in water (Blue) and AuBy@NU-1000 after 5 hours in water.

The quantification of CV encapsulation was performed by measuring fluorescence in the supernatants (SN) after washing steps, before and after polymer functionalization. CV encapsulated per MOF was calculated by comparing SN fluorescence to calibration curves in MeOH and water. The ZIF-based NC exhibited an 8 wt% CV content before the coating process, which was reduced to 6 wt% following the addition of PMA. This reduction suggests that the polymer may enter the pores, displacing the CV, consistent with expectations from previous studies.[197] This wt% corresponds to an estimated value of $1.5 \cdot 10^5$ CV per NC. On the other hand, the NU-1000-based NC demonstrated similar trends, with a 13 wt% CV content before coating and a 10 wt% post-PEGylation, leading to $9 \cdot 10^5$ CV per NC, thus, proving the higher encapsulation capacity of the NU-1000 compared to ZIF-8 thanks to their bigger pore sizes.

The adsorption capacities of the NCs were assessed through N_2 adsorption isotherms, as illustrated in Figure 3.3.6. The type I isotherm of ZIF-8 NCs is preserved post-loading with CV, albeit with reduced N_2 uptake, decreasing from 375.2 $cm^3 \cdot g^{-1}$ before cargo loading to 318.7 $cm^3 \cdot g^{-1}$ post-loading (at 0.8 P/P_0) (Figure 3.3.6.a, Table 3.3.1.). Prior investigations have established the inherent flexibility of ZIF-8 structures, facilitating the opening of the window and accommodating larger molecules than its nominal window size,[202] which has been reported to be about 3.4 Å.[164] In the case of the PMA coated sample, a significant decrease in uptake to 221.4 $cm^3 \cdot g^{-1}$ is observed. This reduction can be ascribed to both the filling of pores with alkyl chains from PMA and the hindrance of N_2 diffusion into the pores due to the coating, resulting in substantial loss of the microporosity region.

USC
UNIVERSIDADE DE SANTIAGO DE COMPOSTELA

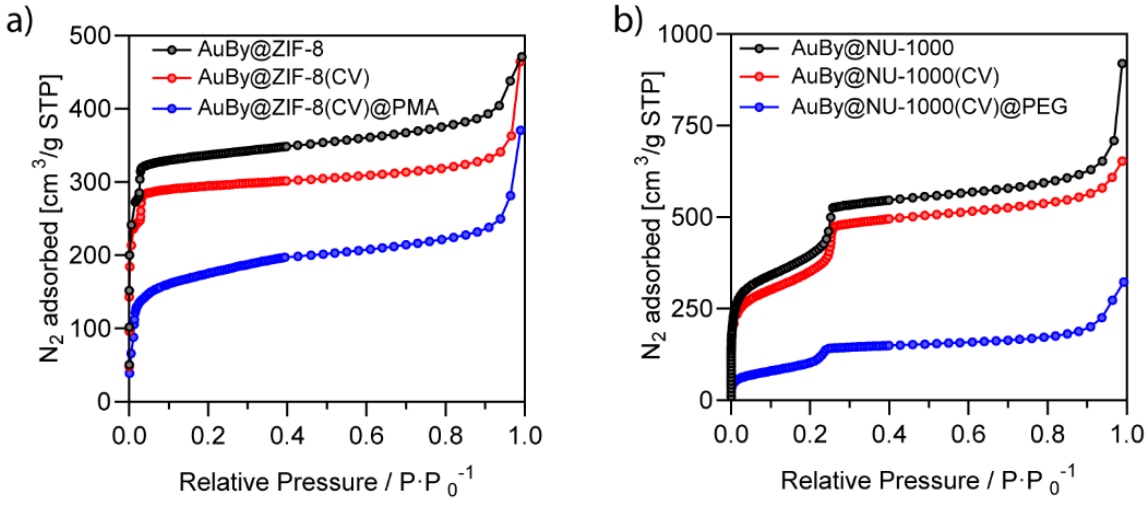

Figure 3.3.6. N_2 adsorption isotherms of a) ZIF-8 NCs and b) NU-1000 NCs

Table 3.3.1. S_{BET} values for ZIF-8 NCs

Sample	S_{BET} / $m^3 \cdot g^{-1}$
AuBy@ZIF-8	1218
AuBy@ZIF-8(CV)	1086
AuBy@ZIF-8(CV)@PMA	650
AuBy@NU-1000	1424
AuBy@NU-1000(CV)	1274
AuBy@NU-1000(CV)@PEG	409

On the other hand, AuBy@NU-1000 exhibited a type IV isotherm, demonstrating an uptake of 593 cm^3 g^{-1} at 0.8 P/P_0 (Figure 3.3.6.b). Upon loading with CV, there was a reduction to 532 $cm^3 \cdot g^{-1}$ attributed to pore occupation. Subsequent PEGylation led to a further decrease in uptake to 172 $cm^3 \cdot g^{-1}$, indicating the infiltration of PEG-PO_3 molecules into the NU-1000 structure, causing a near-complete loss of micropores. BET surface area values were determined using BETSI software (Table 3.3.1), aligning with previously reported values. Notably, the contribution of non-porous gold material to the surface area was considered negligible in comparison to the porous material.

3.3.2. Colloidal stability

The coating of these two NCs with distinct polymers, one physically attached (PMA) and the other chemically attached (PEG-PO_3), aimed to enhance their chemical and structural stability in aqueous media, along with improving their colloidal stability. Figure 3.3.7.

illustrates the colloidal characterization of AuBy@MOF NCs. In Figure 3.3.7.a, DLS measurements of AuBy@ZIF-8 NCs are presented before and after loading with CV, and subsequent coating with PMA. The results revealed that the hydrodynamic diameter (d_h) remained relatively constant at around 160 nm post-loading (Table 3.3.2.). Following PMA coating, a slight increase in size occurred, attributed to the presence of PMA chains on the surface, featuring carboxylic acid groups capable of attracting water molecules and co-ions, thereby marginally expanding the size.[197] These results were corroborated withNTA measurements, allowing the determination of the size and concentration of the samples (particles·mL^{-1}) (Figure 3.3.8.). In Figure 3.3.7.b, ζ-potential measurements of the CV-unloaded and CV-loaded ZIF-8 NCs variants exhibit a decrease from +33.3 mV to +16.7 mV, respectively, possibly attributed to acetate ions from CV binding to the surface. A more significant change is observed when the NCs are coated with PMA, resulting in a ζ-potential of -25.0 mV, indicative of free carboxylic acid groups following the hydrolysis of remaining maleic acid rings.

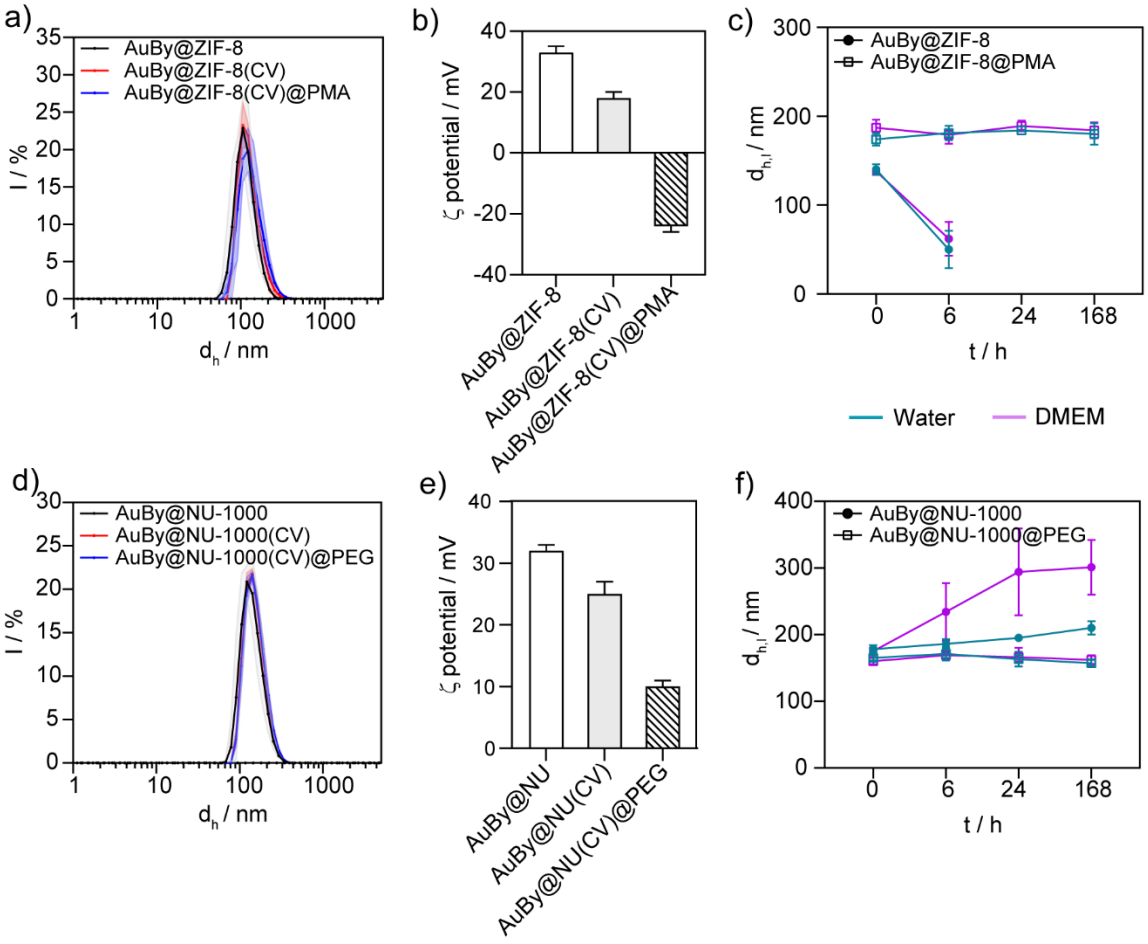

Figure 3.3.7. a) Hydrodynamic diameter (d_h) measurements of AuBy@ZIF-8 NCs by DLS. b) ζ-potential of AuBy@ZIF-8 NCs before and after loading/functionalization. c) Colloidal stability of AuBy@ZIF-8 NCs over time in water and cDMEM media, as determined by DLS. d) d_h measurements of AuBy@NU-1000 NCs by DLS. e) ζ-potential of AuBy@NU-1000 NCs before and after loading/functionalization. f) Colloidal stability of AuBy@NU-1000 NCs over time in water and cDMEM media, as determined by DLS. Experiments were carried out using n = 3. Error bars represent standard deviation.

USC UNIVERSIDADE DE SANTIAGO DE COMPOSTELA

The colloidal stability of AuBy@ZIF-8 is illustrated in Figure 3.3.7.c for both water and completed cell culture media (cDMEM), comparing samples with and without PMA coating. The uncoated sample exhibits a significant reduction in d_h almost instantly in both water and cDMEM, with a near four-fold decrease observed within 6 h. This reduction is attributed to the decomposition of ZIF-8, a finding supported by FE-SEM images presented in Figure 3.3.4. On the contrary, the PMA-coated sample shows remarkable stability, maintaining its hydrodynamic diameter over 168 h. For the NU-1000 based NCs, DLS measurements indicate a stable size profile post-PEGylation around 170 nm, as depicted in Figure 3.3.7.d and Table 3.3.2. This consistency in size is further corroborated by NTA measurements (Figure 3.3.8.). Furthermore, a notable decrease in ζ-potential is observed, dropping from +31.3 mV to +9.9 mV, as illustrated in Figure 3.3.7.e. This reduction is attributed to the negative charge of free phosphate groups, which indicates the successful PEGylation of NU-1000. Despite these changes, colloidal stability in water remains unaffected, both with and without PEGylation. Conversely, within 6 h in cDMEM, the d_h of the NCs nearly doubles, a phenomenon likely due to the presence of salts and amino acids in this medium that affects the colloidal stability of NCs through electrostatic interactions, leading to aggregation. Importantly, this potential destabilization is effectively countered by PEGylation, as evidenced in Figure 3.3.7.f. This aligns with the known properties of this polymer, which is widely used as a coating to enhance stability, prevent opsonization, and promote prolonged circulation in the blood.[73]

Table 3.3.2. DLS and ζ-potential values for ZIF-8 and NU-1000 NCs

Sample	$d_{h,N}$ ± sd	$d_{h,I}$ ± sd	PDI ± sd	ζ-Pot / mV
AuBy@ZIF-8	158 ± 3	187 ± 4	0.14 ± 0.02	33.3 ± 1.1
AuBy@ZIF-8(CV)	166 ± 10	216 ± 8	0.12 ± 0.01	16.7 ± 1.0
AuBy@ZIF-8(CV)@PMA	185 ± 3	208 ± 3	0.05 ± 0.02	-25.0 ± 1.5
AuBy@NU-1000	165 ± 10	195 ± 12	0.20 ± 0.05	31.3 ± 0.9
AuBy@NU-1000(CV)	174 ± 4	199 ± 14	0.18 ± 0.09	26.1 ± 2.0
AuBy@NU-1000(CV)@PMA	181 ± 8	209 ± 20	0.11 ± 0.04	9.9 ± 1.2

USC UNIVERSIDADE DE SANTIAGO DE COMPOSTELA

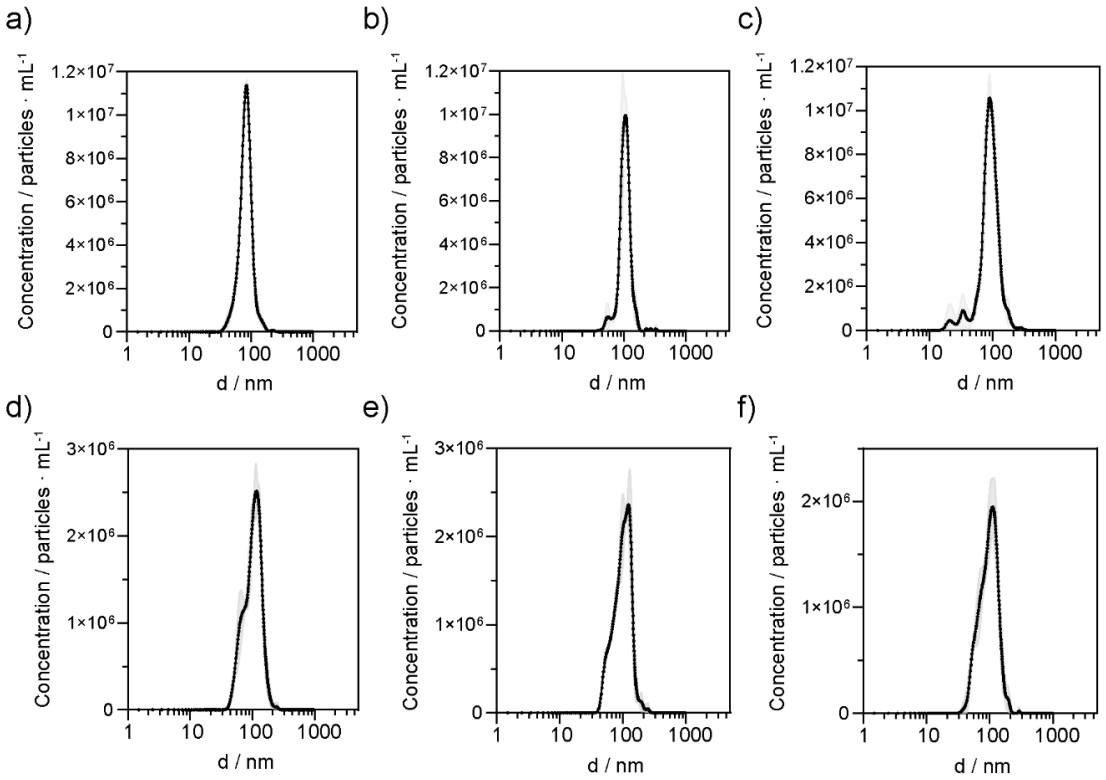

Figure 3.3.8. NTA measurements for a-c) ZIF-8 NCs (a. AuBy@ZIF-8, b. AuBy@ZIF-8(CV), c. AuBy@ZIF-8(CV)@PMA), and d-e) NU-1000 NCs (d. AuBy@NU-1000, e. AuBy@NU-1000(CV) and f. AuBy@NU-1000(CV)@PEG).

3.3.3. Thermal characterization

To examine the photothermal behavior of the NCs, samples were irradiated under a NIR laser (λ = 808 nm) matching the AuBys longitudinal LSPR, with different irradiances (7.5, 10 and 12.5 $W \cdot cm^{-2}$), varying concentrations of NCs (50, 100 and 200 pM, as derived from NTA measurements) and various exposure times (1 and 2 min). All the irradiations were performed in a 96-well plate using aqueous solutions containing 200 μL of each sample. The temperature *T* of the sample during each irradiation was measured using a thermocouple probe to generate the dynamic *T* curves. *ΔT* irradiation time profiles for AuBy@ZIF-8@PMA and for AuBy@NU-1000@PEG NCs are shown in Figure 3.3.9. and Figure 3.3.10., respectively. In both cases, the heating curves show a similar trend, achieving the boiling *T* (100 ºC) for the higher irradiance level (12.5 $W \cdot cm^{-2}$) and NC concentration (200 pM). Figure 3.3.11.a,b present the heatmaps correlating NC concentration with irradiance power after 1 min of exposure. As a baseline, water without NCs served as the control, exhibiting negligible temperature change, underscoring the specificity of the NC photothermal response. The heating patterns for AuBy@ZIF-8@PMA and AuBy@NU1000@PEG NCs showed remarkable similarity, with minor deviations potentially attributable to the unique structural characteristics of each MOF type. These findings prove the NCs' proficiency in absorbing NIR light and converting it to thermal energy, highlighting their potential for photothermal applications.

USC UNIVERSIDADE DE SANTIAGO DE COMPOSTELA

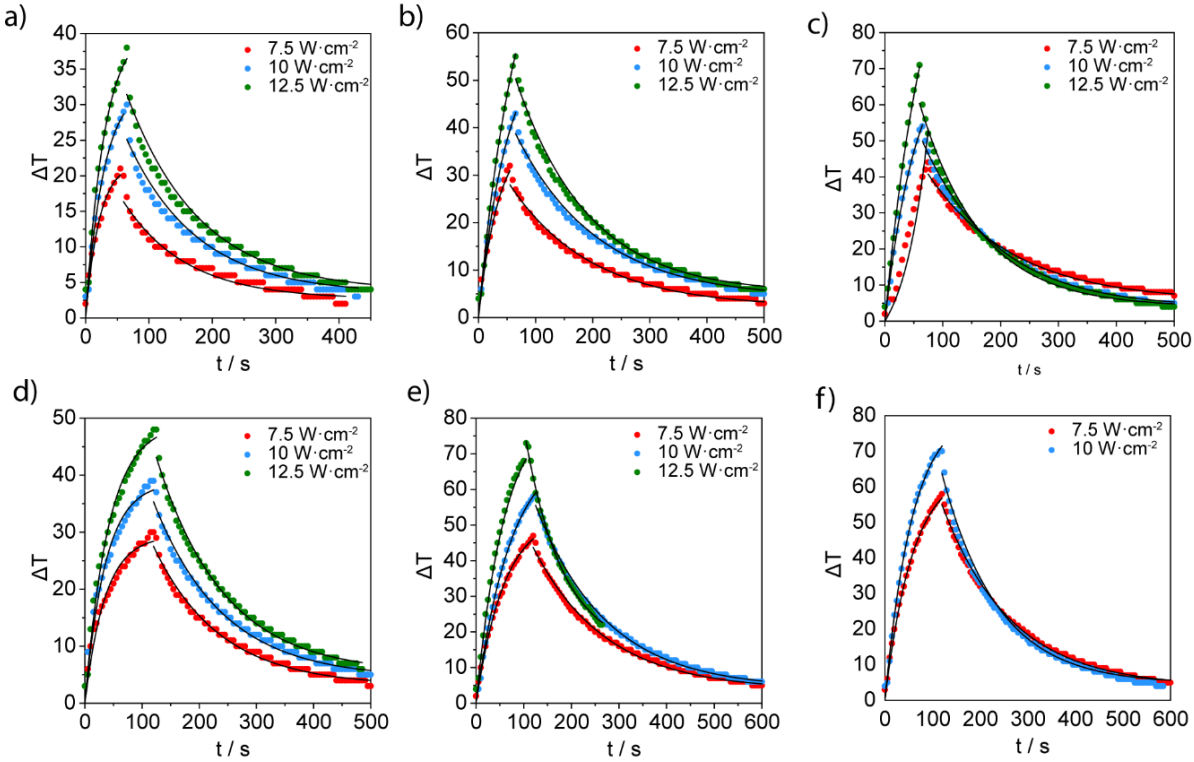

Figure 3.3.9. AuBy@ZIF-8@PEG heating curves in water for 1 minute irradiation at a) 50 pM, b) 100 pM, and 200 pM; and 2 minutes irradiation at d) 50 pM, e) 100 pM and f) 200 pM.

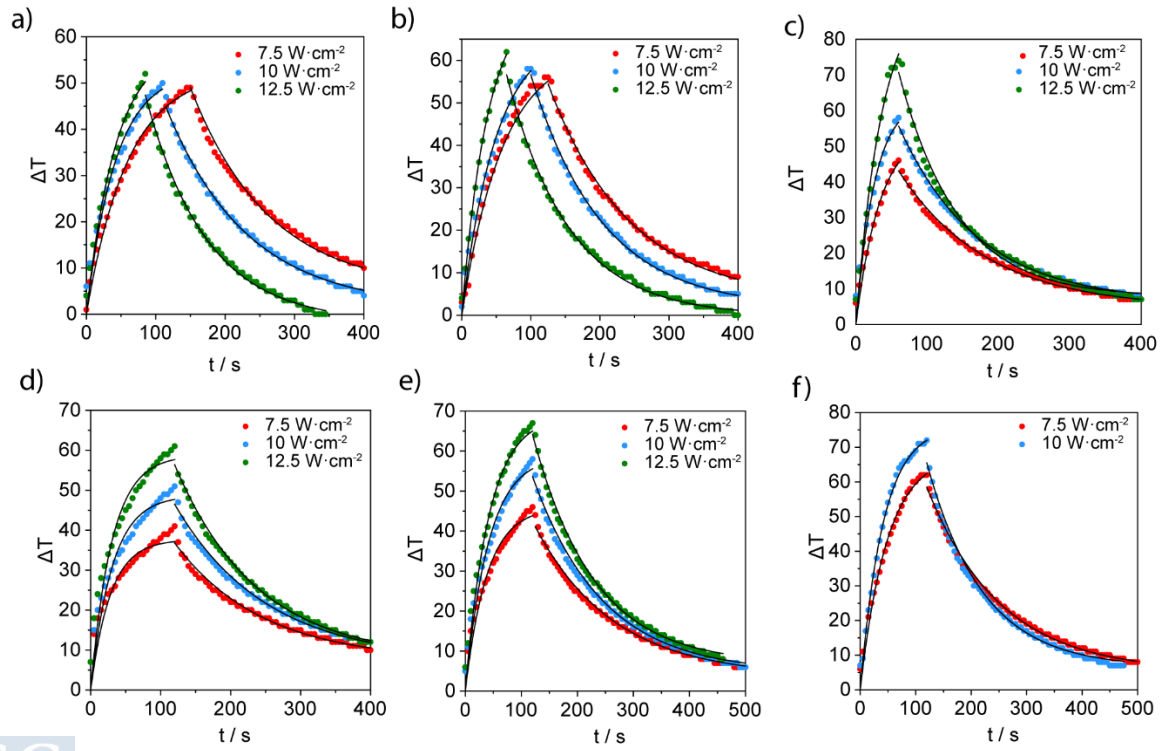

Figure 3.3.10. AuBy@NU-1000@PEG heating curves in water for 1 minute irradiation at a) 50 pM, b) 100 pM, and 200 pM; and 2 minutes irradiation at d) 50 pM, e) 100 pM and f) 200 pM.

To assess the controlled-release performance of the CV-loaded NC systems, irradiation tests were conducted under optimal conditions (100 pM NC concentration, 1 min exposure) using three different irradiance levels. After NIR treatment, the NCs were precipitated, allowing for the quantification of the CV released in the supernatant through fluorescence analysis (Figure 3.3.11.c, Table 3.3.3.-3.3.4.). AuBy@ZIF-8(CV)@PMA exhibited a notable increase in CV release, achieving a three-fold enhancement in fluorescence intensity (FI) relative to the non-irradiated control, highlighting the photothermal-triggered release capability. Impressively, the AuBy@NU-1000(CV)@PEG exhibited a six-fold fluorescence intensity increase in CV release at the highest irradiance compared to control, underscoring their superior responsiveness to NIR-triggered release. Control samples, which did not undergo NIR irradiation, showed only marginal CV release, emphasizing the critical role of photothermal activation in achieving controlled drug release.

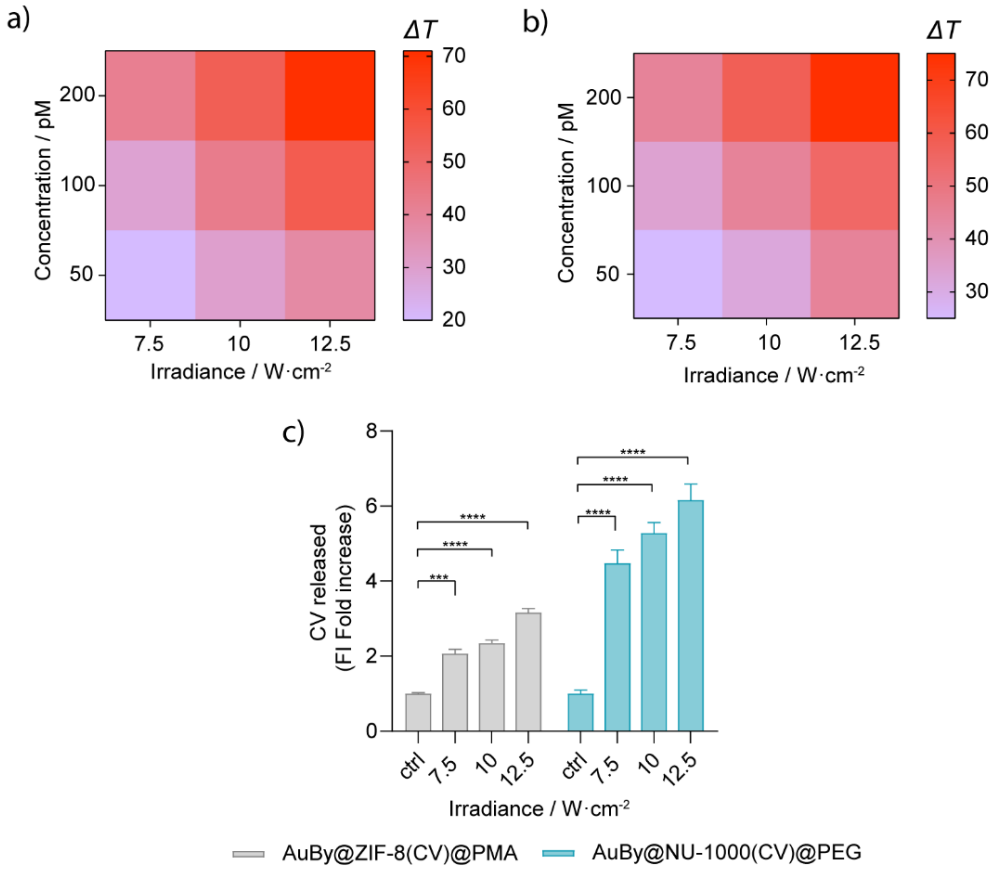

Figure 3.3.11. Heatmaps displaying the peak temperatures reached following 1 min of irradiation for a) AuBy@ZIF-8@PMA NCs and b) AuBy@NU-1000@PEG NCs. c) Fold increase FI associated to the release of CV post 1-min irradiation at a NC´s concentration of 100 pM in water. All experiments were conducted in triplicate. Error bars represent standard deviation. Statistical analysis was assessed by two-way ANOVA test (***p = 0.0002, ****p < 0.0001).

USC
UNIVERSIDADE DE SANTIAGO DE COMPOSTELA

Table 3.3.3. Percentages of the CV released with respect to the encapsulated value inside the AuBy@ZIF-8(CV)@PMA at a concentration of 100 pM.

	CV RELEASED	
$W \cdot cm^{-2}$	%	FI Fold increase
Ctrl	11.07 ± 0.30	1.00 ± 0.03
7.5	22.89 ± 1.27	2.07 ± 0.11
10	26.04 ± 0.86	2.35 ± 0.08
12.5	35.06 ± 1.13	3.17 ± 0.10

Table 3.3.4. Percentages of the CV released with respect to the encapsulated value inside the AuBy@NU-1000(CV)@PEG at a concentration of 100 pM.

	CV RELEASED	
$W \cdot cm^{-2}$	%	FI Fold increase
Ctrl	5.21 ± 0.50	1.00 ± 0.10
7.5	23.31 ± 1.83	4.48 ± 0.35
10	27.19 ± 1.35	5.28 ± 0.28
12.5	30.18 ± 1.21	6.16 ± 0.43

3.3.4. Thermoplasmonic behavior inside living cells in 2D

Next, the interaction of the NCs with cells was evaluated in 2D cell cultures of A549 lung adenocarcinoma cells. The biocompatibility was assessed by determining the cellular metabolic activity using a 3-[4,5-dimethylthiazol-2-yl]-2,5-diphenyltetrazolium bromide (MTT) assay. This study confirmed the high viability related to both NCs at different concentrations. We used values of up to 100 pM for AuBy@ZIF-8@PMA NCs and 200 pM for AuBy@NU-1000@PEG NCs (corresponding to about 40 and 20 $\mu g \cdot mL^{-1}$ of Zn and Zr, respectively) (Figure 3.3.12.a,b). AuBy@NU-1000@PEG NCs showed no significant toxicity at any concentration after 24 h of incubation, related to the high biocompatibility of this MOF.[173] On the contrary, there are notable differences observed among the ZIF-8 based NCs samples. Bare AuBy@ZIF-8 NCs exhibit high viability across all concentrations, attributed to the low toxicity inherent to this MOF. However, a marked increase in toxicity becomes apparent in the CV-loaded samples before the addition of PMA, especially at concentrations exceeding 10 pM. This increase in toxicity is linked to the ZIF-8 instability in aqueous environments, which leads to its degradation and the subsequent release of CV. In contrast, post-functionalization with PMA significantly enhances viability. These findings are consistent with aforementioned CV release studies, revealing that AuBy@ZIF-8(CV)@PMA controls exhibit higher CV release percentages (~10 %) compared to AuBy@NU-1000(CV)@PEG controls (~ 5 %) (Table 3.3.3. and Table 3.3.4.). Consequently, to prevent unspecific CV leakage and its inherent toxicity profile,[19] both PMA and PEG are demonstrated to act as effective blocking agents.

Nevertheless, ZIF-8 based NCs exhibit a marginally higher release rate, leading to increased toxicity at higher concentrations. This observation aligns with prior studies involving these coatings, confirming the efficacy and appropriateness of the selected strategy.[197,249]

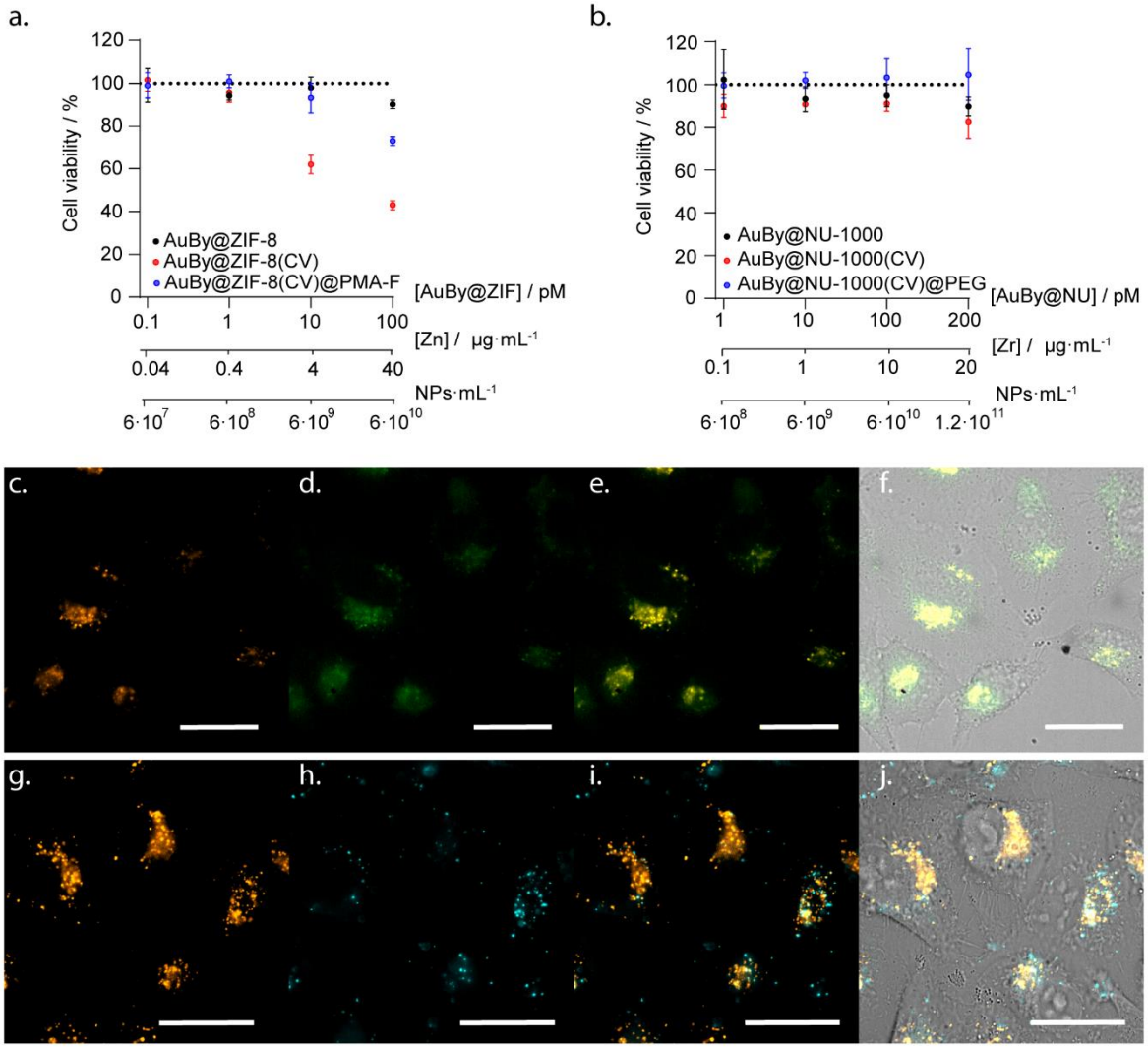

Figure 3.3.12. a) Cell viability of A549 cells incubated with ZIF-8 based NCs and b) NU-1000 based NCs for 24 h, assessed by MTT assay. Fluorescence microscopy images demonstrating the internalization of AuBy@ZIF-8(CV)@PMA by A549 cells: c) CV fluorescence signal (orange), d) fluorescein fluorescence signal (green), e) overlay of CV and fluorescein signal, f) composite image including overlay of fluorescence and brightfield channels. For AuBy@NU-1000(CV)@PEG internalization by A549 cells: g) CV fluorescence signal (orange), h) NU-1000 fluorescence signal (cyan), i) overlay of CV and NU-1000, j) composite image including overlay of fluorescence and brightfield channels. Scale bar: 25 µm.

The uptake of the NCs was further studied using fluorescence microscopy. Epifluorescence microscopy imaging experiments showed the intracellular location of the NCs in the perinuclear region, as expected for the endocytic mechanisms of NCs cellular uptake (Figure 3.3.12.c-j).[66,194] This intracellular localization indicates a clear colocalization of the CV and the NCs. For AuBy@ZIF-8(CV)@PMA samples (Figure 3.3.12.c-f), there is a clear colocalization between the CV and the PMA, whereas for AuBy@NU-1000(CV)@PEG (Figure 3.3.12.g-j), CV colocalization is confirmed using the NU-1000 fluorescence. These findings confirm the

USC UNIVERSIDADE DE SANTIAGO DE COMPOSTELA

NCs' capability to store CV intracellularly, attributed to the effectiveness of polymer functionalization in preventing nonspecific CV leakage.

The in vitro stimuli-responsive release of encapsulated cargo was investigated via NIR laser (808 nm) excitation, integrated with a fluorescence microscope through a laser scanner.[206] This configuration affords precise spatial and temporal irradiation control. For this experiment, A549 cells were incubated with both NCs types for 6 h. Based on prior toxicity evaluations, the used concentration was 100 pM of AuBy@NU-1000(CV)@PEG and 50 pM of AuBy@ZIF-8(CV)@PMA NCs to warrant non-toxic levels while ensuring optimal CV detection.

As discussed previously and illustrated in Figure 3.3.12., CV remained enclosed within the pores of the NCs even after cellular uptake. After incubating cells with both types of NCs, individual cells were selected and exposed to NIR light to evaluate the induced release of encapsulated CV, as observed before and after irradiation (Figure 3.3.13.a,b and Figure 3.3.14.a,b). To illustrate this process, magnified images of two regions of interest (ROI) containing a single cell (ROI 1 and 2) are presented. These images show the cells before and after irradiation in Figure 3.3.13.c,e and Figure 3.3.14.c,e; and in Figure 3.3.13.d,f and Figure 3.3.14.d,f, respectively. Following irradiation, these regions were immediately examined, revealing a pronounced increase in the fluorescence intensity within the CV channel. This controlled release of CV is attributed to the local ΔT in the vicinity of the AuBy under NIR irradiation, leading to the release of CV encapsulated within the NC pores.

Furthermore, this behavior was analyzed over time by capturing multiple images at various time intervals after scanning the selected ROI (up to 5 min). These images revealed a noticeable diffusion of CV across the cell for both systems, with the signal diminishing after a few min compared to the immediate post-irradiation signal (Figure 3.3.13.g-j, Figure 3.3.14. g-j). Over time, the fluorescence intensity of CV slightly decreases as the dye diffuses throughout the cell. Despite this gradual reduction, the intensity remains noticeably higher in irradiated cells compared to non-irradiated ones, indicating a sustained release and presence of CV within the cell.

USC UNIVERSIDADE DE SANTIAGO DE COMPOSTELA

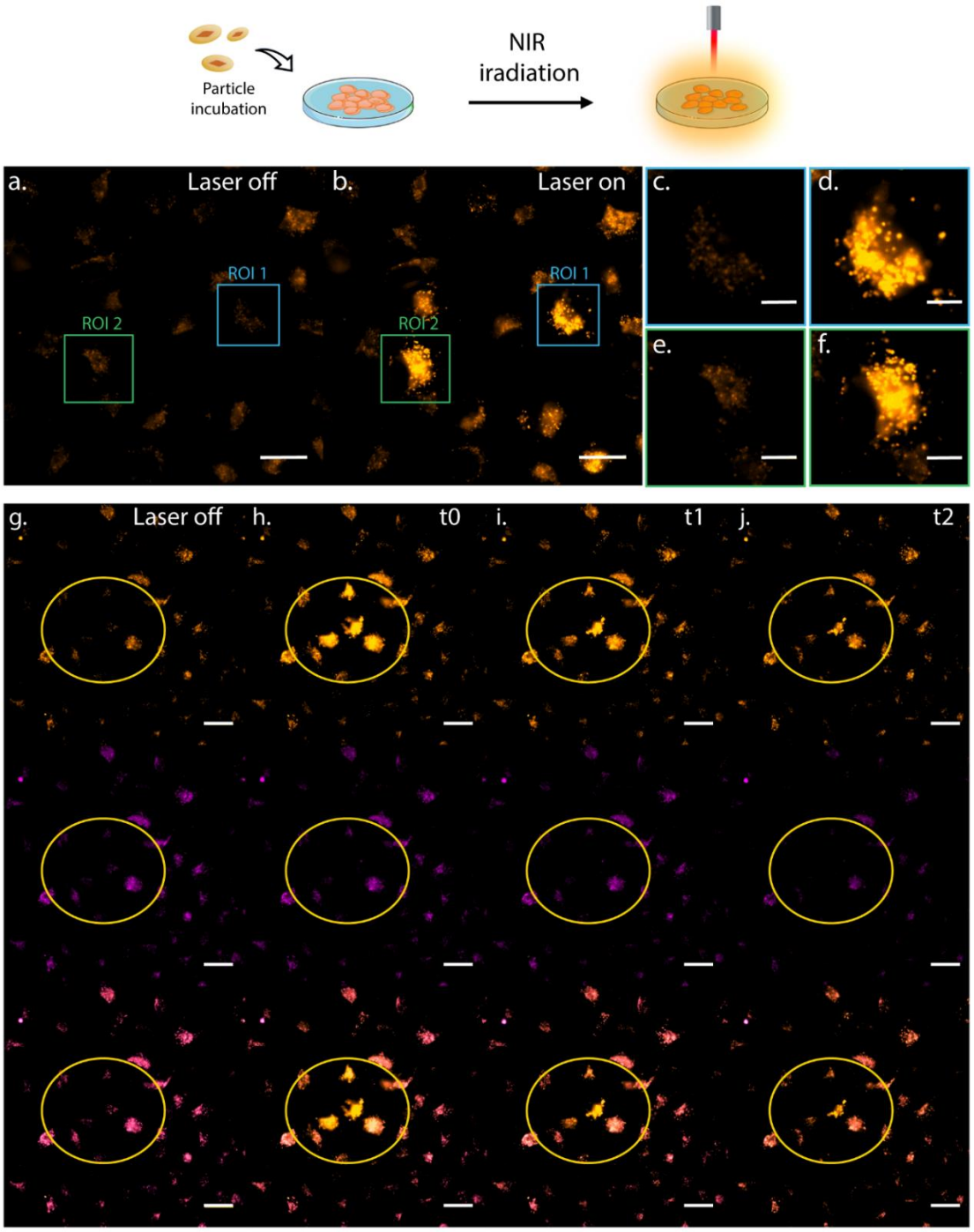

Figure 3.3.13. a) Microscopy images of cells incubates with AuBy@NU-1000(CV)@PEG before NIR laser irradiation and b) after NIR laser irradiation in selected areas. Specific regions of interest (ROIs): c) ROI 1 and e) ROI 2 before irradiation; d) ROI 1 and f) ROI 2 after irradiation. g) Microscopy images show the fluorescence signal before NIR laser irradiation of the selected ROI, and sequential images at h) t0 = 10 s, i) t1 = 1 min, and j) t2 = 5 min after irradiation, highlighting the dynamic release of CV. The images feature the fluorescence signals from CV (orange), Lysotracker® (magenta), and the overlay of both channels. Scale bars are 25 µm. The samples were incubated with A549 cells for 6 h at a concentration of 100 pM.

USC UNIVERSIDADE DE SANTIAGO DE COMPOSTELA

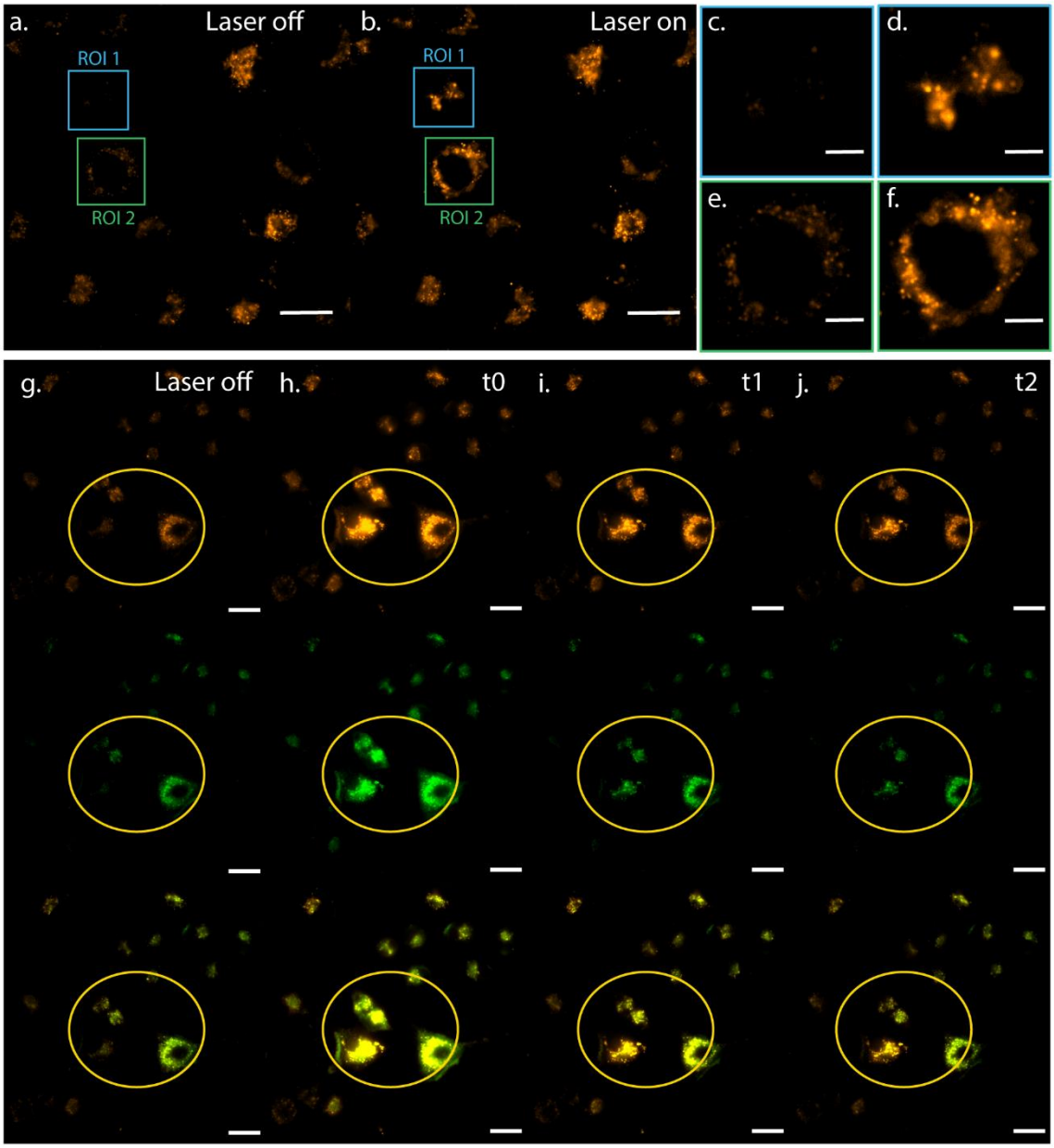

Figure 3.3.14. a) Microscopy images of the AuBy@ZIF-8(CV)@PMA before NIR laser irradiation b) after NIR laser irradiation of selected areas. Specific regions of interest (ROIs): c) ROI 1 and e) ROI 2 before irradiation and d) ROI 1 and f) ROI 2 after irradiation. g) Microscopy images show the fluorescence signal before NIR laser irradiation of the selected ROI, and sequential images at h) t0 = 10 s, i) t1 = 1 min, and j) t2 = 5 min after irradiation, highlighting the dynamic release of CV. The images feature the fluorescence signals from CV (orange), the fluorescence signal from Fluorescein in the PMA (green), and the overlay of the two fluorescence channels. Scale bars 25 μm. Samples were incubated for 6 h at 50 pM.

USC
UNIVERSIDADE DE SANTIAGO DE COMPOSTELA

3.3.5. Drug loading - Efficiency as drug delivery systems

To further explore the potential of nanocomposites as DDSs, NU-1000 based NCs were chosen due to their superior stability, porosity, and cell viability profile, in comparison to those based on ZIF-8. The study involves the encapsulation of various chemotherapeutics (doxorubicin, carboplatin, and oxaliplatin) within the pores of the MOF to perform viability studies. For drug loading within the pores, a post-synthesis encapsulation method similar to the procedure used for the CV samples was used. Then, particles were subsequently functionalized with PEG to prevent drug leakage.

Doxorubicin (DOX), an anthracycline, serves as a highly efficient antineoplastic agent extensively employed in the treatment of diverse cancers such as leukemia, ovarian cancer, and breast cancer.[250] Carboplatin (CbPt), a platinum-based chemotherapeutic agent, finds application in the treatment of ovarian, testicular, cervical, neck, head, and small cell lung cancers.[251,252] Oxaliplatin (OXA), a third-generation platinum-based drug, is commonly used as a first-line chemotherapy for metastatic colorectal cancer.[253,254] Both carboplatin and oxaliplatin exert their therapeutic effects by binding to DNA, inhibiting transcription and replication processes, ultimately inducing cellular apoptosis.[255] However, their clinical use is hampered by limitations such as low aqueous solubility and secondary effects.[250,255] Consequently, these chemotherapeutics would benefit from innovative systems capable of enhancing cellular uptake, drug accumulation at the tumor site, thereby augmenting therapeutic efficacy while mitigating associated toxicity.

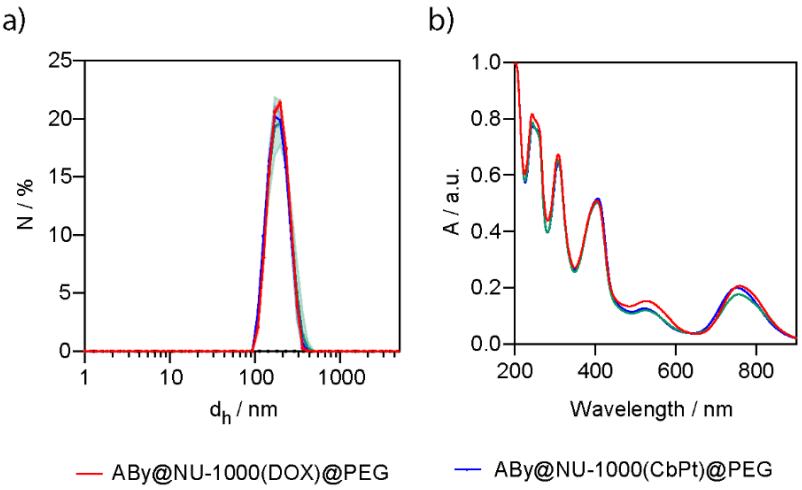

Figure 3.3.15. Sample characterization after the drug loading and PEGylation with a) DLS (number distribution of d_h) and b) UV-Vis spectra.

The size of drug-loaded NCs was characterized using DLS. As presented in Figure 3.3.15.a, the mean d_h does not present any significant differences among the samples (Table 3.3.6.). Similarly, UV-Vis spectroscopy reveals no differences among samples, before and after the encapsulation/coating, leading to a final plasmon at 808 nm (Figure 3.3.15.b). To further verify the size and determine the concentration of the NCs, conducted NTA measurements (Figure 3.3.16) revealed no discernible differences among them. Additionally, ICP-OES analysis was used to evaluate the particle concentration, in combination with NTA values, and calculate the

USC UNIVERSIDADE DE SANTIAGO DE COMPOSTELA

efficiency of drug loading for the Pt-drugs (Table 3.3.6.). For DOX, encapsulation characterization was performed using fluorescence measurements.

Table 3.3.5. DLS values for the drug-loaded NU-1000 NCs.

Sample	$d_{h,N}$ ± sd	$d_{h,I}$ ± sd	PDI ± sd
AuBy@NU-1000(DOX)@PEG	161 ± 4	187 ± 4	0.18 ± 0.10
AuBy@NU-1000(CbPt)@PEG	167 ± 8	180 ± 6	0.20 ± 0.11
AuBy@NU-1000(OXA)@PEG	171 ± 5	182 ± 9	0.11 ± 0.07

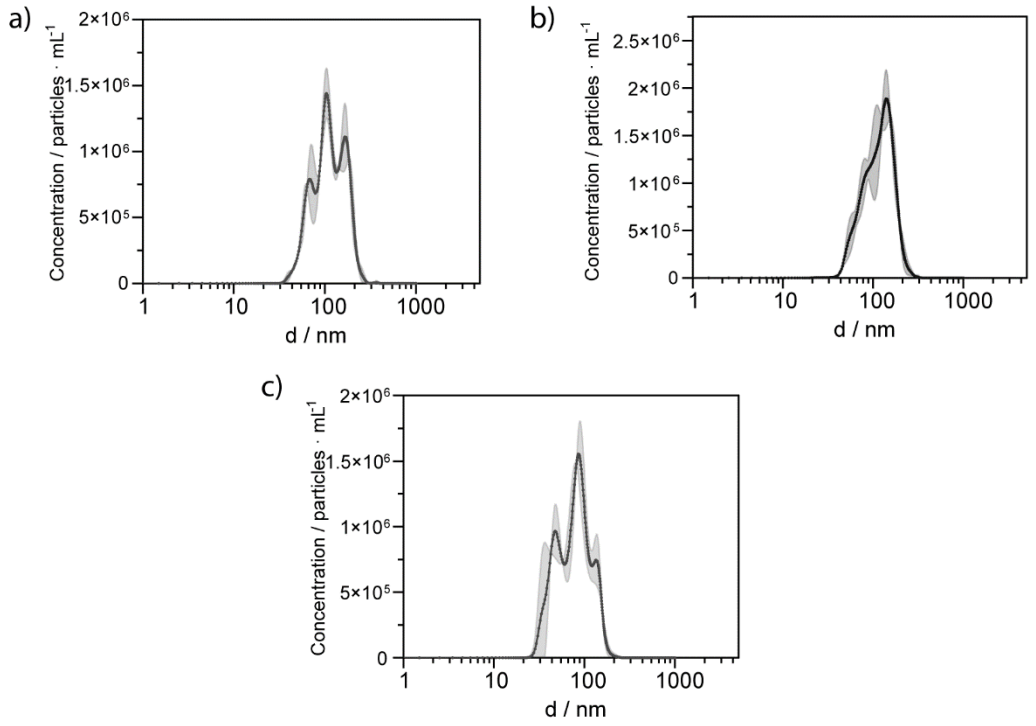

Figure 3.3.16. NTA measurements of a) Aby@NU-1000(DOX)@PEG, b) Aby@NU-1000(CbPt)@PEG and c) Aby@NU-1000(OXA)@PEG.

Table 3.3.6. Concentration values measured with NTA and ICP.

	nM	Part·mL^{-1}	mg·mL^{-1} Zr	mg·mL^{-1} Au	mg·mL^{-1} Pt	mM drug
AuBy@NU1000(DOX)@PEG	10.63	6.40E+12	0.37	1.24	-	5.21
AuBy@NU1000(CbPt)@PEG	8.04	4.84E+12	0.8	2.34	0.37	4.68
AuBy@NU1000(OXA)@PEG	9.96	6.00E+12	0.73	2.16	0.31	3.94

USC UNIVERSIDADE DE SANTIAGO DE COMPOSTELA

Samples were further characterized using PXRD to confirm that crystallinity was maintained after drug encapsulation and PEGylation. The obtained diffraction patterns confirmed the presence of pure-phase NU-1000 in all cases (Figure 3.3.17.). These results are consistent with previous findings involving CV loading.

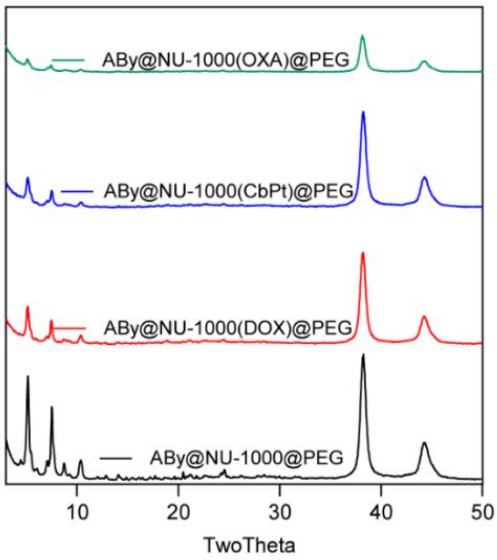

Figure 3.3.17. PXRD crystallographic characterization of the samples after drug loading and PEGylation of NCs.

Then, the interaction between the NCs and cells was evaluated using 2D cell cultures of A549 cells. The biocompatibility was assessed through the MTT assay. NCs were incubated with A549 cells for 24 h at concentrations up to 600 pM (equivalent to a Zr concentration of 60 $\mu g \cdot mL^{-1}$). In parallel, free drugs were incubated with the cells for both 24 and 72 h at concentrations of up to 500 µM, corresponding to the quantities encapsulated within the NCs (Figure 3.3.18.a-c). A noticeable increase in the toxicity effect of the selected drugs becomes more evident following a 72-h incubation period.[173,252,256-258] Upon comparing the toxicity of free versus encapsulated drugs after 24 h, cell viability was preserved when the drugs were encapsulated within the NCs. This underscores the effective surface functionalization with PEG, which mitigates cargo leakage. A slight increase in toxicity, particularly noticeable at the maximum dose of 600 pM compared to non-drug-loaded NCs, is attributed to minor drug leakage. Altogether, these results prove that PEGylation of NCs retains the encapsulated drug more efficiently than observed in previous studies. For instance, Zhao and coworkers reported toxicities exceeding 20 % at concentrations of 300 $\mu g \cdot mL^{-1}$ after 24 h incubation using non-PEGylated DOX-loaded NU-1000 micrometric particles.[173]

USC UNIVERSIDADE DE SANTIAGO DE COMPOSTELA

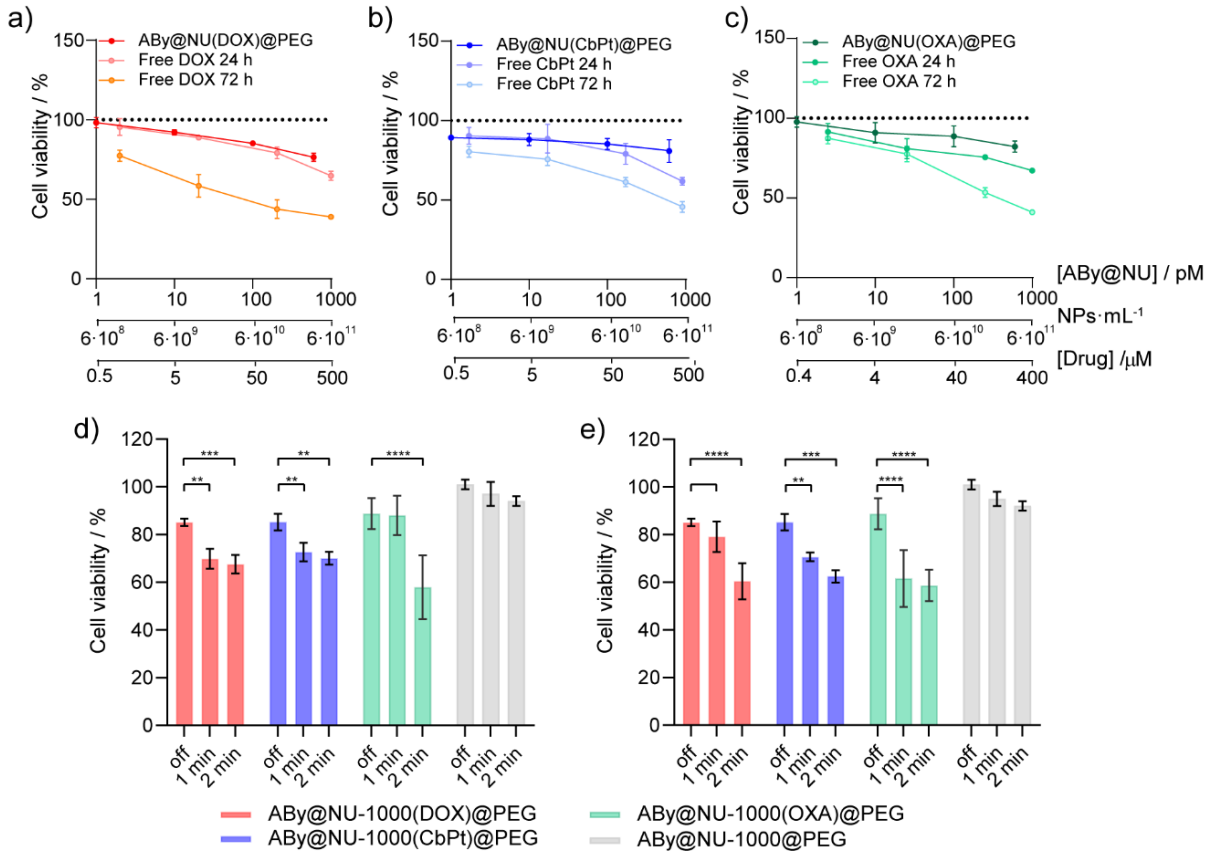

Figure 3.3.18. Cell viability using MTT assay of A549 cells 24 h after the incubation with the drug loaded NCs and the corresponding quantities of the free drug after 24 h and 72 h of incubation a) DOX, b) CbPt and c) OXA. Cell viability of A549 cells incubated for 6 h with the loaded NCs using MTT assay 24 h after the irradiation at d) 15 $W \cdot cm^{-2}$ and e) 20 $W \cdot cm^{-2}$ irradiance (NC´s concentration: 100 pM). Experiments were carried out using n = 4. Error bars represent standard deviation. Statistical analysis was assessed by two-way ANOVA test (***p = 0.0018, ****p < 0.0001, ns = no significant difference).

The efficiency of these NCs as stimuli-responsive DDSs was studied using a NIR irradiation setup, as described in previous work.[206] NCs were incubated with A549 cells for 6 h at a concentration of 100 pM, equivalent to ~ 50 µM of the drug, followed by NIR irradiation at irradiances of 15 and 20 $W \cdot cm^{-2}$ for 1 and 2 min of light exposure. Subsequently, MTT toxicity assays were conducted after 24 h post-irradiation to evaluate cell viability. Figure 3.3.18.d,e display the obtained results. These show a clear drop in cell viability under both irradiance conditions compared to non-irradiated samples (laser off), with higher cell death rates observed after 2 min of NIR exposure (Table 3.3.7.-3.3.9.). Non-drug-loaded NCs demonstrated a negligible reduction in cell survival rates post-irradiation. Notably, the irradiation settings were precisely adjusted to initiate drug release while minimizing hyperthermia induced by the AuBy core. These settings are adequate to trigger the release of the encapsulated cargo without causing cell death associated with hyperthermia.

USC
UNIVERSIDADE DE SANTIAGO DE COMPOSTELA

Table 3.3.7: % of cell viability 24h after NIR irradiation for the DOX loaded NCs

AuBy@NU-1000(DOX)@PEG			
t irr \ power	15 W·cm^{-2}	20 W·cm^{-2}	Ctrl AuBy@NU-1000@PEG
Laser off	85.22 ± 5.31	83.43 ± 4.29	100.98 ± 2.10
1 min	69.89 ± 4.12	79.15 ± 6.37	95.01 ± 3.12
2 min	67.55 ± 3.93	64.44 ± 7.55	91.92 ± 1.97

Table 3.3.8. % of cell viability 24h after NIR irradiation for the CbPt loaded NCs

AuBy@NU-1000(CbPt)@PEG			
t irr \ power	15 W·cm^{-2}	20 W·cm^{-2}	Ctrl AuBy@NU-1000@PEG
Laser off	85.27 ± 3.49	85.27 ± 3.49	100.98 ± 2.10
1 min	72.65 ± 3.94	70.67 ± 1.85	95.01 ± 3.12
2 min	70.08 ± 2.63	62.52 ± 2.55	91.92 ± 1.97

Table 3.3.9. % of cell viability 24h after NIR irradiation for the OXA loaded NCs

AuBy@NU-1000(OXA)@PEG			
t irr \ power	15 W·cm^{-2}	20 W·cm^{-2}	Ctrl AuBy@NU-1000@PEG
Laser off	92.03 ± 5.31	83.40 ± 4.19	100.98 ± 2.10
1 min	88.06 ± 8.29	61.62 ± 11.93	95.01 ± 3.12
2 min	57.92 ± 13.28	60.70 ± 6.51	91.92 ± 1.97

USC UNIVERSIDADE DE SANTIAGO DE COMPOSTELA

3.3.6. DDSs efficiency inside living cells in 3D cell culture

Spheroids and organoids are becoming essential for investigating the interactions between nanomaterials and living cells, increasingly supplanting the role traditionally occupied by 2D adherent cell cultures. These 3D cell models mimic more accurately *in vivo* conditions compared to 2D models, becoming a reliable alternative to animal ones in academic research and drug discovery.[259] Spheroids, which are 3D multicellular aggregates of cells, exhibit properties that closely resemble those of solid tumors, including the formation of a necrotic center with limited access to oxygen and other metabolites.[260,261] These 3D cell cultures develop pH, oxygen, metabolic, and proliferative gradients, leading to stratification in mature spheroids. This stratification mirrors the vascular stages of solid tumors, effectively emulating the in vivo situation.

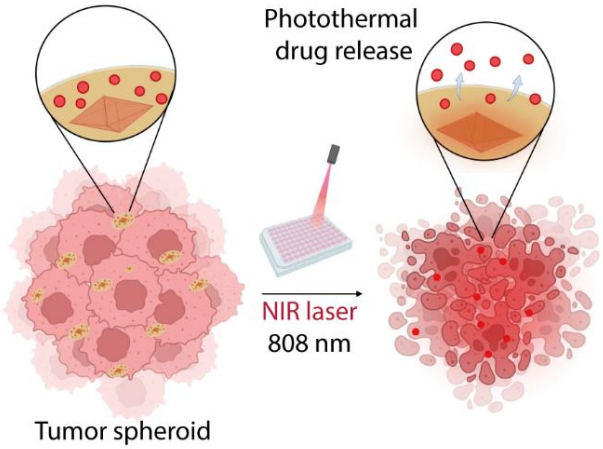

Figure 3.3.19. Schematic representation of the triggered release in 3D spheroids using NIR laser.

In this study, 3D spheroids were growth from A549 cells as an *in vitro* model to closely replicate the *in vivo* tumor microenvironment (Figure 3.3.19.). This model was employed to evaluate the interactions with the NIR-responsive AuBy@NU-1000@PEG NCs, loaded with chemotherapeutics analogously to previous investigations in 2D cultures. Three days after seeding the cells, confocal microscopy was used to examine the morphology of the A549 spheroids. Under the experimental conditions employed, spheroids of approximately 600 µm in diameter were obtained (Figure 3.3.20.-3.3.25). Building on previous findings and optimized protocols for studying the interaction of NCs and spheroids,[19] CbPt and OXA-loaded NU-1000-based NCs were incubated with A549 spheroids at a NC concentration of 100 pM (equivalent to a drug concentration of 50 µM) for 24 h. After incubation, the samples were washed thoroughly and then irradiated with the NIR setup previously described. The conditions for the NIR irradiation of 3D cell models were optimized. 20 $W \cdot cm^{-2}$ in two 1-min pulses (Condition 1) was initially applied to suit the robustness and depth of the spheroids.[262,263] Additionally, an alternative condition of 30 $W \cdot cm^{-2}$ in two 30-s pulses was applied, yielding equivalent results (Condition 2). 24 h and 72 h after NIR irradiation, spheroids were analyzed by microscopy and flow cytometry.

Firstly, microscopy studies were performed both before and 72 h after irradiation to evaluate the size of the spheroids after different treatments.[19] Spheroids treated with AuBy@NU-1000(CbPt)@PEG (Figure 3.3.20.) and AuBy@NU-1000(OXA)@PEG (Figure

3.3.21.) show a decrease in size 72 h after NIR irradiation. Figure 3.3.22 present spheroids treated with non-loaded AuBy@NU-1000@PEG, indicating the morphology is preserved even after the irradiation. Additionally, the experiment included free CbPt and OXA at concentrations (≈ 50 μM) equivalent to those encapsulated within the NCs, alongside control spheroids for comparison are shown in Figure 3.3.23.-3.3.25. Figure 3.3.26. summarize the mean diameter of the spheroids in each scenario, as determined from the microscopy images. The microscopy images, supported by the measured mean diameters, unequivocally show a significant reduction in the size of the spheroids 72 h post-irradiation in samples incubated with drug-loaded NCs. In contrast, no changes in morphology or size were observed in spheroids treated with non-loaded NCs after NIR irradiation (Figure 3.3.22.). This indicates that the thermoplasmonic effect alone is insufficient to achieve cell death under the selected irradiation conditions, as previously demonstrated in 2D cell cultures. Notably, the obvious size reduction observed with drug-loaded NCs can be directly attributed to the controlled drug release, enabled by photothermal activation. In general, precedents in the literature typically combine hyperthermia and photothermal-driven drug release to achieve cell death.[264,265]

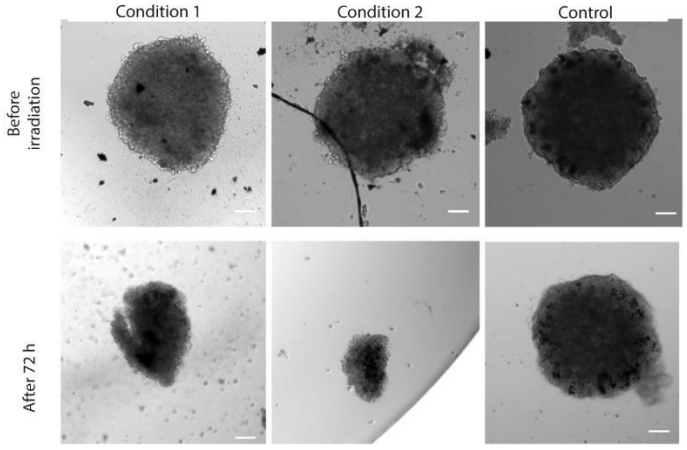

Figure 3.3.20. AuBy@NU-1000(CbPt)@PEG loaded spheroids before and 72 h after the irradiation. Scale bar 100 μm.

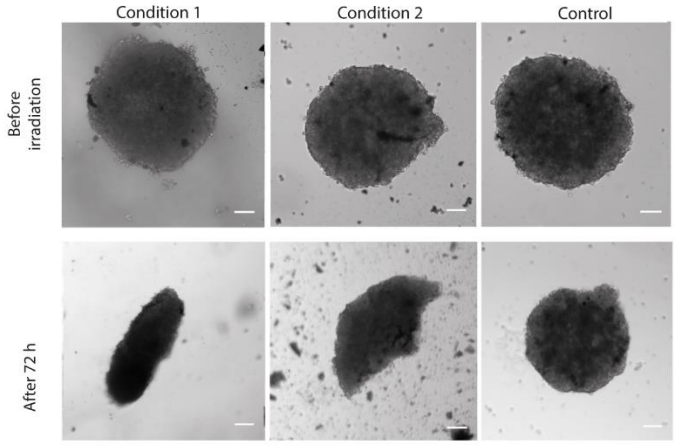

Figure 3.3.21. AuBy@NU-1000(OXA)@PEG loaded spheroids before and 72 h after the irradiation. Scale bar 100 μm.

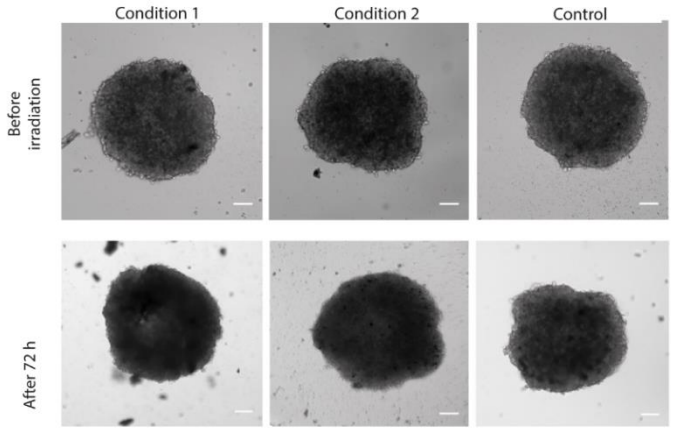

Figure 3.3.22. AuBy@NU-1000@PEG loaded spheroids before and 72 h after the irradiation. Scale bar 100 μm.

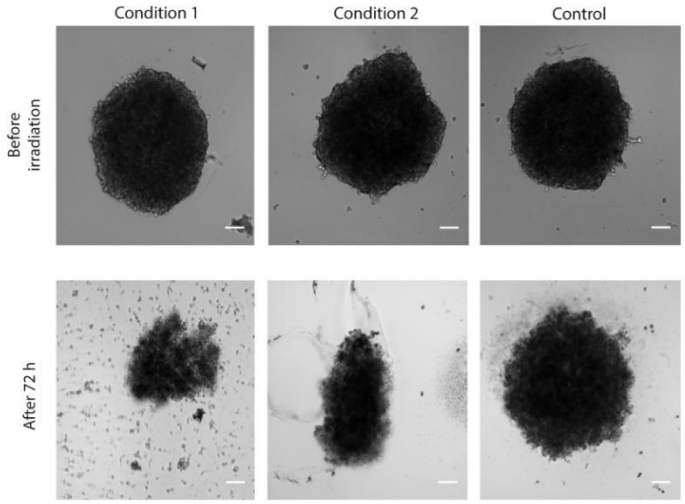

Figure 3.3.23. Free CbPt incubated with spheroids before and 72 h after the irradiation. Scale bar 100 μm.

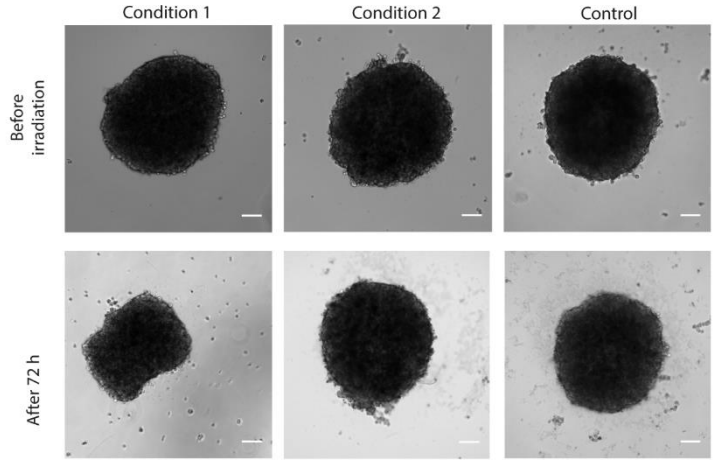

Figure 3.3.24. Free OXA incubated with spheroids before and 72 h after the irradiation. Scale bar 100 μm.

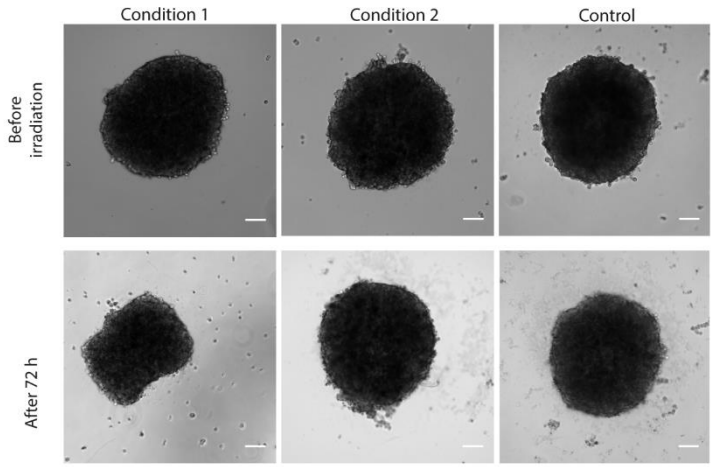

Figure 3.3.25. Control spheroids before and 72 h after the irradiation. Scale bar 100 µm.

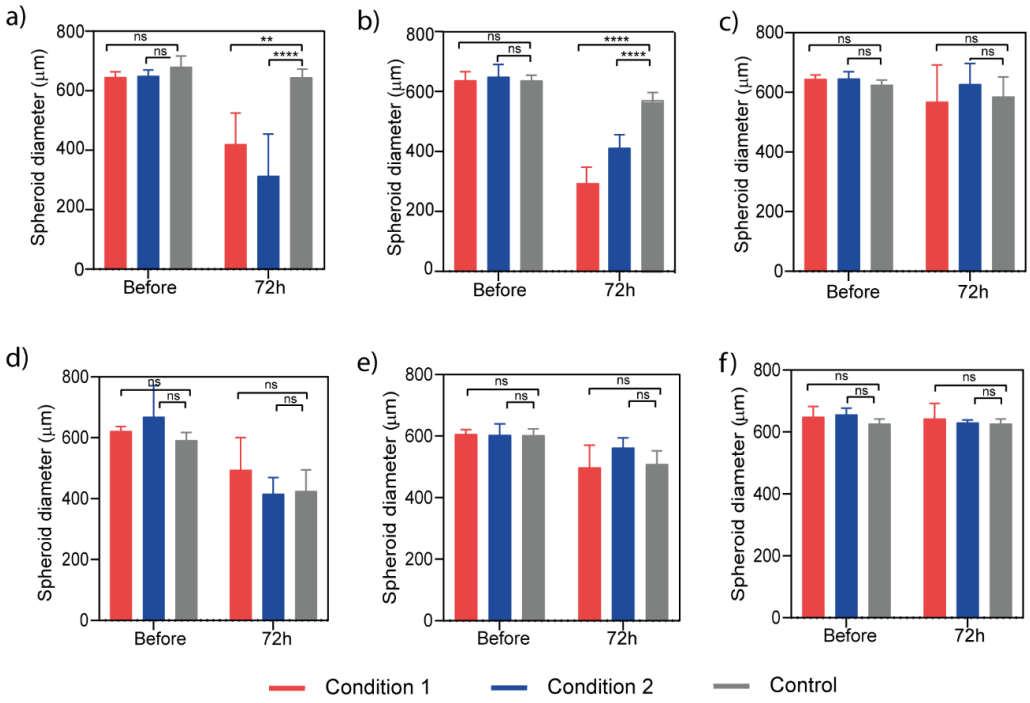

Figure 3.3.26. Spheroids diameter analysed from microscopy images before and 72h after the irradiation for a) AuBy@NU-1000(CbPt)@PEG, b) AuBy@NU-1000(OXA)@PEG, c) AuBy@NU-1000@PEG, d) Free CbPt, b) Free OXA and c) control spheroids. Experiments were carried out using n = 3. Error bars represent standard deviation. Statistical analysis was assessed by two-way ANOVA test (***p = 0.0018, ****p < 0.0001, ns = no significant difference).

Secondly, to corroborate the effect of CbPt and OXA release in 3D spheroids treated with drug-loaded NCs after NIR irradiation, a live-dead assay was carried out by flow cytometry using calcein-AM and propidium iodide (PI) as fluorescence indicators for viable and dead cells, respectively. Cytometry studies of treated spheroids were conducted 24 h and 72 h post-irradiation (Figure 3.3.27.-3.3.28.). Viable cells exhibit strong green fluorescence, resulting from the conversion of Calcein AM into calcein by cellular esterases. Conversely, PI is a nuclear staining dye that cannot penetrate the membranes of viable cells and thus stains dead

(necrotic) cells with red fluorescence. The total percentage of calcein-positive cells (viable cells) is presented in Figure 3.3.29. Elevated percentages of PI staining were observed in all cases, a phenomenon attributable to the necrotic core of the spheroids.[266,267]

Decrease viability assessed by calcein staining (less than 2 % of viable cells) was shown in spheroids treated with drug-loaded NCs after 24 h post-incubation (Figure 3.3.27.a,b), indicating that nearly all the remaining cells were dead or beginning to die. In contrast, spheroids incubated with non-drug-loaded NCs, regardless of whether they were irradiated or not, show an equivalent percentage of viable cells after 24 h (Figure 3.3.27.c), which is also comparable to that of non-irradiated, drug-loaded NCs. These results suggest a negligible effect attributable to photothermal hyperthermia, which has been previously employed to cause cell death in 3D cell models.[268,269] The difference in outcomes between spheroids treated with free drugs and control spheroids, irrespective of whether they were irradiated or not, is negligible (Figure 3.3.27.d-f). This aligns with previous findings, indicating that the quantities of CbPt and OXA employed are not expected to induce toxicity within 24 h.[256,258]

These findings indicate that 24 h post-treatment, the drug-loaded NCs, when coupled with NIR irradiation, result in significant treatment efficacy achieving high sensitivity to CbPt and OXA. This efficacy is attributed to the rapid NIR-controlled diffusion of the drug throughout the spheroid. In contrast, the permeability and efficiency of the drugs are lower without the NCs. Similar effects were observed after 72 hours for the drug-loaded NCs, with a noticeable reduction in cell viability in the controls, as depicted in Figure 3.3.28. It is noted that the hyperthermia effect induced by the irradiated empty NCs can lead to cell death after 72 h, and free drugs also begin to exhibit some level of toxicity after this time frame, regardless of irradiation.

Altogether, these findings suggest that the proposed NIR-responsive NCs could serve as nanocarriers, facilitating the rapid internalization of loaded drugs and enabling their effective, triggered release.

USC
UNIVERSIDADE DE SANTIAGO DE COMPOSTELA

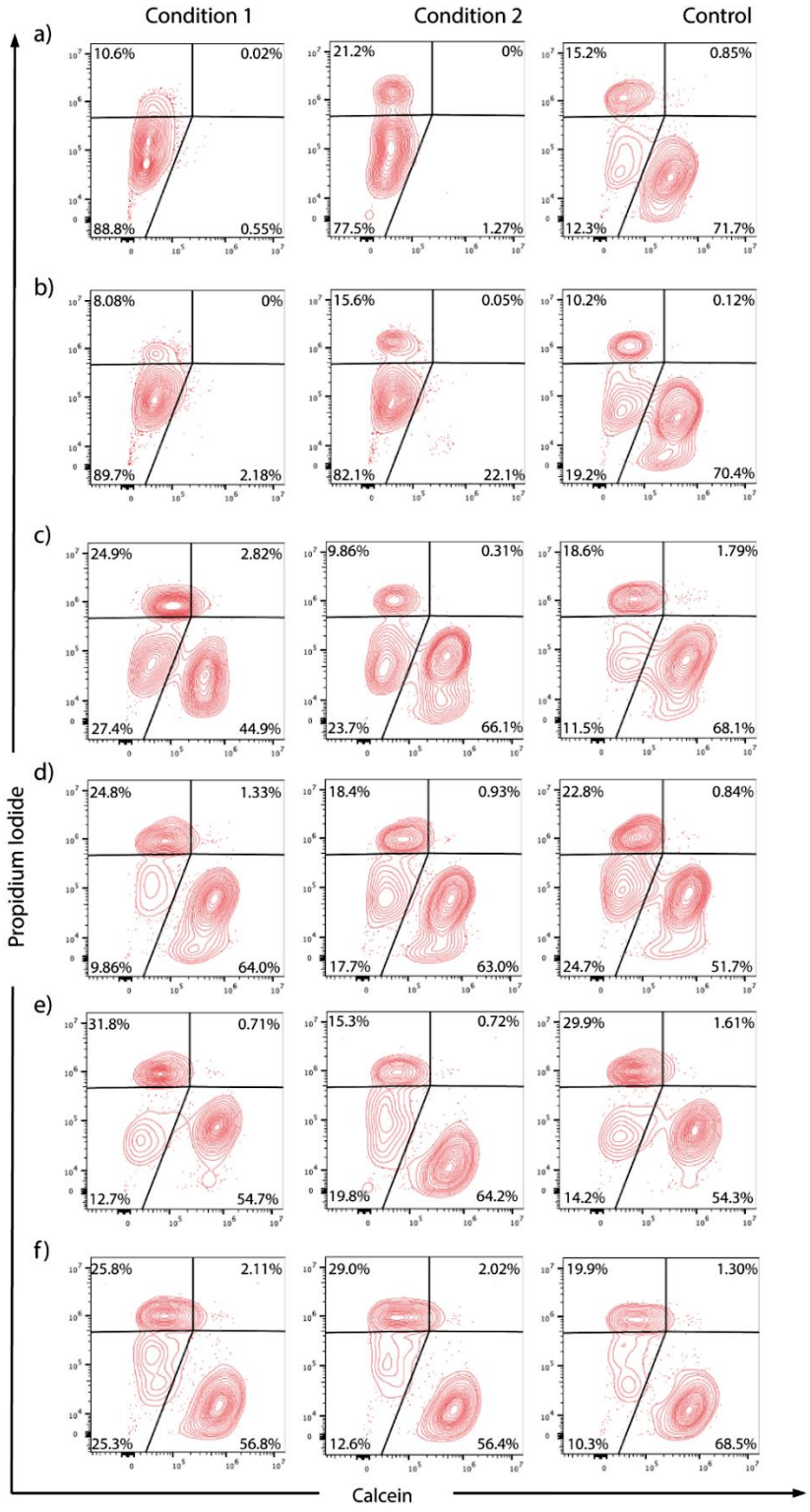

Figure 3.3.27. Representative flow cytometric dot-plots showing Calcein and PI-positive cells 24 h after NIR irradiation of the spheroids for a) AuBy@NU-1000(CbPt)@PEG, b) AuBy@NU-1000(OXA)@PEG, c) AuBy@NU-1000@PEG, d) Free CbPt, e) Free OXA, f) Control spheroids.

USC UNIVERSIDADE DE SANTIAGO DE COMPOSTELA

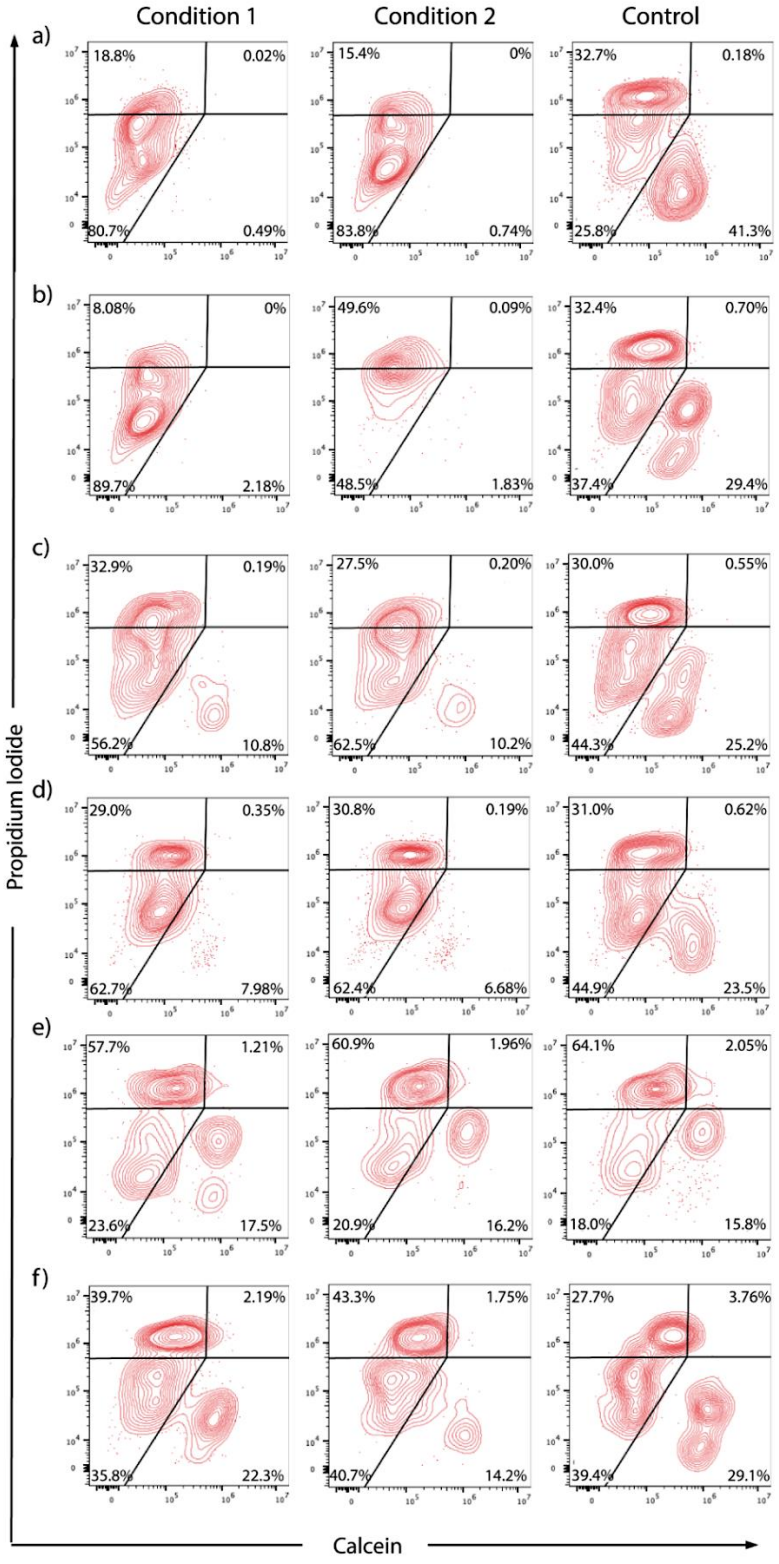

Figure 3.3.28. Representative flow cytometric dot-plots showing Calcein and PI-positive cells 72 h after NIR irradiation of the spheroids for a) AuBy@NU-1000(CbPt)@PEG, b) AuBy@NU-1000(OXA)@PEG, c) AuBy@NU-1000@PEG, d) Free CbPt, e) Free OXA, f) Control spheroids.

USC UNIVERSIDADE DE SANTIAGO DE COMPOSTELA

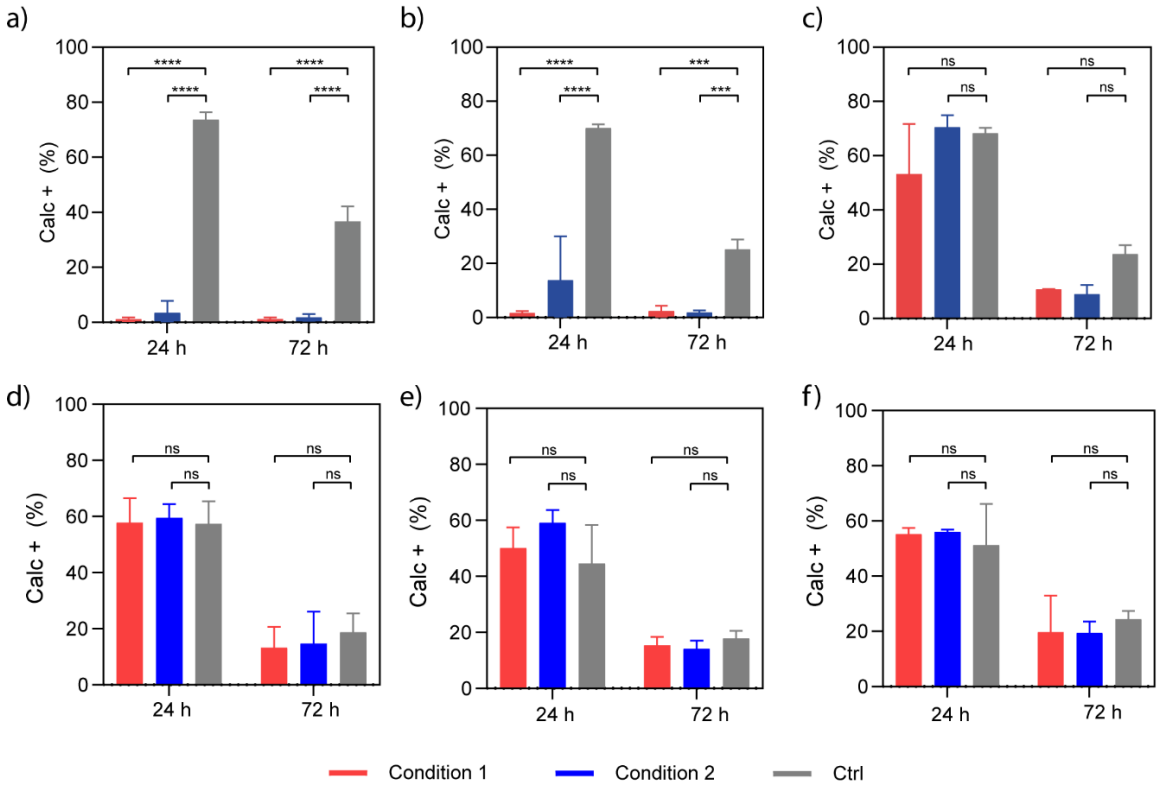

Figure 3.3.29. Flow cytometry results of % of calcein stained cells after 24h and 72h of irradiation for a) AuBy@NU-1000(CbPt)@PEG, b) AuBy@NU-1000(OXA)@PEG, c) AuBy@NU-1000@PEG, d) Free CbPt, b) Free OXA and c) control spheroids.

USC UNIVERSIDADE DE SANTIAGO DE COMPOSTELA

4. Conclusions

USC
UNIVERSIDADE
DE SANTIAGO
DE COMPOSTELA

The experimental results presented in this doctoral thesis shed light on the multifaceted potential of nano metal organic frameworks (NMOFs) in diverse biomedical applications. The exploration of NMOFs pore encapsulation and surface functionalization has demonstrated their capacity as innovative nanocarriers for molecules and drugs. Moreover, their possible combination with metal nanoparticles derived in outstanding stimuli responsive core@shell nanocomposites (NCs) with thermoplasmonic properties and controlled drug release.

Chapter 1 has introduced a novel approach for surface modification of NMOFs using a versatile, clickable amphiphilic polymer derivatized with dibenzo cyclooctyne groups. A selection of NMOFs (UiO-67, NU-1000, PCN-222 and ZIF-8) were produced with high monodispersity and uniformity and were successfully coated with the amphiphilic polymer. This coating rendered the NMOFs remarkably stable both structurally and colloidal-wise in various biologically relevant media, solving one of the main problems of the proposed Zr and Zn NMOFs and making them suitable for bioapplications. Additionally, the selected NMOFs were loaded with cresyl violet, a common histological stain and lysosomal marker, and showcased exceptional loading capacities within their pores and sustained cargo retention post-PMA functionalization.

For comparative purposes, two size-equivalent (150 nm) NMOFs were selected, ZIF-8 and UiO-67, which were functionalized with a library of biologically relevant azide-derivatized (macro)molecules, including polyethylene glycol, mannose, a cell-penetrating peptide, or a fluorescence probe using a biorthogonal reaction. The derivatized NMOFs exhibited distinct cellular uptake patterns attributed to their surface functionalization, thereby highlighting the efficacy and versatility of the proposed coating strategy. These findings underscore the potential of the introduced universal, biorthogonal surface engineering approach for NMOFs in enhancing the effectiveness of targeted drug delivery systems.

In Chapter 2, novel experiments were conducted to characterize particle concentrations, employing a comparative analysis between nanoparticle tracking analysis (NTA) and flow cytometry. These experiments proved the efficiency and precision of flow cytometry, which relies on the scattering and fluorescence properties of the particles, offering faster and more accurate results. Then, two coordinative post-synthesis modification (PSM) methods utilizing phosphate-modified molecules (PEG and DNA) were investigated across three different Zr-based NMOFs (UiO-67, NU-1000, and PCN-222). This innovative approach relies on the coordination of phosphate groups with Zr present on the particle surface, resulting in strong coordination bonds that impart high stability to the particles in biological environments.

Additionally, a pioneering functionalization approach was introduced, building upon the initial DNA surface modification. Utilizing UiO-67 as a model Zr NMOF, the particles were endowed with fluorescence by encapsulating calcein. Using the DNA chains present on the particle surface, hybridization with complementary DNA modified with azide groups was performed, introducing free azides on the surface. These azides facilitated click reactions with DBCO-modified BSA, enabling the attainment of a homogeneous protein coating. This novel strategy for protein immobilization onto NMOF surfaces holds significant promise for bioapplications such as vaccine development.

USC UNIVERSIDADE DE SANTIAGO DE COMPOSTELA

Therefore, this chapter introduced pioneering methodologies for the modification and functionalization of Zr-based NMOFs, offering enhanced stability in biological environments, precise characterization techniques, and innovative strategies for protein immobilization, thereby advancing the field of NMOF-based bioapplications.

Chapter 3 embraced a comprehensive perspective, exploring two core@shell NCs featuring a AuBy nanocore embedded in NMOFs, either ZIF-8 or NU-1000. These NCs not only preserved the plasmonic properties inherent to AuBy but also exhibited exceptional cargo-loading capabilities within their microporous MOF nanoshells. To improve stability and mitigate unspecific cargo leakage, both systems were enhanced with polymer functionalization. Subjected to NIR irradiation, the NCs demonstrated remarkable photothermal properties, enabling controlled cargo release through thermoplasmonic activation. In vitro testing confirmed the efficacy of these NIR-responsive NCs as efficient DDSs, with drug-loaded NU-1000/NCs showing promising results in both 2D and 3D cell cultures.

This study signifies substantial progress in the creation of smart, stable, and biocompatible core@shell NMOF platforms. These platforms excel as robust vehicles for intracellular drug delivery, merging thermoplasmonic capabilities with outstanding cargo-loading capacities. The results position these nanocomposites at the forefront of advanced nanomaterials for bioapplications, establishing them as potential tools in advancing drug delivery techniques within nanomedicine.

USC
UNIVERSIDADE DE SANTIAGO DE COMPOSTELA

USC
UNIVERSIDADE
DE SANTIAGO
DE COMPOSTELA

References

[1] S. Bayda, M. Adeel, T. Tuccinardi, M. Cordani and F. Rizzolio, *Molecules* **2019**, *25*, 112.

[2] J. Jeevanandam, A. Barhoum, Y. S. Chan, A. Dufresne and M. K. Danquah, *Beilstein journal of nanotechnology* **2018**, *9*, 1050-1074.

[3] G. Cao, *Nanostructures & nanomaterials: synthesis, properties & applications*, Imperial college press, **2004**, p.

[4] F. Trotta and A. Mele, *Nanosponges: Synthesis and Applications: First Edition, Wiley, London* **2019**.

[5] L. M. Liz-Marzán, A. E. Nel, C. J. Brinker, W. C. W. Chan, C. Chen, X. Chen, D. Ho, T. Hu, K. Kataoka, N. A. Kotov, W. J. Parak and M. M. Stevens, *ACS Nano* **2022**, *16*, 13257-13259.

[6] B. Pelaz, C. Alexiou, R. A. A. Puebla, F. Alves, A. M. Andrews, S. Ashraf, L. P. Balogh, L. Ballerini, A. Bestetti, C. Brendel, S. Bosi, M. Carril, W. C. W. Chan, C. Chen, X. Chen, X. Chen, Z. Cheng, D. Cui, J. Du, C. Dullin, A. Escudero, N. Feliu, M. Gao, M. George, Y. Gogotsi, A. Grünweller, Z. Gu, N. Halas, N. Hampp, R. K. Hartmann, M. C. Hersam, P. Hunziker, J. Jian, X. Jiang, P. Jungebluth, P. Kadhiresan, K. Kataoka, A. Khademhosseini, J. Kopecek, N. A. Kotov, H. F. Krug, D. S. Lee, C.-M. Lehr, K. W. Leong, X.-J. Liang, M. L. Lim, L. M. L. Marzán, X. Ma, P. Macchiarini, H. Meng, H. Möhwald, P. Mulvaney, A. E. Nel, S. Nie, P. Nordlander, T. Okano, J. Oliveira, T. H. Park, R. M. Penner, M. Prato, V. Puntes, V. M. Rotello, A. Samarakoon, R. E. Schaak, Y. Shen, S. Sjöqvist, A. G. Skirtach, M. G. Soliman, M. M. Stevens, H.-W. Sung, B. Z. Tang, R. Tietze, B. N. Udugama, J. S. VanEpps, T. Weil, P. S. Weiss, I. Willner, Y. Wu, L. Yang, Z. Yue, Q. Zhang, Q. Zhang, X. E. Zhang, Y. Zhao, X. Zhou and W. J. Parak, *ACS Nano* **2017**, *11*, 2313-2381.

[7] G. Nabil, K. Bhise, S. Sau, M. Atef, H. A. El-Banna and A. K. Iyer, *Drug Discov. Today* **2019**, *24*, 462-491.

[8] P. H. Cortés and S. R. Macías, *Metal-organic frameworks in biomedical and environmental field*, Springer, **2021**, p.

[9] Y. Wang, J. Yan, N. Wen, H. Xiong, S. Cai, Q. He, Y. Hu, D. Peng, Z. Liu and Y. Liu, *Biomaterials* **2020**, *230*, 119619.

[10] M. Mitchell, M. Billingsley, R. Haley, M. Wechsler and N. Peppas, *Engineering Precision Nanoparticles for Drug Delivery. Nat. Rev. Drug Discov 20*, 101-124.

[11] E. A. Flügel, A. Ranft, F. Haase and B. V. Lotsch, *J. Mater. Chem.* **2012**, *22*, 10119-10133.

[12] J. Yang and Y. W. Yang, *Small* **2020**, *16*, 1906846.

[13] J. W. Osterrieth and D. Fairen-Jimenez, *Biotechnol. J.* **2021**, *16*, 2000005.

[14] M. J. Kalmutzki, N. Hanikel and O. M. Yaghi, *Science advances* **2018**, *4*, eaat9180.

[15] Y. Kinoshita, I. Matsubara, T. Higuciu and Y. Saito, *Bull. Chem. Soc. Jpn.* **1959**, *32*, 1221-1226.

[16] A. Phan, C. J. Doonan, F. J. Uribe-Romo, C. B. Knobler, M. Okeeffe and O. M. Yaghi, *Acc. Chem. Res.* **2010**, *43*, 58-67.

[17] M. A. Mohamud and A. B. Yurtcan in *Zeolotic imidazolate frameworks (ZIFs) derived porous carbon: A review from crystal growth & green synthesis to oxygen reduction reaction activity, Vol. 46* Elsevier Ltd, **2021**, pp. 33782-33800.

[18] C. Carrillo-Carrion, R. Martínez, M. F. N. Poupard, B. Pelaz, E. Polo, A. Arenas-Vivo, A. Olgiati, P. Taboada, M. G. Soliman, U. Catalán, S. Fernández-Castillejo, R. Solà, W. J. Parak, P. Horcajada, R. Alvarez-Puebla and P. d. Pino, *Angew. Chem.* **2019**, *58*, 7078-7082.

[19] R. Martínez, C. Carrillo-Carrión, P. Destito, A. Alvarez, M. Tomás-Gamasa, B. Pelaz, F. Lopez, J. L. Mascareñas and P. del Pino, *Cell Reports Physical Science* **2020**, *1*.

[20] C. Carrillo-Carrión, R. Martínez, E. Polo, M. Tomás-Gamasa, P. Destito, M. Ceballos, B. Pelaz, F. López, J. L. Mascareñas and P. D. Pino, *ACS Nano* **2021**, *15*, 16924-16933.

[21] H. Li, M. Eddaoudi, M. O'Keeffe and O. M. Yaghi, *Nature* **1999**, *402*, 276-279.

[22] S. S-Y Chui, S. M-F Lo, J. P. H Charmant, A. Guy Orpen and I. D. Williams, *Science* **1999**, *283*, 1148-1150.

[23] V. Guillerm and D. Maspoch, *J. Am. Chem. Soc.* **2019**, *141*, 16517-16538.

[24] C. A. Trickett, K. J. Gagnon, S. Lee, F. Gándara, H.-B. Bürgi and O. M. Yaghi, *Angew. Chem.* **2015**, *127*, 11314-11319.

[25] H. Furukawa, F. Gándara, Y. B. Zhang, J. Jiang, W. L. Queen, M. R. Hudson and O. M. Yaghi, *J. Am. Chem. Soc.* **2014**, *136*, 4369-4381.

[26] J. H. Cavka, S. Jakobsen, U. Olsbye, N. Guillou, C. Lamberti, S. Bordiga and K. P. Lillerud, *J. Am. Chem. Soc.* **2008**, *130*, 13850-13851.

[27] Y. Zhang, X. Zhang, J. Lyu, K. I. Otake, X. Wang, L. R. Redfern, C. D. Malliakas, Z. Li, T. Islamoglu, B. Wang and O. K. Farha, *J. Am. Chem. Soc.* **2018**, *140*, 11179-11183.

[28] R. Wang, Z. Wang, Y. Xu, F. Dai, L. Zhang and D. Sun, *Inorg. Chem.* **2014**, *53*, 7086-7088.

[29] S. Dai, C. Simms, I. Dovgaliuk, G. Patriarche, A. Tissot, T. N. Parac-Vogt and C. Serre, *Chem. Mater.* **2021**, *33*, 7057-7066.

[30] J. E. Mondloch, W. Bury, D. Fairen-Jimenez, S. Kwon, E. J. Demarco, M. H. Weston, A. A. Sarjeant, S. T. Nguyen, P. C. Stair, R. Q. Snurr, O. K. Farha and J. T. Hupp, *J. Am. Chem. Soc.* **2013**, *135*, 10294-10297.

[31] Y. Chen, X. Zhang, K. Ma, Z. Chen, X. Wang, J. Knapp, S. Alayoglu, F. Wang, Q. Xia, Z. Li, T. Islamoglu and O. K. Farha, *ACS Applied Nano Materials* **2019**, *2*, 6098-6102.

[32] X. Zhang, B. L. Frey, Y. S. Chen and J. Zhang, *J. Am. Chem. Soc.* **2018**, *140*, 7710-7715.

[33] M. J. Hurlock, L. Hao, K. W. Kriegsman, X. Guo, M. O'Keeffe and Q. Zhang, *ACS Applied Materials and Interfaces* **2021**, *13*, 51945-51953.

[34] Y. Pan, Y. Liu, G. Zeng, L. Zhao and Z. Lai, *Chem. Commun.* **2011**, *47*, 2071-2073.

[35] Y. R. Lee, M. S. Jang, H. Y. Cho, H. J. Kwon, S. Kim and W. S. Ahn, *Chem. Eng. J.* **2015**, *271*, 276-280.

[36] S. Wang, L. Furchtgott, K. C. Huang and J. W. Shaevitz, *Proceedings of the National Academy of Sciences of the United States of America*

USC
UNIVERSIDADE DE SANTIAGO DE COMPOSTELA

2011, *109*, E595-604.

[37] J. J. Richardson, K. Liang, F. Lisi, M. Björnmalm, M. Faria, J. Guo and P. Falcaro, *Eur. J. Inorg. Chem.* **2016**, *2016*, 4499-4504.

[38] A. J. Howarth, A. W. Peters, N. A. Vermeulen, T. C. Wang, J. T. Hupp and O. K. Farha in *Best practices for the synthesis, activation, and characterization of metal−organic frameworks*, *Vol. 29* American Chemical Society, **2017**, pp. 26-39.

[39] J. Xiong, L. Wang, X. Qin and J. Yu, *Mater. Lett.* **2021**, *302*, 130427-130427.

[40] A. Huang, L. Wan and J. Caro, *Mater. Res. Bull.* **2018**, *98*, 308-313.

[41] A. Schaate, P. Roy, A. Godt, J. Lippke, F. Waltz, M. Wiebcke and P. Behrens, *Chemistry - A European Journal* **2011**, *17*, 6643-6651.

[42] M. J. Katz, Z. J. Brown, Y. J. Colón, P. W. Siu, K. A. Scheidt, R. Q. Snurr, J. T. Hupp and O. K. Farha, *Chem. Commun.* **2013**, *49*, 9449-9451.

[43] J. Hühn, C. Carrillo-Carrion, M. G. Soliman, C. Pfeiffer, D. Valdeperez, A. Masood, I. Chakraborty, L. Zhu, M. Gallego, Y. Zhao, M. Carril, N. Feliu, A. Escudero, A. M. Alkilany, B. Pelaz, P. d. Pino and W. J. Parak, *Chem. Mater.* **2017**, *29*, 399−461.

[44] X. G. Wang, Q. Cheng, Y. Yu and X. Z. Zhang, *Angewandte Chemie - International Edition* **2018**, *57*, 7836-7840.

[45] S. Goswami, H. Noh, L. R. Redfern, K.-i. Otake, C.-W. Kung, Y. Cui, K. W. Chapman, O. K. Farha and J. T. Hupp, *Chem. Mater.* **2019**, *31*, 1485-1490.

[46] Y. H. Wang, C. H. Chuang, T. A. Chiu, C. W. Kung and W. Y. Yu, *Journal of Physical Chemistry C* **2020**, *124*, 12521-12530.

[47] F. Chen, K. Shen, J. Chen, X. Yang, J. Cui and Y. Li, *ACS Central Science* **2019**, *5*, 176-185.

[48] X. Li, B. Zhang, R. Van Zeeland, L. Tang, Y. Pei, Z. Qi, T. W. Goh, L. M. Stanley and W. Huang, *Catal. Lett.* **2018**, *148*, 940-945.

[49] M.-M. Pan, Y. Ouyang, Y.-L. Song, L.-Q. Si, M. Jiang, X. Yu, L. Xu and I. Willner, *Small* **2022**, *18*, 2200548-2200548.

[50] P. del_Pino, F. Yang, B. Pelaz, Q. Zhang, K. Kantner, R. Hartmann, N. M. d. Baroja, M. Gallego, M. Möller, B. B. Manshian, S. J. Soenen, R. Riedel, N. Hampp and W. J. Parak, *Angew. Chem. Int. Ed.* **2016**, *55*, 5483 - 5487.

[51] Z. Ji, H. Wang, S. Canossa, S. Wuttke and O. M. Yaghi, *Adv. Funct. Mater.* **2020**, *30*, 2000238.

[52] M. d. J. Velásquez-Hernández, M. Linares-Moreau, E. Astria, F. Carraro, M. Z. Alyami, N. M. Khashab, C. J. Sumby, C. J. Doonan and P. Falcaro, *Coord. Chem. Rev.* **2021**, *429*, 213651.

[53] B. Maranescu and A. Visa, *International Journal of Molecular Sciences* **2022**, *23*, 4458.

[54] L. Wang, M. Zheng and Z. Xie, *J. Mater. Chem. B* **2018**, *6*, 707-717.

[55] N. Ye, X. Kou, J. Shen, S. Huang, G. Chen and G. Ouyang, *ChemBioChem* **2020**, *21*, 2585-2590.

UNIVERSIDADE DE SANTIAGO DE COMPOSTELA

[56] X. Chen, Y. Zhuang, N. Rampal, R. Hewitt, G. Divitini, C. A. O'Keefe, X. Liu, D. J. Whitaker, J. W. Wills, R. Jugdaohsingh, J. J. Powell, H. Yu, C. P. Grey, O. A. Scherman and D. Fairen-Jimenez, *J. Am. Chem. Soc.* **2021**, *143*, 13557-13572.

[57] P. Li, Q. Chen, T. C. Wang, N. A. Vermeulen, B. L. Mehdi, A. Dohnalkova, N. D. Browning, D. Shen, R. Anderson and D. A. Gómez-Gualdrón, *Chem* **2018**, *4*, 1022-1034.

[58] T. Luo, G. T. Nash, Z. Xu, X. Jiang, J. Liu and W. Lin, *J. Am. Chem. Soc.* **2021**, *143*, 13519-13524.

[59] J. V. Morabito, L.-Y. Chou, Z. Li, C. M. Manna, C. A. Petroff, R. J. Kyada, J. M. Palomba, J. A. Byers and C.-K. Tsung, *J. Am. Chem. Soc.* **2014**, *136*, 12540-12543.

[60] Z. Li, T. M. Rayder, L. Luo, J. A. Byers and C.-K. Tsung, *J. Am. Chem. Soc.* **2018**, *140*, 8082-8085.

[61] F.-S. Liao, W.-S. Lo, Y.-S. Hsu, C.-C. Wu, S.-C. Wang, F.-K. Shieh, J. V. Morabito, L.-Y. Chou, K. C.-W. Wu and C.-K. Tsung, *J. Am. Chem. Soc.* **2017**, *139*, 6530-6533.

[62] J. Cases Díaz, B. Lozano-Torres and M. Giménez-Marqués, *Chemistry of Materials* **2022**, *34*, 7817-7827.

[63] B. Li, Y. Zhang, D. Ma, T. Ma, Z. Shi and S. Ma, *J. Am. Chem. Soc.* **2014**, *136*, 1202-1205.

[64] S. K. Alsaiari, S. Patil, M. Alyami, K. O. Alamoudi, F. A. Aleisa, J. S. Merzaban, M. Li and N. M. Khashab, *J. Am. Chem. Soc.* **2018**, *140*, 143-146.

[65] G. Kaur, S. Øien-Ødegaard, A. Lazzarini, S. M. Chavan, S. Bordiga, K. P. Lillerud and U. Olsbye, *Cryst. Growth Des.* **2019**, *19*, 4246-4251.

[66] E. Linnane, S. Haddad, F. Melle, Z. Mei and D. Fairen-Jimenez, *Chem. Soc. Rev.* **2022**.

[67] M. Kalaj and S. M. Cohen, *ACS central science* **2020**, *6*, 1046-1057.

[68] R. S. Forgan, *Dalton Transactions* **2019**, *48*, 9037-9042.

[69] C. V. McGuire and R. S. Forgan, *Chem. Commun.* **2015**, *51*, 5199-5217.

[70] T. Simon-Yarza, A. Mielcarek, P. Couvreur and C. Serre, *Adv. Mater.* **2018**, *30*, 1870281.

[71] H. Sohrabi, S. Javanbakht, F. Oroojalian, F. Rouhani, A. Shaabani, M. R. Majidi, M. Hashemzaei, Y. Hanifehpour, A. Mokhtarzadeh and A. Morsali, *Chemosphere* **2021**, *281*, 130717.

[72] S. Wang, Y. Chen, S. Wang, P. Li, C. A. Mirkin and O. K. Farha, *J. Am. Chem. Soc.* **2019**, *141*, 2215-2219.

[73] X. Chen, Y. Zhuang, N. Rampal, R. Hewitt, G. Divitini, C. A. O'Keefe, X. Liu, D. J. Whitaker, J. W. Wills and R. Jugdaohsingh, *J. Am. Chem. Soc.* **2021**, *143*, 13557-13572.

[74] A. Kirchon, L. Feng, H. F. Drake, E. A. Joseph and H.-C. Zhou, *Chem. Soc. Rev.* **2018**, *47*, 8611-8638.

[75] A. Zimpel, T. Preiß, R. Röder, H. Engelke, M. Ingrisch, M. Peller, J. O. Rädler, E. Wagner, T. Bein and U. Lächelt, *Chem. Mater.* **2016**, *28*, 3318-3326.

[76] M. G. Soliman, B. P. B, W. J. Parak and P. d. Pino, *Chem. Mater.* **2015**, *27*, 990-997.

[77] R. H. Fang, A. V. Kroll, W. Gao and L. Zhang, *Advanced Materials* **2018**, *30*, 1706759.

[78] C.-M. J. Hu, R. H. Fang, B. T. Luk, K. N. Chen, C. Carpenter, W. Gao, K. Zhang and L. Zhang, *Nanoscale* **2013**, *5*, 2664-2668.

[79] L. Rao, L. L. Bu, Q. F. Meng, B. Cai, W. W. Deng, A. Li, K. Li, S. S. Guo, W. F. Zhang and W. Liu, *Advanced Functional Materials* **2017**, *27*, 1604774.

[80] J. Su, H. Sun, Q. Meng, Q. Yin, P. Zhang, Z. Zhang, H. Yu and Y. Li, *Advanced Functional Materials* **2016**, *26*, 7495-7506.

[81] A. Parodi, N. Quattrocchi, A. L. Van De Ven, C. Chiappini, M. Evangelopoulos, J. O. Martinez, B. S. Brown, S. Z. Khaled, I. K. Yazdi and M. V. Enzo, *Nature nanotechnology* **2013**, *8*, 61-68.

[82] X. Zhu, H. Huang, H. Zhang, Y. Zhang, P. Shi, K. Qu, S.-b. Cheng, A.-l. Wang and Q. Lu, *ACS Applied Materials & Interfaces* **2022**, *14*, 32176-32182.

[83] E. Soprano, A. Alvarez, B. Pelaz, P. Del Pino and E. Polo, *Advanced Biosystems* **2020**, *4*, 1900260.

[84] B. Illes, P. Hirschle, S. Barnert, V. Cauda, S. Wuttke and H. Engelke, *Chemistry of Materials* **2017**, *29*, 8042-8046.

[85] S. Wuttke, S. Braig, T. Preiß, A. Zimpel, J. Sicklinger, C. Bellomo, J. O. Rädler, A. M. Vollmar and T. Bein, *Chemical Communications* **2015**, *51*, 15752-15755.

[86] M. Z. Alyami, S. K. Alsaiari, Y. Li, S. S. Qutub, F. A. Aleisa, R. Sougrat, J. S. Merzaban and N. M. Khashab, *Journal of the American Chemical Society* **2020**, *142*, 1715-1720.

[87] S. Yuan, L. Feng, K. Wang, J. Pang, M. Bosch, C. Lollar, Y. Sun, J. Qin, X. Yang and P. Zhang, *Adv. Mater.* **2018**, *30*, 1704303.

[88] S. Rojas, A. Arenas-Vivo and P. Horcajada, *Coord. Chem. Rev.* **2019**, *388*, 202-226.

[89] J. Schubert and M. Chanana, *Current Medicinal Chemistry* **2019**, *25*, 4556.

[90] X. Ma, M. Lepoitevin and C. Serre, *Materials Chemistry Frontiers* **2021**.

[91] P. del_Pino, B. Pelaz, Q. Zhang, P. Maffre, G. U. Nienhaus and W. J. Parak, *Materials Horizons* **2014**, *1*, 301-313.

[92] H. Li, M. Cosio, K. Wang, W. Burtner and H.-C. Zhou in *Design and Construction of Chemically Stable Metal-Organic Frameworks*, pp. 1-35.

[93] M. Ding, X. Cai and H.-L. Jiang, *Chemical Science* **2019**, *10*, 10209-10230.

[94] A. J. Howarth, Y. Liu, P. Li, Z. Li, T. C. Wang, J. T. Hupp and O. K. Farha, *Nature Reviews Materials* **2016**, *1*, 15018.

[95] T. He, X.-J. Kong and J.-R. Li, *Acc. Chem. Res.* **2021**, *54*, 3083-3094.

[96] R. Ettlinger, U. Lächelt, R. Gref, P. Horcajada, T. Lammers, C. Serre, P. Couvreur, R. E. Morris and S. Wuttke, *Chem. Soc. Rev.* **2022**.

[97] M. S. de Almeida, E. Susnik, B. Drasler, P. Taladriz-Blanco, A. Petri-Fink and B. Rothen-Rutishauser, *Chem. Soc. Rev.* **2021**, *50*, 5397-5434.

[98] S. Behzadi, V. Serpooshan, W. Tao, M. A. Hamaly, M. Y. Alkawareek, E. C. Dreaden, D. Brown, A. M. Alkilany, O. C. Farokhzad and M. Mahmoudi, *Chem. Soc. Rev.* **2017**, *46*, 4218-4244.

USC
DE SANTIAGO DE COMPOSTELA

[99] M. Mahmoudi, J. Meng, X. Xue, X. J. Liang, M. Rahmand, C. Pfeiffer, R. Hartmann, P. R. Gil, B. Pelaz, W. J. Parak, P. d. Pino, S. Carregal-Romero, A. G. Kanaras and S. T. Selvan, *Biotechnol. Adv.* **2014**, *32*, 679– 692.

[100] M. Mahmoudi, J. Meng, X. Xue, X. J. Liang, M. Rahmand, C. Pfeiffer, R. Hartmann, P. R. Gil, B. Pelaz, W. J. Parak, P. d. Pino, S. Carregal-Romero, A. G. Kanaras and S. T. Selvan, *Biotechnol. Adv.* **2014**, *32*, 679–692.

[101] D. J. de Aberasturi, A. B. Serrano-Montes and L. M. Liz-Marzán, *Advanced Optical Materials* **2015**, *3*, 602-617.

[102] E. Hutter and J. H. Fendler, *Adv. Mater.* **2004**, *16*, 1685-1706.

[103] U. Kreibig and M. Vollmer, *Optical properties of metal clusters*, Springer Science & Business Media, **2013**, p.

[104] H. Yu, Y. Peng, Y. Yang and Z.-Y. Li, *npj Computational Materials* **2019**, *5*, 1-14.

[105] K. M. Mayer and J. H. Hafner, *Chem. Rev.* **2011**, *111*, 3828-3857.

[106] J. Olson, S. Dominguez-Medina, A. Hoggard, L.-Y. Wang, W.-S. Chang and S. Link, *Chem. Soc. Rev.* **2015**, *44*, 40-57.

[107] E. Polo, M. F. N. Poupard, L. Guerrini, P. Taboada, B. Pelaz, R. A. Alvarez-Puebla and P. del Pino, *Nano Today* **2018**, *20*, 58-73.

[108] P. K. Jain, X. Huang, I. H. El-Sayed and M. A. El-Sayed, *Plasmonics* **2007**, *2*, 107-118.

[109] M. Kim, J. H. Lee and J. M. Nam, *Advanced Science* **2019**, *6*, 1900471.

[110] J. Mosquera, Y. Zhao, H. J. Jang, N. Xie, C. Xu, N. A. Kotov and L. M. Liz-Marzán, *Adv. Funct. Mater.* **2020**, *30*, 1902082.

[111] X. Huang and M. A. El-Sayed, *J. Adv. Res* **2010**, *1*, 13-28.

[112] H. P. Paudel, A. Safaei and M. N. Leuenberger, *Nanoplasmonics in Metallic Nanostructures and Dirac Systems*, InTech Rijeka, **2017**, p.

[113] A. Farzin, S. A. Etesami, J. Quint, A. Memic and A. Tamayol, *Adv. Healthc. Mater.* **2020**, *9*, 1901058.

[114] M. J. Ndolomingo, N. Bingwa and R. Meijboom, *Journal of Materials Science* **2020**, *55*, 6195-6241.

[115] W. Wang, X. Zhang, R. Huang, C.-M. Hirschbiegel, H. Wang, Y. Ding and V. M. Rotello, *Advanced Drug Delivery Reviews* **2021**, *176*, 113893.

[116] M. Nasrollahzadeh, M. Sajjadi, J. Dadashi and H. Ghafuri, *Adv. Colloid Interface Sci.* **2020**, *276*, 102103.

[117] Y. You, Q. Deng, Y. Wang, Y. Sang, G. Li, F. Pu, J. Ren and X. Qu, *Nat. Commun.* **2022**, *13*, 1-11.

[118] M. Martínez-Calvo and J. L. Mascareñas, *Coord. Chem. Rev.* **2018**, *359*, 57-79.

[119] M. Yang, J. Li and P. R. Chen, *Chem. Soc. Rev.* **2014**, *43*, 6511-6526.

[120] T. T. V. Phan, T.-C. Huynh, P. Manivasagan, S. Mondal and J. Oh, *Nanomaterials* **2019**, *10*, 66.

USC UNIVERSIDADE DE SANTIAGO DE COMPOSTELA

[121] B. Hvolbæk, T. V. Janssens, B. S. Clausen, H. Falsig, C. H. Christensen and J. K. Nørskov, *Nano today* **2007**, *2*, 14-18.

[122] V. I. Shubayev, T. R. Pisanic II and S. Jin, *Advanced drug delivery reviews* **2009**, *61*, 467-477.

[123] V. F. Cardoso, A. Francesko, C. Ribeiro, M. Bañobre-López, P. Martins and S. Lanceros-Mendez, *Adv. Healthc. Mater.* **2018**, *7*, 1700845.

[124] K. Wu, D. Su, J. Liu, R. Saha and J.-P. Wang, *Nanotechnology* **2019**, *30*, 502003.

[125] H. Lee, T.-H. Shin, J. Cheon and R. Weissleder, *Chem. Rev.* **2015**, *115*, 10690-10724.

[126] Y. Sun, L. Zheng, Y. Yang, X. Qian, T. Fu, X. Li, Z. Yang, H. Yan, C. Cui and W. Tan, *Nano-Micro Letters* **2020**, *12*, 1-29.

[127] Q. Wang and D. Astruc, *Chem. Rev.* **2019**, *120*, 1438-1511.

[128] X. Ge, R. Wong, A. Anisa and S. Ma, *Biomaterials* **2022**, *281*, 121322.

[129] B. Nirosha Yalamandala, W. T. Shen, S. H. Min, W. H. Chiang, S. J. Chang and S. H. Hu, *Adv. Nanobiomed. Res.* **2021**, *1*, 2100014.

[130] G. Chedid and A. Yassin, *Nanomaterials* **2018**, *8*, 916.

[131] J. Zhou, G. Tian, L. Zeng, X. Song and X. w. Bian, *Adv. Healthc. Mater.* **2018**, *7*, 1800022.

[132] T. Wen, G. Quan, B. Niu, Y. Zhou, Y. Zhao, C. Lu, X. Pan and C. Wu, *Small* **2021**, *17*, 2005064.

[133] Y. Ma, X. Qu, C. Liu, Q. Xu and K. Tu, *Frontiers in molecular biosciences* **2021**, *8*, 805228.

[134] A. Cabrera-García, E. Checa-Chavarria, E. Rivero-Buceta, V. Moreno, E. Fernández and P. Botella, *J. Colloid Interface Sci.* **2019**, *541*, 163-174.

[135] W. Cai, J. Wang, C. Chu, W. Chen, C. Wu and G. Liu, *Advanced Science* **2019**, *6*, 1801526.

[136] J. Chen, J. Liu, Y. Hu, Z. Tian and Y. Zhu, *Science and Technology of Advanced Materials* **2019**, *20*, 1043-1054.

[137] Z. Zhou, J. Zhao, Z. Di, B. Liu, Z. Li, X. Wu and L. Li, *Nanoscale* **2021**, *13*, 131-137.

[138] J.-L. Kan, Y. Jiang, A. Xue, Y.-H. Yu, Q. Wang, Y. Zhou and Y.-B. Dong, *Inorg. Chem.* **2018**, *57*, 5420-5428.

[139] B. Geng, D. Yang, D. Pan, L. Wang, F. Zheng, W. Shen, C. Zhang and X. Li, *Carbon* **2018**, *134*, 153-162.

[140] B. Tang, W. L. Li, Y. Chang, B. Yuan, Y. Wu, M. T. Zhang, J. F. Xu, J. Li and X. Zhang, *Angew. Chem.* **2019**, *131*, 15672-15677.

[141] Q. Zheng, X. Liu, Y. Zheng, K. W. Yeung, Z. Cui, Y. Liang, Z. Li, S. Zhu, X. Wang and S. Wu, *Chem. Soc. Rev.* **2021**, *50*, 5086-5125.

[142] Y. Liu, P. Bhattarai, Z. Dai and X. Chen, *Chem. Soc. Rev.* **2019**, *48*, 2053-2108.

[143] S. Y. Zhang, D. Li, D. Guo, H. Zhang, W. Shi, P. Cheng, L. Wojtas and M. J. Zaworotko, *J. Am. Chem. Soc.* **2015**, *137*, 15406-15409.

[144] Y. Bai, J. Chen and S. C. Zimmerman, *Chem. Soc. Rev.* **2018**, *47*, 1811-1821.

[145] A. Unciti-Broceta, *Nature Chemistry* **2015**, *7*, 538-539.

[146] P. Destito, C. Vidal, F. López and J. L. Mascareñas, *Chem. - Eur. J.* **2021**, *27*, 4789-4816.

[147] J. G. Rebelein and T. R. Ward, *Curr. Opin. Biotechnol.* **2018**, *53*, 106-114.

[148] S. Yang, L. Peng, S. Bulut and W. L. Queen, *Chem. - Eur. J.* **2019**, *25*, 2161-2178.

[149] J. Liang and K. Liang, *Adv. Funct. Mater.* **2020**, *30*, 2001648.

[150] S. Wang, C. M. McGuirk, A. d'Aquino, J. A. Mason and C. A. Mirkin, *Adv. Mater.* **2018**, *30*, 1800202.

[151] A. Pandey, N. Dhas, P. Deshmukh, C. Caro, P. Patil, M. L. García-Martín, B. Padya, A. Nikam, T. Mehta and S. Mutalik, *Coordination Chemistry Reviews* **2020**, *409*, 213212.

[152] D. Chen, D. Yang, C. A. Dougherty, W. Lu, H. Wu, X. He, T. Cai, M. E. Van Dort, B. D. Ross and H. Hong, *ACS nano* **2017**, *11*, 4315-4327.

[153] S. Ambreen, M. Danish, N. D. Pandey and A. Pandey, *Beilstein Journal of Nanotechnology* **2017**, *8*, 604-613.

[154] K. Lu, T. Aung, N. Guo, R. Weichselbaum and W. Lin, *Advanced Materials* **2018**, *30*, 1707634.

[155] W. J. Rieter, K. M. Taylor, H. An, W. Lin and W. Lin, *Journal of the American Chemical Society* **2006**, *128*, 9024-9025.

[156] J. Lin, P. Xin, L. An, Y. Xu, C. Tao, Q. Tian, Z. Zhou, B. Hu and S. Yang, *Chemical Communications* **2019**, *55*, 478-481.

[157] T. Zhang, L. Wang, C. Ma, W. Wang, J. Ding, S. Liu, X. Zhang and Z. Xie, *Journal of Materials Chemistry B* **2017**, *5*, 2330-2336.

[158] S. Rojas, T. Baati, L. Njim, L. Manchego, F. Neffati, N. Abdeljelil, S. Saguem, C. Serre, M. F. Najjar and A. Zakhama, *J. Am. Chem. Soc.* **2018**, *140*, 9581-9586.

[159] S. Rojas, N. Guillou and P. Horcajada, *ACS applied materials & interfaces* **2019**, *11*, 22188-22193.

[160] L. M. Graham, T. M. Nguyen and S. B. Lee, *Nanomedicine* **2011**, *6*, 921-928.

[161] J. H. Wang, M. Li and D. Li, *Chem. - Eur. J.* **2014**, *20*, 12004-12008.

[162] J. Hühn, C. Carrillo-Carrion, M. G. Soliman, C. Pfeiffer, D. Valdeperez, A. Masood, I. Chakraborty, L. Zhu, M. Gallego and Z. Yue, *Chem. Mater.* **2017**, *29*, 399-461.

[163] C. Carrillo-Carrión, R. Martínez, M. F. Navarro Poupard, B. Pelaz, E. Polo, A. Arenas-Vivo, A. Olgiati, P. Taboada, M. G. Soliman, Ú. Catalán, S. Fernández-Castillejo, R. Solà, W. J. Parak, P. Horcajada, R. A. Alvarez-Puebla and P. del Pino, *Angew. Chem. Int. Ed.* **2019**, *58*, 7078-7082.

[164] C. L. Hobday, C. H. Woodall, M. J. Lennox, M. Frost, K. Kamenev, T. Düren, C. A. Morrison and S. A. Moggach, *Nat. Commun.* **2018**, *9*, 1429.

[165] X. Zhang, S. Zheng, J. Tao and X. Wang, *Catalysis Letters* **2022**, *152*, 699-706.

[166] Z. Wang, Y. Fu, Z. Kang, X. Liu, N. Chen, Q. Wang, Y. Tu, L. Wang, S. Song and D. Ling, *J. Am. Chem. Soc.* **2017**, *139*, 15784-15791.

[167] S. Pal, S.-S. Yu and C.-W. Kung, *Chemosensors* **2021**, *9*, 306.

[168] A. J. Howarth, Y. Liu, P. Li, Z. Li, T. C. Wang, J. T. Hupp and O. K. Farha, *Nat. Rev. Mater.* **2016**, *1*, 1-15.

[169] M. Cedrún-Morales, M. Ceballos, E. Polo, P. Del Pino and B. Pelaz, *Chem. Commun.* **2023**, *59*, 2869-2887.

[170] S. Mandal, S. Natarajan, P. Mani and A. Pankajakshan, *Adv. Funct. Mater.* **2021**, *31*, 2006291.

[171] S. Wang, W. Morris, Y. Liu, C. M. McGuirk, Y. Zhou, J. T. Hupp, O. K. Farha and C. A. Mirkin, *Angew. Chem. Int. Ed.* **2015**, *54*, 14738-14742.

[172] J. Liang and K. Liang, *Nano Today* **2021**, *40*, 101256.

[173] X. Zhao, S. Liu, C. Hu, Y. Liu, M. Pang and J. Lin, *ACS Appl. BioMater.* **2019**, *2*, 4436-4441.

[174] X. Hu, Y. Wu and C. Deng, *Mikrochim. Acta* **2020**, *187*, 1-12.

[175] J. Hu, P. Wei, P. H. Seeberger and J. Yin, *Chem. Asian J.* **2018**, *13*, 3448-3459.

[176] P. S. Gonzalez, J. O'Prey, S. Cardaci, V. J. Barthet, J.-i. Sakamaki, F. Beaumatin, A. Roseweir, D. M. Gay, G. Mackay and G. Malviya, *Nature* **2018**, *563*, 719-723.

[177] R. Yang, J. Xu, L. Xu, X. Sun, Q. Chen, Y. Zhao, R. Peng and Z. Liu, *ACS nano* **2018**, *12*, 5121-5129.

[178] Z. Ye, Q. Zhang, S. Wang, P. Bharate, S. Varela-Aramburu, M. Lu, P. H. Seeberger and J. Yin, *Chem. - Eur. J.* **2016**, *22*, 15216-15221.

[179] I. Lostalé-Seijo, I. Louzao, M. Juanes and J. Montenegro, *Chem. Sci.* **2017**, *8*, 7923-7931.

[180] I. Gallego, A. Rioboo, J. J. Reina, B. Díaz, Á. Canales, F. J. Cañada, J. Guerra-Varela, L. Sánchez and J. Montenegro, *ChemBioChem* **2019**, *20*, 1400-1409.

[181] M. Matijass and I. Neundorf, *Med. Drug Discov.* **2021**, *10*, 100092.

[182] M. Cai, Y. Yao, D. Yin, R. Zhu, T. Fu, J. Kong, K. Wang, J. Liu, A. Yao and Y. Ruan, *J. Colloid Interface Sci.* **2023**, *646*, 370-380.

[183] I. Lostalé-Seijo and J. Montenegro, *Nat. Rev. Chem.* **2018**, *2*, 258-277.

[184] G. Gasparini, E.-K. Bang, J. Montenegro and S. Matile, *Chem. comm.* **2015**, *51*, 10389-10402.

[185] G. Yi, J. Son, J. Yoo, C. Park and H. Koo, *Biomater. Res.* **2018**, *22*, 1-8.

[186] H. C. Kolb and K. B. Sharpless, *Drug Discov. Today.* **2003**, *8*, 1128-1137.

[187] D. Wu, K. Yang, Z. Zhang, Y. Feng, L. Rao, X. Chen and G. Yu, *Chem. Soc. Rev.* **2022**, *51*, 1336-1376.

[188] H. Y. Yoon, D. Lee, D.-K. Lim, H. Koo and K. Kim, *Adv. Mater.* **2022**, *34*, 2107192.

[189] L. Taiariol, C. Chaix, C. Farre and E. Moreau, *Chem. Rev.* **2021**, *122*, 340-384.

[190] Y. Takayama, K. Kusamori and M. Nishikawa, *Molecules* **2019**, *24*, 172.

[191] J. Xiong, L. Wang, X. Qin and J. Yu, *Mater. Lett.* **2021**, *302*, 130427.

USC
UNIVERSIDADE DE SANTIAGO DE COMPOSTELA

[192] A. Huang, L. Wan and J. Caro, *Mater. Res. Bull.* **2018**, *98*, 308-313.

[193] A. Schaate, P. Roy, A. Godt, J. Lippke, F. Waltz, M. Wiebcke and P. Behrens, *Chem. - Eur. J.* **2011**, *17*, 6643-6651.

[194] M. Ceballos, M. Cedrún-Morales, M. Rodríguez-Pérez, S. Funes-Hernando, J. M. Vila-Fungueiriño, G. Zampini, M. F. N. Poupard, E. Polo, P. Del Pino and B. Pelaz, *Nanoscale* **2022**, *14*, 6789-6801.

[195] S. Wang, Y. Chen, S. Wang, P. Li, C. A. Mirkin and O. K. Farha, *J. Am. Chem. Soc.* **2019**, *141*, 2215-2219.

[196] M. G. Soliman, B. Pelaz, W. J. Parak and P. Del Pino, *Chem. Mater.* **2015**, *27*, 990-997.

[197] C. Carrillo-Carrión, R. Martínez, M. F. Navarro Poupard, B. Pelaz, E. Polo, A. Arenas-Vivo, A. Olgiati, P. Taboada, M. G. Soliman and Ú. Catalán, *Angew. Chem. Int. Ed.* **2019**, *131*, 7152-7156.

[198] X. Zhang, X. Shi, Q. Zhao, Y. Li, J. Wang, Y. Yang, F. Bi, J. Xu and N. Liu, *Chem. Eng. J.* **2022**, *427*, 131573.

[199] P. P. Ostrowski, G. D. Fairn, S. Grinstein and D. E. Johnson, *Traffic* **2016**, *17*, 1313-1321.

[200] C. Carrillo-Carrión, R. Martínez, M. F. Navarro Poupard, B. Pelaz, E. Polo, A. Arenas-Vivo, A. Olgiati, P. Taboada, M. G. Soliman and Ú. Catalán, *Angewandte Chemie* **2019**, *131*, 7152-7156.

[201] A. Paul, I. K. Banga, S. Muthukumar and S. Prasad, *ACS omega* **2022**, *7*, 26993-27003.

[202] D. Fairen-Jimenez, S. Moggach, M. Wharmby, P. Wright, S. Parsons and T. Duren, *J. Am. Chem. Soc.* **2011**, *133*, 8900-8902.

[203] S. Wang, S. S. Park, C. T. Buru, H. Lin, P.-C. Chen, E. W. Roth, O. K. Farha and C. A. Mirkin, *Nat. Commun.* **2020**, *11*, 2495.

[204] I. Dalmau-Mena, P. Del Pino, B. Pelaz, M. Á. Cuesta-Geijo, I. Galindo, M. Moros, J. M. de la Fuente and C. Alonso, *J. Nanobiotechnology* **2018**, *16*, 1-13.

[205] E. Dalle Vedove, G. Costabile and O. M. Merkel, *Adv. Healthc. Mater.* **2018**, *7*, 1701398.

[206] M. Ceballos, S. Funes-Hernando, G. Zampini, M. Cedrún-Morales, J. M. Vila-Fungueiriño, B. Pelaz and P. del Pino, *Small Structures* **2024**, 2300464.

[207] S. Lorenz, S. Tomcin and V. Mailänder, *Microsc. Microanal.* **2011**, *17*, 440-445.

[208] J. Li, H. Peng, W. Ji, D. Lu, N. Wang, C. Peng, W. Zhang, M. Li and Y. Li, *Int. J. Pharm.* **2023**, 123119.

[209] X. Chen, S. M. Argandona, F. Melle, N. Rampal and D. Fairen-Jimenez, *Chem* **2023**.

[210] G. Sanità, B. Carrese and A. Lamberti, *Frontiers in molecular biosciences* **2020**, *7*, 587012.

[211] C. Mao, *Chem. Soc. Rev* **2011**, *40*, 5690-5697.

[212] S. B. Ebrahimi, D. Samanta and C. A. Mirkin, *J. Am. Chem. Soc.* **2020**, *142*, 11343-11356.

USC UNIVERSIDADE DE SANTIAGO DE COMPOSTELA

[213] J. D. Brodin, A. J. Sprangers, J. R. McMillan and C. A. Mirkin, *J. Am. Chem. Soc.* **2015**, *137*, 14838-14841.

[214] T. Kim, K. Nam, Y. M. Kim, K. Yang and Y. H. Roh, *ACS nano* **2021**, *15*, 1942-1951.

[215] C. H. J. Choi, L. Hao, S. P. Narayan, E. Auyeung and C. A. Mirkin in *Mechanism for the endocytosis of spherical nucleic acid nanoparticle conjugates*, Jenny Stanford Publishing, **2020**, pp. 475-494.

[216] B. Liu, M. Jiang, D. Zhu, J. Zhang and G. Wei, *Chem. Eng. J.* **2022**, *428*, 131118.

[217] C. D. Spicer, C. Jumeaux, B. Gupta and M. M. Stevens, *Chem. Soc. Rev.* **2018**, *47*, 3574-3620.

[218] P. Yadav and A. B. Yadav, *Future Journal of Pharmaceutical Sciences* **2021**, *7*, 1-9.

[219] M. Tarhini, I. Benlyamani, S. Hamdani, G. Agusti, H. Fessi, H. Greige-Gerges, A. Bentaher and A. Elaissari, *Materials* **2018**, *11*, 394.

[220] V. Filipe, A. Hawe and W. Jiskoot, *Pharm. Res.* **2010**, *27*, 796-810.

[221] N. Comfort, K. Cai, T. R. Bloomquist, M. D. Strait, A. W. Ferrante Jr and A. A. Baccarelli, *JoVE (Journal of Visualized Experiments)* **2021**, e62447.

[222] R. M. Zucker, J. N. Ortenzio and W. K. Boyes, *Cytometry Part A* **2016**, *89*, 169-183.

[223] M. C. Lo Giudice, L. M. Herda, E. Polo and K. A. Dawson, *Nature communications* **2016**, *7*, 13475.

[224] R. Masoudifar, N. Pouyanfar, D. Liu, M. Ahmadi, B. Landi, M. Akbari, S. Moayeri-Jolandan, F. Ghorbani-Bidkorpeh, E. Asadian and M.-A. Shahbazi, *Applied Materials Today* **2022**, *29*, 101646.

[225] G. Sanità, P. Armanetti, B. Silvestri, B. Carrese, G. Calì, G. Pota, A. Pezzella, M. d'Ischia, G. Luciani and L. Menichetti, *Frontiers in Bioengineering and Biotechnology* **2020**, *8*, 765.

[226] D. Hu, H. Xu, B. Xiao, D. Li, Z. Zhou, X. Liu, J. Tang and Y. Shen, *ACS applied materials & interfaces* **2018**, *10*, 34974-34982.

[227] A. Al-Amin, **2016**.

[228] J. S. Nanda and J. R. Lorsch, *Methods Enzymol.* **2014**, *536*, 87-94.

[229] A. Rogozea, I. Matei, I. M. Turcu, G. Ionita, V. E. Sahini and A. Salifoglou, *The Journal of Physical Chemistry B* **2012**, *116*, 14245-14253.

[230] E. Poppleton, J. Bohlin, M. Matthies, S. Sharma, F. Zhang and P. Šulc, *Nucleic Acids Res.* **2020**, *48*, e72-e72.

[231] J. Bohlin, M. Matthies, E. Poppleton, J. Procyk, A. Mallya, H. Yan and P. Šulc, *Nature protocols* **2022**, *17*, 1762-1788.

[232] S. J. Hurst, H. D. Hill and C. A. Mirkin, *J. Am. Chem. Soc.* **2008**, *130*, 12192-12200.

[233] A. E. Prigodich, O.-S. Lee, W. L. Daniel, D. S. Seferos, G. C. Schatz and C. A. Mirkin, *J. Am. Chem. Soc.* **2010**, *132*, 10638-10641.

[234] B. Jachimska and A. Pajor, *Bioelectrochemistry* **2012**, *87*, 138-146.

[235] B. Pelaz, P. del Pino, P. Maffre, R. Hartmann, M. Gallego, S. Rivera-Fernandez, J. M. de la Fuente, G. U. Nienhaus and W. J. Parak, *ACS nano* **2015**, *9*, 6996-7008.

[236] C. Röcker, M. Pötzl, F. Zhang, W. J. Parak and G. U. Nienhaus, *Nature nanotechnology* **2009**, *4*, 577-580.

[237] J. J. Rennick, A. P. Johnston and R. G. Parton, *Nature nanotechnology* **2021**, *16*, 266-276.

[238] J. Park, T. Pho and J. A. Champion, *Biopolymers* **2023**, *114*, e23563.

[239] M. Carvalho, R. Reis and J. M. Oliveira, *J. Mater. Chem. B* **2020**, *8*, 1128-1138.

[240] B. Yin, W. K. H. Ho, X. Xia, C. K. W. Chan, Q. Zhang, Y. M. Ng, C. Y. K. Lam, J. C. W. Cheung, J. Wang and M. Yang, *Small* **2023**, *19*, 2206762.

[241] J. Yang, X. Zhang, X. Zhang, L. Wang, W. Feng and Q. Li, *Adv. Mater.* **2021**, *33*, 2004754.

[242] A. Kumar, S. Kumar, N. Kumari, S. H. Lee, J. Han, I. J. Michael, Y.-K. Cho and I. S. Lee, *ACS Catalysis* **2018**, *9*, 977-990.

[243] A. Sánchez-Iglesias, N. Winckelmans, T. Altantzis, S. Bals, M. Grzelczak and L. M. Liz-Marzán, *J. Am. Chem. Soc.* **2017**, *139*, 107-110.

[244] Y. Li, W.-S. Lo, F. Zhang, X. Si, L.-Y. Chou, X.-Y. Liu, B. P. Williams, Y.-H. Li, S.-H. Jung and Y.-S. Hsu, *J. Am. Chem. Soc.* **2021**, *143*, 5182-5190.

[245] C. Mottillo and T. Friščić, *Angew. Chem.* **2014**, *126*, 7601-7604.

[246] J. W. Osterrieth, D. Wright, H. Noh, C.-W. Kung, D. Vulpe, A. Li, J. E. Park, R. P. Van Duyne, P. Z. Moghadam and J. J. Baumberg, *J. Am. Chem. Soc.* **2019**, *141*, 3893-3900.

[247] W. A. Murray, B. Auguié and W. L. Barnes, *J. Phys. Chem. C* **2009**, *113*, 5120-5125.

[248] M. M. Miller and A. A. Lazarides, *J. Phys. Chem. B* **2005**, *109*, 21556-21565.

[249] X. Chen, B. B. Mendes, Y. Zhuang, J. Conniot, S. Mercado Argandona, F. Melle, D. P. Sousa, D. Perl, A. Chivu and H. K. Patra, *J. Am. Chem. Soc.* **2024**, *146*, 1644-1656.

[250] N. S. Elbialy, M. M. Fathy and W. M. Khalil, *Int. J. Pharm.* **2015**, *490*, 190-199.

[251] M. Pourmadadi, M. M. Eshaghi, M. Shaghaghi, S. Das, R. Arshad, S. Ghotekar, A. Rahdar, A.-L. E. Manicum and S. Pandey, *OpenNano* **2023**, 100175.

[252] L. Zhou, Q. Xu, L. Huang, J. Jin, X. Zuo, Q. Zhang, L. Ye, S. Zhu, P. Zhan and J. Ren, *Cancer Lett.* **2021**, *500*, 163-171.

[253] Y. Li, P. Xu, D. He, B. Xu, J. Tu and Y. Shen, *Int. J. Nanomed.* **2020**, 6721-6734.

[254] E.-S. Cho, J.-M. Yi, J.-S. Park, Y. J. Lee, C. J. Lim, O.-S. Bang and N. S. Kim, *BMC Complement. Altern. Med.* **2016**, *16*, 1-13.

[255] S. D. Brown, P. Nativo, J.-A. Smith, D. Stirling, P. R. Edwards, B. Venugopal, D. J. Flint, J. A. Plumb, D. Graham and N. J. Wheate, *J. Am. Chem. Soc.* **2010**, *132*, 4678-4684.

[256] R. Marullo, E. Werner, N. Degtyareva, B. Moore, G. Altavilla, S. S. Ramalingam and P. W. Doetsch, *PloS one* **2013**, *8*, e81162.

[257] M. Rave-Fränk, H. Schmidberger, H. Christiansen, C. Boll, J. Lehmann and E. Weiss, *Int. J. Radiat Biol.* **2007**, *83*, 41-47.

[258] S. Göschl, E. Schreiber-Brynzak, V. Pichler, K. Cseh, P. Heffeter, U. Jungwirth, M. A. Jakupec, W. Berger and B. K. Keppler, *Metallomics* **2017**, *9*, 309-322.

[259] S. El Harane, B. Zidi, N. El Harane, K.-H. Krause, T. Matthes and O. Preynat-Seauve, *Cells* **2023**, *12*, 1001.

[260] T. Nederman, B. Norling, B. Glimelius, J. Carlsson and U. Brunk, *Cancer Res.* **1984**, *44*, 3090-3097.

[261] D. Rotin, B. Robinson and I. F. Tannock, *Cancer Res.* **1986**, *46*, 2821-2826.

[262] S. Chu and U. Stochaj, *Cancer Drug Resist.* **2020**, *3*, 302.

[263] S. Harringer, M. Hejl, É. A. Enyedy, M. A. Jakupec, M. S. Galanski, B. K. Keppler, P. J. Dyson and H. P. Varbanov, *Dalton Trans.* **2021**, *50*, 8167-8178.

[264] E. Darrigues, Z. A. Nima, R. J. Griffin, J. M. Anderson, A. S. Biris and A. Rodriguez, *Nanoscale Horiz.* **2020**, *5*, 400-430.

[265] G. Chen, B. Ma, Y. Wang, R. Xie, C. Li, K. Dou and S. Gong, *ACS Appl. Mater. Interfaces* **2017**, *9*, 41700-41711.

[266] A. Senrung, S. Lalwani, D. Janjua, T. Tripathi, J. Kaur, N. Ghuratia, N. Aggarwal, A. Chhokar, J. Yadav and A. Chaudhary, *In vitro models* **2023**, *2*, 219-248.

[267] R. Mukomoto, Y. Nashimoto, T. Terai, T. Imaizumi, K. Hiramoto, K. Ino, R. Yokokawa, T. Miura and H. Shiku, *Analyst* **2020**, *145*, 6342-6348.

[268] R. Jiang, J. Li, L. Li, Y. Lu, H. Zhang and M. Li, *Adv. Funct. Mater.* **2024**, *34*, 2307631.

[269] A. Rezaeian, S. M. Amini, M. R. H. Najafabadi, Z. J. Farsangi and H. Samadian, *Lasers Med. Sci.* **2022**, *37*, 1333-1341.

USC
UNIVERSIDADE DE SANTIAGO DE COMPOSTELA

USC
UNIVERSIDADE
DE SANTIAGO
DE COMPOSTELA

Appendices – Rights & Permissions

Appendix I: Conflict of interest

Manuela Cedrún Morales, the doctoral candidate, declares that there is no conflict of interest associated with this Doctoral Thesis.

Santiago de Compostela, May 4th, 2024

USC
UNIVERSIDADE DE SANTIAGO DE COMPOSTELA

Appendix II: PhD publications and permissions

Part of the information presented in the **introduction** is published in:

"Nanosized metal–organic frameworks as unique platforms for bioapplications" Chemical Communications. **2023.**

Manuela Cedrún-Morales[1], Manuel Ceballos[1], Ester Polo[1], Pablo del Pino[1] and Beatriz Pelaz[1]

[1]*Center for Research in Biological Chemistry and Molecular Materials (CiQUS), University of Santiago de Compostela, 15705 Santiago de Compostela, Spain.*

Contributions: Writing – original draft.

Impact Factor: 4.9. Q1 in Nanoscience & Nanotechnology. This article is licensed under a Creative Commons Attribution-NonCommercial 3.0 Unported Licence. No written permission from RSC is necessary. Copyright 2023. ISSN 2869-2887

Nanosized metal–organic frameworks as unique platforms for bioapplications

M. Cedrún-Morales, M. Ceballos, E. Polo, P. del Pino and B. Pelaz, *Chem. Commun.*, 2023, **59**, 2869 **DOI:** 10.1039/D2CC05851K

This article is licensed under a Creative Commons Attribution-NonCommercial 3.0 Unported Licence. **You can use material from this article in other publications, without requesting further permission** from the RSC, provided that the correct acknowledgement is given and it is not used for commercial purposes.

To request permission **to reproduce material from this article in a commercial publication**, please go to the Copyright Clearance Center request page.

If you are **an author contributing to an RSC publication, you do not need to request permission** provided correct acknowledgement is given.

If you are **the author of this article, you do not need to request permission to reproduce figures and diagrams** provided correct acknowledgement is given. If you want to reproduce the whole article in a third-party commercial publication (excluding your thesis/dissertation for which permission is not required) please go to the Copyright Clearance Center request page.

USC UNIVERSIDADE DE SANTIAGO DE COMPOSTELA

Part of the results presented in section 3.3. are published in:

"Light-Responsive Nanoantennas Integrated into Nanoscale Metal-Organic Frameworks for Smart Drug Delivery". Small science. (Published in **2024**)

Manuela Cedrún-Morales[1], Manuel Ceballos[1], Enrica Soprano[1], Giulia Zampini[1], Ester Polo[1], Beatriz Pelaz[1] and Pablo del Pino[1]

[1]*Center for Research in Biological Chemistry and Molecular Materials (CiQUS), University of Santiago de Compostela, 15705 Santiago de Compostela, Spain.*

Contributions: Preparation, optimization, and characterization of the materials, cell studies; writing – original draft.

Impact Factor: 12.7. Q1 in Nanoscience & Nanotechnology. No written permission from Wiley is necessary. Copyright 2024.

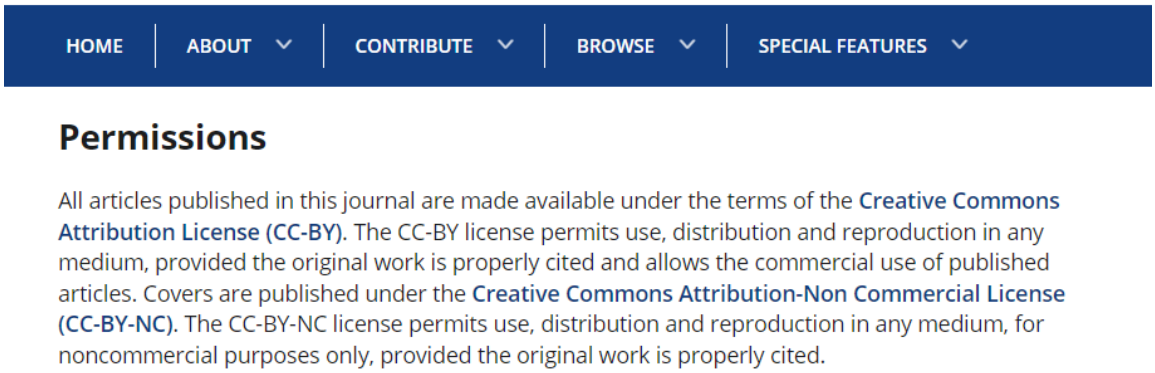

USC
UNIVERSIDADE DE SANTIAGO DE COMPOSTELA

Appendix III: Permissions to publish images, tables, and figures.

IMAGES AND FIGURES: RIGHTS AND PERMISSIONS	
Figure 1.1.2.	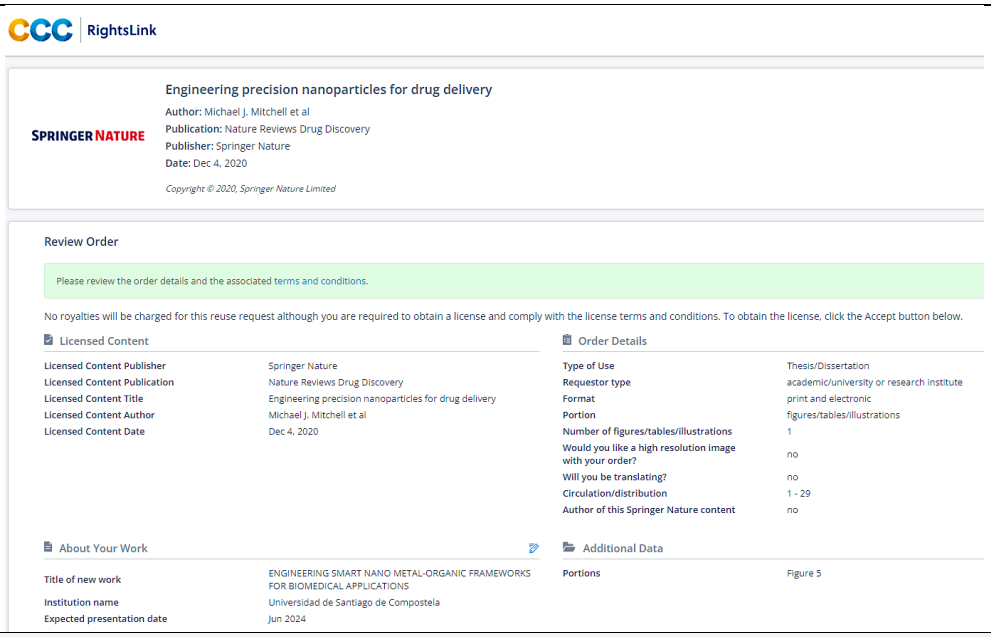
Figure 1.1.7.	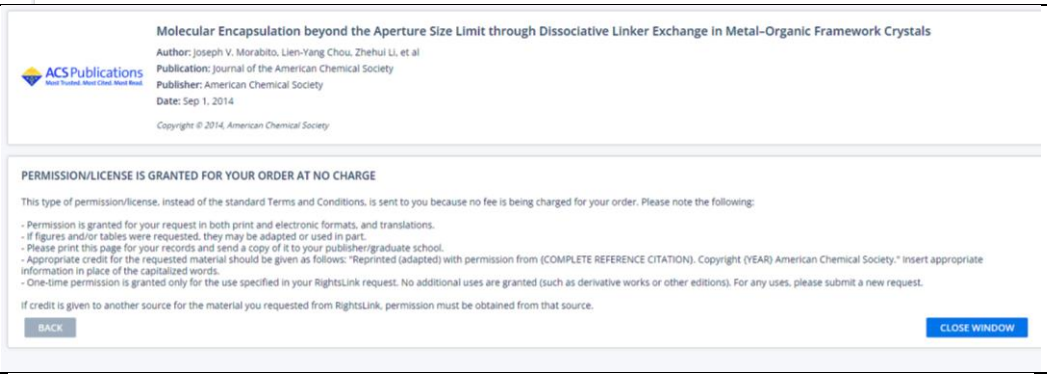
Figure 1.3.3.	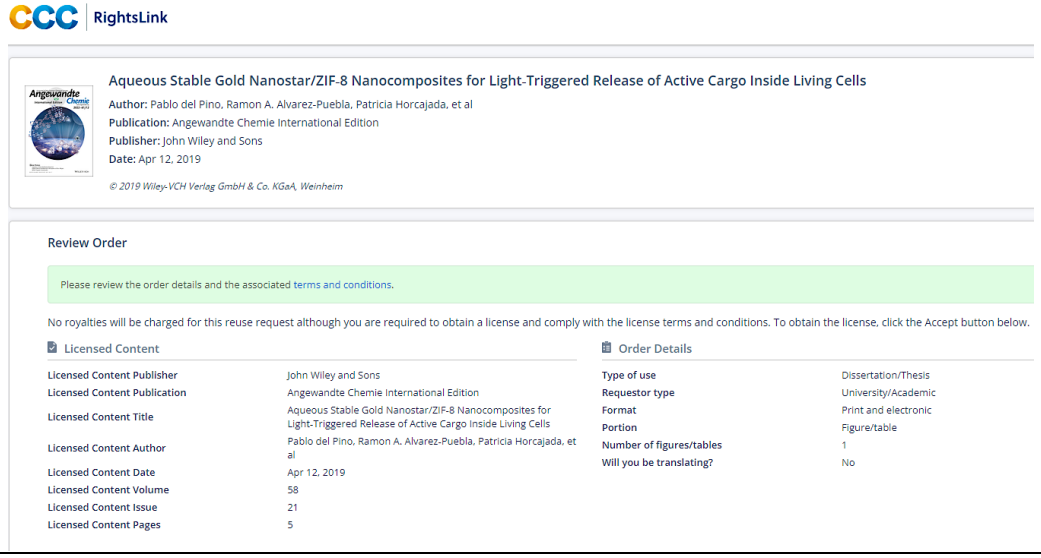

Figure 1.3.4.

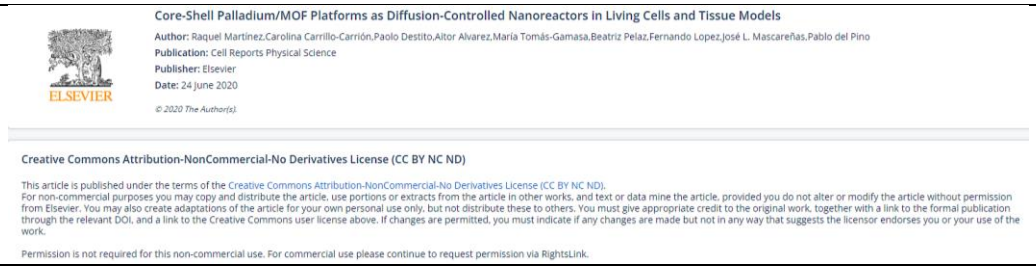

Core-Shell Palladium/MOF Platforms as Diffusion-Controlled Nanoreactors in Living Cells and Tissue Models

Author: Raquel Martínez,Carolina Carrillo-Carrión,Paolo Destito,Aitor Alvarez,María Tomás-Gamasa,Beatriz Pelaz,Fernando Lopez,José L. Mascareñas,Pablo del Pino
Publication: Cell Reports Physical Science
Publisher: Elsevier
Date: 24 June 2020

© 2020 The Author(s).

Creative Commons Attribution-NonCommercial-No Derivatives License (CC BY NC ND)

This article is published under the terms of the Creative Commons Attribution-NonCommercial-No Derivatives License (CC BY NC ND).
For non-commercial purposes you may copy and distribute the article, use portions or extracts from the article in other works, and text or data mine the article, provided you do not alter or modify the article without permission from Elsevier. You may also create adaptations of the article for your own personal use only, but not distribute these to others. You must give appropriate credit to the original work, together with a link to the formal publication through the relevant DOI, and a link to the Creative Commons user license above. If changes are permitted, you must indicate if any changes are made but not in any way that suggests the licensor endorses you or your use of the work.

Permission is not required for this non-commercial use. For commercial use please continue to request permission via RightsLink.

Figure 1.3.5.

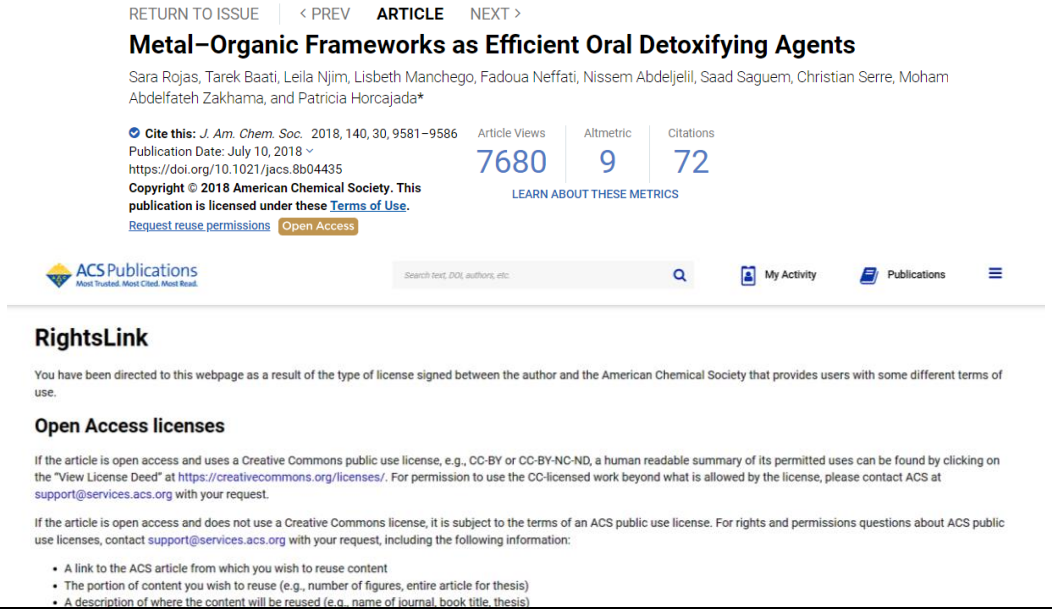

RETURN TO ISSUE | < PREV **ARTICLE** NEXT >

Metal–Organic Frameworks as Efficient Oral Detoxifying Agents

Sara Rojas, Tarek Baati, Leila Njim, Lisbeth Manchego, Fadoua Neffati, Nissem Abdeljelil, Saad Saguem, Christian Serre, Moham Abdelfateh Zakhama, and Patricia Horcajada*

Cite this: *J. Am. Chem. Soc.* 2018, 140, 30, 9581–9586
Publication Date: July 10, 2018
https://doi.org/10.1021/jacs.8b04435

Article Views 7680 | Altmetric 9 | Citations 72

LEARN ABOUT THESE METRICS

Copyright © 2018 American Chemical Society. This publication is licensed under these Terms of Use.
Request reuse permissions Open Access

ACS Publications Most Trusted. Most Cited. Most Read. | Search text, DOI, authors, etc | My Activity | Publications

RightsLink

You have been directed to this webpage as a result of the type of license signed between the author and the American Chemical Society that provides users with some different terms of use.

Open Access licenses

If the article is open access and uses a Creative Commons public use license, e.g., CC-BY or CC-BY-NC-ND, a human readable summary of its permitted uses can be found by clicking on the "View License Deed" at https://creativecommons.org/licenses/. For permission to use the CC-licensed work beyond what is allowed by the license, please contact ACS at support@services.acs.org with your request.

If the article is open access and does not use a Creative Commons license, it is subject to the terms of an ACS public use license. For rights and permissions questions about ACS public use licenses, contact support@services.acs.org with your request, including the following information:

- A link to the ACS article from which you wish to reuse content
- The portion of content you wish to reuse (e.g., number of figures, entire article for thesis)
- A description of where the content will be reused (e.g., name of journal, book title, thesis)

USC UNIVERSIDADE DE SANTIAGO DE COMPOSTELA

Appendix IV: All the other images, tables, and figures

Manuela Cedrún Morales, the doctoral candidate, declares that all the other images, tables and figures shown in this Doctoral Thesis have been personally elaborated.

USC
UNIVERSIDADE DE SANTIAGO DE COMPOSTELA

USC
UNIVERSIDADE
DE SANTIAGO
DE COMPOSTELA

This thesis aims to advance nanomedicine by developing nano metal-organic frameworks for enhanced drug delivery. Various systems were synthesized and tailored to investigate their encapsulation abilities and surface modi ications to provide them with targeting capabilities. Additionally, nanocomposites responsive to near-infrared (NIR) light were created, comprising a core of gold nanoparticles and a shell of nano metal-organic frameworks. These intelligent nanocarriers were designed to facilitate intracellular cargo delivery through innovative strategies.